

STUDIES ON HOT CORROSION BEHAVIOUR OF BOILER TUBE STEEL WELDMENTS

A THESIS

*Submitted in partial fulfilment of the
requirements for the award of the degree*

of

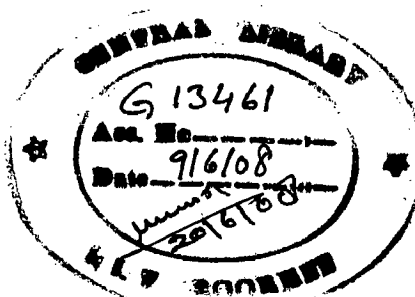
DOCTOR OF PHILOSOPHY

in

METALLURGICAL AND MATERIALS ENGINEERING

By

RAVINDRA KUMAR.



DEPARTMENT OF METALLURGICAL AND MATERIALS ENGINEERING
INDIAN INSTITUTE OF TECHNOLOGY ROORKEE
ROORKEE-247 667 (INDIA)

JULY, 2007



INDIAN INSTITUTE OF TECHNOLOGY ROORKEE ROORKEE


CANDIDATE'S DECLARATION


I hereby certify that the work which is being presented in the thesis, entitled **STUDIES ON HOT CORROSION BEHAVIOUR OF BOILER TUBE STEEL WELDMENTS** in partial fulfilment of the requirements for the award of the degree of Doctor of Philosophy and submitted in the Department of Metallurgical and Materials Engineering of the Indian Institute of Technology Roorkee, Roorkee is an authentic record of my own work carried out during a period from July, 2002 to July, 2007 under the supervision of Dr. Satya Prakash, Professor and Dr. V. K. Tewari, Professor (On leave), Department of Metallurgical and Materials Engineering, Indian Institute of Technology Roorkee, Roorkee.

The matter presented in this thesis has not been submitted by me for the award of any other degree of this or any other Institute.


(RAVINDRA KUMAR)


This is to certify that the above statement made by the candidate is correct to the best of our knowledge.


(Dr. V. K. TEWARI)
Professor (On leave)



(Dr. SATYA PRAKASH)
Professor

Date: 19.07.07

The Ph.D. Viva-Voce Examination of Mr. Ravindra Kumar, Research Scholar, has been held on Nov. 6, 2007


Signature of Supervisors




Signature of External Examiner

© INDIAN INSTITUTE OF TECHNOLOGY ROORKEE, ROORKEE, 2007
ALL RIGHTS RESERVED

These corroded samples were then cut across the cross-section and mounted to study the cross-sectional details by EPMA.

The shielded metal arc and tungsten inert gas welding were found to have no porosity or very less porosity as a result of sound weld. The microhardness plots have indicated reduction in hardness values from weld metal to HAZ in case of SMAW weldment in T11 steel whereas the HAZ have the more hardness in other welded steel. The tensile strength and percentage elongation was measured

Oxidation and hot corrosion products analysed in the scale are mostly oxides of the elements present in the weld and base materials for the samples corroded in all the two environments of this study. The presence of continuous Cr_2O_3 layer at the substrate-scale interface is predominantly revealed in most of the cases. Iron oxide (Fe_2O_3) was the main phase in the scale.

The results obtained for welded steel, corrosion resistance during oxidation in air and molten salt at 900°C had followed the overall trend in following order:

$$\text{T11} > \text{GrA1} > \text{T22}$$

The internal oxidation and cracks in the oxide scale of weldment in steels has been observed for the studies performed in air and molten salt environment at elevated temperature. These cracks were found to be minute in case of studies conducted on different regions of weldment i.e. weld metal and HAZ in the given environment.

The oxide protrusions from the beneath have been observed mainly through the cracks during studies conducted in air and molten salt environments. These protrusions were identified to be of iron oxide in case of all the weldments. The cracking of scale and oxide protrusions from beneath has been observed to be maximum in unwelded T22 steel and the minimum in case of unwelded T11 steel. Among the unwelded steels comparatively maximum resistance to oxidation was indicated by T22 steel and minimum by GrA1 steel during oxidation in air at 900°C .

In case of studies under molten salt, the XRD diffractograms and EDAX analysis have indicated the phases formed identical to those formed during oxidation in air in almost all the corroded weldments.

Among the different regions of SMAW and TIG weldments in different grade of steels the base metal and HAZ showed the more oxidation as compared to weld metal, but this trend has changed in case of welded T11 steel in molten salt environment where the weld metal indicates more oxidation as compared to the base metal and HAZ.

ACKNOWLEDGEMENTS

The author has great privilege and pleasure to express his immense sense of gratitude to Dr. Satya Prakash, Professor and Dr. V. K. Tewari, Professor, Department of Metallurgical and Materials Engineering (MMED), Indian Institute of Technology, Roorkee for their valuable guidance and untiring efforts throughout the tenure of this work. They have been an inspiring and driving force where targets appeared to be difficult during the course of work. Their timely help, constructive criticism and painstaking efforts made the author capable to compile the thesis in its present form.

Author is highly indebted to Dr. S. K. Nath, Head, Metallurgical and Materials Engineering Department (MMED), Indian Institute of Technology Roorkee for necessary facilities during the course of experimental and analysis work. Author wishes to record his deep sense of gratitude to Head, Department of Mechanical and Industrial Engineering (MIED) and the Head, Institute Instrumentation Centre (IIC), Indian Institute of Technology Roorkee for extending necessary facilities during the course of experimental and analysis work. The valuable thanks to Dr. P. K. Ghosh for his suggestions and help during pungent facet of the welding work.

The author is highly obliged and wishes to owe his sincere thanks to the technical and administrative staff of the MMED, especially to Mr. Shamsher Singh, Mr. Rajinder Sharma, Mr. Vidya Prakash, Mr. N. K. Seth, Mr. Shakti Gupta, Mr. S. N. Kaushik, Mr. Vaish, Mr. Dharam Pal, Mr. Dhan Prakash, Mr. Kailash, Mr. Ajmer Singh, Mr. T. K. Sharma and Mr. R. K. Sharma who have helped in all possible ways during the experimental work. Thanks are also due to Mr. Sunil Sharma, Librarian of MMED for providing all the necessary help. Sincere thanks are acknowledged to Mr. Narendra Kumar for help in typing of thesis manuscript. Author would like to owe his special thanks to Mr. Ahuja who has helped in all possible ways during welding work.

Author would like to owe his sincere thanks to Mr. S. K. Saini, Mrs. Rekha Sharma and Dr. T. K. Ghosh of IIC, IIT Roorkee for carrying out XRD, SEM and EPMA work respectively. Special thanks are for Mr. Jagpal Singh of Welding Research Laboratory of MIED of IIT, Roorkee for his cooperation during experimentation work. Thanks are also acknowledged to Mr. Puran Sharma for preparing high quality micrographs.

Author would like to record his sense of gratitude for the library staff of IIT Roorkee, (IIT Kanpur and IIT Kharagpur for their kind cooperation to carry out the literature survey). Author owes his sincere thanks to Dr. R. Maithi of CRF (IIT Kharagpur for performing EDAX analysis). Author wishes to thank friends and colleagues for their encouragement and camaraderie help to keep things in perspective. Thanks are due to, Mr. N. Arivazagan, Mr. P.K. Sapara, Mr. M. R. Ramesh, Mr. Mahesh R. A. and Mr. L.B. Gautam.

The author would like to express his reverence and great admiration for his parents who have always been the guiding force for him. Author is highly grateful to his brother who cooperated his best for the duration of this work. Thanks are due to his other family members who have shown patience for the entire duration of this work.

Above all author is grateful to almighty God who has blessed the spiritual support and courage at each and every step of this work.

(Ravindra Kumar)

PREFACE

The entire work carried out for this investigation has been presented into eight chapters.

Chapter-1 contains the introductory remarks about hot corrosion problem in weldments faced by the various industries and especially in coal fired boilers.

Chapter-2 begins with exhaustive survey of literature regarding various aspects and mechanisms of hot corrosion. Critical review of the existing studies and detailed behaviour of weldments to counteract the hot corrosion degradation have been made. After reviewing the available literature the problem has been formulated.

Chapter-3 deals with the experimental procedure which includes the procedure to obtain the weldments, their characterisation, the hot corrosion studies and the analysis of final corrosion products in systematic way.

Chapter-4 includes the findings and discussions of the study regarding the characterisation of weldments.

Chapter-5 contains the data regarding the cyclic oxidation studies performed on weldments, its different regions and unwelded steels in air at 900⁰C. It also includes the critical discussion of results in view of the existing literature.

Chapter-6 includes the findings regarding the behaviour of weldments, its different region and unwelded steels for cyclic hot corrosion in molten salt (Na_2SO_4 -60% V_2O_5) at 900⁰C along with discussion of results.

Chapter-7 includes the comprehensive discussions of the results with respect to the existing literature.

Chapter-8 compiles the salient conclusions of the present study regarding the characterisation, oxidation, hot corrosion behaviour of weldments, its different regions and unwelded steels in all the two given environments.

CONTENTS

	Page No.
Candidate's Declaration	i
Abstract	ii
Acknowledgements	iv
Preface	vi
List of Figures	xvi
List of Tables	xxxii
List of Research Publications	xxxiv
Abbreviations	xxxv
CHAPTER 1 INTRODUCTION	1
CHAPTER 2 LITERATURE REVIEW	4
2.1 FERRITIC Cr-Mo STEEL	4
2.2 WELDABILITY OF Cr- Mo STEEL	6
2.3 WELDING PROCESS	7
2.3.1 <i>Fusion Welding</i>	7
2.3.1.1 <i>Shielded Metal Arc Welding</i>	7
2.3.1.2 <i>Tungsten Inert Gas Welding</i>	8
2.3.2 <i>Microstructure of Cr-Mo Steel Weldments</i>	8
2.3.3 <i>Causes of Welded Failures</i>	11
2.3.4 <i>Microhardness of the Cr- Mo Steel Weldments</i>	11
2.3.5 <i>Metallurgical effects on Corrosion of Weldments</i>	12
2.4 OXIDATION AT HIGH TEMPERATURE	15
2.4.1 <i>Mechanism of Oxidation</i>	15
2.5 HOT CORROSION	16
2.5.1 <i>Mechanisms of Hot Corrosion</i>	16
2.5.1.1 <i>Type I High temperature hot corrosion (HTHC)</i>	17

2.5.1.2	<i>Type II Low temperature hot corrosion (LTHC)</i>	17
2.5.2	Hot Corrosion Degradation Sequence in the Alloy	17
2.5.3	Salt Fluxing	18
2.5.4	Salt Chemistry	22
2.5.4.1	<i>Sulphate Solution Chemistry</i>	22
2.5.4.2	<i>Vanadate Solution Chemistry</i>	22
2.5.5	<i>Hot Corrosion of Superheater/Reheater Boiler Tube Steel</i>	23
2.5.5.1	Water Side Corrosion	26
2.6	BEHAVIOUR OF BASE AND WELDED METALS, ALLOYS IN VARIOUS OXIDISING ENVIRONMENTS	26
2.6.1	Air	26
2.6.2	Molten Salt (Na ₂ SO ₄ -V ₂ O ₅) Environment	30
2.6.3	Energy Generation Systems	35
2.7	HOT CORROSION PROBLEMS ASSOCIATED WITH WELDING OF BOILER AND PRESSURE PARTS	37
2.7.1	Microstructural Variation Corrosion of Different Regions of Weldments	40
2.7.2	Economic Factors in Weldments	44
2.7.3	Component Integrity and Life Assessment of Weldment	45
2.8	EFFECT OF AQUEOUS CORROSION ON WELDMENTS	46
2.9	FORMULATION OF PROBLEM	48
CHAPTER 3	EXPERIMENTAL PROCEDURE	52
3.1	SELECTION OF SUBSTRATE STEELS	52
3.1.1	Determination of Chemical Compositions	52
3.2	EXECUTION OF WELDMENTS	52
3.2.1	Edge preparation	52
3.2.2	Welding processes	53
3.2.3	Formulation of Weldments	53
3.2.4	Preparation of Samples Materials	55
3.3	CHARACTERISATION OF WELDMENTS	55
3.3.1	Measurement of Weldment Width and Optical Microstructure of Weldments	55

3.3.2	Porosity Analysis	55
3.3.3	Microhardness Measurement	56
3.3.4	Tensile Testing	56
3.3.5	Metallographic Studies	56
3.4	HIGH TEMPERATURE OXIDATION AND HOT CORROSION STUDIES	57
3.4.1	Experimental Setup	57
3.4.2	Oxidation Studies in Air	57
3.4.3	Hot Corrosion Studies in Molten Salt (Na ₂ SO ₄ -60%V ₂ O ₅)	57
	3.4.3.1 Molten Salt coating	57
	3.4.3.2 Hot Corrosion Studies	58
3.5	ANALYSIS OF CORROSION PRODUCTS OF OXIDATION IN AIR, MOLTEN SALT AND BOILER ENVIRONMENT	58
3.5.1	Visual Observation	58
3.5.2	Thermogravimetric Studies	58
3.5.3	Measurement of Scale Thickness	58
3.5.4	X-Ray Diffraction (XRD) Analysis	58
3.5.5	SEM/EDAX Analysis	59
	3.5.5.1 Surface morphology	59
3.5.6	Electron Probe Micro Analyser (EPMA)	59
CHAPTER 4	CHARACTERISATION OF SUBSTRATE STEELS AND WELDMENTS	60
4.1	SUBSTRATE STEELS AND ELECTRODES/FILLER WIRE	60
4.1.1	Chemical Composition	60
4.1.2	Microstructures of Substrate Steels	61
4.2	VISUAL EXAMINATION OF WELDMENTS	61
4.3	MEASUREMENTS OF WELDMENTS WIDTH AND SIZE OF TUBE	64
4.4	POROSITY ANALYSIS	64
4.5	EVALUATION OF MICROHARDNESS OF WELDMENTS	65
4.6	EVALUATION OF TENSILE STRENGTH OF WELDMENTS	65
4.7	METALLOGRAPHIC STUDIES OF WELDMENTS	70

4.7.1	Cross-Sectional Microstructure of SMAW Weldment	70
4.7.1.1	<i>GrA1 Steel</i>	70
4.7.1.2	<i>T11 Steel</i>	70
4.7.1.3	<i>T22 Steel</i>	70
4.7.2	Cross-Sectional Microstructure of TIG Weldment	70
4.7.2.1	<i>GrA1 Steel</i>	70
4.7.2.2	<i>T11 Steel</i>	71
4.7.2.3	<i>T22 Steel</i>	71
4.8	DISCUSSION	78
CHAPTER 5	PART (A) OXIDATION STUDIES OF UNWELDED AND WELDMENTS STEELS IN AIR	80
5.1	RESULTS	80
5.1.1	Unwelded Steels	80
5.1.1.1	<i>Visual Examination</i>	80
5.1.1.2	<i>Thermogravimetric Data</i>	80
5.1.1.3	<i>X-ray Diffraction Analysis</i>	81
5.1.1.4	<i>Scale Thickness Measurement</i>	81
5.1.1.5	<i>SEM/EDAX Analysis</i>	81
5.1.1.5.1	<i>Surface Morphology</i>	81
5.1.2	SMAW Weldment	87
5.1.2.1	<i>Visual Examination</i>	87
5.1.2.2	<i>Thermogravimetric Data</i>	87
5.1.2.3	<i>X-ray Diffraction Analysis</i>	87
5.1.2.4	<i>Scale Thickness Measurement</i>	88
5.1.2.5	<i>SEM/EDAX Analysis</i>	88
5.1.2.5.1	<i>Surface Morphology</i>	88
5.1.3	TIG Weldment	94
5.1.3.1	<i>Visual Examination</i>	94
5.1.3.2	<i>Thermogravimetric Data</i>	94
5.1.3.3	<i>X-ray Diffraction Analysis</i>	94
5.1.3.4	<i>Scale Thickness Measurement</i>	94

5.1.3.5	<i>SEM/EDAX Analysis</i>	95
5.1.3.5.1	<i>Surface Morphology</i>	95
PART (B) OXIDATION STUDIES OF DIFFERENT REGIONS OF STEEL WELDMENTS IN AIR		101
5.2	RESULTS	101
5.2.1	Different Regions of SMAW Weldment i. e. the Base Metal, HAZ and Weld Metal exposed to Air at 900 °C for 50 cycles in GrA1 Steel	101
5.2.1.1	<i>Visual Examination</i>	101
5.2.1.2	<i>Thermogravimetric Data</i>	101
5.2.1.3	<i>X-ray Diffraction Analysis</i>	102
5.2.1.4	<i>Scale Thickness Measurement</i>	102
5.2.1.5	<i>SEM/EDAX Analysis</i>	102
5.2.1.5.1	<i>Surface Morphology</i>	102
5.2.2	Different Regions of SMAW Weldment i. e. the Base Metal, HAZ and Weld Metal exposed to Air at 900 °C for 50 cycles in T11 Steel	108
5.2.2.1	<i>Visual Examination</i>	108
5.2.2.2	<i>Thermogravimetric Data</i>	108
5.2.2.3	<i>X-ray Diffraction Analysis</i>	108
5.2.2.4	<i>Scale Thickness Measurement</i>	109
5.2.2.5	<i>SEM/EDAX Analysis</i>	109
5.2.2.5.1	<i>Surface Morphology</i>	109
5.2.3	Different Regions of SMAW Weldment i. e. Base Metal, HAZ and Weld Metal exposed to 900 °C in Air for 50 cycles in T22 Steel	115
5.2.3.1	<i>Visual Examination</i>	115
5.2.3.2	<i>Thermogravimetric Data</i>	115
5.2.3.3	<i>X-ray Diffraction Analysis</i>	115
5.2.3.4	<i>Scale Thickness Measurement</i>	115
5.2.3.5	<i>SEM/EDAX Analysis</i>	116
5.2.3.5.1	<i>Surface Morphology</i>	116
5.2.4	Different Regions of TIG Weldment i. e. the Base Metal, HAZ and Weld Metal exposed to Air at 900 °C for 50 cycles in GrA1 Steel	122
5.2.4.1	<i>Visual Examination</i>	122

5.2.4.2	<i>Thermogravimetric Data</i>	122
5.2.4.3	<i>X-ray Diffraction Analysis</i>	122
5.2.4.4	<i>Scale Thickness Measurement</i>	123
5.2.4.5	<i>SEM/EDAX Analysis</i>	123
5.2.4.5.1	<i>Surface Morphology</i>	123
5.2.5	Different Regions of TIG Weldment i. e. the Base Metal, HAZ and Weld Metal exposed to Air at 900 °C for 50 cycles in T11 Steel	129
5.2.5.1	<i>Visual Examination</i>	129
5.2.5.2	<i>Thermogravimetric Data</i>	129
5.2.5.3	<i>X-ray Diffraction Analysis</i>	129
5.2.5.4	<i>Scale Thickness Measurement</i>	130
5.2.5.5	<i>SEM/EDAX Analysis</i>	130
5.2.5.5.1	<i>Surface Morphology</i>	130
5.2.6	Different Regions of TIG Weldment i. e. the Base metal, HAZ and Weld Metal exposed to Air at 900 °C for 50 cycles in T22 Steel	136
5.2.6.1	<i>Visual Examination</i>	136
5.2.6.2	<i>Thermogravimetric Data</i>	136
5.2.6.3	<i>X-ray Diffraction Analysis</i>	136
5.2.6.4	<i>Scale Thickness Measurement</i>	137
5.2.6.5	<i>SEM/EDAX Analysis</i>	137
5.2.6.5.1	<i>Surface Morphology</i>	137
5.3	SUMMARY OF RESULTS	143
5.4	DISCUSSION	145
5.4.1	Unwelded Steels	145
5.4.2	SMAW Weldment	146
5.4.3	TIG Weldment	146
5.4.4	Different Regions of SMAW and TIG Weldment in GrA1 Steel	147
5.4.5	Different Regions of SMAW and TIG Weldment in T11 Steel	147
5.4.6	Different Regions of SMAW and TIG Weldment in T22 Steel	148
CHAPTER 6	PART (A) HOT CORROSION STUDIES OF UNWELDED AND WELDMENTS STEELS IN MOLTEN SALT ENVIRONMENT	149
6.1	RESULTS	149

6.1.1	Unwelded Steels	149
6.1.1.1	<i>Visual Examination</i>	149
6.1.1.2	<i>Thermogravimetric Data</i>	150
6.1.1.3	<i>X-ray Diffraction Analysis</i>	150
6.1.1.4	<i>Scale Thickness Measurement</i>	150
6.1.1.5	<i>SEM/EDAX Analysis</i>	158
6.1.1.5.1	Surface Morphology	158
6.1.1.6	<i>EPMA Analysis</i>	158
6.1.2	SMAW Weldment	158
6.1.2.1	<i>Visual Examination</i>	158
6.1.2.2	<i>Thermogravimetric Data</i>	159
6.1.2.3	<i>X-ray Diffraction Analysis</i>	159
6.1.2.4	<i>Scale Thickness Measurement</i>	159
6.1.2.5	<i>SEM/EDAX Analysis</i>	170
6.1.2.5.1	Surface Morphology	170
6.1.2.6	<i>EPMA Analysis</i>	170
6.1.3	TIG Weldment	171
6.1.3.1	<i>Visual Examination</i>	171
6.1.3.2	<i>Thermogravimetric Data</i>	171
6.1.3.3	<i>X-ray Diffraction Analysis</i>	177
6.1.3.4	<i>Scale Thickness Measurement</i>	177
6.1.3.5	<i>SEM/EDAX Analysis</i>	177
6.1.3.5.1	Surface Morphology	177
6.1.3.6	<i>EPMA Analysis</i>	178

**PART (B) HOT CORROSION STUDIES OF DIFFERENT REGIONS
OF STEEL WELDMENTS IN MOLTEN SALT
ENVIRONMENT**

6.2	RESULTS	185
6.2.1	Different Regions of SMAW Weldment i.e. Base Metal, Weld Metal and HAZ exposed to Molten Salt at 900°C in GrA1 Steel	185
6.2.1.1	<i>Visual Examination</i>	185
6.2.1.2	<i>Thermogravimetric Data</i>	186
6.2.1.3	<i>X-ray Diffraction Analysis</i>	186
6.2.1.4	<i>Scale Thickness Measurement</i>	186
6.2.1.5	<i>SEM/EDAX Analysis</i>	186
6.2.1.5.1	Surface Morphology	186

6.2.1.6	<i>EPMA Analysis</i>	194
6.2.2	Different Regions of SMAW Weldment i.e. Base Metal, Weld Metal and HAZ exposed to Molten Salt at 900°C in T11 Steel	194
6.2.2.1	<i>Visual Examination</i>	194
6.2.2.2	<i>Thermogravimetric Data</i>	194
6.2.2.3	<i>X-ray Diffraction Analysis</i>	195
6.2.2.4	<i>Scale Thickness Measurement</i>	195
6.2.2.5	<i>SEM/EDAX Analysis</i>	195
	6.2.2.5.1 Surface Morphology	195
6.2.2.6	<i>EPMA Analysis</i>	195
6.2.3	Different Regions of SMAW Weldment i.e. Base Metal, Weld Metal and HAZ exposed to Molten Salt at 900°C in T22 Steel	203
6.2.3.1	<i>Visual Examination</i>	203
6.2.3.2	<i>Thermogravimetric Data</i>	203
6.2.3.3	<i>X-ray Diffraction Analysis</i>	203
6.2.3.4	<i>Scale Thickness Measurement</i>	204
6.2.3.5	<i>SEM/EDAX Analysis</i>	204
	6.2.3.5.1 Surface Morphology	204
6.2.3.6	<i>EPMA Analysis</i>	204
6.2.4	Different Regions of TIG Weldment i.e. Base Metal, Weld Metal and HAZ exposed to Molten Salt at 900°C in GrA1 Steel	212
6.2.4.1	<i>Visual Examination</i>	212
6.2.4.2	<i>Thermogravimetric Data</i>	212
6.2.4.3	<i>X-ray Diffraction Analysis</i>	212
6.2.4.4	<i>Scale Thickness Measurement</i>	212
6.2.4.5	<i>SEM/EDAX Analysis</i>	213
	6.2.4.5.1 Surface Morphology	213
6.2.4.6	<i>EPMA Analysis</i>	213
6.2.5	Different Regions of TIG Weldment i.e. Base Metal, Weld Metal and HAZ exposed to Molten Salt at 900°C in T11 Steel	221
6.2.5.1	<i>Visual Examination</i>	221
6.2.5.2	<i>Thermogravimetric Data</i>	221
6.2.5.3	<i>X-ray Diffraction Analysis</i>	221
6.2.5.4	<i>Scale Thickness Measurement</i>	222
6.2.5.5	<i>SEM/EDAX Analysis</i>	222

6.2.5.5.1	Surface Morphology	222
6.2.5.6	<i>EPMA Analysis</i>	222
6.2.6	Different Regions of TIG Weldment i.e. Base Metal, Weld Metal and HAZ exposed to Molten Salt at 900°C in T22 Steel	230
6.2.6.1	<i>Visual Examination</i>	230
6.2.6.2	<i>Thermogravimetric Data</i>	230
6.2.6.3	<i>X-ray Diffraction Analysis</i>	230
6.2.6.4	<i>Scale Thickness Measurement</i>	230
6.2.6.5	<i>SEM/EDAX Analysis</i>	231
6.2.6.5.1	Surface Morphology	231
6.2.6.6	<i>EPMA Analysis</i>	231
6.3	SUMMARY OF RESULTS	239
6.4	DISCUSSION	241
6.4.1	Unwelded Steels	241
6.4.2	SMAW weldments	242
6.4.3	TIG weldment	243
6.4.4	Different regions of SMAW and TIG weldment in GrA1 Steel	244
6.4.5	Different regions of SMAW and TIG weldment in T11 Steel	245
6.4.6	Different regions of SMAW and TIG weldment in T22 Steel	245
CHAPTER 7	COMPREHENSIVE DISCUSSION	246
CHAPTER 8	CONCLUSIONS	251
	SUGGESTIONS FOR FUTURE WORK	253
	APPENDIX	254
	REFERENCES	257

LIST OF FIGURES

Figure No.	Particulars	Page No.
Fig. 2.1	Principle of the manual metal arc process or SMAW (Castro and De Cadenet, 1975).	10
Fig. 2.2	Principle of the TIG process (Castro and De Cadenet, 1975).	10
Fig. 2.3	An illustration of the essential constituents of the primary microstructure of a steel weld deposit (Bhadeshia et al. 1993).	13
Fig. 2.4	Location of the microhardness traverses at the root and bay regions of a weld bead with in the HAZ of (a) tempered bead weld (b) conventional weaving weld (Peddle and Pickles, 2000).	14
Fig. 2.5	Effects of aging at 538 °C on the hardness of the HAZ produced by the tempered bead welding process (Bass et al, 1994).	14
Fig. 2.6	Schematic illustration of the growth of chromia scales in (i) the absence of oxygen active elements and with predominant outward transport of chromia through the scale, and (ii) the presence of oxygen active elements and with predominant inward transport of oxygen (Kofstad, 1990).	19
Fig. 2.7	(a) Schematic diagram for fluxing showing dissolution of metal oxide at the oxide/salt interface (Shores, 1983) and (b) Precipitation of a porous MO oxide supported by the solubility gradient in a fused salt film (Rapp and Zhang, 1994).	24
Fig. 2.8	Na-Cr-S-O phase stability diagram for 1200 K (Rapp, 1986).	25
Fig. 2.9	Phase stability diagram for Na-V-S-O system at 900 °C (Hwang and Rapp, 1989).	28

Fig. 2.10	Phase Diagram for Na ₂ SO ₄ -V ₂ O ₅ System (Otero et al, 1987).	33
Fig. 2.11	Showing grain boundary attack at 650 °C due to coating of sulphate chloride mixture in welded 2.2Cr-1Mo steel (a) HAZ (b) unwelded (c) Weld Metal (Ahila et al, 1993).	42
Fig. 2.12	SEM micrograph showing extensive grain boundary oxidation causing grain detachment during air-oxidation of 2.25Cr-1Mo steel at 823 K (Raman et al, 1992).	47
Fig. 2.13	Representative SEM micrographs showing cross-sections through oxide scales and subscale zones formed over (a) the base metal/weld metal specimens, and (b) HAZ, during steam oxidation at 873 K (Raman and Muddle, 2000A).	47
Fig. 3.1	Schematic view of weldment design (a) for GrA1 and T11 tube (b) for T22 tube.	54
Fig. 4.1	Optical micrographs of substrate steels (a) ASTM-SA210-Grade A1 (GrA1), 250X (b)ASTM-SA213-T-11 (T11), 250X (c) ASTM-SA213-T-22 (T22), 250 X.	62
Fig. 4.2	Macrograph for the cross-sectional view of the SMAW weldment in steels (a) GrA1 (b) T11 (c) T22.	63
Fig. 4.3	Macrograph for the cross-sectional view of the TIG weldment in steels (a) GrA1 (b) T11 (c) T22.	63
Fig. 4.4	Microhardness profiles of SMAW weldment in GrA1, T11 and T22 boiler steel.	66
Fig. 4.5	Microhardness profiles of TIG weldment in GrA1, T11 and T22 boiler steel.	66
Fig. 4.6	Stress vs strain curve for SMAW weldment in GrA1 steel.	67
Fig. 4.7	Stress vs strain curve for SMAW weldment in T11 steel.	67
Fig. 4.8	Stress vs strain curve for SMAW weldment in T22 steel.	68
Fig. 4.9	Stress vs strain curve for TIG weldment in GrA1 steel.	68
Fig. 4.10	Stress vs strain curve for TIG weldment in T11 steel.	69
Fig. 4.11	Stress vs strain curve for TIG weldment in T22 steel.	69

Fig. 4.12	Optical microstructure of SMAW weldment in GrA1 steel (a) Weld Metal, 200X (b) Weld Metal, 100X (c) HAZ Coarse Grain, 200X (d) HAZ Coarse +Fine Grain, 100X.	72
Fig. 4.13	Optical microstructure of SMAW weldment in T11 steel (a) Weld Metal, 200X (b) Weld Metal, 100X (c) HAZ Coarse Grain, 200X (d) HAZ Coarse Grain, 100X.	73
Fig. 4.14	Optical microstructure of SMAW weldment in T22 steel (a) Weld Metal, 200X (b) Weld Metal, 100X (c) HAZ Coarse Grain, 200X (d) HAZ Coarse Grain, 100X.	74
Fig. 4.15	Optical microstructure of TIG weldment in GrA1 steel (a) Weld Metal, 200X (b) Weld Metal, 100X (c) HAZ Coarse Grain, 200X (d) HAZ Coarse Grain, 100X.	75
Fig. 4.16	Optical microstructure of TIG weldment in T11 steel (a) Weld Metal, 200X (b) Weld Metal, 100X (c) HAZ Coarse Grain, 200X (d) HAZ Coarse Grain, 100X.	76
Fig. 4.17	Optical microstructures of TIG weldment in T22 steel (a) Weld Metal, 200X (b) Weld Metal, 100X (c) HAZ Coarse Grain, 100X (d) HAZ Fine Grain, 100X.	77
Fig. 5.1	Macrographs of unwelded steels subjected to cyclic oxidation in air at 900 °C for 50 cycles (a) GrA1, (b) T11 and (c) T22.	82
Fig. 5.2	Weight gain plot for unwelded steels exposed to air at 900°C for 50 cycles.	83
Fig. 5.3	Weight gain square (mg^2/cm^4) plot for unwelded steels exposed to air at 900°C for 50 cycles.	83
Fig. 5.4	X-ray diffraction profiles for GrA1, T11 and T22 boiler steels subjected to cyclic oxidation in air at 900°C for 50 cycles.	84
Fig. 5.5	SEM backscattered image of the cross-section of unwelded steels after cyclic oxidation in air at 900°C for 50 cycles (a) GrA1, 200X (b) T11, 200X (c) T22, 50X.	85
Fig. 5.6	SEM micrographs showing surface scale morphology and EDAX analysis for unwelded boiler steels oxidized in air at 900 °C for 50 cycles (a) GrA1, 1000X (b) T11, 1000X (c) T22, 200X.	86

Fig. 5.7	Macrographs of the corroded SMAW weldments of (a) GrA1, (b) T11 and (c) T22 steels subjected to cycle oxidation in air at 900 °C for 50 cycles	89
Fig. 5.8	Weight gain plot for unwelded and SMAW weldment of different steels exposed to air at 900 °C for 50 cycles.	90
Fig. 5.9	Weight gain square (mg^2/cm^4) plot for unwelded and SMAW weldment of different steels exposed to air at 900 °C for 50 cycles.	90
Fig. 5.10	X- ray diffraction profiles for corroded SMAW weldment in GrA1, T11 and T22 boiler steels subjected to cycle oxidation in air at 900 °C for 50 cycles.	91
Fig. 5.11	SEM back scattered image of cross section for SMAW weldment in (a) GrA1(weld),150X (b) GrA1(HAZ), 150X (c) T11(weld), 50X (d) T11 (HAZ), 50X (e) T22(weld), 60X (f) T22 (HAZ), 60X steels after cyclic oxidation in air at 900 °C for 50 cycles.	92
Fig. 5.12	SEM micrographs showing surface scale morphology and EDAX analysis for SMAW weldment of different steels in air at 900 °C for 50 cycles (a) GrA1(weld, 1000X (b) GrA1 (HAZ), 3000X (c) T11 (weld), 1000X (d) T11 (HAZ), 1000X (e) T22 (weld), 1000 X (f) T22 (HAZ), 3000X.	93
Fig. 5.13	Macrographs of TIG weldment in (a) GrA1, (b) T11 and (c) T22 steels subjected to cycle oxidation in air at 900 °C for 50 cycles.	96
Fig. 5.14	Weight gain plot for unwelded and TIG weldment of the different steels exposed to air at 900 °C for 50 cycles.	97
Fig. 5.15	Weight gain square (mg^2/cm^4) plot for TIG Weldment of the different steels exposed to air at 900 °C for 50 cycles.	97
Fig. 5.16	X-ray diffraction profiles for corroded TIG weldment in GrA1, T11 and T22 boiler steels subjected to cyclic oxidation in air at 900 °C for 50 cycles.	98
Fig. 5.17	SEM back scattered image of cross section for TIG weldment steels after cyclic oxidation in air at 900 °C for 50 cycles (a) GrA1 (weld), 200X (b) GrA1 (HAZ), 200X (c) T11(weld), 150X and (d) T11 (HAZ), 150X (e) T22 (weld), 150X (f) T22 (HAZ), 150X.	99

Fig. 5.18	Surface morphology and EDAX analysis for TIG weldment of the different steels oxidized in air at 900 °C for 50 cycles (a) GrA1 (weld), 1000X (b) GrA1 (HAZ), 1000X (c) T11 (weld), 1000X (d) T11 (HAZ), 1000K (e) T22 (weld), 1000X (f) T22 (HAZ), and 1000 X.	100
Fig. 5.19	Macrographs of different regions of SMAW weldments in GrA1 steel subjected to cyclic oxidation in air at 900 °C for 50 cycles (a) Base Metal, (b) Weld Metal and (c) HAZ.	103
Fig. 5.20	Weight gain plot for different regions of SMAW weldment in GrA1 steel exposed to air at 900 °C for 50 cycles.	104
Fig. 5.21	Weight gain square (mg^2/cm^4) plot for different regions of SMAW weldment in GrA1 steel exposed to air at 900 °C for 50 cycles.	104
Fig. 5.22	X-ray diffraction profiles for different regions of SMAW weldment in GrA1 steel exposed to air at 900 °C for 50 cycles.	105
Fig. 5.23	SEM back scattered image of the cross section of different regions of SMAW weldment in GrA1 steel exposed to air at 900 °C for 50 cycles (a) Weld Metal, 200X (b) HAZ, 200X.	106
Fig. 5.24	Surface morphology and EDAX analysis for different regions of SMAW weldment in GrA1 steel exposed to air at 900 °C for 50 cycles (a) Weld Metal, 1000X and (b) HAZ, 1000X.	107
Fig. 5.25	Macrographs of different regions of SMAW weldments in T11 steel subjected to cyclic oxidation in air at 900 °C for 50 cycles (a) Base Metal, (b) Weld Metal and (c) HAZ.	110
Fig. 5.26	Weight gain plot for different regions of SMAW weldment in T11 steel exposed to air at 900 °C for 50 cycles.	111
Fig. 5.27	Weight gain square (mg^2/cm^4) plot for different regions of SMAW weldment in T11 steel exposed to air at 900 °C for 50 cycles.	111
Fig. 5.28	X-ray diffraction profiles for different regions of SMAW weldment in T11 steel exposed to air at 900 °C for 50 cycles.	112

Fig. 5.29	SEM back scattered image of the cross section of different regions of SMAW weldment in T11 steel exposed to air at 900 °C for 50 cycles (a) Weld Metal, 200X (b) HAZ, 250X.	113
Fig. 5.30	Surface morphology and EDAX analysis of the scale on different regions of SMAW weldment in T11 steel exposed to air at 900 °C for 50 cycles (a) Weld Metal, 1000X and (b) HAZ, 1000X.	114
Fig. 5.31	Macrographs of different regions of SMAW weldment in T22 steel subjected to cyclic oxidation in air at 900 °C for 50 cycles (a) Base Metal, (b) Weld Metal and (c) HAZ.	117
Fig. 5.32	Weight gain plot for different regions of SMAW weldment in T22 steel exposed to air at 900 °C for 50 cycles.	118
Fig. 5.33	Weight gain square (mg^2/cm^4) plot for different regions of SMAW weldment in T22 steel exposed to air at 900 °C for 50 cycles.	118
Fig. 5.34	X-ray diffraction profiles for different regions of SMAW weldment in T22 steel exposed to air at 900 °C for 50 cycles.	119
Fig. 5.35	SEM back scattered image of the cross section of different regions of SMAW weldment in T22 steel exposed to air at 900 °C for 50 cycles (a) Weld Metal, 200X (b) HAZ, 200X.	120
Fig. 5.36	SEM micrographs showing surface morphology and EDAX analysis for different regions of SMAW weldment in T22 steel exposed to air at 900°C for 50 cycles (a) Weld Metal, 1000X and (b) HAZ, 1000X.	121
Fig. 5.37	Macrographs of different regions of TIG weldments in GrA1 steel subjected to cyclic oxidation in air at 900 °C for 50 cycles (a) Base Metal, (b) Weld Metal and (c) HAZ.	124
Fig. 5.38	Weight gain plot for different regions of TIG weldment in GrA1 steel exposed to air at 900 °C for 50 cycles.	125
Fig. 5.39	Weight gain square (mg^2/cm^4) plot for different regions of TIG weldment in GrA1 steel exposed to air at 900 °C for 50 cycles.	125

Fig. 5.40	X-ray diffraction profiles for different regions of TIG weldment in GrA1 steel exposed to air at 900 °C for 50 cycles.	126
Fig. 5.41	SEM back scattered image of the cross section of different regions of TIG weldment in GrA1 steel exposed to air at 900 °C for 50 cycles (a) Weld Metal, 150X (b) HAZ, 150X.	127
Fig. 5.42	SEM micrographs showing the surface morphology and EDAX analysis for different regions of TIG weldment in GrA1 steel exposed to air at 900 °C for 50 cycles (a) Weld Metal, 1000X and (b) HAZ, 1000X.	128
Fig. 5.43	Macrographs of different regions of TIG weldments in T11 steel subjected to cyclic oxidation in air at 900 °C for 50 cycles (a) Base Metal, (b) Weld Metal and (c) HAZ.	131
Fig. 5.44	Weight gain plot for different regions of TIG weldment in T11 steel exposed to air at 900 °C for 50 cycles.	132
Fig. 5.45	Weight gain square (mg^2/cm^4) plot for different regions of TIG weldment in T11 steel exposed to air at 900 °C for 50 cycles.	132
Fig. 5.46	X-ray diffraction profiles for different regions of TIG weldment in T11 steel exposed to air at 900 °C for 50 cycles.	133
Fig. 5.47	SEM back scattered image of cross section of the different regions of TIG weldment in T11 steel exposed to air at 900 °C for 50 cycles (a) Weld Metal, 60X (b) HAZ, 150X.	134
Fig. 5.48	SEM micrographs showing surface morphology and EDAX analysis for different regions of TIG weldment in T11 steel exposed to air at 900 °C for 50 cycles (a) Weld Metal, 1000X and (b) HAZ, 1000X.	135
Fig. 5.49	Macrographs of different regions of TIG weldments in T22 steel subjected to cyclic oxidation in air at 900 °C for 50 cycles (a) Base Metal, (b) Weld Metal and (c) HAZ.	138
Fig. 5.50	Weight gain plot for different regions of TIG weldment in T22 steel exposed to air at 900 °C for 50 cycles.	139

Fig. 5.51	Weight gain square (mg^2/cm^4) plot for different regions of TIG weldment in T22 steel exposed to air at 900 °C for 50 cycles.	139
Fig. 5.52	X-ray diffraction profiles for different regions of TIG weldment in T22 steel exposed to air at 900 °C for 50 cycles.	140
Fig. 5.53	SEM back scattered image of cross section of different regions of TIG weldment in T22 steel exposed to air at 900 °C for 50 cycles (a) Weld Metal, 150X (b) HAZ, 200X.	141
Fig. 5.54	SEM micrographs showing surface morphology and EDAX analysis for different regions of TIG weldment in T22 steel exposed to air at 900 °C for 50 cycles (a) Weld Metal, 1000X and (b) HAZ, 1000X.	142
Fig. 6.1	Macrographs of unwelded steels subjected to cyclic hot corrosion in Na_2SO_4 -60% V_2O_5 at 900 °C for 50 cycles (a) GrA1, (b) T11 and (c) T22.	151
Fig. 6.2	Weight gain plot for unwelded steels exposed to Na_2SO_4 -60% V_2O_5 at 900°C for 50 cycles.	152
Fig. 6.3	Weight gain square (mg^2/cm^4) plot for unwelded steels exposed to Na_2SO_4 -60% V_2O_5 at 900°C for 50 cycles.	152
Fig. 6.4	X-ray diffraction profiles for unwelded GrA1, T11 and T22 boiler steels subjected to cyclic oxidation in Na_2SO_4 -60% V_2O_5 at 900°C for 50 cycles.	153
Fig. 6.5	SEM back scattered image for the cross-section of unwelded steels after cyclic hot corrosion in Na_2SO_4 -60% V_2O_5 at 900°C for 50 cycles (a) GrA1, 100 X and (b) T11, 60 X.	154
Fig. 6.6	SEM micrographs showing surface scale morphology and EDAX analysis for boiler steels oxidized in Na_2SO_4 -60% V_2O_5 at 900°C for 50 cycles (a) GrA1, 2000X (b) T11, 2500X.	155
Fig. 6.7	BSEI and X-ray mapping of the cross-section of GrA1 boiler steel subjected to cyclic oxidation in Na_2SO_4 - 60% V_2O_5 at 900°C for 50 cycles at 200X.	156

Fig. 6.8	BSEI and X-ray mapping of the cross-section of T11 boiler steel subjected to cyclic oxidation in Na ₂ SO ₄ - 60% V ₂ O ₅ at 900°C for 50 cycles at 200X.	157
Fig. 6.9	Macrographs of SMAW weldment steels subjected to cyclic hot corrosion in Na ₂ SO ₄ -60%V ₂ O ₅ at 900°C for 50 cycles (a) GrA1 (b) T11 and (c) T22.	160
Fig. 6.10	Weight gain plot for unwelded and SMAW weldment steels exposed to Na ₂ SO ₄ -60%V ₂ O ₅ at 900°C for 50 cycles.	161
Fig. 6.11	Weight gain square (mg ² /cm ⁴) plot for unwelded and SMAW weldment steels exposed to Na ₂ SO ₄ -60%V ₂ O ₅ at 900°C for 50 cycles.	161
Fig. 6.12	X-ray diffraction profiles for SMAW weldment in GrA1, T11 and T22 boilers steels exposed to Na ₂ SO ₄ -60%V ₂ O ₅ at 900°C for 50 cycles.	162
Fig. 6.13	SEM back scattered image of the cross section of SMAW weldment steels exposed to Na ₂ SO ₄ -60%V ₂ O ₅ at 900°C for 50 cycles. (a) GrA1 (weld), 150X. (b) GrA1 (HAZ), 150X (c) T11 (weld), 150X (d) T11 (HAZ), 150X (e) T22 (weld), 40X (f) T22 (HAZ), 40X.	163
Fig. 6.14	SEM micrographs showing surface scale morphology and EDAX analysis for SMAW weldment in boiler steels in Na ₂ SO ₄ -60% V ₂ O ₅ at 900°C for 50 cycles (a) GrA1 (weld), 500X (b) GrA1 (HAZ), 3000X (c) T11 (weld), 1000X (d) T11 (HAZ), 1000X (e) T22 (weld), 500X (f) T22 (HAZ), 3000X.	164
Fig. 6.15	BSEI and X-ray mapping of the cross-section of weld zone of SMAW weldment in GrA1 boiler steel subjected to cyclic oxidation in Na ₂ SO ₄ - 60% V ₂ O ₅ at 900°C for 50 cycles at 200X.	165
Fig. 6.16	BSEI and X-ray mapping of the cross-section of HAZ of SMAW weldment in GrA1 boiler steel subjected to cyclic oxidation in Na ₂ SO ₄ - 60% V ₂ O ₅ at 900°C for 50 cycles at 200X.	166

Fig. 6.17	BSEI and X-ray mapping of the cross-section of weld zone of SMAW weldment in T11 boiler steel subjected to cyclic oxidation in Na ₂ SO ₄ - 60% V ₂ O ₅ at 900°C for 50 cycles at 200X.	167
Fig. 6.18	BSEI and X-ray mapping of the cross-section of weld zone of SMAW weldment in T22 boiler steel subjected to cyclic oxidation in Na ₂ SO ₄ - 60% V ₂ O ₅ at 900°C for 50 cycles at 200X.	168
Fig. 6.19	BSEI and X-ray mapping of the cross-section of HAZ of SMAW weldment in T22 boiler steel subjected to cyclic oxidation in Na ₂ SO ₄ - 60% V ₂ O ₅ at 900°C for 50 cycles at 200X.	169
Fig. 6.20	Macrographs of TIG weldment steels subjected to cyclic hot corrosion in Na ₂ SO ₄ -60%V ₂ O ₅ at 900°C for 50 cycles (a) GrA1, (b) T11 and (c) T22.	172
Fig. 6.21	Weight gain plot for unwelded and TIG weldment GrA1, T11 and T22 boiler steels exposed to Na ₂ SO ₄ -60%V ₂ O ₅ at 900°C for 50 cycles.	173
Fig. 6.22	Weight gain square (mg ² /cm ⁴) plot for unwelded and TIG weldment in GrA1, T11 and T22 boiler steels exposed to Na ₂ SO ₄ -60%V ₂ O ₅ at 900°C for 50 cycles.	173
Fig. 6.23	X-ray diffraction profiles for TIG weldment in GrA1, T11 and T22 boiler steels exposed to Na ₂ SO ₄ -60%V ₂ O ₅ at 900°C for 50 cycles.	174
Fig. 6.24	SEM back scattered image of the cross section of TIG weldment in GrA1, T11 and T22 boiler steels exposed to Na ₂ SO ₄ -60%V ₂ O ₅ at 900°C for 50 cycles.(a) GrA1(weld), 60X (b) GrA1(HAZ), 60X (c) T11(weld), 60X (d) T11(HAZ), 70X (e) T22 (weld), 150X (f) T22 (HAZ), 100X.	175
Fig. 6.25	SEM micrographs showing surface scale morphology and EDAX analysis for TIG weldment steels in Na ₂ SO ₄ - 60%V ₂ O ₅ at 900°C for 50 cycles (a) GrA1 (weld), 1000X (b) GrA1 (HAZ), 1000X (c) T11 (weld), 1000X (d) T11 (HAZ), 2000X (e) T22 (weld), 1000 X (f) T22 (HAZ), and 3000X.	176

Fig. 6.26	BSEI and X-ray mapping of the cross-section of weld zone of TIG weldment in GrA1 boiler steel subjected to cyclic oxidation in Na ₂ SO ₄ -60%V ₂ O ₅ at 900°C for 50 cycles at 200X.	179
Fig. 6.27	BSEI and X-ray mapping of the cross-section of HAZ of TIG weldment in GrA1 boiler steel subjected to cyclic oxidation in Na ₂ SO ₄ -60%V ₂ O ₅ at 900°C for 50 cycles at 200X.	180
Fig. 6.28	BSEI and X-ray mapping of the cross-section of weld regions of TIG weldment in T11 boiler steel subjected to cyclic oxidation in Na ₂ SO ₄ -60%V ₂ O ₅ at 900°C for 50 cycles at 200X.	181
Fig. 6.29	BSEI and X-ray mapping of the cross-section of HAZ regions of TIG weldment in T11 boiler steel subjected to cyclic oxidation in Na ₂ SO ₄ -60%V ₂ O ₅ at 900°C for 50 cycles at 200X.	182
Fig. 6.30	BSEI and X-ray mapping of the cross-section of weld regions of TIG weldment in T22 boiler steel subjected to cyclic oxidation in Na ₂ SO ₄ -60%V ₂ O ₅ at 900°C for 50 cycles at 200X.	183
Fig. 6.31	BSEI and X-ray mapping of the cross-section of HAZ regions of TIG weldment in T22 boiler steel subjected to cyclic oxidation in Na ₂ SO ₄ -60%V ₂ O ₅ at 900°C for 50 cycles at 200X.	184
Fig. 6.32	Macrographs of different regions of SMAW weldments in GrA1 steel subjected to cyclic hot corrosion in Na ₂ SO ₄ -60%V ₂ O ₅ at 900°C for 50 cycles (a) Base Metal, (b) Weld Metal and (c) HAZ.	187
Fig. 6.33	Weight gain plot for different regions of SMAW weldment in GrA1 steels exposed to Na ₂ SO ₄ -60%V ₂ O ₅ at 900°C for 50 cycles.	188
Fig. 6.34	Weight gain square (mg ² /cm ⁴) plot for different regions of SMAW weldment in GrA1 steel exposed to cyclic hot corrosion in Na ₂ SO ₄ -60%V ₂ O ₅ at 900°C for 50 cycles.	188

Fig. 6.35	X-ray diffraction profiles for different regions of SMAW weldment in GrA1 steel exposed to cyclic hot corrosion in Na ₂ SO ₄ -60%V ₂ O ₅ at 900°C for 50 cycles.	189
Fig. 6.36	SEM back scattered image of the cross section of different regions of SMAW weldment in GrA1 steel exposed to cyclic hot corrosion in Na ₂ SO ₄ -60%V ₂ O ₅ at 900°C for 50 cycles (a) Weld Metal, 200X (b) HAZ, 200X.	190
Fig. 6.37	Surface morphology and EDAX analysis for different regions of SMAW weldment in GrA1 steel exposed to Na ₂ SO ₄ -60%V ₂ O ₅ at 900°C for 50 cycles (a) Weld Metal, 1000X and (b) HAZ, 1000X.	191
Fig. 6.38	BSEI and X-ray mapping of the cross-section of weld metal of SMAW weldment in GrA1 steel subjected to cyclic oxidation in Na ₂ SO ₄ -60%V ₂ O ₅ at 900°C for 50 cycles at 200X.	192
Fig. 6.39	BSEI and X-ray mapping of the cross-section of HAZ of SMAW weldment in GrA1 steel subjected to cyclic oxidation in Na ₂ SO ₄ -60%V ₂ O ₅ at 900°C for 50 cycles at 200X.	193
Fig. 6.40	Macrographs of different regions of SMAW weldments in T11 steel subjected to cyclic hot corrosion in Na ₂ SO ₄ -60%V ₂ O ₅ at 900°C for 50 cycles (a) Base Metal, (b) Weld Metal and (c) HAZ.	196
Fig. 6.41	Weight gain plot for different regions of SMAW weldment in T11 steels exposed to Na ₂ SO ₄ -60%V ₂ O ₅ at 900°C for 50 cycles.	197
Fig. 6.42	Weight gain square (mg ² /cm ⁴) plot for different regions of SMAW weldment in T11 steel exposed to cyclic hot corrosion in Na ₂ SO ₄ -60%V ₂ O ₅ at 900°C for 50 cycles.	197
Fig. 6.43	X-ray diffraction profiles for different regions of SMAW weldment in T11 steel exposed to cyclic hot corrosion in Na ₂ SO ₄ -60%V ₂ O ₅ at 900°C for 50 cycles.	198
Fig. 6.44	SEM back scattered image of the cross section of different regions of SMAW weldment in T11 steel exposed to cyclic hot corrosion in Na ₂ SO ₄ -60%V ₂ O ₅ at 900°C for 50 cycles (a) Weld Metal, 200X (b) HAZ, 250X.	199

Fig. 6.45	SEM micrographs showing surface morphology and EDAX analysis for different regions of SMAW weldment in T11 steel exposed to Na ₂ SO ₄ -60%V ₂ O ₅ at 900°C for 50 cycles (a) Weld Metal, 1000X and (b) HAZ, 1000X.	200
Fig. 6.46	BSEI and X-ray mapping of the cross-section of weld metal of SMAW weldment in T11 steel subjected to cyclic oxidation in Na ₂ SO ₄ -60%V ₂ O ₅ at 900°C for 50 cycles at 200X.	201
Fig. 6.47	BSEI and X-ray mapping of the cross-section of HAZ of SMAW weldment in T11 steel subjected to cyclic oxidation in Na ₂ SO ₄ -60%V ₂ O ₅ at 900 °C for 50 cycles at 200X.	202
Fig. 6.48	Macrographs of different regions of SMAW weldments in T22 steel subjected to cyclic hot corrosion in Na ₂ SO ₄ -60%V ₂ O ₅ at 900°C for 50 cycles (a) Base Metal, (b) Weld Metal and (c) HAZ.	205
Fig. 6.49	Weight gain plot for different regions of SMAW weldment in T22 steels exposed to Na ₂ SO ₄ -60%V ₂ O ₅ at 900°C for 50 cycles.	206
Fig. 6.50	Weight gain square (mg ² /cm ⁴) plot for different regions of SMAW weldment in T22 steel exposed to cyclic hot corrosion in Na ₂ SO ₄ -60%V ₂ O ₅ at 900°C for 50 cycles.	206
Fig. 6.51	X-ray diffraction profiles for different regions of SMAW weldment in T22 steel exposed to cyclic hot corrosion in Na ₂ SO ₄ -60%V ₂ O ₅ at 900°C for 50 cycles.	207
Fig. 6.52	SEM back scattered image of the cross section of different regions of SMAW weldment in T22 steel exposed to cyclic hot corrosion in Na ₂ SO ₄ -60%V ₂ O ₅ at 900°C for 50 cycles (a) Weld Metal, 200X (b) HAZ, 200X.	208
Fig. 6.53	SEM morphology showing surface morphology and EDAX analysis for different regions of SMAW weldment in T22 steel exposed to cyclic hot corrosion in Na ₂ SO ₄ -60%V ₂ O ₅ at 900°C for 50 cycles (a) weld metal, 1000X (b) HAZ, 1000X.	209

Fig. 6.54	BSEI and X-ray mapping of the cross-section of weld metal of SMAW weldment in T22 steel subjected to cyclic oxidation in Na ₂ SO ₄ -60%V ₂ O ₅ at 900°C for 50 cycles at 200X.	210
Fig. 6.55	BSEI and X-ray mapping of the cross-section of HAZ of SMAW weldment in T22 steel subjected to cyclic oxidation in Na ₂ SO ₄ -60%V ₂ O ₅ at 900°C for 50 cycles at 200X.	211
Fig. 6.56	Macrographs of different regions of TIG weldments in GrA1 steel subjected to cyclic hot corrosion in Na ₂ SO ₄ -60%V ₂ O ₅ at 900°C for 50 cycles (a) Base Metal, (b) Weld Metal and (c) HAZ.	214
Fig. 6.57	Weight gain plot for different regions of TIG weldment in GrA1 steels exposed to Na ₂ SO ₄ -60%V ₂ O ₅ at 900°C for 50 cycles.	215
Fig. 6.58	Weight gain square (mg ² /cm ⁴) plot for different regions of TIG weldment in GrA1 steel exposed to cyclic hot corrosion in Na ₂ SO ₄ -60%V ₂ O ₅ at 900°C for 50 cycles.	215
Fig. 6.59	X-ray diffraction profiles for different regions of TIG weldment in GrA1 steel exposed to cyclic hot corrosion in Na ₂ SO ₄ -60%V ₂ O ₅ at 900°C for 50 cycles.	216
Fig. 6.60	SEM back scattered image of the cross section of different regions of TIG weldment in GrA1 steel exposed to cyclic hot corrosion in Na ₂ SO ₄ -60%V ₂ O ₅ at 900°C for 50 cycles (a) Weld Metal, 140X (b) HAZ, 150X.	217
Fig. 6.61	SEM micrographs of surface morphology and EDAX analysis for different regions of TIG weldment in GrA1 steel exposed to Na ₂ SO ₄ -60%V ₂ O ₅ at 900°C for 50 cycles (a) Base Metal, 2000X (b) Weld Metal, 1000X and (c) HAZ, 1000X.	218
Fig. 6.62	BSEI and X-ray mapping of the cross-section of weld metal of TIG weldment in GrA1 steel subjected to cyclic oxidation in Na ₂ SO ₄ -60%V ₂ O ₅ at 900°C for 50 cycles at 200X.	219

Fig. 6.63	BSEI and X-ray mapping of the cross-section of HAZ of TIG weldment in GrA1 steel subjected to cyclic oxidation in Na ₂ SO ₄ -60%V ₂ O ₅ at 900°C for 50 cycles at 200X.	220
Fig. 6.64	Macrographs of different regions of TIG weldments in T11 steel subjected to cyclic hot corrosion in Na ₂ SO ₄ -60%V ₂ O ₅ at 900°C for 50 cycles (a) Base Metal, (b) Weld Metal and (c) HAZ.	223
Fig. 6.65	Weight gain plot for different regions of TIG weldment in T11 steels exposed to Na ₂ SO ₄ -60%V ₂ O ₅ at 900°C for 50 cycles.	224
Fig. 6.66	Weight gain square (mg ² /cm ⁴) plot for different regions of TIG weldment in T11 steel exposed to cyclic hot corrosion in Na ₂ SO ₄ -60%V ₂ O ₅ at 900°C for 50 cycles.	224
Fig. 6.67	X-ray diffraction profiles for different regions of TIG weldment in T11 steel exposed to cyclic hot corrosion in Na ₂ SO ₄ -60%V ₂ O ₅ at 900°C for 50 cycles.	225
Fig. 6.68	SEM back scattered image of the cross section of different regions of TIG weldment in T11 steel exposed to cyclic hot corrosion in Na ₂ SO ₄ -60%V ₂ O ₅ at 900°C for 50 cycles. (a) Weld Metal, 140X (b) HAZ, 80X.	226
Fig. 6.69	Surface morphology and EDAX analysis for different regions of TIG weldment in T11 steel exposed to Na ₂ SO ₄ -60%V ₂ O ₅ at 900°C for 50 cycles (a) Weld Metal, 1000X and (b) HAZ, 1000X.	227
Fig. 6.70	BSEI and X-ray mapping of the cross-section of weld metal of TIG weldment in T11 steel subjected to cyclic oxidation in Na ₂ SO ₄ -60%V ₂ O ₅ at 900°C for 50 cycles at 200X.	228
Fig. 6.71	BSEI and X-ray mapping of the cross-section of HAZ of TIG weldment in T11 steel subjected to cyclic oxidation in Na ₂ SO ₄ -60%V ₂ O ₅ at 900°C for 50 cycles at 200X.	229
Fig.6.72	Macrographs of different regions of TIG weldments in T22 steel subjected to cyclic hot corrosion in Na ₂ SO ₄ -60%V ₂ O ₅ at 900°C for 50 cycles (a) Base Metal, (b) Weld Metal and (c) HAZ.	232

Fig. 6.73	Weight gain plot for different regions of TIG weldment in T22 steels exposed to Na ₂ SO ₄ -60%V ₂ O ₅ at 900°C for 50 cycles.	233
Fig. 6.74	Weight gain square (mg ² /cm ⁴) plot for different regions of TIG weldment in T22 steel exposed to cyclic hot corrosion in Na ₂ SO ₄ -60%V ₂ O ₅ at 900°C for 50 cycles.	233
Fig. 6.75	X-ray diffraction profiles for different regions of TIG weldment in T22 steel exposed to cyclic hot corrosion in Na ₂ SO ₄ -60%V ₂ O ₅ at 900°C for 50 cycles.	234
Fig. 6.76	SEM back scattered image of the cross section of different regions of TIG weldment in T22 steel exposed to cyclic hot corrosion in Na ₂ SO ₄ -60%V ₂ O ₅ at 900°C for 50 cycles (a) Weld Metal, 150X (b) HAZ, 150X.	235
Fig. 6.77	Surface morphology and EDAX analysis for different regions of TIG weldment in T22 steel exposed to cyclic hot corrosion in Na ₂ SO ₄ -60%V ₂ O ₅ at 900°C for 50 cycles (a) weld metal, 1000X (b)HAZ, 1000X.	236
Fig. 6.78	BSEI and X-ray mapping of the cross-section of weld metal of TIG weldment in T22 steel subjected to cyclic oxidation in Na ₂ SO ₄ -60%V ₂ O ₅ at 900°C for 50 cycles at 200X.	237
Fig. 6.79	BSEI and X-ray mapping of the cross-section of HAZ of TIG weldment in T22 steel subjected to cyclic oxidation in Na ₂ SO ₄ -60%V ₂ O ₅ at 900°C for 50 cycles at 200X.	238
Fig. 7.1	Bar chart indicating weight gain (mg/cm ²) for weldments, different regions of weldment and unwelded steels exposed to cyclic oxidation in air at 900°C for 50 cycles.	248
Fig. 7.2	Bar chart indicating weight gain (mg/cm ²) for weldments , different regions of weldment and unwelded steels exposed to cyclic hot corrosion in Na ₂ SO ₄ -60%V ₂ O ₅ at 900°C for 50 cycles.	248

LIST OF TABLES

Table No.	Particulars	Page No.
Table 2.1	Chemical composition and mechanical properties of boiler tube steel (ASME Boiler and pressure vessels code, 1978).	5
Table 2.2	AWS classifications of welding and allied process (Cary, 1979).	5
Table 3.1	Welding parameters for SMAW weldment in GrA1, T11 and T22 steels.	53
Table 3.2	Welding parameters for TIG weldment in GrA1, T11 and T22 steels.	55
Table 4.1	Chemical composition (Wt%) for various boiler tube steels.	60
Table 4.2	Chemical composition of electrode/ filler metal	61
Table 4.3	Average weldment width and tube size	64
Table 4.4	Porosity (%age) of SMAW and TIG weldments.	64
Table 4.5	Typical all weld metal tensile data	65
Table 5.1	Summary of the results for weldments, different regions of weldments and unwelded steels oxidised in air at 900 °C for 50 cycles.	143
Table 6.1	Summary of the results for weldments, different regions of weldments and unwelded steels oxidised in molten salt (Na ₂ SO ₄ -60%V ₂ O ₅) at 900°C for 50 cycles.	239
Table 7.1	The weight gain for different steel when exposed in air at 900 °C.	247
Table 7.2	The weight gain for different steels when exposed in Na ₂ SO ₄ -60% V ₂ O ₅ at 900 °C.	247
Table A.1	Thermal expansion coefficients and Thermal diffusivity of substrate steels.	254
Table A.2	Values of parabolic rate constant K _p (10 ⁻⁸ g ² cm ⁻⁴ s ⁻¹) for weldments, different regions of weldment and unwelded steels exposed to air and molten salt environment for 50 cycles at 900°C.	254

Table A.3	Scale thickness values of weldments, different regions of weldment and unwelded steels exposed to air and molten salt environment for 50 cycles at 900 °C.	255
Table A.4	Chemical composition (Wt%) for boiler tube steels and electrode/filler metal, used for obtaining the weldments and the environment of study.	256

Research Papers Presented /Published

1. Ravindra kumar, V. K. Tewari and S. Prakash, (2007), "Studies on Hot Corrosion of the 2.25 Cr- 1 Mo Boiler Tube Steel and Its Weldments in molten salt Na_2SO_4 -60% V_2O_5 Environment," Metallurgical and Materials Transaction A, Vol. 38, No. 1, pp. 54-57.
2. Ravindra kumar, V. K. Tewari and S. Prakash, (2006) "Studies on High Temperature Oxidation performance of Shielded Metal Arc Weldments in 1Cr-0.5 Mo Boiler Tube Steel," International Symposium of High Temperature Degradation of Fe-, Ni-, and Co-Based Alloys Including Metal Dusting, Materials Science and Technology 2006, held at Cincinnati, Ohio (USA) on 12-16 October, 2006, pp. 74.
3. Ravindra kumar, V. K. Tewari and S. Prakash, (2005) "Characterization of High Temperature Oxidation of 2.25Cr -1 Mo Boiler Tube Steel and Its Weldments in Air at 900 $^{\circ}\text{C}$," Abstract accepted to International Symposium of Failure Analysis", Materials Science and Technology 2005, held at Pittsburgh (USA) on 26th-28th September, 2005. pp. 140
4. Ravindra kumar, V. K. Tewari and S. Prakash, (2007), "Studies on Hot corrosion behaviour of Microstructurally different regions of 2.25 Cr -1 Mo (T22) Boiler Tube Steel Weldment in Molten Salt Environment," Journal of Materials Science and Engineering A, (Communicated).
5. Ravindra kumar, V. K. Tewari and S. Prakash, (2007), "Studies on Hot Corrosion of the 1 Cr- 0.5 Mo Boiler Tube Steel and Its Weldments in Molten Salt Environment," Metallurgical and Materials Transaction A, (Communicated).
6. Ravindra kumar, V. K. Tewari and S. Prakash, (2007), "Oxidation behavior of Base Metal, Weld Metal and HAZ regions of SMAW Weldment in ASTM SA210 GrA1 Steel," Materials Letters, (Communicated).

ABBREVIATIONS

BSEI	Back Scattered Electron Image
EDAX	Energy Dispersive X-ray Analysis
EPMA	Electron Probe Micro Analysis
GrA1	SA-210-GradeA1
T11	SA-213-T11
T22	SA-213-T22
K_p	Parabolic rate constant
SMAW	Shielded Metal Arc Welding
TIG	Tungsten Inert Gas Welding
SEM	Scanning Electron Microscopy
Wt. %	Weight percentage
Wt. Gain	Weight Gain
m.p.	Melting point
XRD	X-ray Diffraction
Sc	Scale
Sb	Substrate
hr	Hour
A	Ampere
V	Voltage

Corrosion is a natural process that causes the deterioration of metals and alloys by their interaction with the environments in contact with them. High temperature oxidation, aqueous (or electrochemical) corrosion and corrosion-erosion are processes that cause metallic components to suffer metal loss and damage (often) rendering them incapable of performing the functions for which they are originally designed.

It has been stated that the natural and spontaneous corrosion of metal components should not be a surprising occurrence, because corrosion is thermodynamically predictable. Metals are won from their ores with great expenditures of energy and corrosion simply reflects the natural process of reversion of the metals back to their natural, impure (oxide or sulfide) states. However, corrosion mechanisms and rates can be influenced strongly by many environmental and materials factors, including variability in the microstructures of the metallic components. Microstructural variability arising from thermomechanical processing methods including welding, at times may significantly accelerate localized corrosion.

Steel is most commonly and widely used metal in structures, machineries, plants and industrial installations, railways, shipping, atomic reactors, bridges, off-shore industry, etc. Even in developed countries the loss due to corrosion is quite high to the extent of 3% to 4% of GDP. In India also, an estimated loss of Rs.36, 000 crores (US \$ 8 billion) occurs every year due to corrosion (Balu, 2005).

Ferritic chromium molybdenum steels are popular engineering alloys for a variety of moderate temperature, high pressure applications such as the steam generators/boilers of fossil-fuel and nuclear power plants, refining and processing of petroleum, high temperature high-pressure vessels for thermal reforming and pressure vessels for coal liquefaction. Such steels possess a good combination of mechanical properties, formability and weldability, and resistance to high temperature oxidation and other forms of corrosion (Raman, 1998).

The materials used for high temperature applications are subjected to hot corrosion and high temperature wear. The corrosion is the deterioration of the materials by its reaction with surrounding and the rate increases with increase in temperature known as hot corrosion. Hot corrosion is an accelerated oxidation of materials at elevated temperatures,

induced by a thin film of fused salt deposit. In hot corrosion, metals and alloys are subjected to degradation at much higher rates than in gaseous oxidation, with a porous nonprotective oxide scale formed at the surface and sulfides in the substrate, Hot corrosion is a serious problem in power generation equipment in gas turbines for ships and aircrafts and in other energy conversion and chemical process systems. Because of the high thermodynamic stability of Na_2SO_4 , it is found to be common or dominant component of the salt deposit (Otero et al, 1992)

Sulphur is a principal impurity in fossil fuels and sodium is introduced into the combustion air-usually in an aerosol originating from seawater. Some other alkali or alkaline sulphates may also exist in the deposit, depending upon the impurities contained in the fuel and in the intake air, these thin liquid sulfate film may be deposited onto the hot hardware either from the condensation of combustion products of fossil fuels or else from the direct impingement of liquid droplets from the hot gas stream. The deposits often contain sulphates or chlorides with metallic constituents of Na, Ca, Mg, K, or V. The sources for these contaminants are the fuel and the air necessary for combustion. This type of degradation is especially severe when the condensed phase is liquid.

High tube metal temperatures allow the oil ash to become molten, causing rapid corrosion. Molten oil ash deposits are now known to be extremely corrosive agents and are responsible for causing oil ash corrosion. Corrosion occurs when molten vanadate compounds dissolve the protective oxide layers, which naturally form on tube surface during boiler operation. The vanadate compounds are also good oxidation catalysts and allow oxygen and other gases in the combustion atmosphere to diffuse rapidly to the metal surface and cause further oxidation. As soon as the metal is oxidized, the cycle starts over again and high corrosion rates result.

Ultra super critical boilers operated under the condition of a temperature over $600\text{ }^\circ\text{C}$ and steam pressure over 24MPa are expected to have higher heat conversion efficiency. For the tube materials applied in the boilers operating at higher temperature and in higher steam pressures, the improvement in strength at elevated temperature is preferable to avoiding the increasing of wall thickness when using conventional Cr-Mo steel for super heater or reheater tubes.

Weld corrosion has been a problem since materials were first joined by welding processes. As new materials are developed for use in corrosive environments, new incidents of corrosion failure are discovered. For most alloy systems, weld area and stress associated corrosion phenomena can be reduced to manageable proportions by the

correct matching of parent and consumable and by specifying an appropriate weld procedure and manufacturing route.

Any welded components can be broadly divided into three different regions the weld metal, the base metal, and the heat-affected zone (HAZ). The microstructure in these three regions is caused by the different peak temperature and cooling rates. In fact, as one moves away from the fusion line toward the base metal, one comes across sharp changes in the microstructure even within the HAZ due to different heating cycles experienced by the HAZ at different distances from the fusion line (Raman, 1995).

The welded components of steels suffer deleterious microstructural degradation during welding. Since most of the in service failures are reported to occur in the HAZ, there have been extensive research efforts into correlating weld failures with some aspects of HAZ microstructure. The characteristics of the microstructures through weld zones and the size and extent of heat affected zones (HAZ) of weldments will depend on, among other factors, the type of metals being joined whether or not they are heat treatable, and classes of welding or joining processes used.

There are at least three distinct regions in the cross section: a thick outer layer, a subscale region consisting of extensive internal oxide precipitates, and a thinner layer that formed between the external layer and the subscale. The subscale region was populated with internal oxide precipitates with internal oxidation occurring along the alloy grain boundaries (Raman, 2000).

The localized corrosion attack occurs at preferred sites of the materials, those sites being either of microscopic dimensions, such as grain boundaries or of macroscopic size such as areas with deviating compositions or microstructure as in the case of weldments. Localized attack indicates the preference of one site to another to undergo corrosion. When two regions of different compositions or structures are in contact, the one which is more active will undergo corrosion leading to localized attack.

The objective of this study is to investigate the hot corrosion behaviour of boiler tube steel weldments in air and molten salt ($\text{Na}_2\text{SO}_4\text{-60}\%\text{V}_2\text{O}_5$) corrosive environment especially at high temperature. Since it is found that in boiler operating conditions such mixture are often found to be responsible for tube failures (weldment).

2.1 FERRITIC Cr-Mo STEEL

Chromium molybdenum steel also referred to as heat resistant low alloy steel, find frequent application in power generation stations, refining, and chemical industries for pressure vessels, piping systems, furnace components and rotating equipment. Elevated operating temperature usually taken to be higher than about 260 °C, frequently required that weldment be produced of alloy steels because of the inferior hot strength and corrosion properties of carbon steels. The type of weldments and its specific application dictates whether hot tensile strength, creep or stress rupture can be used as the basis of steel selection. The high temperature corrosion problem may be complicated by other factors such as stress corrosion cracking, hydrogen attack etc. The use of alloy steels does not always effectively control the corrosion of the weldments. Some times reduction of the service temperature/ or elimination of corrosive element from the operating atmosphere are other means to alleviate this problem (Indacochea, 1992).

Alloying elements such as chromium, molybdenum, tungsten, etc. are added to carbon steel to improve properties such as hardness, strength and toughness. The classic methods of strengthening low alloy steel are

- solution hardening
- quenching and tempering
- precipitation hardening
- controlled rolling

Molybdenum is an effective strengthener in all cases. The majority of low alloy steels is quenched and tempered – Q+T.

The addition of chromium to this alloy provides oxidation resistance and microstructural stability. Cr forms carbides within the grains that anchor the structure at high temperatures. Cr additions also significantly increase the hardenability of the alloy, thus as increases welded strength. Cr in solution acts as a ferrite former in steel (Castro and De Cadenet, 1975). The substitutional Mo atoms increase the intrinsic matrix strength by solid solution strengthening. Mo also improves the creep performance of the alloy through forming

Mo₂C as a coherent precipitate. Mo in solution also causes an increase in the eutectoid temperature and austenitic transformation temperature (Olson et al, 1992).

Sufficient carbon is also needed to form carbides with iron and the above alloying elements to provide the precipitation strengthening. Carbon increases the strength of the materials. High level of carbon however decrease weldability and for this reason 0.1-0.2 wt % carbon is considered to be the optimum range in terms of balancing the weld ability (Olson et al, 1992). The chemical compositions of some boiler tube steels are shown in Table 2.1 along with ASTM code and mechanical properties.

Table 2.1: Chemical composition and mechanical properties of boiler tube steel (ASME Boiler and pressure vessels code, 1978).

Chemical composition of Boiler Tube Steels										Mechanical Properties		
ASTM code	Composition	C	Mn	Si	S	P	Cr	Mo	Fe	Tensile strength (MPa)	Yield strength (MPa)	Elongation %
SA210 GrA1	Nominal	0.27	0.93	0.1	0.058	0.048	-	-	Bal.	414	255	30
SA213 T11	Nominal	0.15	0.3-0.6	0.5-1	0.03	0.03	1-1.5	0.44-0.65	Bal.	414	207	30
SA213 T22	Nominal	0.15	0.3-0.6	0.5	0.03	0.03	1.9-2.6	0.87-1.13	Bal.	414	172	30

A wide variety of welding and allied processes are available with which to join metals these have been classified by the American Welding Society (AWS) and are listed in Table 2.2.

Table 2.2: AWS classifications of welding and allied process (Cary, 1979).

Welding processes	Allied Process
Solid state welding (SSW)	Thermal spraying (THSP)
Arc welding (AW)	Adhesive bonding
Resistance welding (RW)	Oxygen cutting (OC)
Oxyfuel gas welding (OFW)	Thermal cutting (TC)
Soldering (S)	Arc cutting
Brazing (B)	Other cutting
Other welding	

2.2 WELDABILITY OF Cr-Mo STEEL

Many process variations and disciplines needed for problem solving are distinguished for welding and joining of materials like steels. One of them in fusion welding is the intensity of the heat source to melt the weld that is approximately $100\text{W}/\text{cm}^2$ for most metals.

The weld thermal cycle generated by the moving heat source cause physical state changes, grain growth and metallurgical transformations, and transient thermal stress and residual stresses and distortions. Physical discontinuities like cracks occur under the transient thermal condition. Structural transformations occur under the operation of three gradients: thermal, concentration and stress. A transient thermal model is needed to analyze cracking and embrittlement problems. Rapid solidification and cooling of the weldment, the minimum amount of heat input within the allowable welding speed range must be determined. With modern steels welds of acceptable quality usually can be produced without the need for preheating, post heating, or special welding techniques. The need for preheating is based not only on carbon content, but also on the combination of other alloying elements along with various aspects of joint configuration, and section thickness (Lvan, 1995).

The boiler steels can be welded with any of the arc welding processes using suitable welding procedure. High heat input may, however, cause excessive grain growth and precipitation of micro alloying elements, both of which lead to reduced mechanical properties.

The most important properties when welding which result in mechanical properties are the grain growth and microstructural transformations. The grain in the underbead zone is considerably coarser when compared to the grain size of parent metal. The extent of grain growth is dependent upon the weld thermal cycle, i.e. its heating rate and dwell time at high temperature, and upon the steels chemistry.

During the weld thermal cycle, extremely high temperatures are reached within the HAZ and this can cause the carbide distribution to differ significantly from that of the original, unaffected base metal. The initial carbides may coarsen, transform to subsequent carbide species in situ or completely dissolve and be replaced by a dispersion of new carbides. The manner in which the carbides are affected depends upon factors such as peak temperature, dwell time and cooling rate. Manual fusion welding, typically shielded metal arc welding (SMAW), is often employed to make modifications and repairs to damaged components.

Welding subjects the base metal to intense thermal cycling resulting in a significantly altered, inhomogeneous microstructure adjacent to the weld deposit. This region is known as the heat affected zone (HAZ). In the temper bead welding procedure, the mean size, maximum size and areal fraction of grain boundary carbides within the martensitic temper bead increased at a much higher rate than within the bainitic conventional weaving heat affected zone. Tempering up to 4000 hours at the simulated operating temperature caused the precipitation and agglomeration of coarse M_6C , $M_{23}C_6$ and M_7C_3 alloy carbides at the prior austenite grain boundaries within the temper bead heat affected zone. It would be expected that this would result in a decrease in the impact toughness. The carbide species distributions were independent of the welding procedures. In the as-welded condition, the dominant carbide species was M_3C . In situ transformation of fine M_2C precipitates had occurred in a region near of HAZ as discussed by (Peddle and Pickles, 2001). This is believed to be a primary cause of Type IV cracking. Subsequent tempering at 538 °C resulted in the development of M_2C , M_7C_3 , $M_{23}C_6$ and M_6C . M_3C was eventually replaced by M_7C_3 and $M_{23}C_6$. M_7C_3 was found to dissolve as M_6C precipitated.

2.3 WELDING PROCESS

2.3.1 Fusion welding

Fusion welding is a process of joining materials by localized melting of the surfaces to be joined, with or without the addition of a filler metal. The process inevitably generates zones in which the material composition and characteristics vary, for a fusion weld with a filler metal.

Several techniques have been developed to manipulate an electric discharge arc to provide localized heating, melting and solidification of material to form a bond between components. The most commonly used techniques in the fabrication of Cr Mo boiler tube steel are discussed below.

2.3.1.1 Shielded Metal Arc Welding (SMAW)

The most common types of arc welding is shielded metal arc welding (SMAW), which is also known as manual metal arc welding (MMAW) or stick welding. Electric current is used to strike an arc between the base material and consumable electrode rod, which is made of steel and is covered with a flux that protects the weld area from oxidation and contamination by producing CO_2 gas during the welding process. The electrode core itself acts as filler material, making separate filler unnecessary. This technique is most widely

used for welding of ferritic and Cr-Mo boiler steel (Viswanathan and Gandy, 1999). Fig. 2.1 is Diagrammatically principle representation of SMAW.

2.3.1.2 Tungsten Inert Gas Welding (TIG)

TIG welding is a commonly used high quality welding process. TIG welding has become a popular choice of welding processes when high quality, precision welding is required.

For this purpose the arc is made between the work piece and a fixed electrode (usually made of tungsten). The filler metal is supplied in the form of a rod introduced in the vicinity of the arc the shielding is supplied as an inert gas through a nozzle around the electrode. Principle representation of this process is shown in Fig. 2.2. This process finds use in welding thin section of Cr-Mo boiler steel or in welding a root before filling by SMAW (Castro and De Cadenet, 1975; Paulo et al, 2000).

The difference between the techniques are based on how the arc is formed and how the weld pool is shielded from the atmosphere which in turn influence the amount of heat applied to the work piece and how effectively the weld pool can be controlled. These parameters influence cooling rate and inclusion concentration.

The TIG welding operation is a very complex process, which is affected by a number of parameters, such as transient conduction, buoyancy, electromagnetic and surface tension as discussed by (Oreper and Szekely, 1984). Many factors influence the development of the heating and cooling cycle experienced by a welded component. The welding operation delivers both heat and liquid metal to the component which subsequently cools through a combination of process radiation to surrounding heat conduction into the parent metal, forced convection due to any shielding gas flow and natural convection at the surface after the weld pass. The weld metal also provides a further source of heat as the latent heat of fusion is evolved during solidification. The description of process occurring in the weld metal has been the subject of significant study (Oreper and Szekely, 1984).

2.3.2 Microstructure of Cr- Mo Steel Weldment

Matching consumables are typically used when welding carbon and boiler tube steel such as the low hydrogen coated electrode according to (AWS D1.1, 1998) welding practice of Cr-Mo boiler steel. The characteristics of the microstructures through weld zones and the size and extent of heat affected zones (HAZ) of weldments will depend on, among other factors, the type of metals being joined whether or not they are heat treatable, and classes of welding or joining processes used. For example tungsten inert gas (TIG) welding usually will

produce a much narrower HAZ than will conventional arc welding process (Cary, 1979; Metal Hand Book, 1976).

2.25 Cr-1 Mo HAZ structure adjacent to the line of fusion in a multipass weld has been described as predominantly tempered bainite. This study found the structure to contain relatively large bainite packets some small ferritic zone and tempered martensite (Bass et al, 1994). The microstructures of the HAZ after a typical weld cycle as lower bainite with some martensite was described by (Peddle and Pickles, 2000).

The microstructure of normalized and tempered base material shows ferrite and bainite. Typical structures consist of ~70% bainite and 30% ferrite (Peddle and Pickles, 2000). The microstructure obtained as the weld cools from the liquid phase to ambient temperature is called the as-deposited or primary microstructure. It consists of allotriomorphic ferrite α , widmanstätten ferrite α_w , acicular ferrite α_a , and the so-called microphases, which might include small amounts of martensite, retained austenite or degenerate pearlite (Fig. 2.3). The diagram is inaccurate in one respect, that inclusions cannot be expected to be visible in all of the acicular ferrite plates on a planar section of the microstructure. This is because the inclusion size is much smaller than that of an acicular ferrite plate, so that the chances of sectioning an inclusion and plate together are very small indeed. Bainite is also found in some weld deposits, particularly of the type used in the power generation industry (Lundin et al., 1986). Allotriomorphic ferrite is sometimes called “polygonal” ferrite or “proeutectoid” ferrite, but polygonal simply means many sided (like all ferrite morphologies) and widmanstätten ferrite can also be proeutectoid. Widmanstätten ferrite is sometimes included under the general description “ferrite with aligned MAC”, the abbreviation referring to martensite, austenite and carbide. However, bainite plates can also form in a similar shape, although their thermodynamic and kinetic characteristics are quite different. From a phase transformations point of view, the classification of ferrite grains remains the most useful to this day (Dube et al., 1958; Heckel and Paxton, 1961).

The microstructure across the weld zone were typical for arc welded conventional steel consisting of columnar grains of weld metal containing widmanstätten ferrite and pearlite, epitaxial grain growth along the fusion lines, large equiaxed grains (widmanstätten ferrite and pearlite) in the over heated zone of the HAZ and decreasing grain size through the HAZ to the original, unaffected microstructure (banded ferrite and pearlite) in the parent metal (William, 1992).

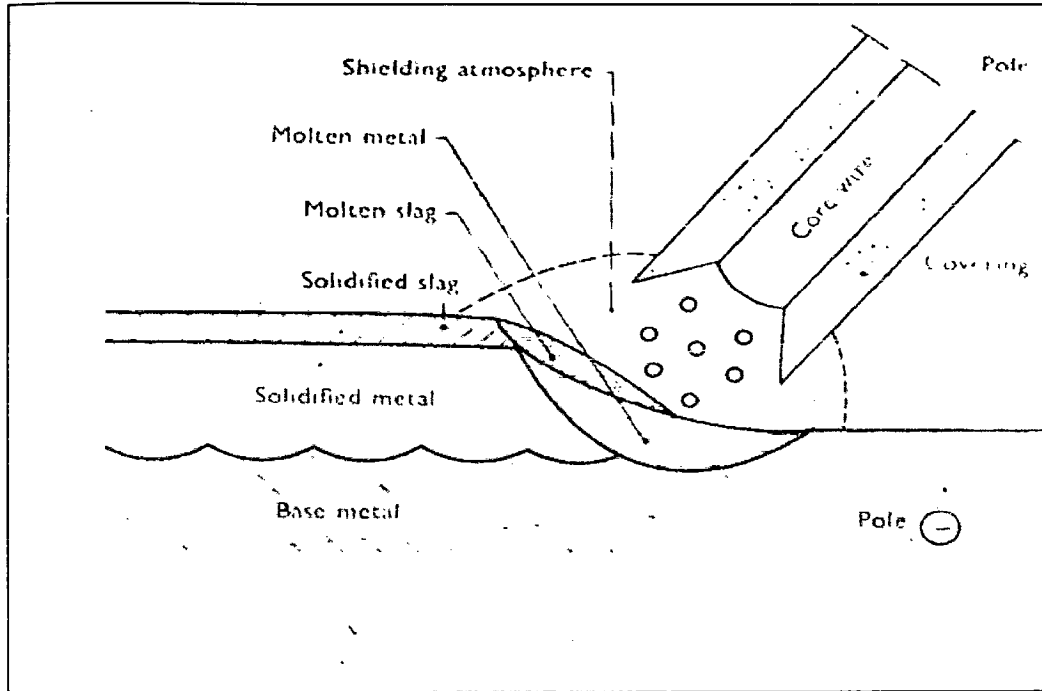


Fig. 2.1: Principle of the manual metal arc process or SMAW (Castro and De Cadenet, 1975).

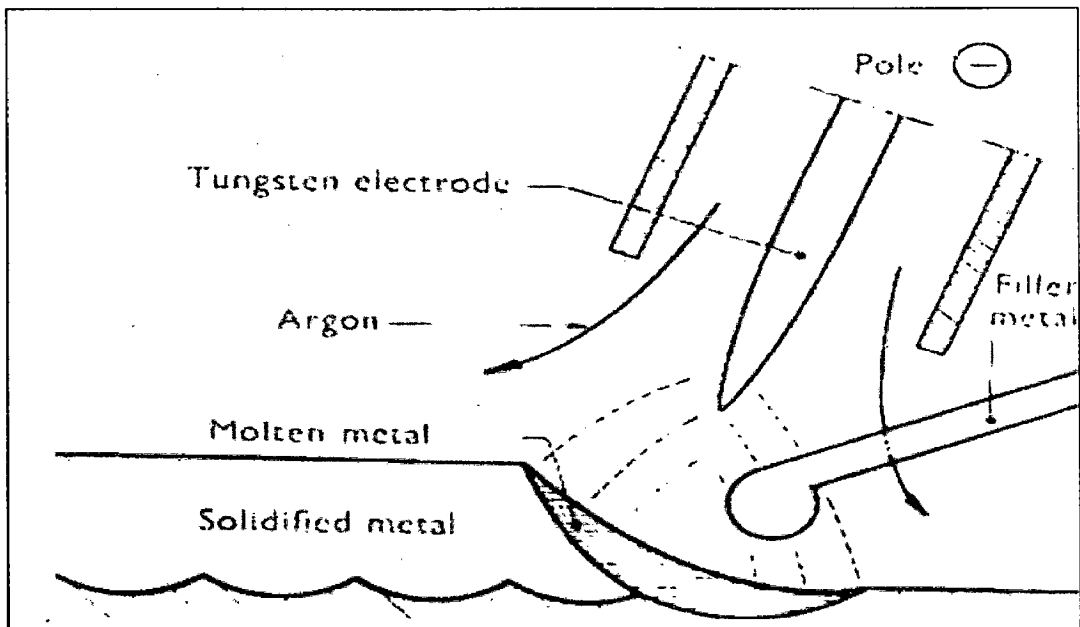


Fig. 2.2: Principle of the TIG process (Castro and De Cadenet, 1975).

2.3.3 Causes of Welded Failures

Weld failures can normally be related to welding problems in five categories, these are:

- i) Failures resulting from improper weld geometrical design.
- ii) Failures resulting from inappropriately specified weld process parameters.
- iii) Failures resulting from incompatibilities of the materials being welded and processes employed.
- iv) Failures resulting from improperly executed welds.
- v) Failures resulting from unanticipated service conditions.

There are some welding failures that fit more than one of these five broad categories, that is they might be placed in the category of improper weld design but might equally would be placed in the category of inadequate welds execution (Bruce and Alan, 1994).

2.3.4 Microhardness of the Cr- Mo Steel Weldments

The microhardness of the 2.25 Cr-1 Mo steel weldments was taken along the cross section, a portion of weld metal, the HAZ and a portion of the unaffected base metal as shown in Fig. 2.4. The maximum hardness values occurred within the as welded coarse grain HAZ and the hardness decreased with increasing distance from the fusion line until a constant value of approximately 160 HV was reached in the base metal.

Microhardness results showed by (Peddle and Pickles, 2000) that the hardness within the coarse grain HAZ and fine grain HAZ of the temper –bead weld decreased very rapidly, dropping by as much as 140HV within the first 500h of tempering at 538 °C (Fig. 2.5). The hardness decreased with increasing tempering time. For both welding procedure (conventional welding and two layer temper bead welding procedure), a substantial increase in the as welded base metal hardness occurred within the HAZ this is due to the thermal cycling of the material during the welding process. Initially the increase in temperature experienced by the base material HAZ due to the welding process brings about a corresponding increase in the solubility of alloying constituents leading to the relatively quick dissolution of some of the carbides. Upon cooling the solubility levels decrease and new finely dispersed carbides form within the thermally altered microstructure resulting in a relative increase in the HAZ hardness above the base metal level. The maximum hardness value of the profile occurs in the area of the HAZ directly adjacent to the fusion line as discussed by (Bass et al, 1994). The inhomogeneous fine grained microstructure of this area is a result of the subsequent thermal cycles which transform to once coarse grained region.

2.3.5 Metallurgical effects on Corrosion of Weldments.

It is generally thought that enhanced attack at welds in service environments is due to the weld metal being anodic with respect to the parent metal. Such a galvanic effect might result from the different microstructures which exist between the weld metal, HAZ and parent metal. Thus one way in which the problem might be avoided is by undertaking a post weld heat treatment. It would appear from the results that the tendency towards accelerated attack at the weld is reduced by heat treatments which homogenize the metallurgical structure of the welded samples by heating into the austenitic range followed by either air cooling or oil quenching. However, such heat treatments do not appear to eliminate the effect. This indicates that other factors- such as small composition difference between the electrode and the steel also contribute to the aforementioned galvanic effects. In any case, from a practical point of view, post weld austenitising heat treatments may not be possible or desirable (Hodgkiess et al, 1978).

Welding affects the metallurgical properties and corrosion of the weldments. Welding causes inhomogeneities. Weld metal may not have the same composition and microstructure as the parent metal and the surface of the weld metal is generally rough. Residual stresses will be introduced in the weld because welding involves heating and cooling. Weld metal also has higher hardness and strength levels than the parent metal.

The difference in chemical composition, surface conditions, microstructure and mechanical stresses in the weldments make the corrosion behaviour of the weld different from that of the parent metal, galvanic corrosion occurs. Severe attack on the weld metal will occur if the weld metal is anodic with respect to the parent metal. This is due to the small area of the anode compared with the area of the cathode. If the weld metal is cathodic with respect to the parent metal, the corrosion problem is less serious because the attack is distributed over the large anodic area (Balakrishnan, 1994).

The major challenges facing the Power Generation Industry in the 21st Century are focused primarily on achieving the difficult targets of increased efficiencies, increased reliability and stringent environmental standards. The challenge for coal, in particular, is to develop new, and evolve existing clean technologies, in order to achieve these goals the attention comes on the boiler steel (Mayer et al, 1998).

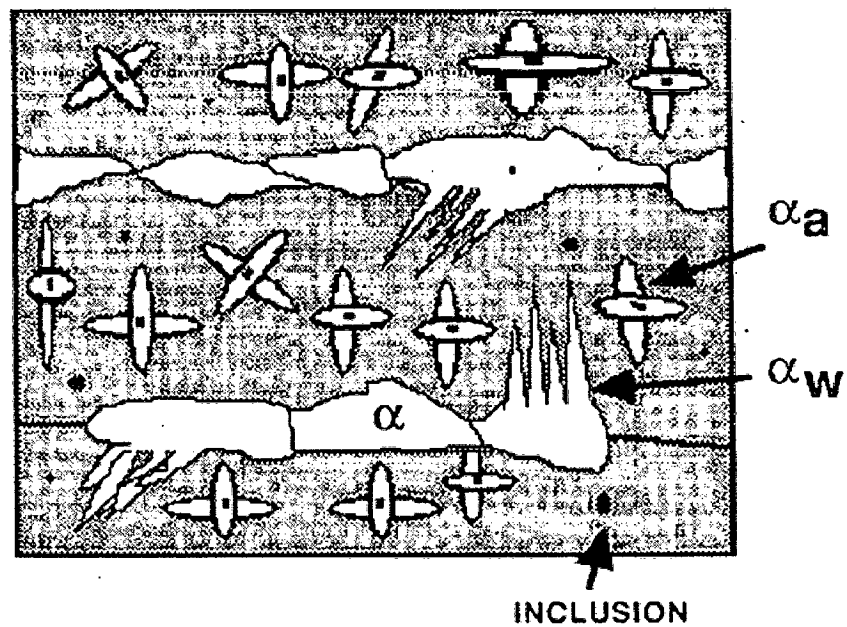


Fig. 2.3: An illustration of the essential constituents of the primary microstructure of a steel weld deposit (Bhadeshia et al, 1993).

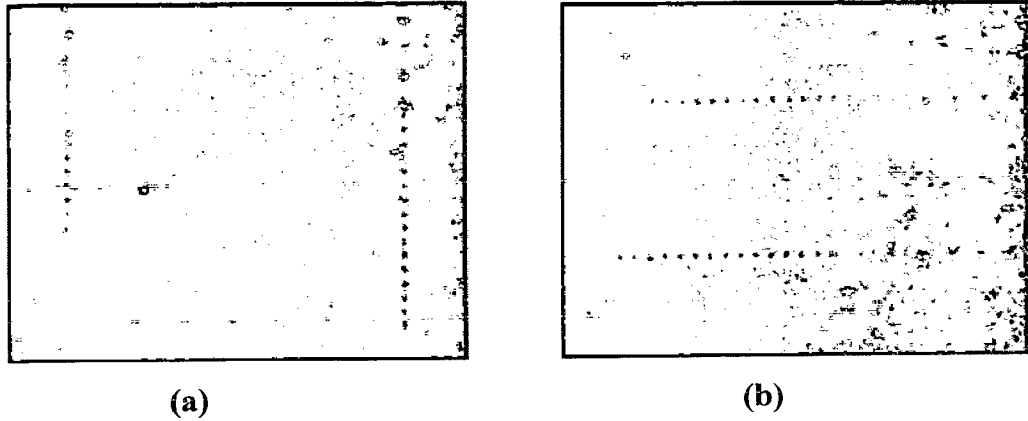


Fig. 2.4: Location of the microhardness traverses at the root and bay regions of a weld bead with in the HAZ of (a) tempered bead weld (b) conventional weaving weld (Peddle and Pickles, 2000).

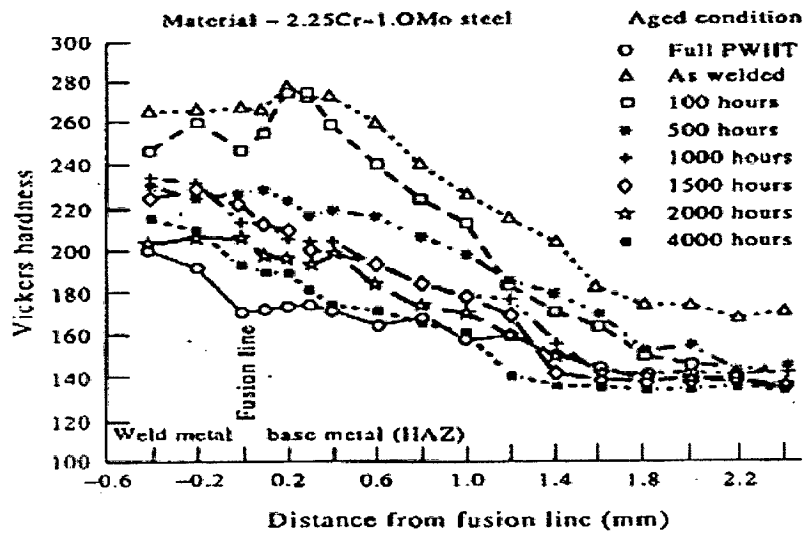


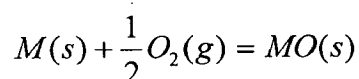
Fig. 2.5: Effects of aging at 538 °C on the hardness of the HAZ produced by the tempered bead welding process (Bass et al, 1994).

2.4 OXIDATION AT HIGH TEMPERATURE

Oxidation is a type of corrosion involving the reaction between a metal and air or oxygen at high temperature in the absence of water or an aqueous phase. It is also called dry-corrosion. The rate of oxidation of a metal at high temperature depends on the nature of the oxide layer that forms on the surface of metal. Creep, mechanical fatigue, thermal fatigue, oxidation and sulphidation are the main possible causes of failure of a turbine blade in a hot station (He et al, 2001). However, a serious drawback of metallic material (and of other materials too) is the deterioration in properties originating from their interaction with the environments in which they are to perform. Often this leads to a premature failure of metallic components with the allied hazards of plant shutdown and loss of economy, environmental pollution and risk to human lives. The annual direct loss of natural resources, i.e. metals, due to environmental degradation is also substantial (Chatterjee et al, 2001).

2.4.1 Mechanism of Oxidation

From the consideration of the equation:



In order for the reaction to proceed further, one or both reactants must penetrate the scale, either metal must be transported through the oxide to the oxide-gas interface (Birks and Meier, 1983; Kofstad, 1990) and react there or oxygen must be transported to the oxide-metal interface to react has explained diffusion processes with the help of neat sketches shown in Fig. 2.6, which illustrate the growth of chromia scales in the presence or absence of oxygen active elements. When inward oxygen diffusion predominates, oxide formation takes place at the scale-alloy interface, reducing void or cavity formation and thereby increased scale adhesion is achieved. Metals and alloys get oxidized when they are heated to elevated temperatures in air or highly oxidizing environments, such as combustion gas with excess of air or oxygen. They often rely on the oxidation reaction to develop a protective oxide scale to resist corrosion attack, such as sulphidation, carburization, ash/salt deposit corrosion etc, that is why oxidation is considered to be the most important high temperature corrosion reaction. Further the rate of oxidation for metals and alloys increases with increasing temperature (Lai, 1990).

2.5 HOT CORROSION

Metals and alloys sometimes experience accelerated oxidation when their surfaces are covered with a thin film of fused salt in an oxidizing atmosphere at elevated temperatures. This mode of attack is called the “Hot Corrosion”. Hot corrosion can be defined as deposit modified gas-induced degradation of materials at high temperature (Rapp and Zhang, 1994).

- According to Hancock (1987), hot corrosion is an accelerated form of oxidation which occurs when metals are heated in the temperature range 700-900⁰C in the presence of sulphate deposits formed as a result of the reaction between sodium chloride and sulphur compounds in the gas phase around the metals.

Because of its high thermodynamic stability in the mutual presence of sodium and sulphur impurities in the oxidizing gas, Na₂SO₄ is often found to be the common or dominant component of salt in the deposit. Sulphur is a principal impurity in fossil fuels and sodium is introduced into the combustion air usually in an aerosol originating from seawater. During combustion of certain low-grade fossil fuels, vanadium compounds such as NaVO₃ and V₂O₅ may also be deposited in the salt film (Rapp and Zhang, 1994). This type of attack is commonly called “Hot Corrosion”. The accelerated corrosion can also be caused by the other salts, viz. vanadates or sulphate-vanadate mixtures and in the presence of solid or gaseous salts such as chlorides.

2.5.1 Mechanisms of Hot Corrosion

The fundamental mechanism of high temperature fireside corrosion is well established, being first proposed in the mid 1940's (Reid, 1971) and it is quite distinct from that operating on furnace walls, involving molten sulphatic phases derived from deposited ash. These molten sulphatic phases, specifically those of alkali metals, exacerbate metal loss by a combination of direct sulphidation and scale fluxing to form alkali metal tri-sulphates.

Hot corrosion can occur at high temperatures where the deposit is in the liquid state right from the beginning or the solid deposit turns into liquid during the exposure as a result of reaction with the environment. These two types of hot corrosion processes are termed as Type I High Temperature Hot Corrosion (HTHC) and Type II Low Temperature Hot Corrosion (LTHC) (Khanna and Jha, 1998).

2.5.1.1 Type I High temperature hot corrosion (HTHC)

It is normally observed in the temperature range of about 825-950⁰C when the condensed phase is clearly liquid. The typical microstructure for HTHC shows the formation of sulphides and a corresponding depletion of the reactive components in the alloy substrate. The external corrosion products consist of oxide precipitates dispersed in the salt film. The presence of the pore, crevice or crack across a protective film can lead to the sulphidation of the alloy substrate. This results in a significant shift in the basicity of the salt film. Once the fused salt contacts the alloy substrate, the rate and duration of the rapid corrosion kinetics is decided by the magnitude and gradient of salt basicity relative to the local solubilities for the oxide scale phases (Rapp and Zhang, 1994).

2.5.1.2 Type II Low temperature hot corrosion (LTHC)

This occurs well below the melting point of Na₂SO₄ (884⁰C). The reaction product morphology is characterised by a non-uniform attack in the form of pits, with only little sulphide formation close to the alloy/scale interface and little depletion of Cr or Al in the alloy substrate (Rapp and Zhang, 1994).

Luthra (1985) reported LTHC behaviour for a number of Co-Cr, Co-Al and Co-Cr-Al alloys. After a low melting CoSO₄-Na₂SO₄ liquid phase was formed, the acidic dissolution of CoO at the oxide/salt interface supported the precipitation of either Co₃O₄ or CoSO₄ near the salt/gas interface. The negative solubility gradient was maintained by gradients in the basicity and oxygen activity in the salt film. For sufficient acidic cobalt-solute ions in the salt film, counter-transportation of Co²⁺/Co³⁺ ions carried the reduction reaction to the salt/gas interface. In this case the dissolution/precipitation of cobalt compounds prevent the formation of protective scale of Cr₂O₃ or Al₂O₃.

2.5.2 Hot Corrosion Degradation Sequence in the Alloy

This process almost always consists of two stages

1- An initiation stage during which the hot corrosion elements in the alloy are oxidised and transferred from metallic atoms to the reducible substances in the deposit. In some cases of hot corrosion an increasing amount of sulphide particles becomes evident in the alloy beneath the protective reaction product barrier. In other, small holes become evident in the protective reaction product barrier where the molten deposit begins to penetrate it.

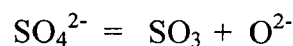
Eventually the protective barrier formed via selective oxidation is rendered ineffective and the hot corrosion process enters into the propagation stage (Pettit and Giggin, 1987). Numerous factors (Pettit & Giggins, 1987; Pettit & Meier, 1984), affect the time at which the hot corrosion process moves from the initiation stage into the propagation stage and the time for which the protective scales are stable beneath the salt layer. These same factors also play the dominant role in determining the type of reaction product that is formed during the propagation stage. Alloy composition, gas composition, salt composition, salt composition rate, temperature, temperature cycles and erosion are some of the important factors.

It is a fact that all corrosion resistant alloys degrade via such a sequence and it is the result of using selective oxidation to develop oxidation or corrosion resistance. It is convenient to place emphasis on the two stages, namely, an initiation stage during which the alloys behave as they would have behaved in the absence of the deposit and a propagation stage where the deposit has caused the protective properties of the oxide scales to become significantly different than what they would have been, had no deposit been present.

2- The propagation stage of the hot corrosion sequence is the stage for which the superalloy must be removed from service since this stage always has much larger corrosion rates than for the same superalloy in the initiation stage. Before describing the types of propagation modes by which superalloys undergo hot corrosion attack, it is of value to examine how deposits upon the surfaces of superalloys may affect their corrosion behaviour.

2.5.3 Salt Fluxing

The processes by which the reaction product barrier becomes non-protective due to the formation of species, which are soluble in the liquid deposit, are called “fluxing” reactions. In a molten sulphate deposit, the following equilibrium can be used to define acidity or basicity:-



With the equilibrium constant, $K = \frac{P_{\text{SO}_3}}{a_{\text{O}^{2-}}}$ where P_{SO_3} is the pressure of SO_3 and $a_{\text{O}^{2-}}$ is the activity of the oxide ions in the melt. Magnitude of K is determined by the standard free energies of formation for Na_2SO_4 , SO_3 and Na_2O and $a_{\text{O}^{2-}}$ equals the activity of Na_2O in such melts.

In sulphate melts, the acidity is determined by the SO_3 pressure and the acidity increases as the SO_3 pressure is increased. The acidity need not only be controlled by the SO_3 pressure in the gas since there are other ingredients in some systems that may affect acidity.

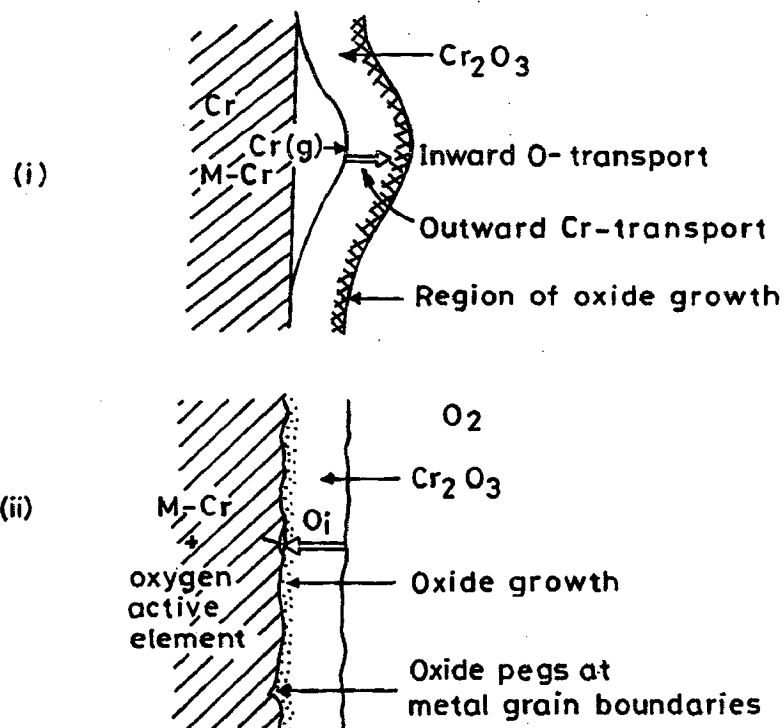
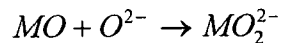


Fig. 2.6: Schematic illustration of the growth of chromium scales in (i) the absence of oxygen active elements and with predominant outward transport of chromia through the scale, and (ii) the presence of oxygen active elements and with predominant inward transport of oxygen (Kofstad, 1990).

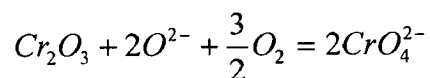
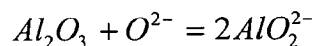
For example V_2O_5 can react with Na_2SO_4 to increase the acidity of the melt via reaction: $Na_2SO_4 + V_2O_5 \longrightarrow 2NaVO_3 + SO_3$

Molybdenum and Tungsten in alloy can cause similar effects when their oxides are formed as corrosion products (Pettit and Giggins, 1987).

The initial concept of basic fluxing was first proposed by Bornstein and Decrescent (1970) and then described in thermodynamic terms for the hot corrosion of nickel by Goebel and Petit (1970). This process is that oxide ions are produced in the Na_2SO_4 deposit due to removal of oxygen and sulphur from the deposit via reaction with the alloy and metal as suggested by Pettit and Giggins (1987). Furthermore, oxide scales (MO) that normally would form as protective barrier on the surface of these alloys can react with oxide ions via reaction such as:



The protective oxide scales e.g. Al_2O_3 or Cr_2O_3 can react with O^{2-} ions to form soluble aluminates or chromate ions respectively:



and their protective properties are destroyed. Such basic fluxing has a number of distinct features. Sulphides are usually found in the alloy substrate as a result of sulphur removal from Na_2SO_4 to produce oxide ions. The amount of attack depends upon the production of oxide ions by the melt. Hence a supply of Na_2SO_4 is necessary for the attack to continue and this type of fluxing is often not self-sustaining. This form of attack is usually restricted to high temperatures (above 900 °C) since the O^{2-} ion production is slow at lower temperatures, and is more likely to be important in gases without an acidic component (e.g. SO_3). However, according to Rapp and Goto (1981) basic fluxing can also occur in gases with acidic components. Their mechanism permits fluxing to be either basic or acidic, within the need for a source or sink for O^{2-} ions which means that attack may continue without the additional supply of the deposit. But Shores (1983) has examined the Rapp-Goto precipitation criteria for a variety of conditions and remarked that basic fluxing reactions are not always self sustaining.

Rapp and Goto (1981) proposed that, if the gradient in solubility of the protective oxide with distance into the salt layer was negative at the oxide /salt interface, accelerated attack could be sustained. This provides a quantitative expression of the earlier concepts of solubility gradients and oxide precipitation, that is, when

$$\left(\frac{d(\text{solubility of oxide})}{dx} \right)_{x=0} < 0$$

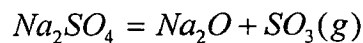
Oxide can dissolve at the oxide/salt interface; migrate down a concentration gradient away from that side to a region of low solubility and precipitate. At steady state, oxide dissolves and is transferred away from the oxide/salt interface, just as fast as the oxide layer grows (Fig. 2.7). They recognized that such a gradient can be established across a thin salt film and that it need not be a consequence of the removal of sulfur from Na₂SO₄ or the introduction of acidic ions from the corrosion products as required by the Goebel and Pettit model (1970). When Rapp-Goto (1981) criterion for the oxide solubility is satisfied, fluxing is expected.

The acidic fluxing reactions involve the development of non-protective reaction products on superalloys as the result of a liquid deposit on the surface of the superalloy which has a deficiency of oxide ions. The deficiency of oxide ions in the Na₂SO₄ can arise due to an acidic component present in the gas or an acidic phase formed as an oxidation product upon the superalloy. When the acidic component is present in the gas the nonprotective oxide scale ensues due to rapid transport of certain ionic species in the acidic melt. If the melt becomes acidic due to formation of an oxide from an element in the superalloy, the attack becomes self-sustaining even with a small amount of Na₂SO₄. The refractory elements Mo, W and V form oxides that cause Na₂SO₄ to become acidic and hence, these elements when oxidised in the presence of Na₂SO₄ deposit on superalloys usually cause catastrophic self-sustaining hot corrosion via acidic fluxing (Pettit and Meier, 1984).

2.5.4 Salt Chemistry

2.5.4.1 Sulphate Solution Chemistry

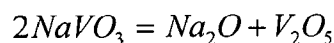
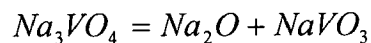
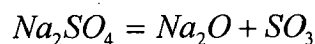
As described by Rapp (1986 and 2002) oxyanion melts of alkali nitrates, carbonates, hydroxides and sulphates exhibit an acid base character. Whereby the acid components may be considered as $\text{NO}_2(\text{g})$, $\text{CO}_2(\text{g})$, $\text{H}_2\text{O}(\text{g})$ or $\text{SO}_3(\text{g})$ respectively. Although the use of the Lux-Fluid selection of NO_3^- , CO_3^{2-} , OH^- and SO_4^{2-} as the basic components is common for such fused salts. The oxide ion can be alternatively changed as the Lewis base is common for all of these salts. For a melt of pure Na_2SO_4 , the equilibrium:



In examining the expected stability of the protective oxide Cr_2O_3 , they explained with respect to dissolution either as acidic solutes such as $\text{Cr}_2(\text{SO}_4)_3$ or as basic solutes such as Na_2CrO_4 or NaCrO_2 . The phase stability diagram for the Cr-S-O system can be superimposed on that for Na-S-O, as shown in Fig. 2.8. The two abscissa scales at the bottom and top of figure provide alternate parameters for melt basicity (or acidity). Under no conditions, the metal chromium remains stable in contact with Na_2SO_4 at 1200 K (927°C).

2.5.4.2 Vanadate Solution Chemistry

Figure 2.9 is the phase stability diagram for the Na-V-S-O system at 900°C. The dashed lines are isoactivity lines for the vanadate species in the salt solution. The dependence of the equilibrium concentrations of various vanadate solutes in sodium sulphate-vanadate solutions on the melt basicity, defined as $-\log a_{\text{Na}_2\text{O}}$, is determined by considering the equilibrium reactions:



The equilibrium concentration of each vanadium compound varies continuously with melt basicity. Na_3VO_4 is the dominant component in the melt at basicity less than 8.2 and V_2O_5 is dominant at basicity greater than 16.3. For basicities between 8.2 and 16.3, NaVO_3 is the most important vanadium solute (Hwang and Rapp, 1989).

2.5.5 Hot Corrosion of Superheater/Reheater Boiler Tube Steel

Superheater and reheater tubes may fail well inside their intended design life by a combination of fireside corrosion (James and Pinder, 1997). Excessive corrosion attack of the leading tubes in a pendant stage is generally characterized by the formation of wastage flats on the tube surface at approximately the 2 and 10 o'clock positions in relation to the gas flow. This is associated with the preferential accumulation of ash debris on the radiant crown, sculpted by the gas flow around the tube. The accumulated debris thermally insulates the crown section from the flue gas, displacing the hottest operating section of the tube surface towards the 2 and 10 o'clock positions where the deposits are thinner and, consequently, the transmitted heat flux is greatest. Metal loss on tubes deeper within the bank is invariably less pronounced, by virtue of their more sheltered position, and any wastage flats that form tend to be located at the 3 and 9 o'clock positions relative to the gas flow.

The primary factors which dictate the rate of metal loss, either in isolation or synergistically, have been identified as tube metal temperature, incident heat flux determined by the gas temperature and fuel chemistry, together with the tube material and the position and alignment of the tube within an element.

The influence of tube metal temperature on molten salt corrosion was characterized by classic work in the late 1950's and early 1960's (Koopman et al, 1959; Nelson and Cain, 1960). At relatively low tube metal operating temperatures, typically below 550 °C, the ash deposits in contact with the tube substrate and/or corrosion scale are present as a porous solid layer. These deposits allow relatively free access of the bulk flue gas to the metal substrate/scale and the corrosion proceeds according to the temperature dependent rate for the gas phase oxidation-sulphidation of the metal. As the tube metal temperature increases, sodium and potassium sulphates, formed earlier in the furnace section, gradually accumulate on the tube surface facing the gas flow by condensation at the base of the porous aluminosilicate deposit. As the temperature increases through the melting range of the deposit, the chemical activity of the melt is heightened, causing a rapid increase in the corrosion rate. However, as the temperature increases, the stability of iron sulphate/irontrisulphate under the prevailing SO₃ partial pressure decreases. Eventually, a temperature is reached at which the instability of sulphated iron species becomes dominant, causing the rate of attack to diminish back to that associated with corrosion by gaseous species in the bulk flue gas.

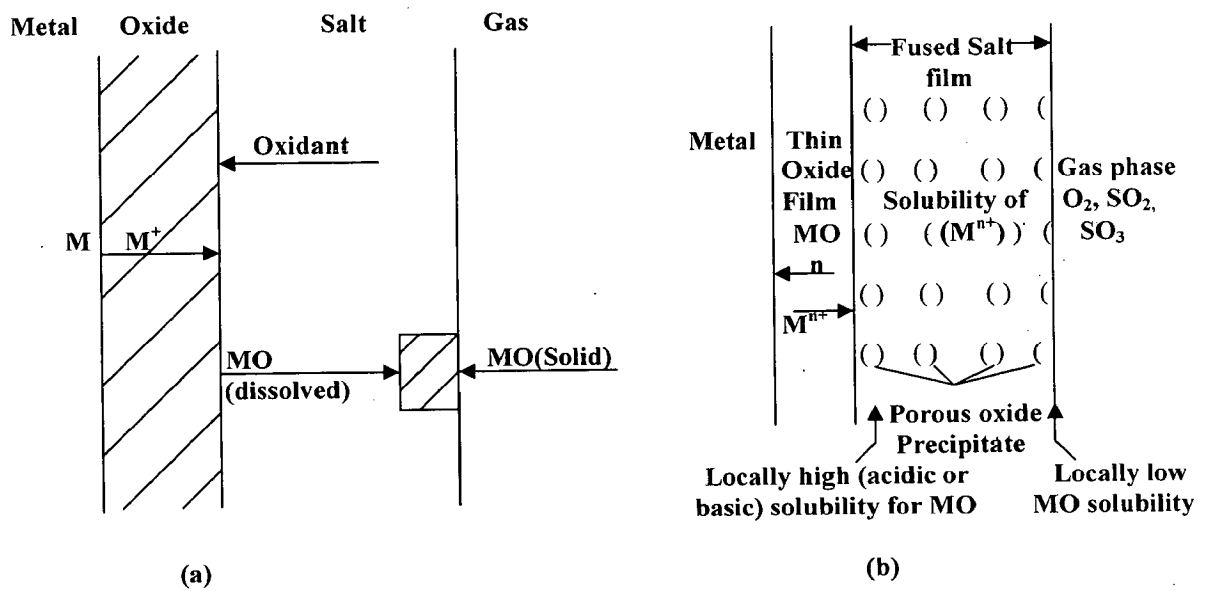


Fig. 2.7 (a) Schematic diagram for fluxing showing dissolution of metal oxide at the oxide/salt interface (Shores, 1983) and (b) Precipitation of a porous MO oxide supported by the solubility gradient in a fused salt film (Rapp and Zhang, 1994).

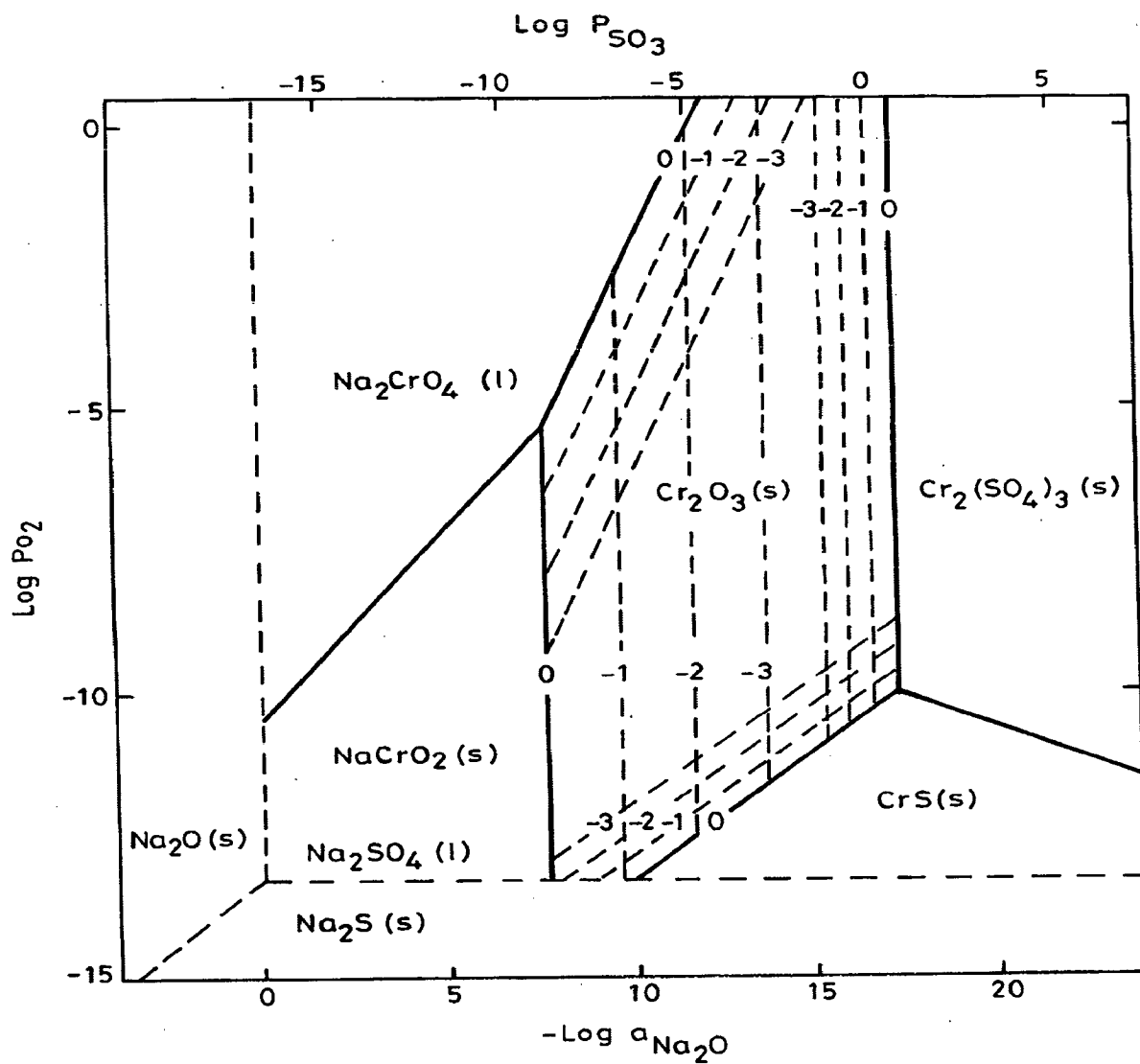
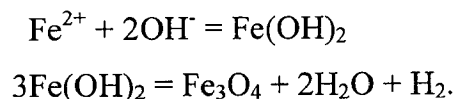


Fig. 2.8: Na-Cr-S-O phase stability diagram for 1200 K (Rapp, 1986).

The dominance of melt activity, or corrosion product instability with temperature, gives rise to the classic 'bell shaped' temperature dependence of corrosion under molten sulphates which starts at 600°C and reaches a peak around 670°C (Fleming et al, 2000). Superheater tubes must be designed to operate at temperatures some 35°C above live steam Temperature (Staubli et al, 1998). For current steam temperatures of up to around 580°C, metal temperatures will be around 615°C and low alloy steel tubes such as T22 may be adequate. However, not only do the advanced steam parameters for supercritical plant impose higher stresses and temperatures on the superheater tubes, they also increase the potential rates of both fireside and steam side corrosion.

2.5.5.1 Water Side Corrosion

The primary reaction involved in the waterside corrosion of high temperature boilers (Kingerley, 1994) is the formation of magnetite, via the intermediary formation of ferrous hydroxide:



In approximately neutral conditions, a magnetite scale forms on the tube, the growth of which is dominated by solid state diffusion through the scale. In the absence of sufficient hydrogen, the solubility of magnetite in the boiler water is markedly temperature dependent and the corrosion rates of steels approach minimum (acceptable) levels around neutral pH values (Dooley, 1993; James et al, 1997; Viswanathan and Bakker, 2001). Excursions from neutral values lead to increasingly severe attack.

2.6 BEHAVIOUR OF BASE AND WELDED METALS, ALLOYS IN VARIOUS OXIDISING ENVIRONMENTS

2.6.1 Air

The establishment of an oxide scale on an alloy occurs by a nucleation and growth process. When the clean component is exposed to an oxygen-rich gas, small, impinging nuclei of all the thermodynamically stable oxides develop on the surface. These initial nuclei of oxide coalesce rapidly to give a complete layer. During this initial or transient stage the rate of oxidation is rapid. All the elements in the alloy oxidise and the amounts of the various oxides in the layer are approximately proportional to the concentration of the elements in the alloy. Once the transient oxide layer has been established, it continues to

grow following diffusion of metal ions to the scale/gas interface or oxygen to the scale/alloy interface. The rate of thickening of the layer is determined by the temperature, the oxygen pressure and the spatial distribution, the amount, the composition and the structure of the initial oxide phases (Stott, 1998).

Raman (1999) concluded that no external oxidation occurs during air oxidation of the weld metal, HAZ, or base-metal regions at 873K. Cross sections of the air-oxidised specimens have not suggested any features which could facilitate crack initiation/propagation such as notch sharpening or grain-boundary cavitation. Steam oxidation of all the three weldment regions results in extensive internal oxide precipitation and formation of distinct subscale. The characteristics of the external scale and subsurface features developed during steam oxidation of HAZ are considerably different from those in the oxidized weld metal and base metal.

Microstructurally different regions of weld metal, heat affected zone (HAZ) and base metal were identified in the weld pads of 2.25 Cr-1 Mo steel. The specimens from the weld metal, the HAZ and the base metal were separated out of the weld pads and oxidized for different durations from 2 to 500 h in air at 773 K. All three types of specimens followed parabolic kinetics until the weld metal suffered spallation. While the oxidation rates of the base metal and the weld metal were similar, the HAZ had a much higher rate than those in the other regions. The composite weldment, consisting of the three regions, when oxidized at 773 K, was found to have developed a considerably thicker oxide scale over the HAZ as compared to those of the base metal and the weld metal. When measured by a surface profilometer, the difference in thicknesses that was found to be a fraction of a micrometer higher over the HAZ in 2 h of exposure had increased to more than 14 μm in 500 h. (Raman and Gnanamoorthy, 1993).

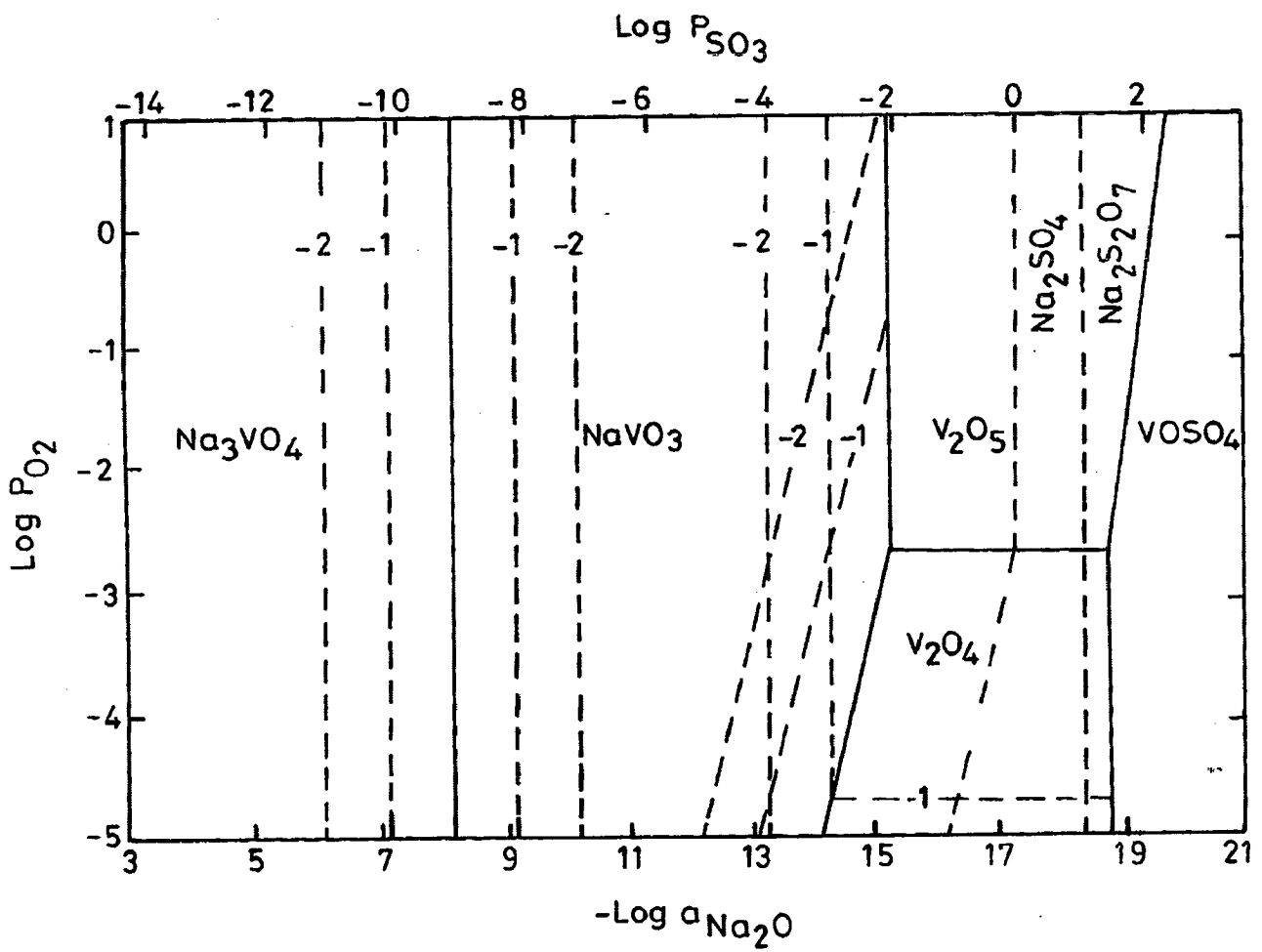


Fig. 2.9: Phase stability diagram for Na-V-S-O system at 900 °C (Hwang and Rapp, 1989).

Raman (1995) investigate the oxidation rate on weld metal, base metal and the HAZ and its constituents (the intercriticle region, fine grain bainite and coarse grain bainite) in the weldment of 2.25 Cr-1 Mo steel in air at 873 K for 50 hours. It was indicated that the HAZ and its constituents subzones oxidize at a much higher rate than the weld metal and base metal regions, and consequently the HAZ develops a thicker oxide scale than the base metal and the weld metal. The oxide scale formed on the weld metal alone suffers spallation. The higher oxidation rate of the HAZ and the formation of a thicker scale over it have been attributed to the absence of a protective inner scale of Cr rich oxide due to the nonavailability of free Cr from the alloy as a result of carbide formation in this region. Formation of a protective inner scale over the weld metal and the base metal impedes outward diffusion of Fe and hence results in the formation of Fe_2O_3 , an oxide with lower Fe content, as the major phase. In the absence of a protective scale, the major oxide formed over the HAZ is Fe_3O_4 . The intercriticle region (ICG) oxidizes at a higher rate than the coarse grain bainite and the fine grain bainite regions. The higher oxidation rate of the intercriticle region is due to the cumulative influence of grain size and precipitation of Cr-based carbide in the ICG.

The high temperature behaviour of pure metals, as well as Fe-Cr binary and ternary Fe-Cr-Ni alloys is strongly dependent on the method of their surface preparation procedure (Kuiry et al, 1994). They have further reported that mechanically polished surfaces exhibit a shorter incubation period for initial oxidation but better oxidation resistance during isothermal holding at 1423 K (1150⁰C) as compared to electropolished surfaces. This has been reportedly attributed to the enhanced outward diffusion of Cr and establishment of Cr-rich oxide layer on mechanically polished surfaces.

Sadique et al (2000) showed that aluminium addition have marked effects on the oxidation characteristics of Fe-Cr at all temperatures. They observed reduction in rate of oxidation in terms of specific weight gain with increasing aluminium content. The amount of spallation of the oxide scale was also formed to decreasing with increasing Al content. Al content was shown to help in enhancing the adhesion of Cr_2O_3 . Failure of the protective scale was inhibited either through the immediate reformation of an external protective scale or through the internal oxidation and subsequent formation of a subscale layer. It was concluded that a minimum level of aluminium exists for the formation of a complete protective scale on the alloy surface depending upon the temperature.

2.6.2 Molten Salt ($\text{Na}_2\text{SO}_4\text{-V}_2\text{O}_5$) Environment

Sachs (1958) studied accelerated high temperature corrosion of steels and stainless steel in V_2O_5 environment. They reported that oxidation of pure Cr in V_2O_5 occurs with a very rapid diffusion rate and so only the initial stages of the curve were supposed to be more important. Later slowing down of the oxidation rate was attributed mainly to the effect of scale thickening. Loose and spongy appearance of the scale was observed by them at the beginning of the process; V_2O_5 was present in excess and did dissolve the products of oxidation. According to them at the same point the liquid was saturated with the oxide which subsequently could get precipitated. The presence of various phases in a thin layer of scale would impose such severe strain on the film that cracking and exfoliation could be expected. This would permit liquid phase to reach the metal surface again and the conditions to form a spongy scale were seen to prevail. This mechanism would apply only to iron base alloys, which are susceptible to the catastrophic corrosion.

Corrosion resistance of various metals and alloys has also been analysed by Kerby and Wilson (1973) in the liquid vanadates. They found that the stainless steels and particularly 440 stainless steel (25 wt% Cr) shows the best corrosion resistance to liquid V_2O_5 . The rate of corrosion of Armco iron by liquid V_2O_5 has been reported to be controlled initially by the diffusion of oxygen across the metal oxide-liquid vanadate interface. As the available oxygen ions get depleted from the melt, the rate controlling mechanism is observed to be changed to the sorption of oxygen at the liquid vanadate gas phase interface.

Many fossil-fueled devices for energy conversion are susceptible to rapid degradation of high temperature alloy components when subjected to molten salt deposits. Because of the nearly universal presence of sulfur and alkali metals in fossil fuels, the corrosive deposits usually contain alkali sulfates (Na_2SO_4 , K_2SO_4). The mechanism of Na_2SO_4 -induced corrosion at high temperatures, where Na_2SO_4 (m.p. = 884°C) is liquid, has been extensively studied. This form of attack, commonly known as hot corrosion, results in typical sulfidation with an aluminum and/or chromium depletion zone in the alloy. The alloys were rapidly attacked at temperatures between 650°C and 750°C when a liquid sulfate phase was obtained from an initially pure solid Na_2SO_4 deposit. The rapid rate of attack resulted from sulfation of the transient surface nickel or cobalt oxides and the dissolution of these transition metal sulfates into Na_2SO_4 to yield a liquid phase. This retarded the formation of a protective Cr_2O_3 scale discussed by (Luthra and Shores, 1980).

Vanadium and sodium are common impurities in low-grade petroleum fuels. Molten sulphate-vanadate deposits resulting from the condensation of combustion products of such fuels are extremely corrosive to high temperature materials in the combustion systems. Thermodynamic calculations for the equilibrium concentrations of Na_3VO_4 , NaVO_3 and V_2O_5 in a mixed sodium sulphate-vanadate solution containing 30 mol% vanadate as a function of melt basicity have been reported by Hwang and Rapp (1989). They suggested that vanadate ions greatly increase the acidic solubility of all metal oxides compared to that in pure Na_2SO_4 .

The mechanisms of hot corrosion by molten sulphate-vanadate deposits were investigated by Sidky and Hocking (1987) by studying the corrosion of Ni-10Cr, Ni-30Cr, Ni-20Cr-3Al, Ni-21Cr-0.3Si, Ni-20Cr-5V and IN738 superalloys. The effect of adding Cr to Ni was found by them to be beneficial in the Na_2SO_4 melt, however, on increasing the VO_3^{3-} concentration in the melt, this effect diminished, becoming harmful in pure NaVO_3 due to the formation of the non protective CrVO_4 . According to them alloying element Al was found to be harmful in Na_2SO_4 - NaVO_3 melts. Cr depletion was observed in rich VO_3^{3-} melts but internal corrosion was more obvious in the SO_4^{2-} rich melts. Corrosion in rich VO_3^{3-} melts was aggressive due to the fluxing action of the salt, which takes place along internally sulphidised areas. According to their study, IN738 suffered tremendous internal attack due to its γ precipitates those became sulphidation prone areas, which in turn were fluxed by the VO_3^{3-} melt. Hocking (1993) have also suggested the use of high temperature corrosion resistance alloys having good mechanical properties.

The kinetics of the reactions between Na_2SO_4 (X) and V_2O_5 (Y) has been studied by Kolta et al (1972). They have concluded that the rate of the reaction depends both on the temperature (600-1300⁰C) and the molar ratios of X : Y. They further found that with increase in the reaction period (>30 min.) there was decrease in reaction rate which finally reached to zero order. This decrease in the reaction rate has been attributed to the formation of vanadosulphate complexes such as $(\text{NaV}_3\text{O}_8)_2 \cdot \text{Na}_2\text{SO}_4$ and $(\text{NaVO}_3)_2 \cdot \text{Na}_2\text{SO}_4$ which get decomposed at higher temperatures giving the meta- and pyro-vanadates respectively.

Thermogravimetric studies which delineate the conditions for simultaneous sulphate and vanadate induced corrosion at 650 to 800⁰C have been carried out by Seiersten and Kofstad (1987). They found that the corrosion caused by sodium sulphate/sodium vanadate mixtures have a complex mechanism. Samples coated with sodium vanadate were exposed to $\text{O}_2 + 4\% \text{SO}_2$ and the initial reaction was observed to be same as that observed in pure

oxygen. After an incubation period the duration was found to decrease with increasing temperature and sufficient SO_3 had got dissolved in the molten vanadate which resulted in formation of a mixture of NiSO_4 and Na_2SO_4 near the metal. When a molten NiSO_4 - Na_2SO_4 solution containing small amounts of vanadate was formed as an intermediate layer the reaction reportedly proceeded as sulphate-induced hot corrosion. The corrosion mechanism was observed to be changed from initial vanadate-induced to essentially sulphate induced hot corrosion when the sulphur trioxide pressure was high enough to form sodium sulphate.

Oxidation and hot corrosion in sulphate, chloride and vanadate environment of a cast nickel base superalloy have been reported by Deb et al (1996). Weight gain studies were carried out in air for the uncoated samples and coated with 100% Na_2SO_4 , 75% Na_2SO_4 + 25% NaCl and 60% Na_2SO_4 + 30% NaVO_3 + 10% NaCl . The presence of sulphur in the form of sulphates has been reported to cause internal sulphidation of the alloy beneath the external oxide layer. They observed the formation of volatile species by chlorides which further led to formation of voids and pits at grain boundaries those reportedly provide easy path for flow of corrodents. The presence of vanadate in conjunction with sulphate and chloride is proposed to provide additional fluxing action. According to them this destroys the integrity of the alloy and weakens its mechanical properties.

According to Otero et al (1987) Na_2SO_4 -60% V_2O_5 deposit was detected on a number of components in actual service which were operated at high temperature and were in contact with high-temperature gases from combustion of dirty fuels, containing certain amounts of impurities, i.e. Na, V, S etc. The presence of sulphur and its oxidised compounds were reported to favour the formation of isolated lobes with radial morphology having great permeability to facilitate the access of oxygen which further led to reduction in the protector character of scale. The presence of vanadium and its oxidised products was observed to generate compounds with aciculate morphology, identified to look like alkaline vanadate complexes. These aciculated shapes further contribute to reduce the protective character of the scale. The equilibrium diagram for varying composition of Na_2SO_4 is shown in Fig. 2.10 and the mixture of Na_2SO_4 -60% V_2O_5 is seen to be the lowest eutectic temperature.

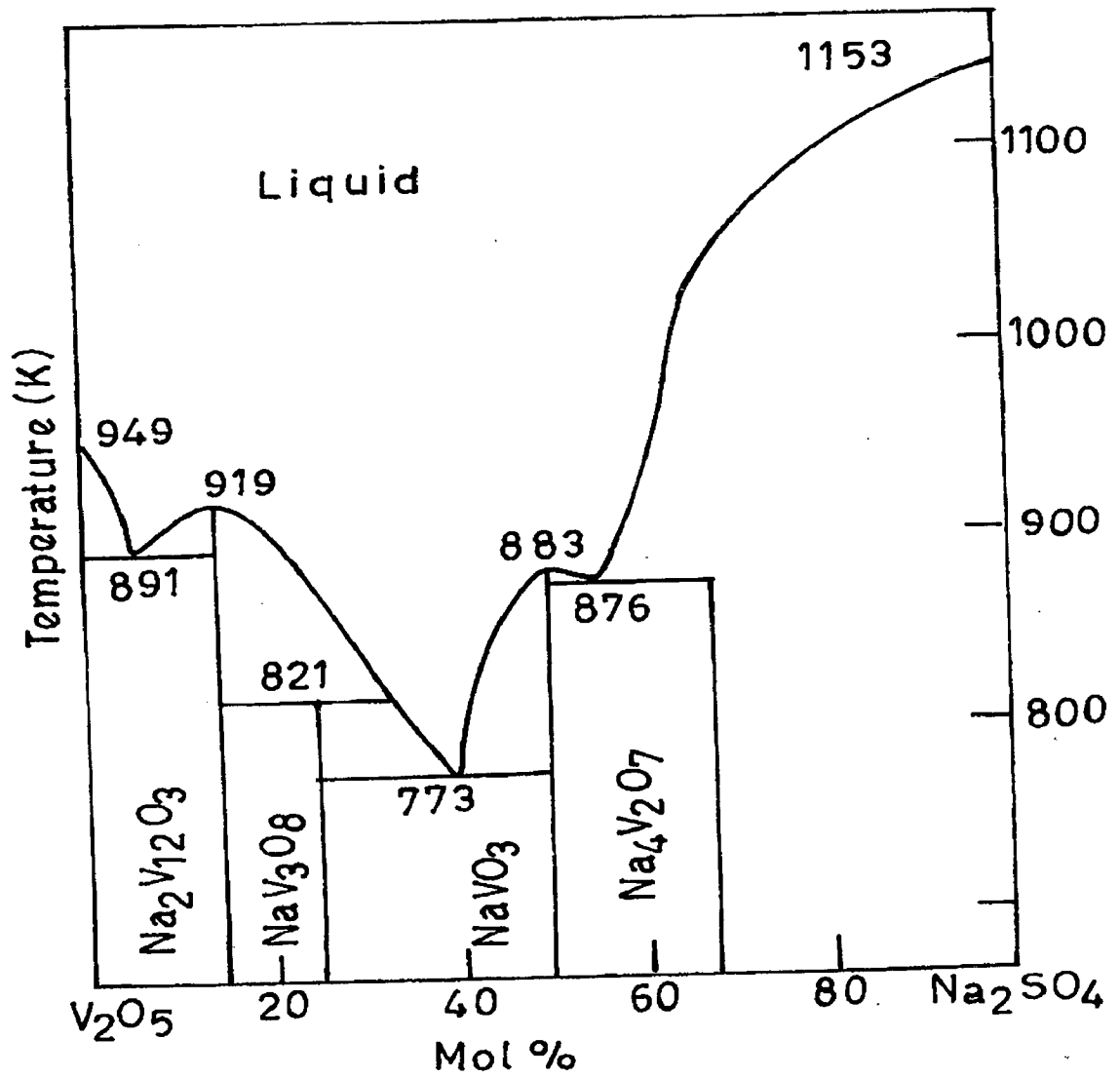


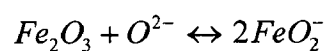
Fig. 2.10: Phase Diagram for Na₂SO₄-V₂O₅ System (Otero et al, 1987).

The thermogravimetric studies on hot corrosion of 2.25Cr-1Mo boiler tube steel and its weldments in the Na₂SO₄-60 pct V₂O₅ environment at 900 °C, was indicated the unweld steel showed intense spalling and sputtering and the weight gain was enormous. The SMAW weldment showed more weight gain than that of the unweld, which may be due to the presence of oxides of manganese and chromium with Fe₂O₃. The TIG weldment shows less weight gain. The weight gain of unweld and welded specimens follows the parabolic law in molten salt. The susceptibility to hot corrosion of unweld and welded joints has been found to be in the following order: TIG < unwelded < SMAW. Maximum cracking was observed in the case of SMAW weldment during hot corrosion studies, whereas it was least in the case of TIG weldment as discussed by (Kumar et al, 2007).

Tiwari and Prakash (1996) and Tiwari (1997) have also reported studies on superalloys in temperature range 700-900°C in pure Na₂SO₄, Na₂SO₄-15%V₂O₅ and Na₂SO₄-60%V₂O₅. They observed accelerated corrosion rates for Na₂SO₄-60%V₂O₅ composition i.e. eutectic with melting point of 500°C.

Sidhu and Prakash (2003) and Sidhu (2003A) have studies on boiler steel at 900 °C in Na₂SO₄-60%V₂O₅ environment. They concluded the base metal showed the more sputtering and spallation in molten salt. Weight gain studies were carried out for the uncoated samples and coated with Na₂SO₄-60% V₂O₅. The presence of sulphur in the form of sulphates has been reported to cause internal sulphidation of the alloy beneath the external oxide layer. They observed that the Mo containing T22 boiler steel showed least resistant to hot corrosion on attack. This was attributed to the formation of a low melting point MoO₃ phase, which reacted with molten salt resulting in formation of Na₂MoO₄. This low melting point oxide was suggested to cause the acidic fluxing of the protective scale.

To understand the accelerated oxidation of metals and alloys under sulphate salt coating wide ranges of corrosion kinetics and morphologies have been observed by Shi (1993) under controlled laboratory conditions and several kinds of mechanisms have been proposed by him. The Na₂SO₄-Na₂O eutectic melt was reported to be responsible for the formation of the abundant sulphide in the scale and believed to play an important role in the present form of accelerated corrosion. Moreover Fe₂O₃ can dissolve into the eutectic melt according to the reaction:



According to him the reduction of sulphate ions occurs at the scale/melt interface a negative gradient of concentration of O^{2-} and thereby of $2FeO_2^-$ could established across the melt. Further fluxing of Fe_2O_3 with the dissolution of Fe_2O_3 at the scale/melt interface and reprecipitating at the melt/gas interface was proposed by him.

The mechanism of Na_2SO_4 induced hot corrosion for nickel super alloys has been reported by Goebel et al (1973) in temperature range 650-1000 $^{\circ}C$ and by Misra (1986) in temperature range of 750-950 $^{\circ}C$. According to them the alloys underwent catastrophic corrosion. The accelerated oxidation has been ascribed to the formation of the liquid flux based on Na_2SO_4 which normally dissolves the protective oxide scales. They proposed the occurrence of catastrophic or self-sustaining rapid oxidation, in alloys which contain Mo, W or V because solution of oxides of these elements with Na_2SO_4 decreases the oxide ion activity of the molten salts which further produces the melts which are acidic fluxes for oxide scales.

The effect of Mo on the hot corrosion of superalloys has been further reported by Peters et al (1976), Pettit and Meier (1984), and Fryburg et al (1984). They observed the alloy containing Mo suffers catastrophic oxidation. It has been reported that MoO_2 react with Na_2SO_4 to produce an acid (SO_2 - rich) salt, leading to acidic fluxing. The MoO_3 gets incorporated into the Na_2SO_4 via the formation of compounds such as Na_2MoO_4 , $Na_2MoO_4 \cdot MoO_3$ and $Na_2MoO_4 \cdot 2MoO_4$. All these are liquid and reported to have high solubility for Al_2O_3 and Cr_2O_3 .

2.6.3 Energy Generation Systems

The corrosion of 9 Cr-Mo (T91 and EM12) steels has been evaluated by Colot et al (1997) in synthetic environments related to those experienced by tubes in coal-fired boilers. They have compared the effects of water vapour, SO_2 and ash deposits with and without alkali salts on the corrosion to that in ambient air in the temperature range 460 -800 $^{\circ}C$. In the synthetic atmospheres, a maximum in the corrosion rate was observed at approximately 600 $^{\circ}C$ which has been attributed to the effect of water vapour and/or SO_2 . This maximum was also observed for specimens oxidised with an ash deposit enriched in alkali salts which is ascribed to melting of alkali iron trisulphates, $(Na, K)_3Fe(SO_4)_3$. The alkali silicates were found to be responsible for high rates of corrosion as temperature reaches 800 $^{\circ}C$.

The variation of corrosion rate of mild steel as a function of moisture content of the coal and iron ore has been investigated by Gardiner and Melchers (2002). Two types of black

coal sieved to three different size fractions up to 2360 μm particle diameter and one type of iron ore of 600-1180 μm particle diameter were tested. A pronounced increase in corrosion rate was observed at moisture content between 60% and 80% of the maximum water holding capacity for all samples. The corrosion rate was also reported to increase with decreasing particle size distribution.

Moujahid (1987) has observed the ash corrosion, mechanical deformation and cracks on the cast iron chains of moving grate used to air burning of coal. The material design reportedly does not pay enough attention to the structure behaviour during the thermal cycling. Liquid coal ash at 1300⁰C strongly acidic has been observed to dissolve the basic wustite/spinel layers which got formed on the chains at elevated oxidation temperature. The fused ash embeds coal particles and also reduces the thermal efficiency of the equipment. Drastic enhancement in ash corrosion rate has been attributed to the mechanical damages.

Coal gasification systems operate at temperature of up to 2000 F. (1093⁰C) and at a pressure of up to 100 atm depending on the specific process and the product, coal gas generates the greatest problems. In addition to hydrogen and carbon-containing gaseous species, there are many undesirable species including sulphides, sulphites, sulphates, ammonia, cyanides, volatilised oils, phenols and aggressive trace elements such as potassium, sodium, vanadium and lead (Rapp et al, 1981). Metallic components in coal gasification pilot plants are exposed to severe corrosive atmospheres and high temperatures. The corrosive nature of the gaseous environments which contain oxygen, sulphur and carbon may cause rapid material degradation and result in the premature failure of components (Danyluk and Park, 1979). The characterisation of complex industrial atmospheres, both with respect to composition and oxidation, carburisation and sulphidation potentials is important in the design and operation of laboratory tests for materials evaluation (Kane, 1980).

Prakash et al (2001) have studied the boiler tube failure in coal fired boilers. A case study covering one-year duration has been conducted by them for a coal fired power plant in northwestern region of India. The number of failures occurred in the study year have been found to be 89 and out of which 50 failures were attributed to the hot corrosion and erosion of ash. They further investigated five samples of failed boiler tubes which were randomly selected from the same installation. The main cause of tube failures was found to be overheating which may be due to one or the other reason as out of five three failures were reportedly attributed to the overheating.

Severe pitting corrosion of carbon steel tube was observed in the air preheater of a power plant by Krishna and Sidhu (2002). They suggested that the extended non operation of

the plant resulted in the settlement of corrosive species on the tube surface. The complete failure reportedly occurred due to diffusion of these elements into the base metal and precipitation of potassium and chlorine compounds along the grain boundaries with subsequent dislodging of grains.

2.7 HOT CORROSION PROBLEMS ASSOCIATED WITH WELDING OF BOILER AND PRESSURE PARTS

Fusion welding is by far the most important process used in the fabrication of modern boilers. Components are joined by the formation of a molten pool of metal between them. The production of high quality welds with a high degree of consistency is readily achievable. However, defects are more likely to occur in welds than in wrought material. Whilst there are several modes of weld failure, these are generally associated with inadequacies in weld procedure or practice and should readily be detectable by non-destructive testing during manufacture. The welding of pressure parts can lead to other failure modes that only reveal themselves with time in service.

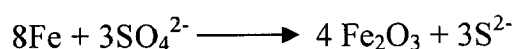
Hot corrosion is a serious problem in engineering systems such as steam boilers, gas turbines, waste incinerators, internal combustion engines, aircrafts, and chemical process systems, where low-grade fossil fuels are used (Prakash et.al., 1992).

Ahila et al (1994) investigated the hot corrosion of 2.25 Cr-1 Mo boiler tube steel and its weldment in the temperature range of 550 -700 °C. The corrodent used was a mixture of potassium sulphate and sodium chloride. Thermogravimetric and metallurgical studies indicated that the weight gain increased with time in all cases. Dissimilar metal welded joint showed the largest weight gain whereas the induction pressure weld showed the least. Hot corrosion of 2.25Cr-1M steel is classified as accelerated oxidation as the weight gain of coated specimens in two to three times higher than that of uncoated specimens.

Tsuge et al (1988) investigated the effect of nitrogen for resistance to pitting corrosion and stress corrosion cracking in various environments. The increase in nitrogen content increases the resistance of the base metal which results from improvement in the resistance of the gamma-phase which has lower chromium and molybdenum contents compared to alpha phase. Nitrogen is an important element in sustaining the corrosion resistance of the heat affected zone which is heated to 1350°C or higher because nitrogen promotes the formation of gamma-phase during cooling and avoids the precipitation of chromium carbides or nitrides at grain boundaries. Nitrogen has little effect on the precipitation behaviour of the other phase during aging heat treatment of around 700° C.

Tsay et al (1997) observed that the heterogeneous welds using a stainless steel ER309-16 as a filler metal displayed inferior mechanical properties. In the as welded condition, the heat affected zone with coarse grained structures initiated the crack. The propagation proceeded with in the diluted region along the fusion boundary, owing to the formation of martensite in that region. Both the untempered HAZ and the diluted region revealed a high susceptibility to hydrogen embrittlement. The precipitation of Cr-carbides along the fusion boundary is found after tempering at 690 °C for 1h, creating a more path-for the crack growth. The homogeneous weld which is made by using the equivalent composition alloy as a filler (ER9016-B3), revealed that the coarse grained HAZ of the as welded specimen caused premature failure in H₂S, but the crack still initiated at the coarse grained HAZ of a weld.

Ahila et al (1994A) discussed that extent of hot corrosion attack depends on various factors such as (1) porosity of oxide layer (2) transport of the corrosive species through the outer layer (3) dissociation of sulphate to establish a sulphur pressure at the inner layers (4) rate of reaction between the alloying elements and the reactants such as oxygen and sulphur, and (5) internal penetration of oxygen or sulphur into the substrate. The formation of nonprotective and discontinuous oxides of iron such as Fe₂O₃ and Fe₃O₄ at the start gives rise to a high rate of attack. Once a layer has been established, the rate of reaction decreases. The reactant which is in the liquid form can flow along the discontinuities such as pores, cracks or the grain boundaries to the scale/alloy interface and made available for further reaction. At the alloy/scale interface, the oxygen availability is governed by diffusion through the defects in the outer layer and the utilization of oxygen for the formation of oxides. The oxygen partial pressure at the subsurface is low. So at a certain stage, this will result to increased sulphur activity as



A significant sulphide pressure in the reaction zone greater than that required for Fe/FeS, Cr/Cr₂S₃ equilibria is resulted by the above reaction. The released sulphide ion reacts to form iron sulphide which also acts as a fast diffusion path for additional penetration of corrodents. They observed the weight gain of molten salt coated dissimilar metal weldments (DMW) was found to be higher than that in the base metal and other weldments. The scaling on Cr-Mo side was also found to be higher in DMW specimens than in unwelded and other weldments.

At moderately high temperature Cr-Mo steels are an extensively used family of engineering materials for applications such as steam generation/handling, petroleum

processing/refining, thermal reforming/polarization/cracking (Khare, A.K., 1981). The corrosion characteristics of similar and dissimilar metal weldments in Incoloy 800 and various nickel base alloys for use in advanced gas-cooled nuclear steam generators were tested in isothermal exposures in dynamic steam at 1100 and 1200 F (595 and 650 °C) at 900 psi pressure for periods to 16,000 h (2 years). General corrosion was determined by weight gain, weight loss, and scale thickness measurements, and preferential attack in fusion line areas was assessed by metallographic means. Projected long time corrosion amounts were very small for the weldments tested except those in Inconel 600, and for this weldment the projected corrosion was only 43 mg/cm² after 20 years. No evidence of aggravated attack at fusion line areas was disclosed. These findings appear to be applicable to weldments in the same alloys exposed to steam at lower temperatures (Hammond et al, 1973).

The localized corrosion attack occurs at preferred sites of the materials, those sites being either of microscopic dimensions, such as grain boundaries or of macroscopic size such as areas with deviating compositions or microstructure as in the case of weldments. Localized attack indicates the performance of one site to another to undergo corrosion. When two regions of different compositions or structures are in contact, the one which is more active will undergo corrosion leading to localized attack (Heubner and Hoffman, 1989).

Cracks permit the unimpeded transport of aggressive species into the bulk of the specimen. Within the cracks, the oxygen and sulphur activities may diverge widely from their equilibrium levels in the atmosphere and coating, with the result that more severe corrosive degradation can occur internally than would be expected with a given salt mixture at the surface. Due to this, the activity of oxygen at the surface is different from that at the subsurface. The lower activity of oxygen at the subsurface results in the formation of sulphides. The formation of various oxides and sulphides of alloying elements can be predicted thermodynamically considering the activity of the alloying elements in the material and assuming Henry's law of dilute solutions as indicated by (Baxter, 1986).

Ahila et al (1993A) concluded that the oxide formation on the uncoated and molten salt coated samples follows parabolic kinetics. These oxides are not protective in hot corrosion environments. The presence of sulphur in the form of sulphates can cause internal sulphidation of the alloy beneath the external oxide layer, causing internal degradation which is damaging. This destroys the integrity of the alloy and weakens its mechanical properties.

Exworthy et al (2002) discussed the cracks were the result of the stress relief heat treatment of the boilers, and follow an intergranular path as a result of interlinkage of grain boundary creep cavitation associated predominantly within the coarse grain heat affected

zone microstructure. The depth of the cracks was limited by the residual and thermal stress distribution to about half the wall thickness of the boiler shells. There were no obvious chemical, microstructural or mechanical property differences between cracked and uncracked boiler shell plates that could be identified to account for the observed cracks. The diagnosis of the cracking mechanism provides factors that could be taken into account to minimize the risk of further stress relief cracks forming during the post weld heat treatment weld option selected for the repair.

Ahila et al (1993) investigate the welded specimens showed a lower degree of attack in both molten salt coated and uncoated conditions. Oxides were observed on uncoated specimens while in coated specimens sulphide in addition to oxides. Attack on coated specimens was due to the formation of a liquid phase which could flow along the grain boundaries and weaken them as shown in Fig. 2.11. This led to accelerated corrosion.

2.7.1 Microstructural Variation Corrosion of Different Regions of Weldments

Microstructurally different regions (namely the weld metal, heat affected zone (HAZ), and base metal) were characterized in weldments of 9 Cr-1 Mo steel, and composite specimens comprising the three regions were oxidised in air at 923 K. As measured by surface profilometry, the weld metal region was found to form a thicker oxide scale than the other regions of the weldment. The difference in thickness between the scales over the weld and adjoining HAZ regions was found to be $\sim 5 \mu\text{m}$ after 4 h but had increased to $\sim 100 \mu\text{m}$ in 100 h. Difference in thickness between the scales was also confirmed by a few examinations using scanning electron microscopy (SEM); this method also described the difference in morphology of the scales developed over the three regions. Secondary ion mass spectroscopy (SIMS) depth profiles of iron and chromium in scales developed over the different regions of the weldments have suggested a considerably higher chromium content of the inner scales on the HAZ and base metal than that of the scale over the weld metal; SIMS profiles have also corroborated formation of a thicker scale over the weld metal, as assessed earlier by surface profilometry and SEM (Raman et al, 1998A).

In the weldments of 2.25 Cr-1 Mo and 9 Cr-1 Mo ferritic steels, the regions with different microstructures were identified as weld metal, heat-affected zone (HAZ) and base metal. When exposed to high temperatures, the HAZ of 2.25 Cr-1 Mo steel and the weld crown region of 9 Cr-1 Mo steel were found to oxidize at higher rates, and develop much

thicker scale than other regions in the weldments of the respective steels. SEM/EDS point analyses and SIMS depth profiles indicate that the scale over the regions showing inferior oxidation resistance are considerably less in free chromium content. The difference in the oxidation behavior of the different regions was found to arise from the difference in the Cr content of the inner layer of the protective oxide. Possible remedial measures to minimize the high oxidation rates in certain regions of the weldments of the two steels are also discussed (Raman and Gnanamoorthy, 1995A).

Penetration at prior austenitic grain boundaries was observed in the heat-affected zones of weldments after the metal was exposed to 500 °C for short times to liquid lithium containing 17.6 wt. pct lead. Corrosion increases with increasing austenitizing temperature is insensitive to quench rate. The penetration kinetics exhibited a change in mechanism which is hypothesized to be associated with the conversion of epsilon -carbide to cementite. The initial penetration mechanism is thought to be controlled by carbon diffusion in liquid lithium. The secondary penetration rate exhibited activation energy of 117 kJ/mol, which suggests that reaction of lithium with cementite at the grain boundaries might be the rate controlling step (Anderson and Edwards, 1981).

Raman (2002) investigate the thermal scaling behavior of weldments of 9 Cr- 1 Mo steel and compares the recent findings of nonuniform scaling observed during air oxidation of 2.25 Cr-1 Mo steel weldments. The article also discusses the bearing of the nonuniform scaling on the life assessment.

The fatigue crack growth rate (FCGR) properties of SA508 Cl 2a and SA533 Gr A Cl 2 pressure vessel steels and the corresponding automatic submerged arc weldments were developed in a high-temperature pressurized water (HPW) environment at 288 degrees C and 7.2 MPa at load ratios of 0.20 and 0.50. The HPW environment FCGR properties of these pressure vessel steels and submerged arc weldments were generally conservative, compared with the appropriate American Society of Mechanical Engineers (ASME) Section XI water environment reference curve. The growth rate of fatigue cracks in the base materials, however, was considerably faster in the HPW environment than in a corresponding 288 degrees C base line air environment. The growth rate of fatigue cracks in the two submerged arc weldments was also accelerated in the HPW environment but to a significantly lesser degree than that demonstrated by the corresponding base materials. In the air environment, fatigue striations were observed, independent of material and load ratio, while in the HPW environment, some intergranular facets were present. The greater environmental effect on



(a) HAZ



(b) Unwelded



(c) Weld metal

Fig. 2.11: Showing grain boundary attack at 650 °C due to coating of sulphate chloride mixture in welded 2.2Cr-1Mo steel (a) HAZ (b) Unwelded (c) Weld Metal (Ahila et al, 1993).

crack growth rates displayed by the base materials, as compared with the weldments, was attributed to a different sulfide composition and morphology (Liaw et al, 1989).

Supermartensitic stainless steel (SMSS) grades are gaining popularity as an alternate material to duplex and super duplex stainless steels for applications in oil and gas industries. The weldability of these steels, though reported to be better when compared to conventional martensitic stainless steels, so far has been addressed with duplex stainless steel electrodes/fillers. This work addresses the stress-cracking behaviour of weldments of a high-grade supermartensitic stainless steel (11% Cr, 6.5% Ni and 2% Mo) in the presence of hydrogen. Welds were produced with matching consumables, using electron beam welding (EBW) process. Weldments were subjected to slow strain rate tests in 0.1 M NaOH solution, with introduction of hydrogen into the specimens by means of potentiostatic cathodic polarisation at a potential of -1200 mV versus Ag/AgCl electrode. Reference tests were performed in air for comparison, and the results suggest that both the SMSS base material and the EB weld metal are susceptible to embrittlement under the conditions of hydrogen charging. (Srinivasan et al, 2004).

Raman (1998) investigate the influence of the free chromium content in the three weldment regions on protective scale formation and on the subscale features in the HAZ of 2.25 Cr-1 Mo steel weldment in 35% steam + nitrogen environment at 873K for 10 hours. A less protective inner scale is developed in the HAZ region, which causes a higher oxidation rate in the HAZ than in the weld metal and base metal regions. The formation of less protective inner scale is attributed to the trapping of free Cr, to form Cr based secondary precipitates, exclusively in the HAZ. The less protective scale formation on the HAZ surface also results in a subscale zone with extensive internal oxidation void formation in the subscale and grain boundary cavitation in the adjacent alloy matrix. It is inferred that the extensive void formation in the subscale region and the grain boundary cavitation occurring exclusively in the neighboring alloy matrix of the HAZ can contribute to in service mechanical failures in the HAZ of 2.25 Cr-1 Mo steel weldments.

In air, high temperature corrosion of weldments of Cr-Mo ferritic steel revealed that the HAZ oxidized at a much higher rate than the weld metal and base metal. The disappearance of fine Mo based carbide precipitates (enriched in Cr) are believed to be responsible for the inferior mechanical properties of the HAZ. The Cr depletion has been found to be responsible as well for the inferior corrosion resistance of the HAZ (Raman and Gnanamoorthy, 1993).

Low-Cr steels are also known to undergo internal oxidation resulting in distinct subscale formation (subscale is the region under beneath the external oxide scale (Raman et al, 1992; Birks and Meier, 1983). Extensive internal oxidation and oxidation induced void formation in the subscale zone and grain-boundary cavitation in the neighboring region were found to occur during oxidation of Cr-Mo steel weldments in the steam and synthetic (bottled) air environment at 873 K. However, the internal oxidation and void formation were much more extensive in the subscale regions of the HAZ than in the subscales of the weld metal and base metal regions. As a result the alloy matrix in the area neighboring the subscale region of the HAZ specimen suffered extensive grain boundary cavitation. This behavior has been attributed to a rather specific combination and nature of the resulting external scale in causing and sustaining internal oxidation (Raman, 1999).

Raman & Muddle (2000A) concluded that the greater scaling rate of HAZ than weld and base metal regions of a 2.25 Cr-1 Mo steel weldments to be taken into account while using scale thickness measurement as a tool for life assessment of high temperature welded components. Given a suitable environment, a combination of Cr-rich secondary precipitation and extensive internal precipitation in the HAZ can result in further degradation of alloy microstructure which can facilitate crack propagation.

Kazuhio et al (1995) investigates the properties of weld metal of 18Cr heat resistant austenitic steel containing high copper, niobium and nitrogen using TIG welding process. The hardness of weld metal decreased in the welded joint of lower thickness tube and on the condition of higher interpass temperature. The Mo was effective in improving the tensile strength of weld metal but an additive over 1 Mass % deteriorated the corrosion resistance was effective in improving the tensile strength of weld metal. The nitrogen content in weld metal decreased to about 80% of that in welding material by vaporization during the TIG welding process. Manganese addition was effective in preventing N₂ decrease trough welding.

2.7.2. Economic Factors in Weldments

Firstly, failures of superheater and reheater boiler tubes are due to long-term creep and fireside corrosion. A method of life assessment is described which allows economic tube replacement prior to failure. Secondly, failures of dissimilar metal weldments in boiler tubing have been encountered when high system loads are developed. An approach to quantify operating life in terms of stress and temperature is described and procedures to reduce system loading are discussed. Thirdly, damage accumulation in thick-section components, e. g. superheater and reheater outlet headers, constitute safety and economic problems (Parker and Sidey, 1986).

2.7.3 Component Integrity and Life Assessment of Weldment

Operating conditions and environments represent an ongoing threat to component integrity in steam raising plant. There is no prospect of any utility being able to adopt a 'fit and forget' philosophy within the design life of a boiler. Indeed, current life extension means that much of the fired plant in India is approaching, or has already exceeded, twice the original design life. Further, with changes in commercial markets and regulation, existing plant is currently having to operate in a much less certain and much more flexible regime than its original design intent. Accordingly, components are increasingly being subjected to ever more onerous operating conditions under ever more aggressive environments. Hence, all utilities are obliged to develop, adopt and continually improve methods for assessing the integrity and future safe life of components in service. These life assessment methods incorporate the most up to date non destructive (NDE) techniques and metallographic assessment procedures to determine materials' degradation in service. These are supplemented by extensive databases of materials' properties, fracture mechanics, knowledge of microstructural evolution with time at temperature, measurement and analysis of corrosion mechanisms and finite element stress analysis, in order that risks to component integrity can be minimized.

Boiler tubes in power plants have finite life because of prolonged exposure to high temperature, stress and aggressive environment. Service-exposed platen super heater and reheater tubes (148,900 h) made of 2.25Cr-1 Mo steels in a 120 MW boiler of a thermal power plant were evaluated for remnant life. Remaining life assessment (RLA) of aged power plant components in the present highly competitive industrial scenario has become very popular both for economy and safety reasons. In India there is a great demand for RLA since some of the 60,000 MW capacity power sectors have become older than 20 years. In real life both premature retirement and life extension (in relation to design life) can be encountered. The decision for retiring a component is not purely technical but also one of economics and safety. Boiler components used in power plants have finite life because of prolonged exposure to high temperature, stress and aggressive environment. However, past experience has shown that for a variety of reasons these may have significant remaining life beyond the design specification (Ray et al, 2003).

The prevalence of in-service failures in the welds of chromium-molybdenum ferritic steels causes great concern in steam generating/handling systems of power plants, and components of petroleum/petrochemical industries. Raman and Muddle (2002A) discussed

the non-uniform scaling behaviour across microstructural gradients in weldments of pressure vessel steels in order to develop a global model for life-assessment by relating oxide scale thickness with time-temperature history of in-service components. They observed the following points

- i) Examining the applicability of the recent practice of life assessment by scale thickness to the welded components, by establishing kinetics of the scale thickness growth across the broadly different (microstructural) zones (viz. weld metal, HAZ and base metal) of the steel weldments, in the environments of steam and air.
- ii) Developing a suitable model for life assessment by relating scale thickness with time-temperature history (and hence, creep damage) in the different zones of the steel weldments.
- iii) Characterizing corrosion-assisted microstructural degradation in the alloy matrix across the broadly different (microstructural) zones (viz. weld metal, HAZ and base metal) of the steel weldments, in the environments of air and steam, and thus investigating the role of the environment in facilitating microstructural degradation.

Intergranular cavitation and rupture life of metallic materials are reported to be influenced by both the environment and secondary precipitation as well as the internal precipitation caused by the residual oxygen in the alloy matrix. Localized effects of gaseous corrosion include formation of corrosion notches and extensive grain boundary oxidation causing grain detachment during air-oxidation of 2.25 Cr-1Mo steel is shown in Fig. 2.12.

A cross-section through a typical oxidised specimen (base metal) is shown in Fig. 2.13, which suggests the presence of at least three distinct regions, viz. a thick compact outer layer, a sub-scale region consisting of extensive internal oxide precipitates, and a thin inner layer which formed between the external layer and the subscale. The subscale region was populated with internal oxide precipitates, with the internal oxide precipitates forming more extensively at the alloy grain boundaries (Raman and Muddle, 2000A). Cross-sections of the oxidized weld metal had features similar to those in the oxidised base metal.

2.8 EFFECT OF AQUEOUS CORROSION ON WELDMENTS

In recent times a considerable effort has been made to undertake a systematic and fundamental approach in the study the corrosion behaviour of the steel weldments used in power boilers. The induction-pressure welding process (IPW) is widely used, especially for



Fig. 2.12: SEM micrograph showing extensive grain boundary oxidation causing grain detachment during air-oxidation of 2.25Cr-1Mo steel at 823 K (Raman et al, 1992).

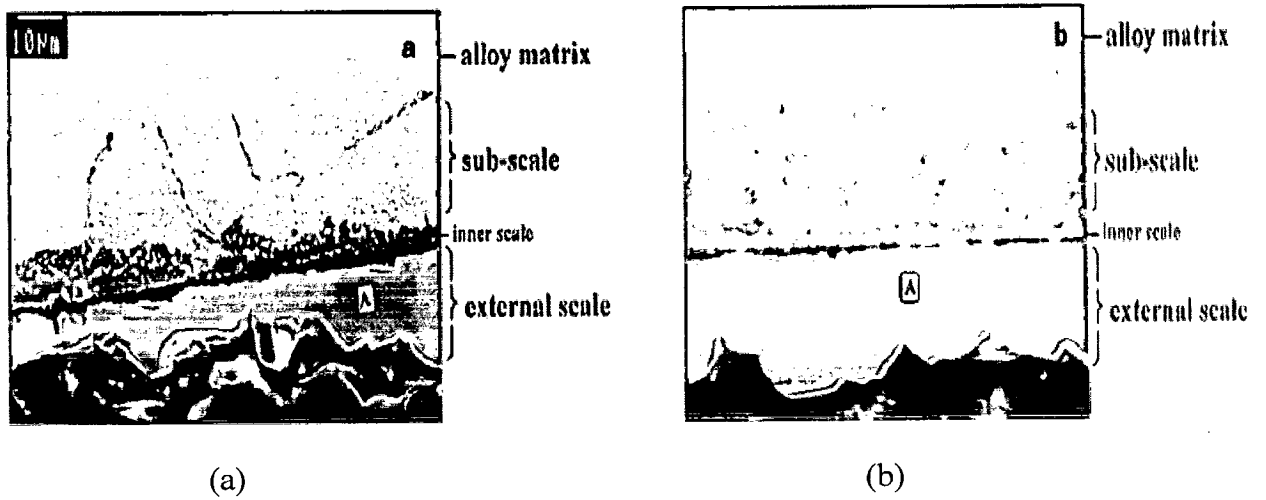


Fig. 2.13: Representative SEM micrographs showing cross-sections through oxide scales and subscale zones formed over: (a) the base metal/weld metal specimens, and (b) HAZ, during steam oxidation at 873 K (Raman and Muddle, 2000A).

tubular products, for three important reasons: (i) cost effectiveness; (ii) Fit is faster than any other fusion methods; and (iii) it is suitable for mass production. This technical paper describes experimental work carried out to evaluate and compare corrosion and its inhibition in SA 210 Gr A1 carbon steel boiler steel weldments prepared by induction pressure welding process in HCl at 0.1M, 0.5M, and 1.0M concentrations. The parent metal and the weld root were chosen as the regions of exposure for the study, which was made at room temperature and at 100°C after all the test specimens were suitably stress relieved. Electrochemical polarization techniques such as Tafel line extrapolation and linear polarization resistance were used to measure the corrosion current (Natarajan and Sivan, 2003). It is well known that the corrosion phenomenon in boiler (steam-generator) installations can occur on the water side of the boiler, inside the boiler tubes, inside the super heater, economizer, condensing unit. The water used for raising steam often contains dissolved solid and gaseous impurities which can cause scaling and corrosion, such scale is normally removed by acid cleaning. In SA 210 GrA1 carbon steel and SA 213 T11 boiler steel weldment prepared by manual metal arc welding and tungsten inert gas welding and evaluate the corrosion and its inhibition in an HCl acid medium at different concentrations, conclude that manual metal arc weld (MMAW) corrodes less than TIG welding in all regions with a gradual increase in acid concentration (Natarajan and Sivan, 2003).

Failures of industrial boilers have been reported to be mainly due to water side corrosion and scaling. Boiler corrosion is due to highly alkaline or acidic conditions of the boiler water. Natarajan and Babu (2006) discussed the corrosion behaviour of T22 (2.25 Cr-1 Mo) boiler steel TIG weldments in neutral and alkaline media. The parent metal and weld root regions are chosen as regions of exposure for the study made at room temperature and at 100 °C. Parent metal experiences by and large two to three times higher corrosion rate when compared to weld metal region at all concentrations in neutral and alkaline media.

2.9 FORMULATION OF PROBLEM

High-temperature corrosion engineering appears well placed for development in the current climate, with appropriate integration in design and systems engineering approaches. High temperature corrosion science research is extensive worldwide, there is no shortage of interesting work to be done, or enthusiasts to do it, but it would benefit from several really novel new areas, particularly in a competitive funding scenario which favors technology transfer and industrially oriented research (Wood and Stott, 1995).

Due to depletion of high-grade fuels and for economic reason use of residual fuel oil in these systems is well known. Residual fuel oil contains sodium, vanadium and sulphur as impurities. Sodium and sulphur form Na_2SO_4 (melting point 884°C) by reactions in the combustion system. Vanadium is usually present as porphyrin or other organometallic complexes but inorganic compounds of vanadium have also been reported. During combustion of the fuel, vanadium reacts with oxygen to form an oxide V_2O_5 (melting point 670°C). Thus V_2O_5 is a liquid at gas turbine operating temperature. These compounds (known as ash) deposit on the surface of the materials and induce accelerated oxidation (hot corrosion) in energy generation systems.

Knowledge of the reaction kinetics and the nature of the surface scales formed during oxidation are important for evaluating the alloys for their use and degradation characteristics in high- temperature applications. The oxidation behaviour of complex alloys has not been studied extensively and is not well understood. Therefore further studies are needed on oxidation behaviour of complex commercial alloys, particularly those used for high temperature applications (Hussain et al, 1994).

Fusion welding is by far the most important process used in the fabrication of modern boilers. Components are joined by the formation of a molten pool of metal between them. The production of high quality welds with a high degree of consistency is readily achievable. However, defects are more likely to occur in welds than in wrought material. Whilst there are several modes of weld failure, these are generally associated with inadequacies in weld procedure or practice and should readily be detectable by non-destructive testing during manufacture. The welding of pressure parts can lead to other failure modes that only reveal themselves with time in service.

Ahila et al, (1994) have studies on the 2.25 Cr-1 Mo (T22) SA 213 boiler tube steel and its weldments in the molten salt ($\text{K}_2\text{SO}_4\text{-NaCl}$) at the temperature range $550\text{-}700^\circ\text{C}$. The weldment were made with the three different processes viz manual metal arc weld, induction pressure weld (IPW) and dissimilar metal weld and observed that IPW show the better corrosion resistance in Cr-Mo steel. More cracks and spallation were noticed in manual metal arc weld and dissimilar weld as compared to induction pressure weld.

In air, high temperature corrosion of weldments of Cr-Mo ferritic steel at 873K revealed that the HAZ oxidized at a much higher rate than the weld metal and base metal. The disappearance of fine Mo based carbide precipitates (enriched in Cr) are believed to be responsible for the inferior mechanical properties of the HAZ. The Cr depletion has been found to be responsible as well for the inferior corrosion resistance of the HAZ (Raman and Ganamoorthy, 1993).

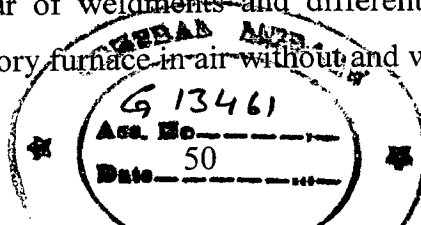
It has been learnt from the literature that the hot corrosion is a serious problem in power generation equipments, in gas turbines for ships and aircrafts and in other energy conversion and chemical process systems. Hot corrosion is the accelerated oxidation of materials at elevated temperatures induced by a thin film of fused salt deposits. Corrosion has been attributed to the fluxing action of the molten salt deposits on the oxide scales formed on the tubes, leading to rapid localized corrosion, accompanied by some sulphidation also. Hot corrosion first became known to engineers and researchers with the failure of boiler tube and later with the severe attack of gas turbine component materials.

Weld corrosion has been a problem since materials were first joined by welding processes. As new materials are developed for use in corrosive environments, new incidents of corrosion failure are discovered. Most of the failures are reported in weldment region when the materials are subjected to corrosive environment at elevated temperature.

In view of the fact that further investigation on these weldments process subjected to hot corrosion are needed some boiler tube materials are proposed to be chosen. These boiler tube steel are procured from Guru Nanak Dev Thermal Power Plant Bhatinda, Punjab, India, namely SA 210-GrA1 (GrA1), SA 213-T11 (T11) and SA213 -T22 (T22). Relatively fewer studies are conducted on weldments of boiler tube material.

Little information is available on the combined effect of vanadium oxide and sodium sulphate. Vanadium oxide can react with Na_2O to form sulphate-vanadate compounds, which modify the attack rate of the oxide layer or even attack the alloy (Lambert et al, 1991). As learnt from the literature that oil ash corrosion occurs at a rapid rate in the initial hours of the test and then the rate decreases. Hence the corrosion of weldments in vanadic environment is of particular interest in the initial period. Most industrial processes involve the use of metals and alloys at elevated temperature followed by cooling to room temperature numerous times. The operating conditions in such plants conform more too cyclic, rather than to isothermal processes. Therefore oxidation under cyclic conditions constitutes a more realistic approach towards solving the problem of metal corrosion (Sadique et al, 2000). Relatively fewer studies are reported under cyclic conditions, which actually simulate the working conditions of boilers and gas turbines. In cyclic conditions, high thermal stresses are developed. Cyclic oxidation in air was carried to get information on the spalling tendency of the oxide scale (Burman and Ericsson, 1983).

Hence it is decided to select 50 cycles (cycle of 1 hour heating followed by 20 minutes cooling) to study the behaviour of weldments and different regions of weldment in the temperature at 900°C in laboratory furnace in air without and with aggressive environment of



oil fired boilers ($\text{Na}_2\text{SO}_4\text{-V}_2\text{O}_5$). It was also proposed to measure weight change to study the corrosion kinetics and to use X-ray Diffractometer (XRD), Scanning Electron Microscope (SEM), Energy Dispersive X-ray Analysis (EDAX) and Electron Probe Micro Analyser (EPMA) to characterize the corrosion product and to make an attempt to understand the mechanism of corrosion.

Many welding processes are available, among which are included: shielded metal arc (MMA) welding, metal inert gas (MIG) welding, friction welding, submerged arc welding and tungsten inert gas (TIG) welding. These welding processes are generally used to weld most common materials in an electric generating industry.

EXPERIMENTAL PROCEDURE

In this chapter the experimental procedure used for the study has been summarised. It includes the procedure to obtain the weldments, their characterisation, the hot corrosion studies and the analysis of final corrosion products.

3.1 SELECTION OF SUBSTRATE STEELS

Three types of selected substrate materials are low carbon steel “ASTM-SA210-Grade A1 (GrA1),” 1Cr-0.5Mo steel “ASTM-SA213-T-11 (T11)” and 2.25Cr-1Mo steel “ASTM-SA213-T-22(T22).” These steels are used as boiler tube materials in some of power plants in Northern, India. GrA1 has a wide range of applications in boilers, especially in the construction of their water walls. When the service conditions are stringent from the point of temperature and pressure other two types of steel mentioned above are being employed.

3.1.1 Determination of Chemical Compositions

The actual chemical composition of these steels has analysed with the help Optical Emission Spectrometer of Thermo Jarrel Ash (TJA 181/81), USA make. Nominal and actual compositions of these steels are reported in Chapter 4 of the present study.

3.2 EXECUTION OF WELDMENTS

3.2.1 Edge Preparation

The boiler tube was cut into approximate length of 150 mm each. Each tube was machined to obtained a single conventional V-groove, with 37.5° bevel angle for SA210 Grade A1 (GrA1), SA213 T11 and 30° bevel angle for SA213 T22 steel with constant root gap of 1 mm and root face 1 mm as shown in Fig. 3.1 (a), (b).

3.2.2 Welding processes

Two types of welding processes were used for weldments in boiler tube steels. One is shielded metal arc welding (SMAW) was used with coated electrode (procured from D&H Secheron Electrodes (P) Ltd., Indore, India) having the similar composition to the base metal. Other one tungsten inert gas welding (TIG) was used with filler wire having the same composition to the base metal where the 99% pure argon gas was used for TIG welding. The chemical compositions of electrode and filler wire for the weldments are reported in Chapter 4 of the present study.

3.2.3 Formulation of Weldments

Prior to welding the tube were thoroughly cleaned with brush and acetone so as to remove any oxide layer and dirt or grease adhering to the tube. ESAB (Elektriska vetnsnings-Aktiebolaget) welding machine (Model S-69581, Aristo, 2002, Made in Sweden) was used to obtain the weldments. Argon gas was used for TIG welding and shielding electrodes were used for SMAW. All the process parameters including the root were constant throughout the welding process. The process conditions were as reported in Table 3.1 & 3.2.

Table 3.1: Welding parameters for SMAW weldment in GrA1, T11 and T22 steels.

Process type Base steel	Manual GrA1	Manual T11	Manual T22
Electrode	AWS A5.1 E7018	AWS A5.5 E8018-B2	AWS A5.5 E9018-B3
Root	By Electrode	By Electrode	By Electrode
Electrode size	3.15 mm	3.15 mm	3.15 mm
Arc current	95 A	95 A	95 A
Arc voltage	22 V	22 V	22 V
Number of pass	2	2	4
Average welding speed	140.47 mm/min	140.47 mm/min.	71.77mm/min
Average Heat Input	8927J/cm.	8927 J/cm	17472 J/cm

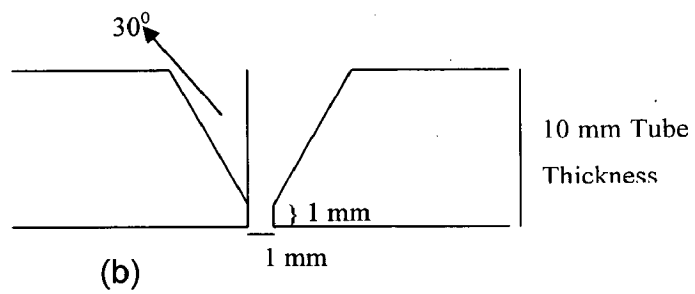
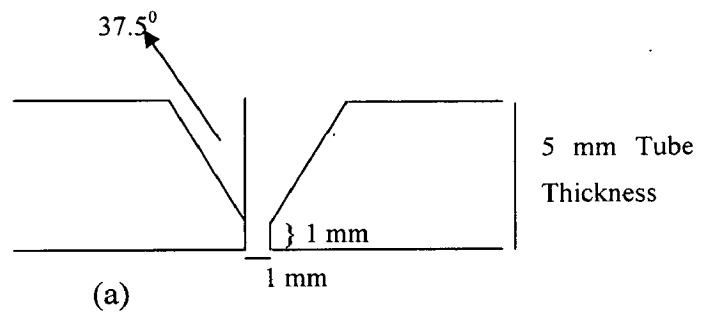


Fig 3.1: Schematic view of weldment design (a) for GrA1 and T11 tube (b) for T22 tube

Table 3.2: Welding parameters for TIG weldment in GrA1, T11 and T22 steels.

Process type Base steel	Manual GrA1	Manual T11	Manual T22
Filler wire	AWS A5.18 ER 70S-2	AWS A5.28 ER 80S-B2	AWS A5.28 ER 90S- B3
Root	By Filler wire	By Filler wire	By Filler wire
Filler wire size	2.4 mm	2.4 mm	2.4 mm
Arc current	95 A	95 A	95 A
Arc voltage	12V	12 V	12 V
Number of pass	4	4	6
Average welding speed	46.93 mm/min.	46.93 mm/min.	19.407 mm/min.
Argon flow rate	8 l/min.	8 l/min.	8 l/min.
Average Heat Input	14575 J/cm.	14575 J/cm	35245 J/cm

3.2.4 Preparation of Samples Materials

The circular weldments were cut from the tube to form approximately 20x15x5 mm size specimens for composite weldment and 15x5x2 mm size specimen for different regions of weldment. The specimens were polished with 220 grade of SiC paper and 1/0, 2/0, 3/0, 4/0 grade emery papers and then wheel polished before corrosion studies.

3.3 CHARACTERISATION OF WELDMENTS

3.3.1 Measurement of Weldment Width and Optical Microstructure of Weldments

The size of boiler tube before welding and the width of SMAW and TIG weldments were measured after welding and optical microstructure of different regions of weldments are reported in Chapter 4 of the present study.

3.3.2 Porosity Analysis

The porosity measurements for SMAW and TIG weldments have been made after polishing samples. The porosity measurements were made with image analyser having software of Dewinter Matelal Plus 1.01 based on ASTM B276. The image was obtained

through the attached PMP3 Inverted Metallurgical Microscope made in Japan. The porosity values so determined are the mean of the five measurements and reported in Chapter 4 of the present study.

3.3.3 Microhardness Measurement

The microhardness of cross-section of weldments was measured by Leitz's, Hardness Tester Mini Load-2, German make microhardness tester. 15 pound (147.1 mN) load was provided to the needle for penetration and hardness value is taken from the relation

$$Hv = 1854.4 \times \frac{P}{d^2} \text{ (Where P is load in pound and d is the mean penetrated diameter in } \mu\text{m).}$$

Each reported value is the mean of five measurements performed and reported in Chapter 4. The analysis was carried out at Mechanical and Industrial Engineering Department (MIED), Indian Institute of Technology, Roorkee (India).

3.3.4 Tensile Testing

Circular tensile test specimens with weld at centre, having dimension (diameter 5 mm) according to ASTM E8M were prepared from the weldments produced under constant welding parameters. The load versus extension plots was recorded during the testing. From these tests ultimate tensile strength and percentage elongation were evaluated and reported in chapter 4.

3.3.5 Metallographic Studies

For metallographic studies the weldments and unwelded samples were cut along the cross-section with diamond cutter (Low speed saw, 04006, Buehler, USA make). After cutting, these samples were hot mounted in Buehler transoptic powder (20-3400-080) using Simplemet-II (04002), Buehler USA make mounting machine. The surface of the specimen is first made plane by specially designed motor-driven emery belt. The samples were than polished manually using SiC metallographic emery papers up to 800 grit. After manual polishing the samples were polished on high speed polishing wheel using diamond polishing series of 6 μm and then 3 μm sizes. The final polishing is carried out on a sylvet-cloth using 1 μm size alumina powder suspension on polishing wheel machine. Samples were etched with 2% nital for 20 second, washed, dried and finally examined under MeF, Reichert-jung optical microscope made in Austria. The typical microstructures of the different regions of welded samples were photographed and have been reported in Chapter 4 of the present study.

3.4 HIGH TEMPERATURE OXIDATION AND HOT CORROSION STUDIES

3.4.1 Experimental Setup

Oxidation and hot corrosion studies were conducted at 900⁰C in the laboratory silicon carbide tube furnace, Digitech, India make. The furnace was calibrated with the variation of $\pm 5^{\circ}\text{C}$ using Platinum-Rhodium thermocouple and temperature indicator of Electromek (Model-1551 P), India. Al₂O₃ boat was pre heated upto 1200⁰C for 6 h with the assumption that its weight would remain constant during the cycle of study. The composite weldment, different regions of weldment and unwelded samples were subjected to mirror polishing following to wheel cloth polishing for 5 minutes before study. After polishing the samples were washed properly and dried in the hot air to remove the moisture. For every experiment the sample was kept in the boat, weight of boat and sample was measured before inserting into the hot zone of the furnace at 900⁰C. The holding time in the furnace was one hour and after one hour the boat with sample was taken out and cooled at the ambient temperature for 20 minutes. Weight of the boat along with sample was measured and this constitutes one cycle. All oxidation and hot corrosion studies carried out for such 50 cycles. Any spalled scale in the boat is taken into consideration for the weight change measurements. The Electronic Balance Model CB-120 (Contech, Mumbai, India) with a sensitivity of 1 mg was used to measure the weight change values.

3.4.2 Oxidation Studies in Air

The oxidation tests at 900⁰C were performed on the base steels, composite weldments and its different regions in steels in laboratory furnace up to 50 cycles as discussed in section 3.4.1. Visual observation for the oxide scale was recorded after each cycle along with the weight change measurements.

3.4.3 Hot Corrosion Studies in Molten Salt (Na₂SO₄-60%V₂O₅)

3.4.3.1 Molten Salt coating

The composite weldments, its different regions and unwelded metal samples were prepared for studies as discussed in section 3.2.4. The samples were heated in the oven upto 250⁰C and the salt mixture of Na₂SO₄-60%V₂O₅ dissolved in distilled water was coated on the warm polished samples with the help of camel hair brush. The amount of the salt coating varies from 3.0 -5.0 mg/cm². The coated samples were then dried at 110⁰C for 3-4 hours in the oven and weighed along with the Al₂O₃ boat.

3.4.3.2 Hot Corrosion Studies

The salt coated samples were subjected to hot corrosion in the laboratory furnace at 900°C for 50 cycles. At the end of each cycle critical observations were made regarding the corrosion products along with the weight change measurements.

3.5 ANALYSIS OF CORROSION PRODUCTS OF OXIDATION IN AIR AND MOLTEN SALT

All the samples subjected to hot corrosion were analysed for the identification of corrosion products for both the surface as well as cross-section. The analysis was performed for surface and cross-section of the corroded samples. Corroded samples were subjected to XRD, SEM, EDAX, measurement of scale thickness and EPMA analysis.

3.5.1 Visual Observation

Visual examination was made and recorded after each cycle for any change in colour, lustre, adherence-spalling tendency and development of cracks in the scale etc. After the completion of 50 cycles (each cycle of 1 hr heating and 20 minutes cooling) in laboratory furnace and then their macrographs were taken.

3.5.2 Thermogravimetric Studies

The weight change values were measured at the end of each cycle with the aim to understand the kinetics of corrosion. The data was plotted with respect to number of cycles for each sample and the plots are given in the subsequent chapters. In many cases spalling and scaling occurred in the alumina boat and the same is also added in the weight change values.

3.5.3 Measurement of Scale Thickness

After exposure at 900°C in laboratory furnace, the samples were cut across the cross-section and polished as discussed in section 3.3.5. Scanning Electron Microscope (LEO 435VP) with attached Robinson Back Scattered Detector (RBSD) was used to obtain the BSE images. The average thickness of the scale was determined from the measurements taken on BSE images.

3.5.4 X-Ray Diffraction (XRD) Analysis

XRD studies performed on the as corroded weldments, its different regions and unwelded samples to identify the different phases formed during hot corrosion studies in

the scale. The diffraction patterns were obtained by Bruker AXS D-8 Advance Diffractometer (Germany) with CuK_α radiation and nickel filter at 20 mA under a voltage of 35 kV. The specimens were scanned with a scanning speed of 1 K_{cps} in 2θ range of 10 to 110° and the intensities were recorded at a chart speed 1 cm/min with $1^\circ/\text{min}$ as Goniometer speed. Assuming height of the most prominent peak as 100%, the relative intensities were calculated for all the peaks. The diffractometer being interfaced with Bruker, DIFFRAC^{plus} X-ray diffraction software provides 'd' values directly on the diffraction pattern. These 'd' values were then used for identification of various phases with the help of inorganic ASTM X-ray diffraction data cards.

3.5.5 SEM/EDAX Analysis

3.5.5.1 Surface morphology

EDAX of corroded sample surfaces were performed at Central Research Facilities (CRF), Indian Institute of Technology, Kharagpur (India) on JEOL (JSM-5800) Scanning Electron Microscope with EDAX attachment of Oxford (Model-6841) made in England on as weldment and its different regions samples. Samples were scanned under the microscope and the critical areas of interests were photographed with an aim to identify the inclusions, microcracks and morphology of the surface scale. Point analysis was performed on various locations on these identified areas of interest on corroded surfaces of the samples with an aim to identify the various corrosion products. The typical microstructures and elemental analysis are reported in Chapter 5, 6 of the present study.

3.5.6 Electron Probe Micro Analyser (EPMA)

Composite weldments, its different regions and unwelded samples were cut along the cross-section with diamond cutter, mounted and polished as per the procedure discussed in section 3.3.5 and subjected to EPMA analysis. The mounted samples were subjected to carbon coating before performing the EPMA analysis. The elemental X-ray mapping was obtained for the critical area of interest on each sample. The selected area could have the three i.e. base sample, oxide scale and some epoxy region at the top of the scale. First Backscattered Electron Image (BSEI) was photographed and then elemental X-ray mapping was taken for various elements. The elements selected for X-ray mapping were as per the composition of the base steels, type of weldment and environment of study. Most of the EPMA analysis was done at Institute Instrumentation Centre (IIC), Indian Institute of Technology, Roorkee (India) on JXA-8600M microprobe.



CHARACTERISATION OF SUBSTRATE STEELS AND WELDMENTS

This chapter deals with critical evaluation of the base steels and the various weldments obtained with different welding processes. The metallographic examinations of base steels as well as the weldments have been discussed. The physical and mechanical properties like porosity, microhardness and tensile properties of as weldment have been reported and discussed with respect to the existing literature.

4.1 SUBSTRATE STEELS AND ELECTRODES/FILLER WIRE

4.1.1 Chemical Composition

The actual chemical composition for the substrate steels was determined by spectroscopy. Actual (as measured) and nominal compositions are given in Table 4.1. The nominal chemical compositions of electrode/filler wire are given in Table 4.2.

Table 4.1: Chemical composition (Wt %) for various boiler tube steels.

Type of Steel	ASTM code	Composition	C	Mn	Si	S	P	Cr	Mo	Fe
GrA1	SA210 Grade A1	Nominal	0.27	0.93	0.1	0.058	0.048	-	-	Bal.
		Actual	0.2952	0.5977	0.2873	0.0056	0.0089	-	-	Bal.
T-11	SA213 -T-11	Nominal	0.15	0.3-0.6	0.5-1	0.03	0.03	1-1.5	0.44- 0.65	Bal.
		Actual	0.1359	0.4272	0.3056	0.0064	0.0123	0.9113	0.5135	Bal.
T-22	SA213 -T-22	Nominal	0.15	0.3-0.6	0.5	0.03	0.03	1.9-2.6	0.87- 1.13	Bal.
		Actual	0.1359	0.1703	0.4458	0.0092	0.0210	2.6460	1.0652	Bal.

Table 4.2: Chemical composition of electrode/ filler metal.

Welding Process/Materials	Electrode and Filler wire AWS specification	C	Mn	Si	S	P	Cr	Mo	Fe
SMAW/ GrA1	AWS A5.1 E 7018	0.08	1.2	0.52	0.016	0.015	-	-	Bal.
SMAW/ T11	AWS A 5.5 E8018-B2	0.08	0.65	0.48	0.023	0.018	1.3	0.48	Bal.
SMAW/ T22	AWS A 5.5 E9018-B3	0.08	0.6	0.54	0.021	0.019	2.37	1.15	Bal.
TIG/ GrA1	AWS A5.18 ER 70S-2	0.05	1.15	0.45	0.018	0.02	-	-	Bal.
TIG/ T11	AWS A 5.28 ER 80S-B2	0.09	0.55	0.48	0.006	0.012	1.35	0.55	Bal.
TIG/T22	AWS A 5.28 ER 90S-B3	0.10	0.62	0.48	0.006	0.009	2.55	1.08	Bal.

4.1.2 Microstructures of Substrate Steels

The optical microstructures of the substrate steels are as shown in Fig. 4.1. The microstructures for all the steels show ferrite (white constituent) and pearlite (dark constituent), those could be resolved at certain locations showing alternate lamellas of ferrite and cementite. Fig. 4.1 (b & c) shows dispersed chromium carbides in the ferrite matrix of T11 and T22 type of steels.

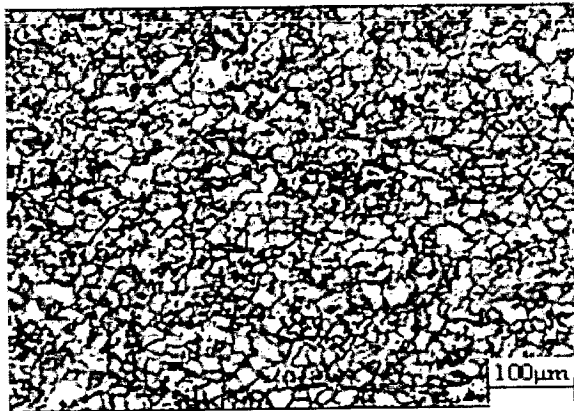
4.2 VISUAL EXAMINATION OF WELDMENTS

The two types of weldments were made by shielded metal arc welding and tungsten inert gas welding process in three types of the boiler tube steels namely GrA1, T11 and T22 are shown in Fig 4.2 and Fig. 4.3.

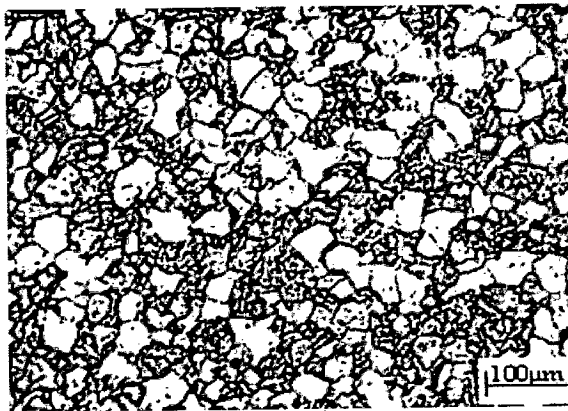
The macrographs for the as SMAW weldments shown multilayer pass zone clearly. In TIG weldments, the weldments showed no pass having greenish brown colour, whereas a change in v shape to y shape has been observed in TIG welded GrA1 steel Fig.4.3 (a). The light black colour band along the fusion line towards base metal showed HAZ (2 mm width).



(a)



(b)



(c)

Fig. 4.1 : Optical micrographs of substrate steels (a) ASTM-SA210-Grade A1 (GrA1), 250X (b) ASTM-SA213-T-11 (T11), 250X (c) ASTM-SA213-T-22 (T22), 250 X.

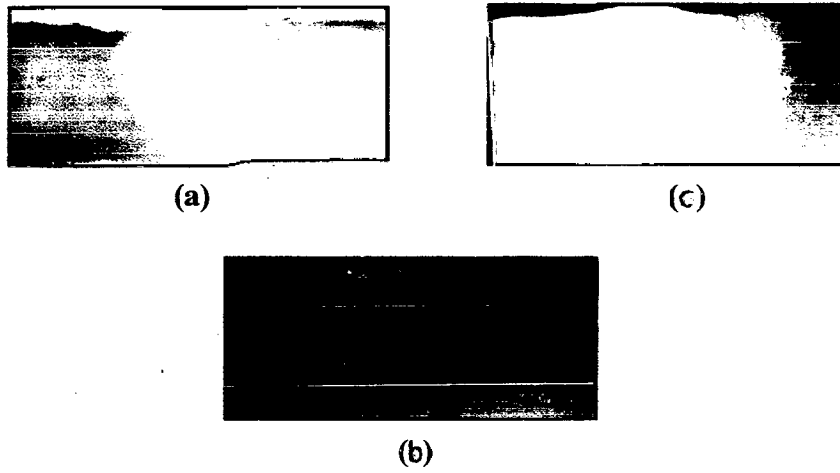


Fig. 4.2: Macrograph for the cross-sectional view of the SMAW weldment in steels (a) GrA1 (b) T11 (c) T22.

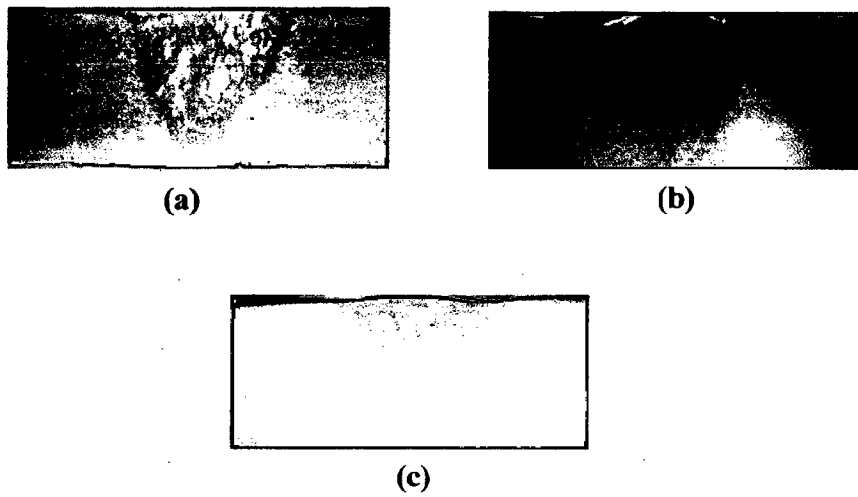


Fig. 4.3: Macrograph for the cross-sectional view of the TIG weldment in steels (a) GrA1 (b) T11 (c) T22.

4.3 MEASUREMENTS OF WELDMENT WIDTH AND SIZE OF TUBE

The weldment width measurements have been performed for the SMAW and TIG weldments. SMAW weldment showed the more width than TIG weldment as shown in Table 4.3. Tube size is also mentioned in the table. For each welding the width of weldment had been measured.

Table 4.3: Average weldment width and tube size.

Materials	Weldment width (mm)		Tube Size (mm)	
	SMAW	TIG	Thickness (mm)	Diameter (mm)
GrA1	11	9	5	33
T11	11	9.5	5	33
T22	12	10	10	26

4.4 POROSITY ANALYSIS

The porosity of weldment is of prime importance in the hot corrosion studies. The dense weldments are supposed to provide very good corrosion resistance as compared to porous weldment. The porosity measurements were made for as SMAW weldment and TIG weldment. The porosity for SMAW weldment was found to be in the range of 0.05-0.1%. A considerable decrease in porosity had been observed in case of TIG weldment and it was found to be less than 0.08% (Table 4.4).

Table 4.4: Porosity (%age) of SMAW and TIG weldments.

Materials	Porosity (%age)	
	SMAW	TIG
GrA1	0.05-0.1	< 0.07
T11	0.05-0.1	< 0.08
T22	0.08	< 0.06

4.5 EVALUATION OF MICROHARDNESS OF WELDMENT

The microhardness of weldment in different boiler steels has been measured along the cross-section. Profiles for microhardness vs distance from the centre of the weldment are given in Fig. 4.4 and 4.5. The critical hardness values of the substrate steels were found to be in the range 200 to 345 HV. The maximum microhardness values of the weld metal of SMAW and TIG weldment in T11 steel are determined to be about 270 HV which decreases as one move towards HAZ and base metal. Hardness of the weldment showed no significant difference with different welding processes. As indicated in the profiles, SMAW (Fig. 4.4) and TIG (Fig. 4.5) in T22 steel have shown maximum microhardness of the order of 360 HV. Whereas in GrA1 steel weld metal had least hardness 210 HV which is very near to the microhardness of base metal. Least microhardness values are indicated at fusion line in both the welding processes. The fluctuation in hardness profile is more across the weldment made by TIG process. Maximum hardness of HAZ for SMAW weldment in T22 steel is observed.

4.6 EVALUATION OF TENSILE STRENGTH OF WELDMENT

The tensile strength of weldment in different boiler steels has been measured using the round tensile specimen and prepared by keeping weld in the center. Profiles for stress vs strain of the weldment are given in Fig. 4.6 to 4.11. The proof stress, ultimate tensile strength and percentage elongation in measured and their values are shown in Table 4.5. The critical tensile strength values of the weld steels were found to be in the range 535 to 620 MPa. The tensile strength of TIG welded GrA1 steel is the least as compared to other welded boiler steel.

Table 4.5: Typical all weld metal tensile data.

Materials	Welding process	Test Temperatur	Ultimate Tensile strength (MPa)	Yield strength (Proof stress) at 0.2% offset (MPa)	Elongation percentage
GrA1	SMAW	Room	592	200	27.99
T11	SMAW	Room	618	150	22.44
T22	SMAW	Room	536	379	20.49
GrA1	TIG	Room	489	167	16.16
T11	TIG	Room	548	208	24.45

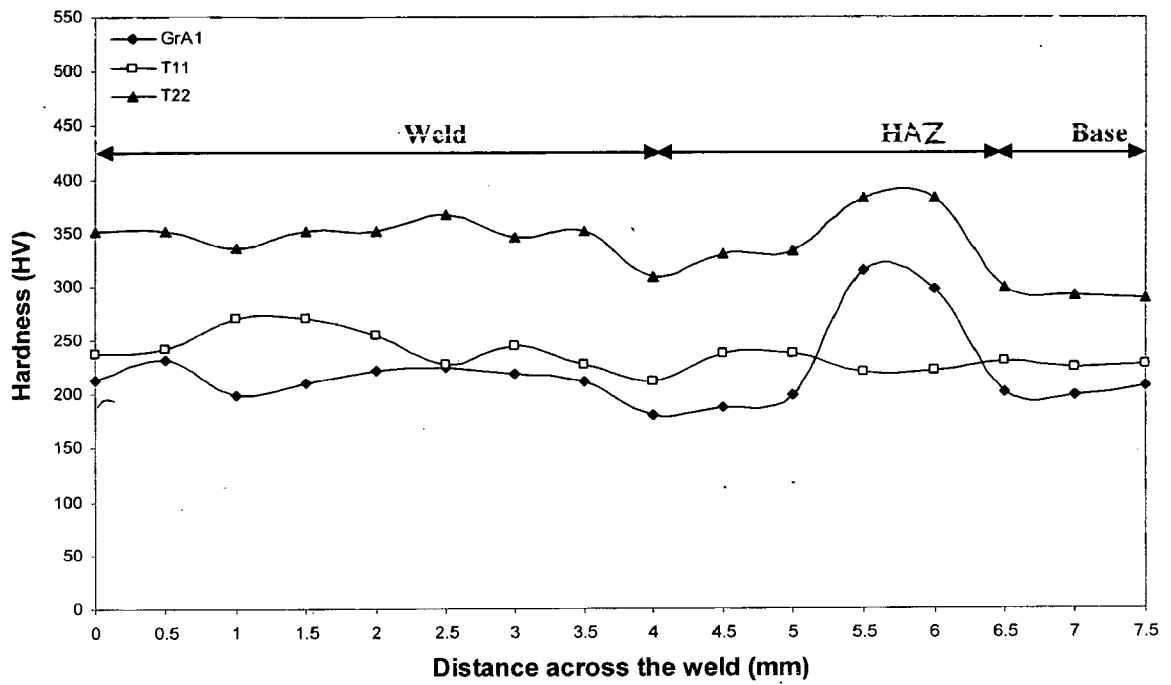


Fig. 4.4: Microhardness profiles of SMAW weldment in GrA1, T11 and T22 boiler steel.

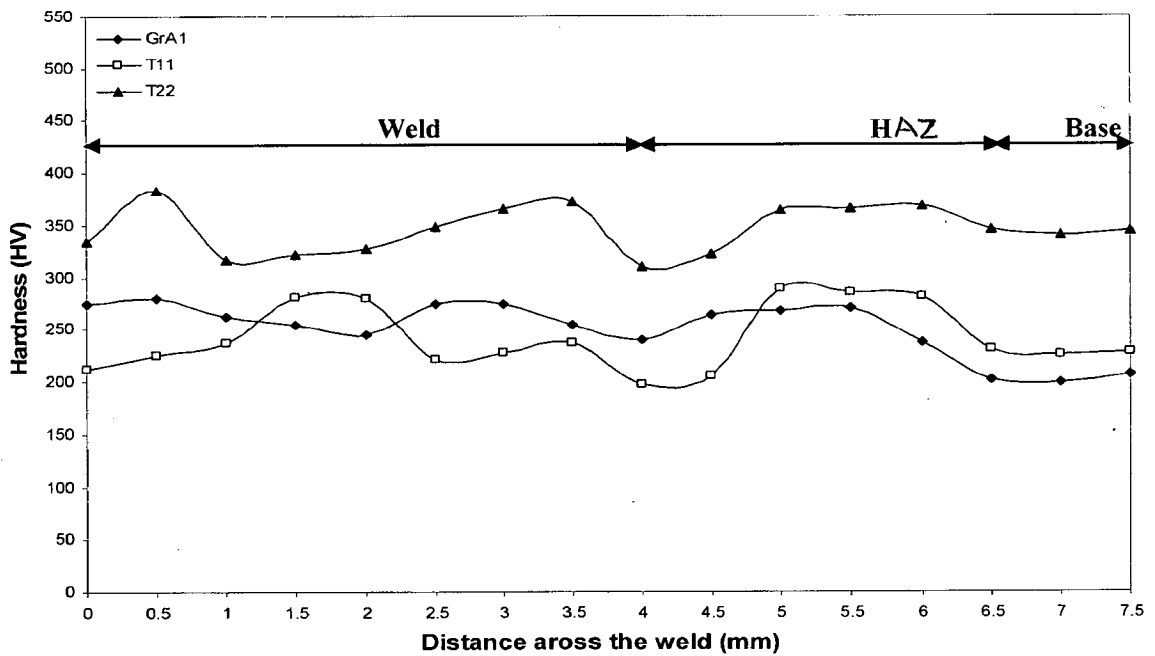


Fig. 4.5: Microhardness profiles of TIG weldment in GrA1, T11 and T22 boiler steel.

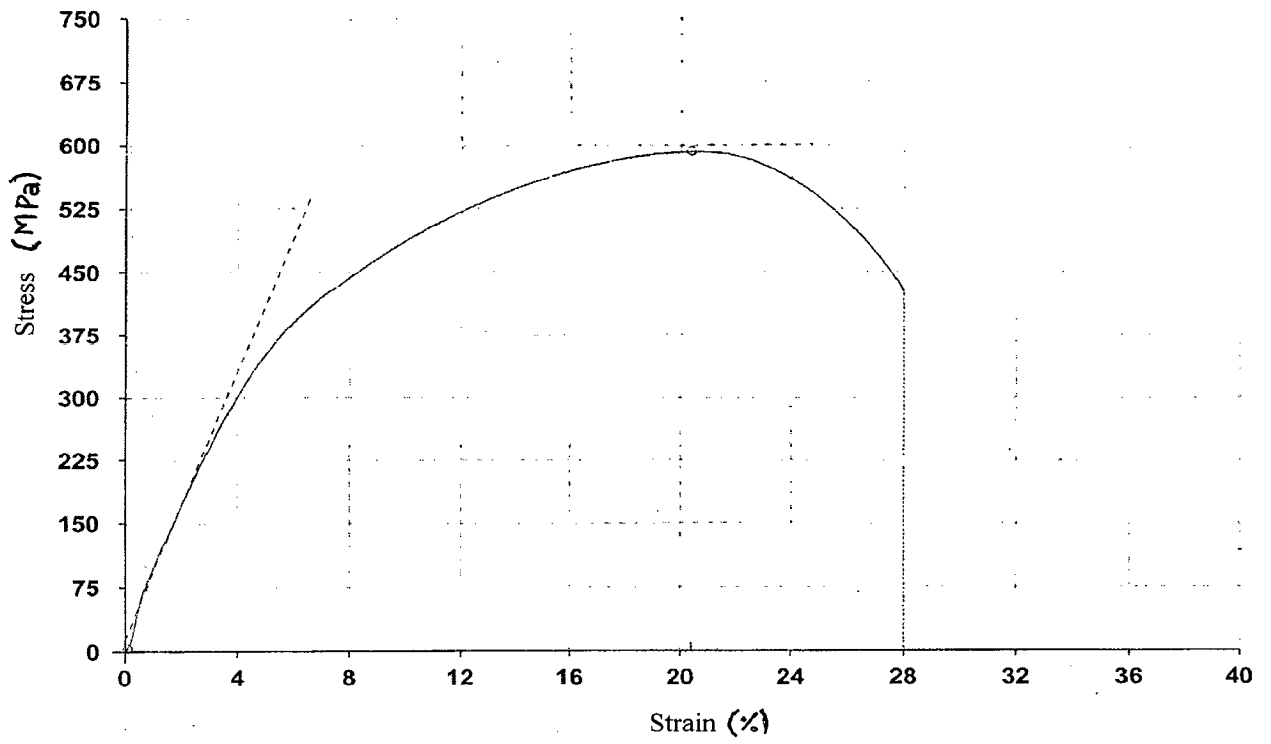


Fig. 4.6: Stress vs strain curve for SMAW weldment in GrA1 steel.

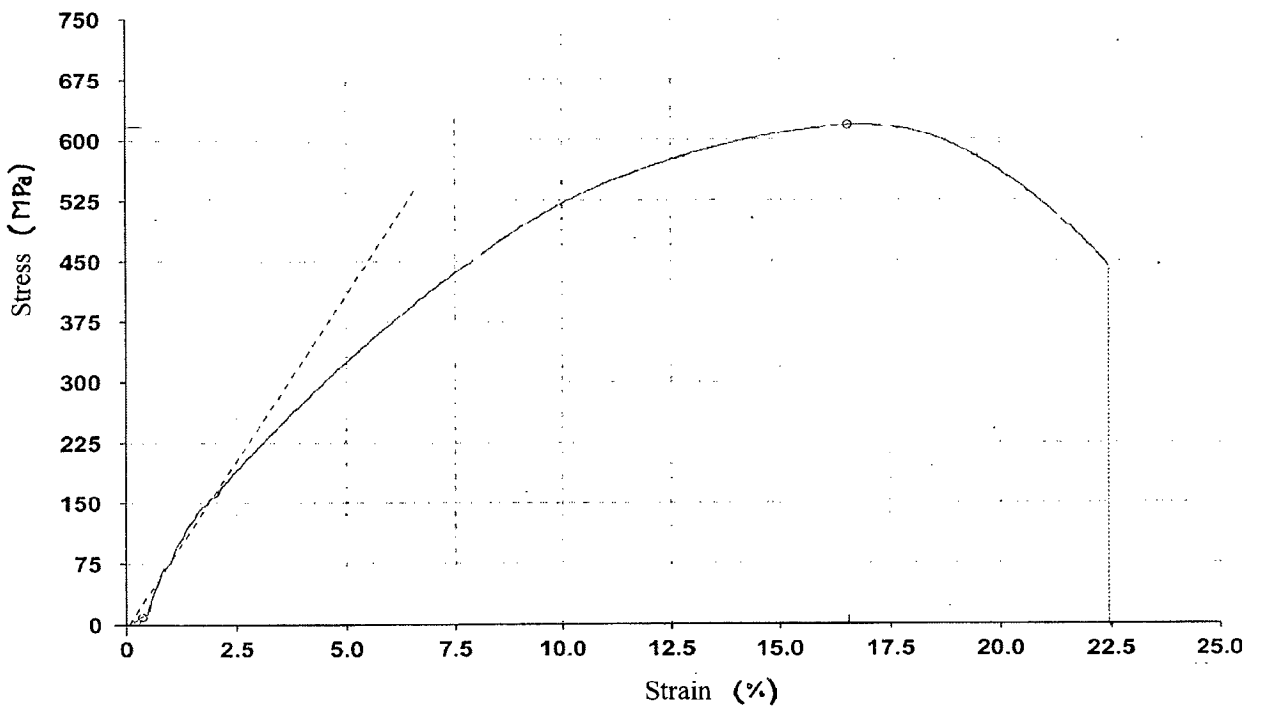


Fig. 4.7: Stress vs strain curve for SMAW weldment in T11 steel.

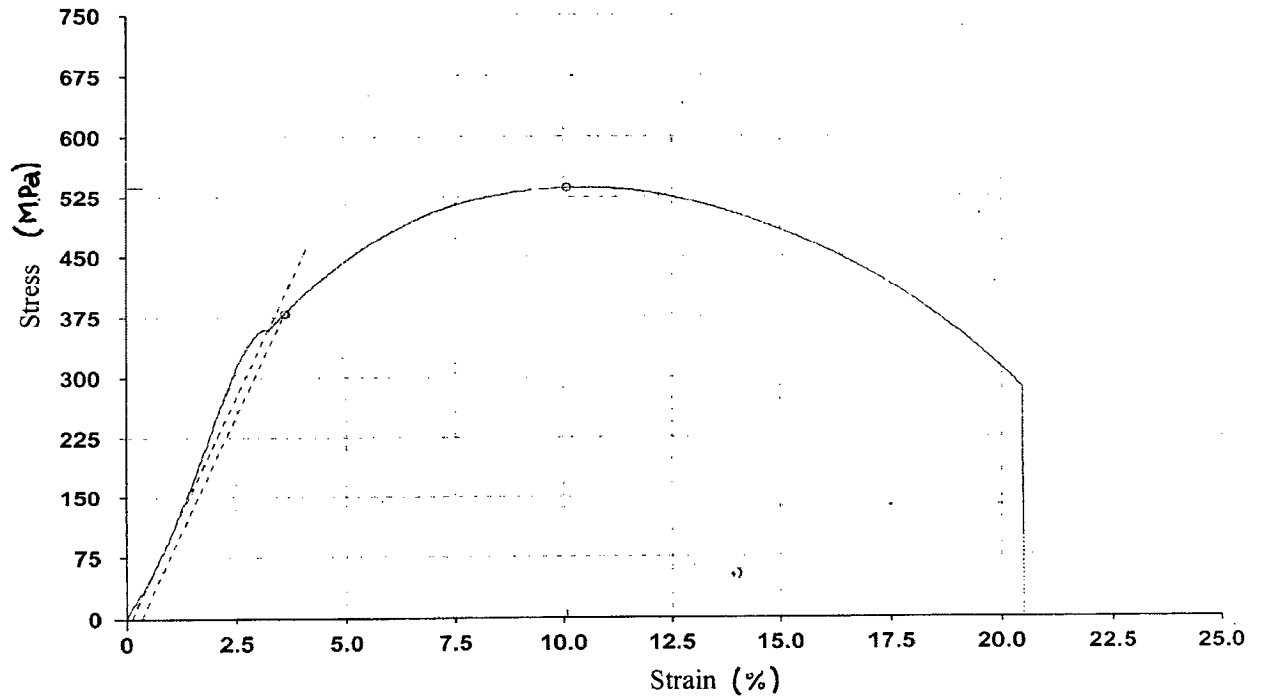


Fig. 4.8: Stress vs strain curve for SMAW weldment in T22 steel.

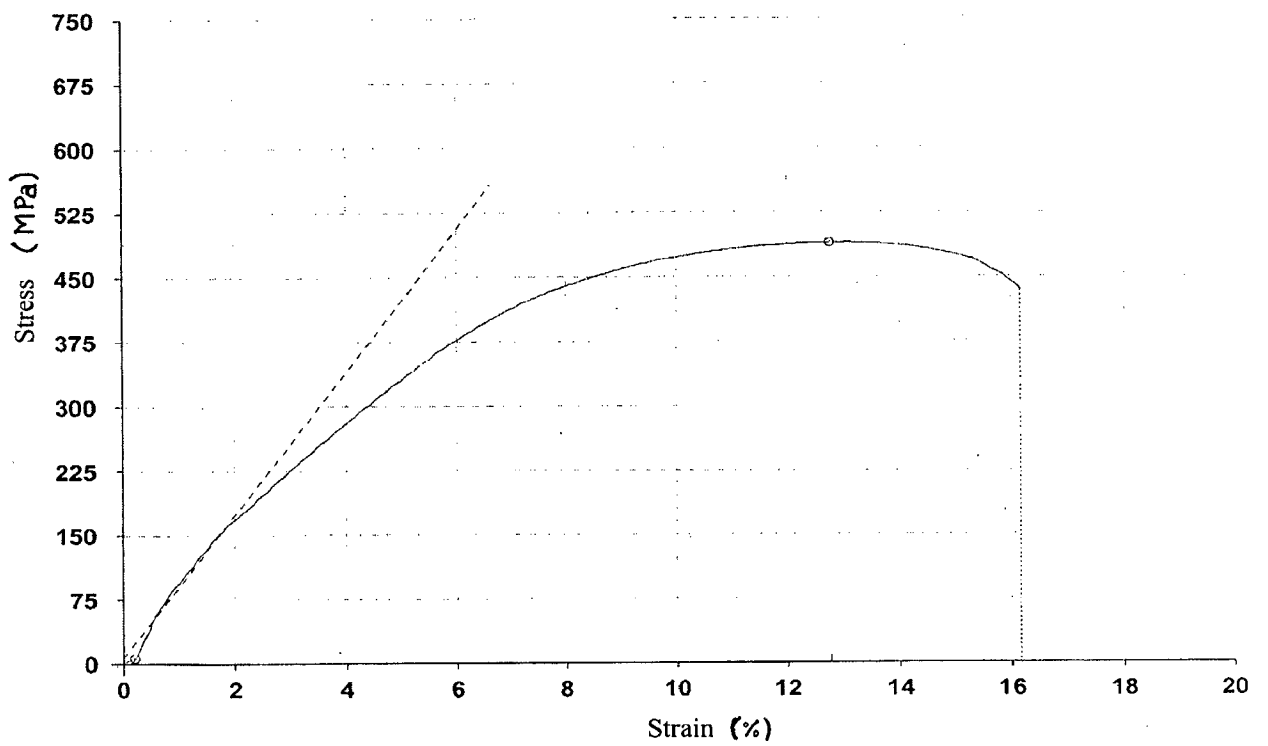


Fig. 4.9: Stress vs strain curve for TIG weldment in GrA1 steel.

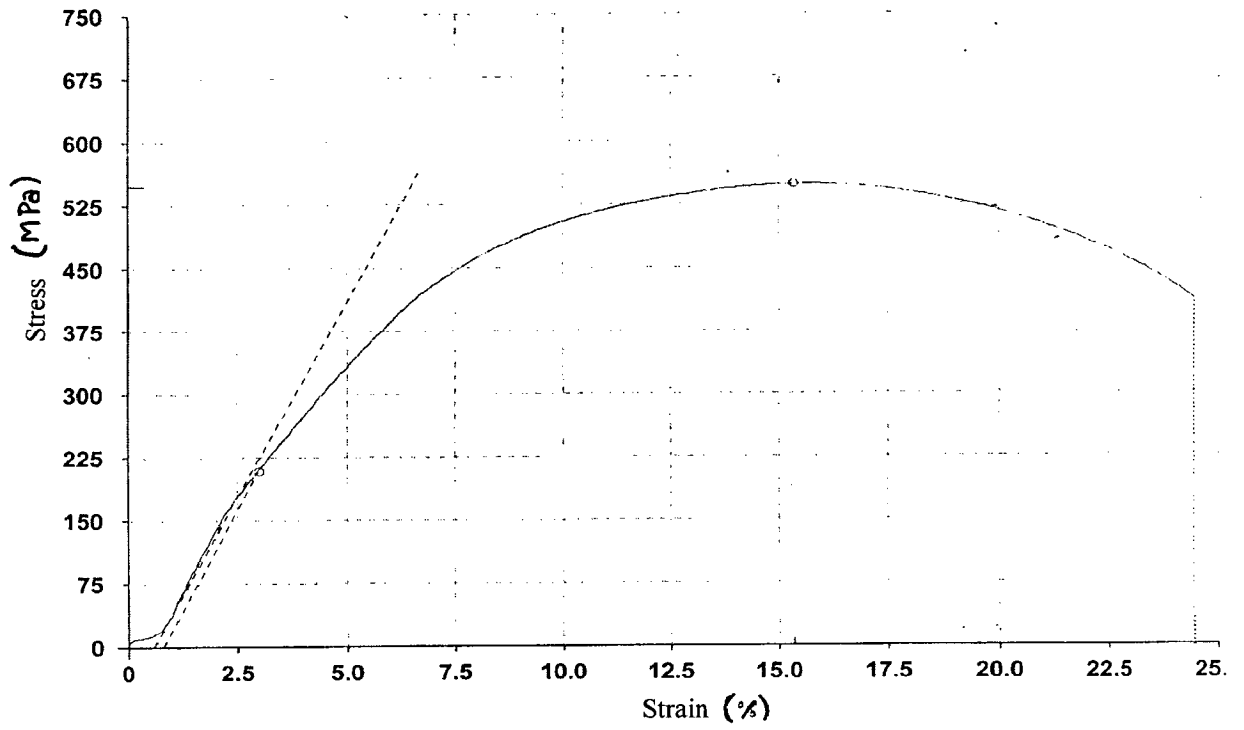


Fig. 4.10: Stress vs strain curve for TIG weldment in T11 steel

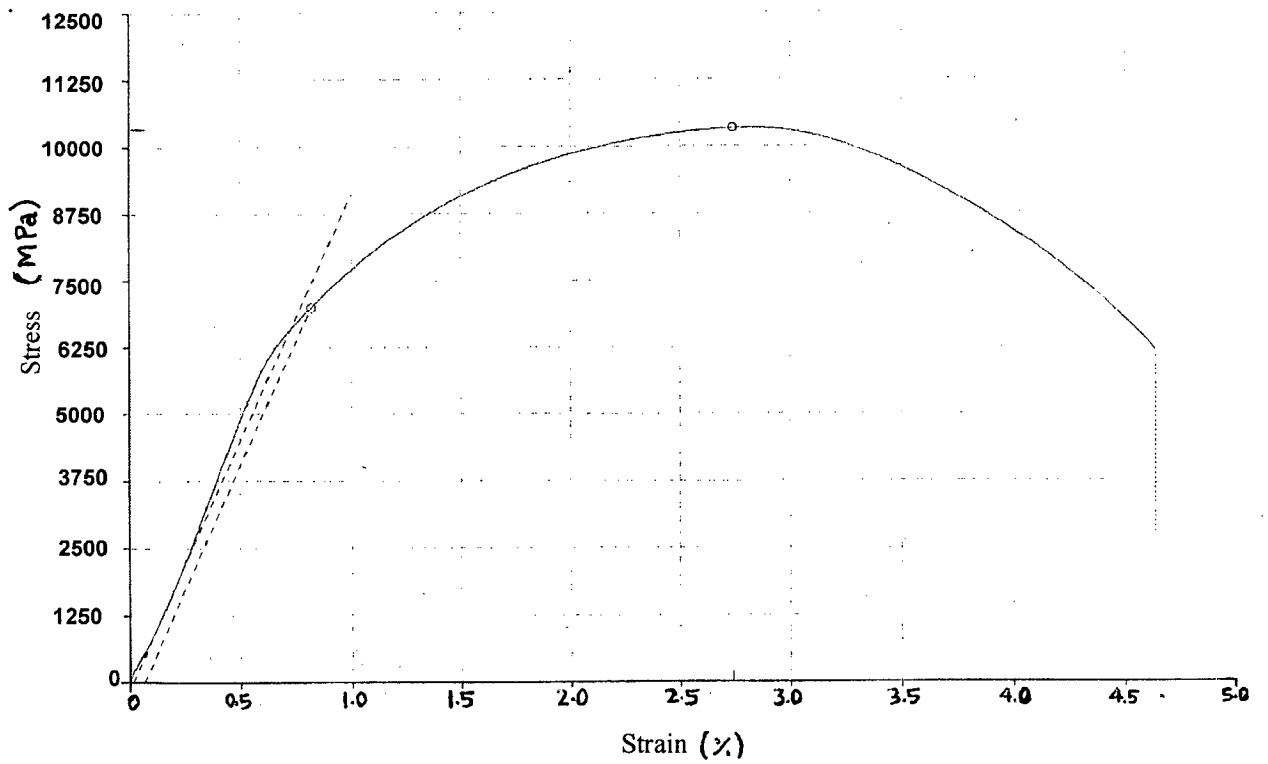


Fig. 4.11: Stress vs strain curve for TIG weldment in T22 steel.

4.7 METALLOGRAPHIC STUDIES

4.7.1 Cross-Sectional Microstructure of SMAW Weldment

4.7.1.1 GrA1 Steel

Figure 4.12 shows the optical micrographs for SMAW weldment in GrA1 steel. Optical micrograph of the weld metal is indicate in Fig. 4.12 (a), (b) bainaitic structure with acicular ferrite and small dendrites formation. HAZ region with coarse grain are shown in Fig. 4.12 (c), (d).

4.7.1.2 T11 Steel

The microstructures of SMAW weldment in T11 steel are shown in Fig. 4.13. Optical micrograph of the weld region indicates martensitic structure shown in Fig. 4.13 (a), (b). In the HAZ region it was coarse grain structure with carbide precipitation Fig. 4.13 (c), (d).

4.7.1.3 T22 Steel

The weld metal shows the formation of bainitic structure Fig. 4.14 (a), (b). HAZ region showed coarse bainitic structure Fig. 4.14 (c). Finer structure is shown in Fig. 4.14 (d).

4.7.2 Cross-Sectional Microstructure of TIG Weldment

4.7.2.1 GrA1 Steel

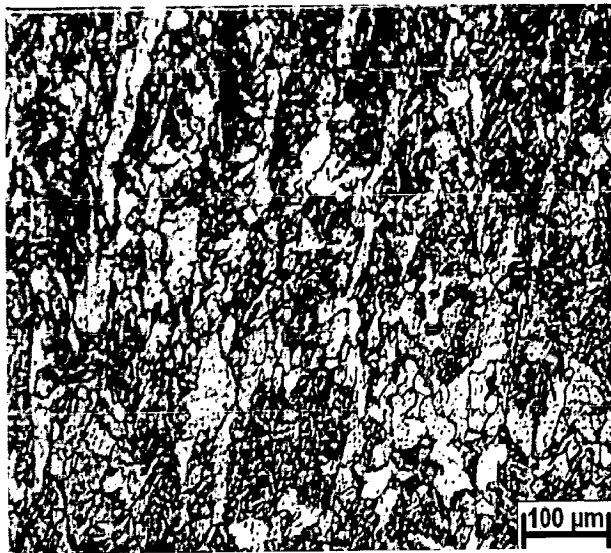
Figure 4.15 shows the optical micrographs for TIG weldment in GrA1 steel. Optical micrographs of the weld metal are shown in Fig. 4.15 (a), (b) indicating bainaitic structure with irregular boundary. HAZ region with coarse grain and fine grain are shown in Fig. 4.15 (c) & (d) respectively.

4.7.2.2 T11 Steel

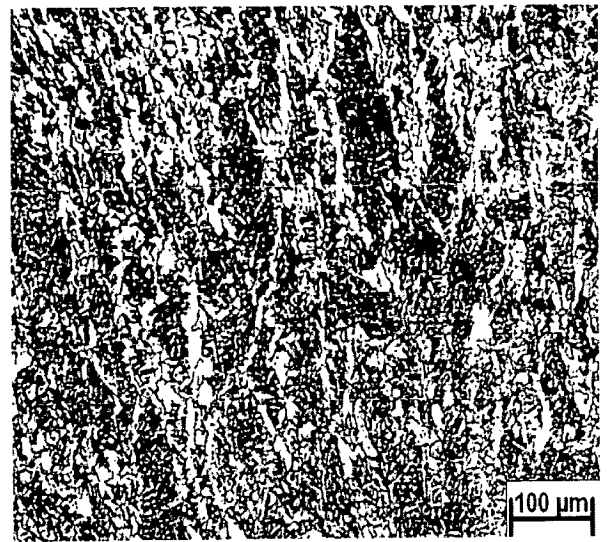
The microstructure of TIG weldment in T11 steel are shown in Fig. 4.16. Optical micrograph of weld metal showed the martensitic structure with lath like arrangement of ferrites in Fig. 4.16 (a), (b). In the HAZ region more coarse grains were seen as compared to finer grain size structure Fig. 4.16 (c), (d).

4.7.2.3 T22 Steel

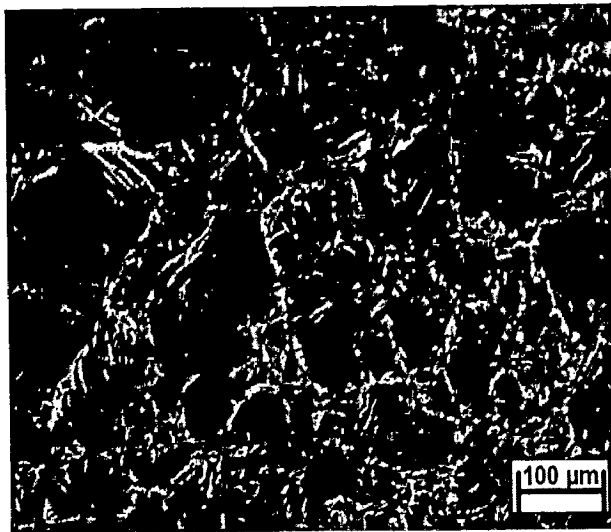
The weld metal shows a combination of widmanstatten type ferrite, pearlite and bainite. The presence of Cr and Mo in the alloy enhances hardenability and promotes bainite formation even on relatively slow cooling Fig. 4.17 (a), (b). HAZ region showed coarsed structure Fig. 4.17 (c). Finer structure is shown in Fig. 4.17 (d).



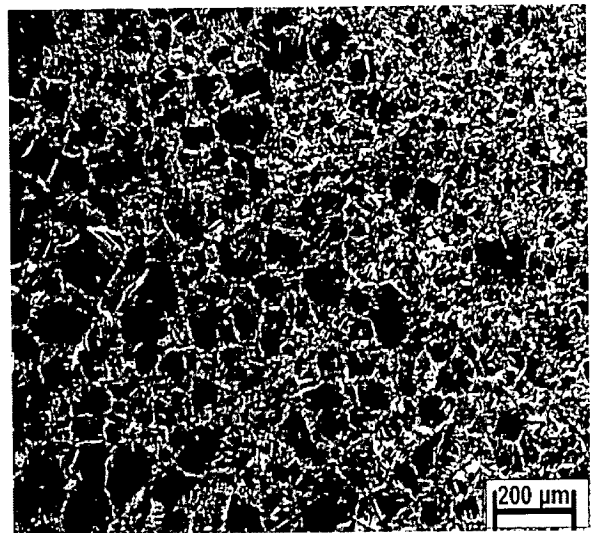
(a)



(b)



(c)



(d)

Fig. 4.12: Optical microstructure of SMAW weldment in GrA1 steel (a) Weld Metal, 200X (b) Weld Metal, 100X (c) HAZ Coarse Grain, 200X (d) HAZ Coarse +Fine Grain, 100X.

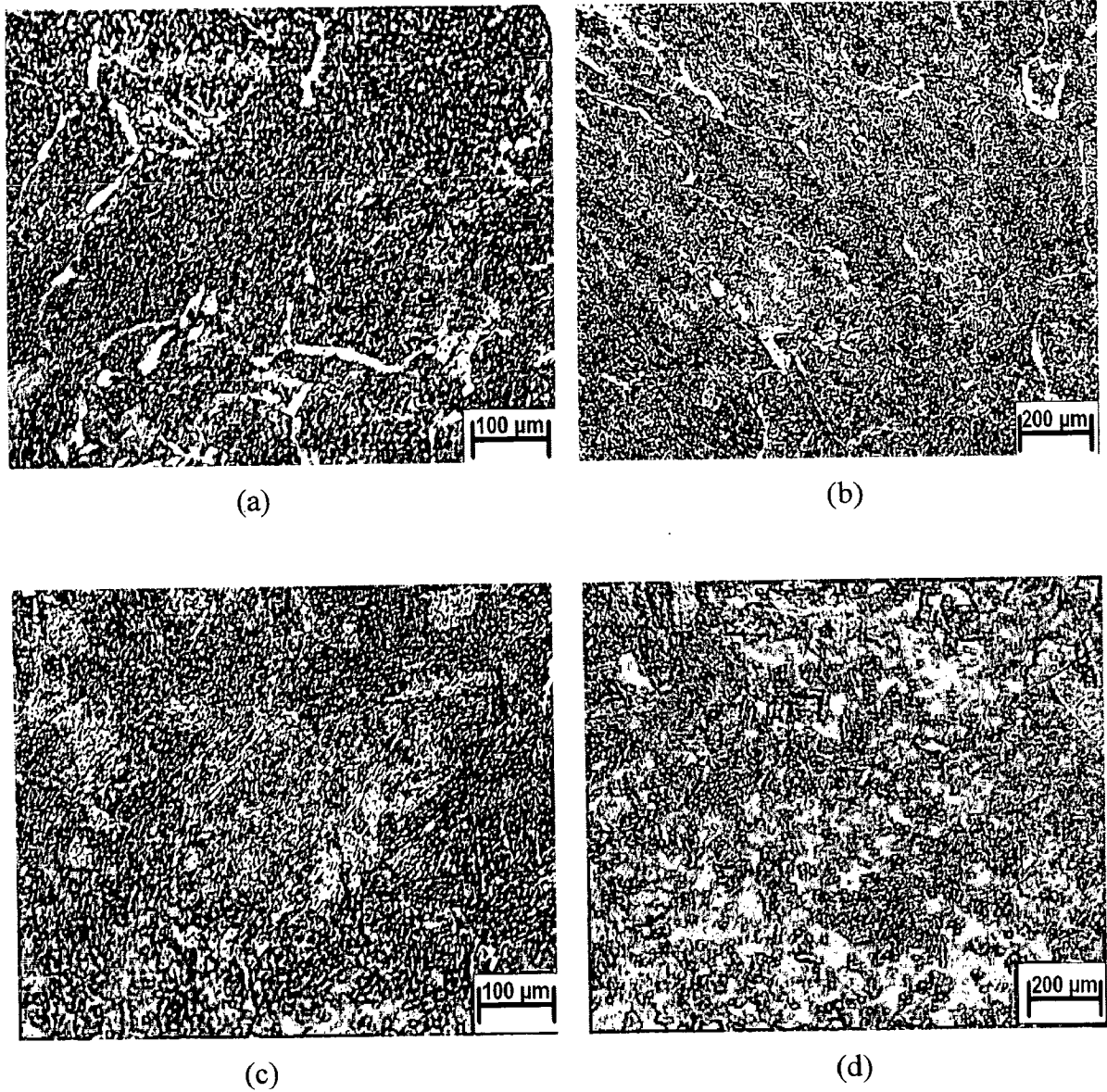


Fig. 4.13: Optical microstructure of SMAW weldment in T11 steel (a) Weld Metal, 200X (b) Weld Metal, 100X (c) HAZ Coarse Grain, 200X (d) HAZ Coarse Grain, 100X.

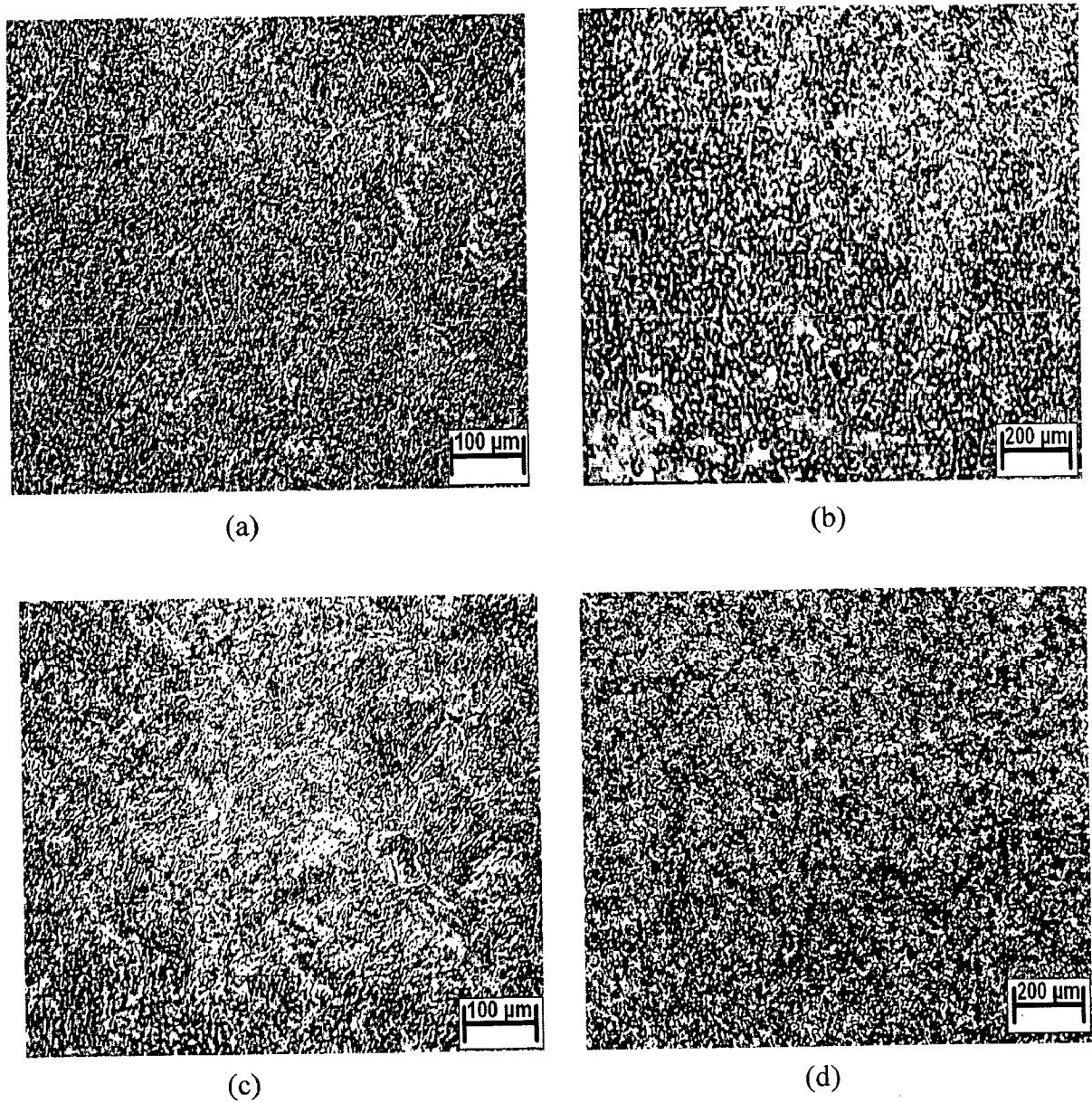
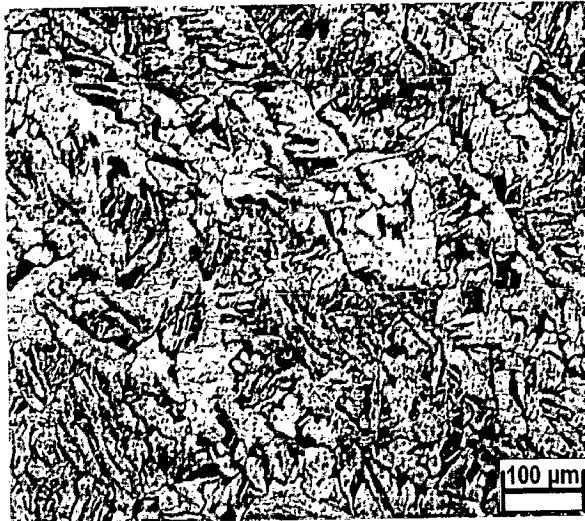
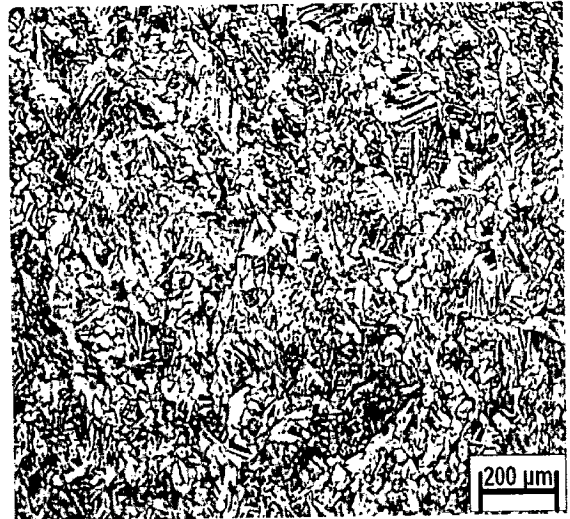


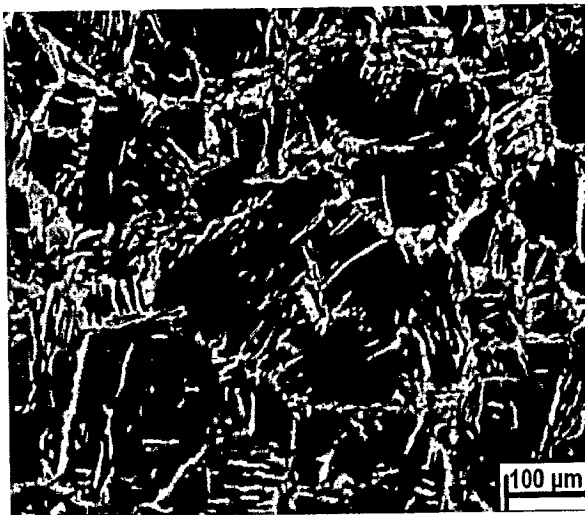
Fig. 4.14: Optical microstructure of SMAW weldment in T22 steel (a) Weld Metal, 200X (b) Weld Metal, 100X (c) HAZ Coarse Grain, 200X (d) HAZ Coarse Grain, 100X.



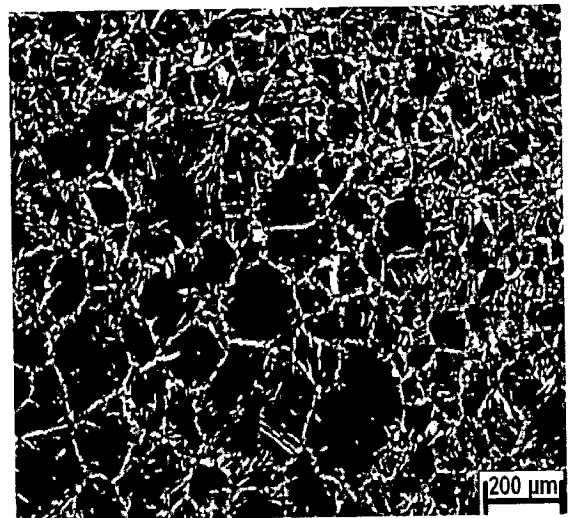
(a)



(b)



(c)



(d)

Fig. 4.15: Optical microstructures of TIG weldment in GrA1 steel (a) Weld Metal, 200X (b) Weld Metal, 100X (c) HAZ Coarse Grain, 200X (d) HAZ Coarse Grain, 100X.

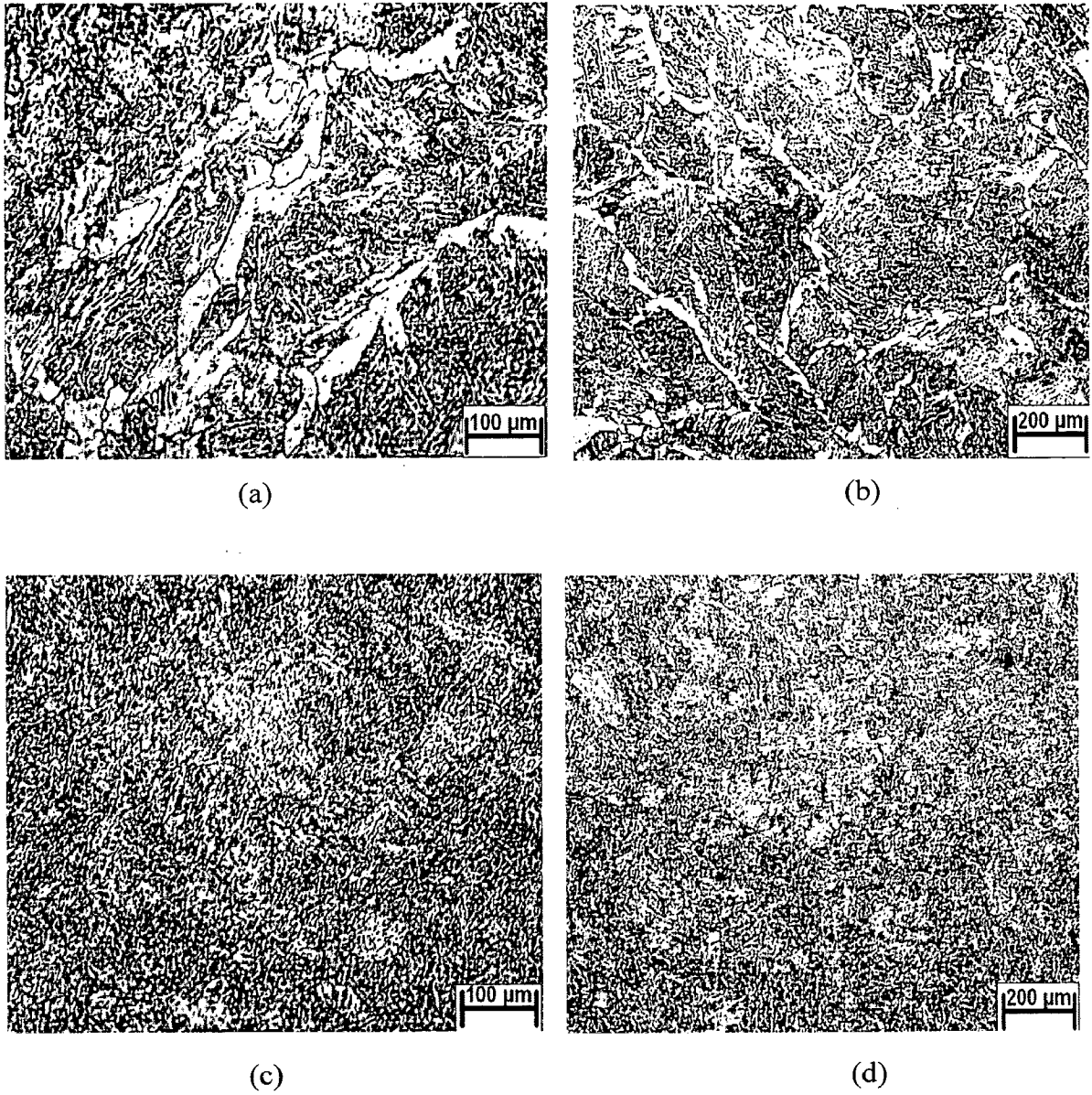


Fig. 4.16: Optical microstructures of TIG weldment in T11 steel (a) Weld Metal, 200X (b) Weld Metal, 100X (c) HAZ Coarse Grain, 200X (d) HAZ Coarse Grain, 100X.

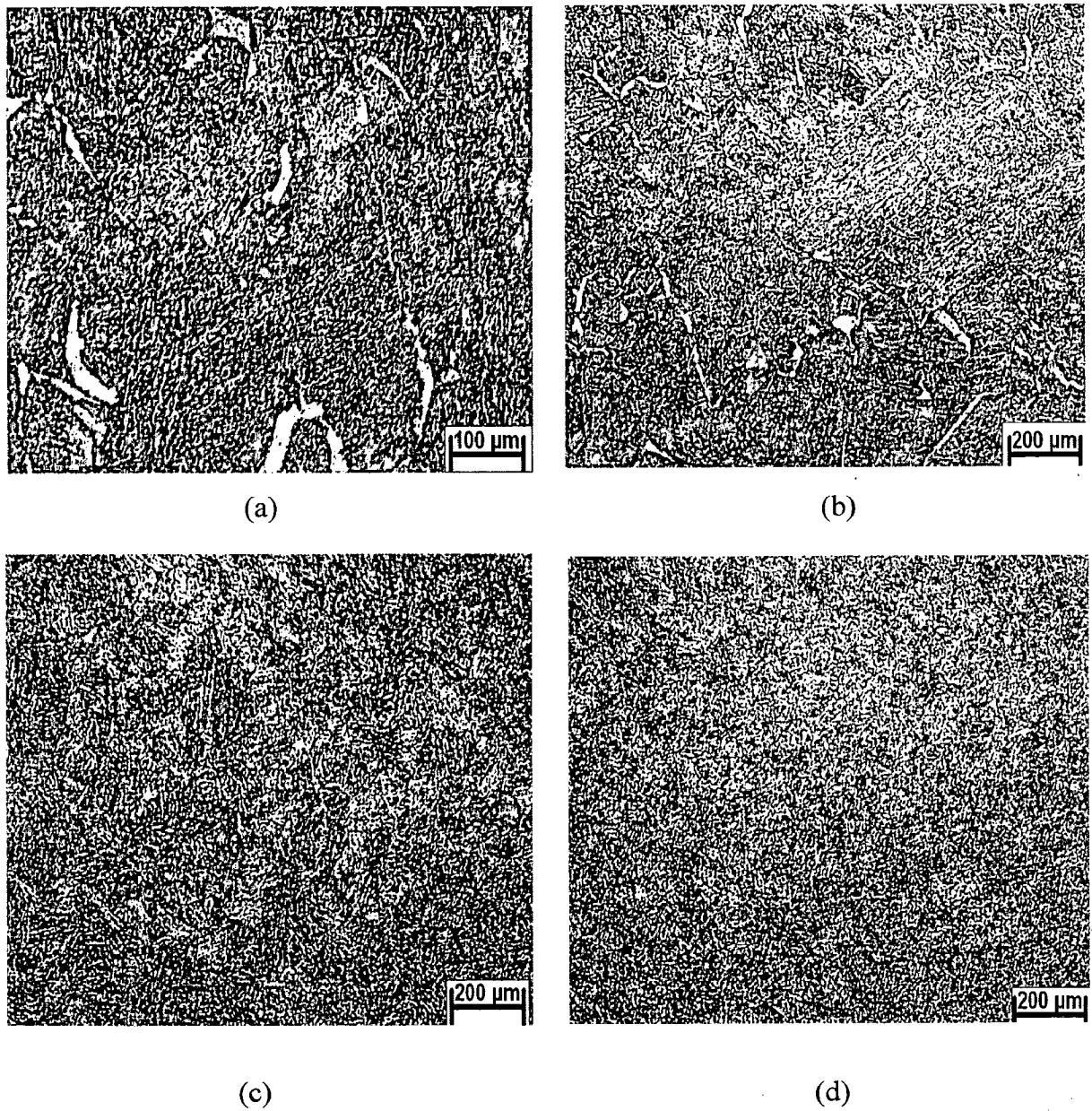


Fig. 4.17: Optical microstructures of TIG weldment in T22 steel (a) Weld Metal, 200X (b) Weld Metal, 100X (c) HAZ Coarse Grain, 100X (d) HAZ Fine Grain, 100X.

4.8 DISCUSSION

The SMAW and TIG weldment in boiler tube steel were made with constant amperage and root gap using shielded electrode and filler wire respectively. Slag formed during welding was removed at each welding pass. Weldment width was measured after each welding process to compare the dissolution of substrate metal in the weld metal. The dissolution of base metal in the weld may reduce the strength of weldment. SMAW and TIG weldment width was observed. Visual examination of cross sectional weldments showed in the Fig. 4.1 and the slightly change has been observed from v shape in case of GrA1 TIG welded steel. Microhardness of different weldments was measured.

The measured porosity of SMAW and TIG weldments is given in Table 4.4. The porosity percentage for TIG weldment is less than SMAW weldment. Microhardness plots indicate higher microhardness of weld metal and HAZ. Base metal showed the little less hardness. The large values of microhardness as indicated in plot (Fig. 4.5) for base metal in case of TIG weldments may be due to the thermal cycling. But the microhardness values for HAZ of both weldments showed higher value. This may be only due to carbide precipitation as well as stresses developed during cooling of weldment.

Stress vs strain graph of the weldments are given in Fig. 4.6 to 4.11. The proof stress, ultimate tensile strength and percentage elongation in measured and their values are shown in Table 4.5. The critical tensile strength values of the weld steels were found to be in the range 500 to 560 MPa. The tensile strength of TIG welded GrA1 steel is least as compared to other welded boiler steel.

The optical microstructures of the substrate steels are as shown in Fig. 4.1. The microstructures for all the steels show ferrite (white constituent) and pearlite (dark constituent), those could be resolved at certain locations showing alternate lamellas of ferrite and cementite. Fig. 4.1 (b & c) shows dispersed chromium carbides in the ferrite matrix of T11 and T-22 type of steels. Optical micrograph in case of GrA1 steel, the SMAW weld metal indicates in Fig. 4.12 (a), (b) bainitic structure with irregular boundary and small dendrite formations. HAZ region with coarse grain are shown in Fig. 4.12 (c), (d). Whereas for TIG weld metal indicates in Fig. 4.15 (a), (b) bainitic structure with irregular boundary and small dendrites formation. HAZ region with coarse grain and fine grain are shown in Fig. 4.15 (c) & (d) respectively.

In case of T11 optical micrograph of the SMAW weld region indicates martensitic structure shown in Fig. 4.13 (a), (b). In the HAZ region was coarse grain structure with carbide precipitation Fig. 4.13 (c), (d). Optical micrograph of same steel welded by TIG, weld metal also showed the martensitic structure with lath like arrangement of ferrites in Fig. 4.16 (a), (b). In the HAZ region coarse grains were seen Fig.4.16 (c), (d).

In T22 steel, SMAW Weld metal and HAZ shows the formation of bainitic structure Fig. 4.14 ((a), (b), (c), (d)) observed Raman (1999). Whereas TIG weld metal shows a combination of widmanstatten type ferrite, pearlite and bainite structure. The presence of Cr and Mo in the alloy enhances hardenability and promotes bainite formation even on relatively slow cooling Fig. 4.17 (a), (b) as also suggested by Natrajan and Babu (2006). HAZ region showed coarsed structure Fig. 4.17 (c). Finer structure is shown in Fig. 4.17 (d).

PART (A) OXIDATION STUDIES ON UNWELDED STEELS AND WELDMENTS IN AIR

This part of chapter 5 deals with the critical examination of corrosion products and the behaviour of unwelded and weldments steels when subjected to high temperature cyclic oxidation in air at 900°C for 50 cycles. The samples were visually examined at the end of each cycle during study. Efforts have been made to understand the mechanism of corrosion.

The corrosion products were analyzed with XRD and SEM/EDAX. The results for unwelded and weldment steels have been reported under different subheadings. In view of the thermogravimetric data for the each unwelded steel is reported along with the each welded steel. The parabolic rate constants and scale thicknesses have been evaluated.

5.1 RESULTS

5.1.1 Unwelded Steels

5.1.1.1 Visual Examination

Macrographs for corroded specimens of boiler steel after 50 cycles of oxidation at 900°C are shown in Fig. 5.1. During cyclic study the colour of scale for all the steels was light purplish grey during first few cycles and turned to dark grey after fifth cycle. In case of T22 type steel the small spalling and sputtering started just after 4th cycle. Where as minimum spalling was observed in case of GrA1 steel. The cracks in the oxide scale for GrA1 steel appeared after 25th cycle and same had appeared after 29th cycle for T11 type of steel. Very interesting observation was noticed for T11 type of steel after 35th cycle. It appeared as the scale had bulged out from the middle of the surface and remained adhered at the edges. The scale formed on GrA1 steel is of uniform thickness and has dull appearance. Lustrous dark grey colour scale was noticed for T11 type of steel. Where as irregular and fragile scale is observed for T22 steel in Fig. 5.1 (c) showing spalled areas.

5.1.1.2 Thermogravimetric Data

The plots of cumulative weight gain (mg/cm^2) as a function of time (number of cycles) for GrA1, T11 and T22 steel at 900°C in air upto 50 cycles are shown in Fig. 5.2. Extensive

spalling and sputtering has limited the study upto 50 cycles. The plot for all the steels shows a large weight gain during the first few cycles followed by gradual weight gain. The amount of the spalled scale has also been incorporated in weight gain measurements. The total weight gain at the end of 50 cycles for GrA1, T11 and T22 steels is 135.275, 128.387 and 121.610 mg/cm² respectively. The (weight gain/unit area)² plot against number of cycles Fig. 5.3 further confirms that parabolic law is followed by all the three steels. The values of parabolic rate constant, K_p ($10^{-8} \text{ g}^2 \text{ cm}^{-4} \text{ s}^{-1}$) are 10.282, 9.384 and 8.515 for GrA1, T11 and T22 steel respectively.

5.1.1.3 X-ray Diffraction Analysis

The XRD analysis for GrA1, T11 and T22 steel after exposure to air at 900°C for 50 cycles is shown in Fig. 5.4 and these diffractograms has almost similar phases for all the steels. As obvious from the composition all the steels have indicated the formation of iron oxide (Fe_2O_3). Where as weak peaks of Cr_2O_3 along with Fe_2O_3 are indicated in the oxide scale of steel T22.

5.1.1.4 Scale Thickness Measurement

The samples were cut across the cross-section after exposure to air at 900°C for 50 cycles and mounted. The scale thickness was measured from SEM back scattered images as shown in Fig. 5.5. Very thick oxide scale was identified in case of T11 steel and was around 1.69 times more than the scale thickness measured for T22 steel. The scale thickness values are 1.100, 1.289 and 0.763 mm for GrA1, T11 and T22 type of steel respectively.

5.1.1.5 SEM/EDAX Analysis

5.1.1.5.1 Surface Morphology

SEM micrograph of the scale formed after 50 cycles of oxidation in air 900°C for GrA1 steel indicates a scale containing distorted grains. EDAX analysis indicates the formation of mainly iron oxide, Fig. 5.6 (a). The micrograph of top surface of the scale in case of T11 steel indicates intergranular cracking. EDAX analysis shows the presence of little amount of MnO (3.17%) in the scale at point 1 in micrograph of Fig. 5.6 (b). The subscale has higher content of MnO (17.50%) with main phase being Fe_2O_3 at point 2. Whereas spalling is indicated and top scale is mainly Fe_2O_3 in case of oxidized T22 steel. At point 2 on micrograph in Fig. 5.6 (c) presence of Cr_2O_3 (4.8%) is indicated. The subscale has oxides, Fe_2O_3 (95.30%) and MnO (3.47%) (Point 1).

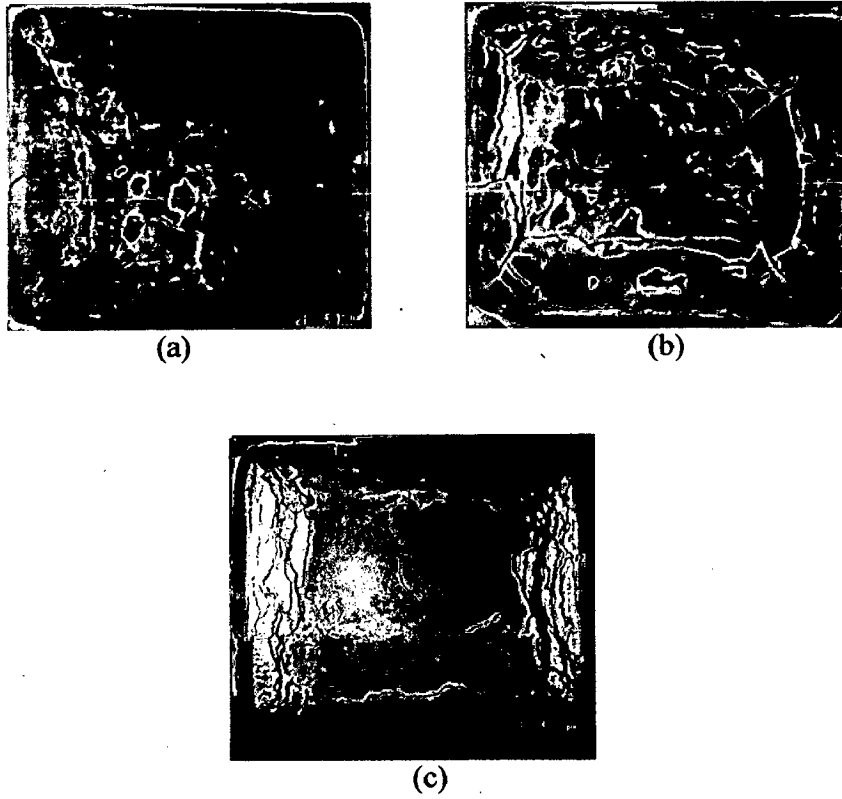


Fig. 5.1: Macrographs of unwelded steels subjected to cyclic oxidation in air at 900 °C for 50 cycles (a) GrA1, (b) T11 and (c) T22.

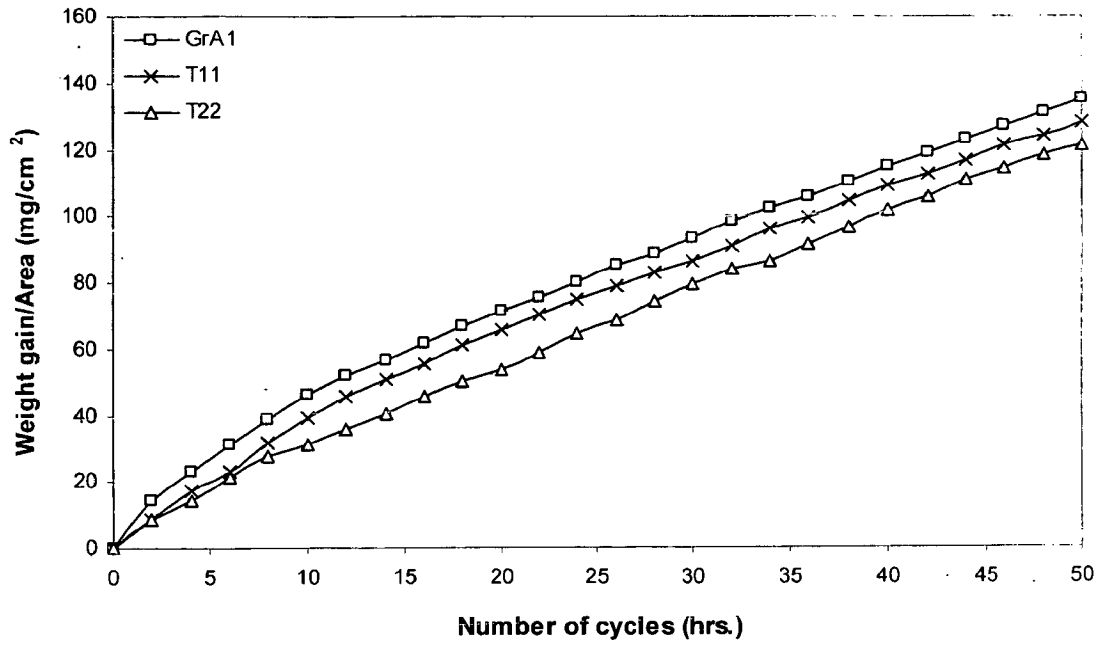


Fig. 5.2: Weight gain plot for unrolled steels exposed to air at 900°C for 50 cycles.

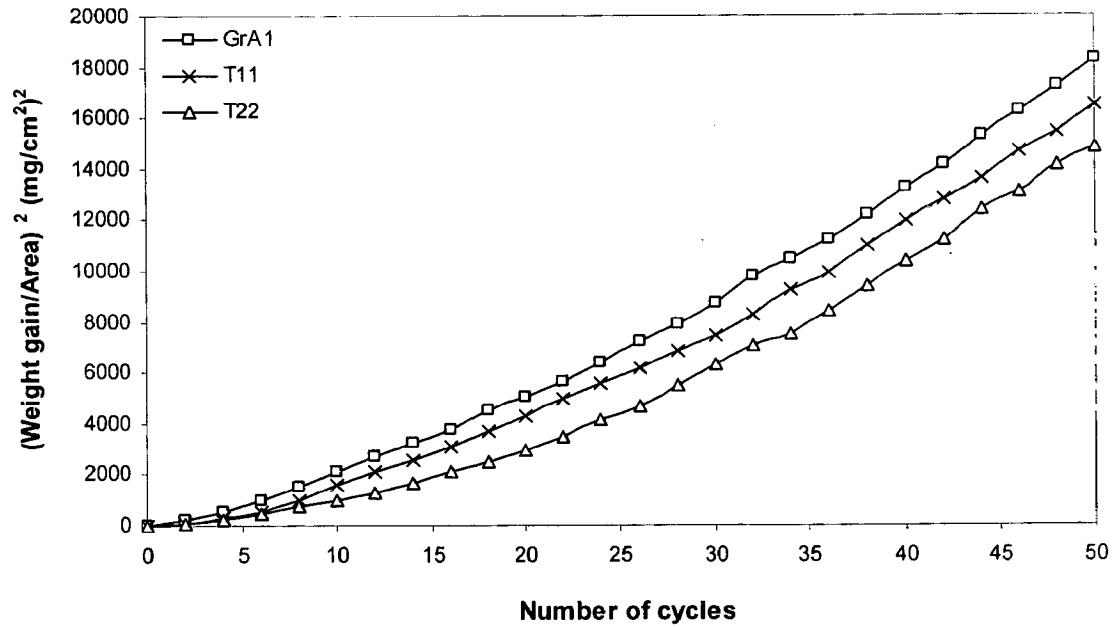


Fig. 5.3: Weight gain square (mg²/cm⁴) plot for unrolled steels exposed to air at 900°C for 50 cycles.

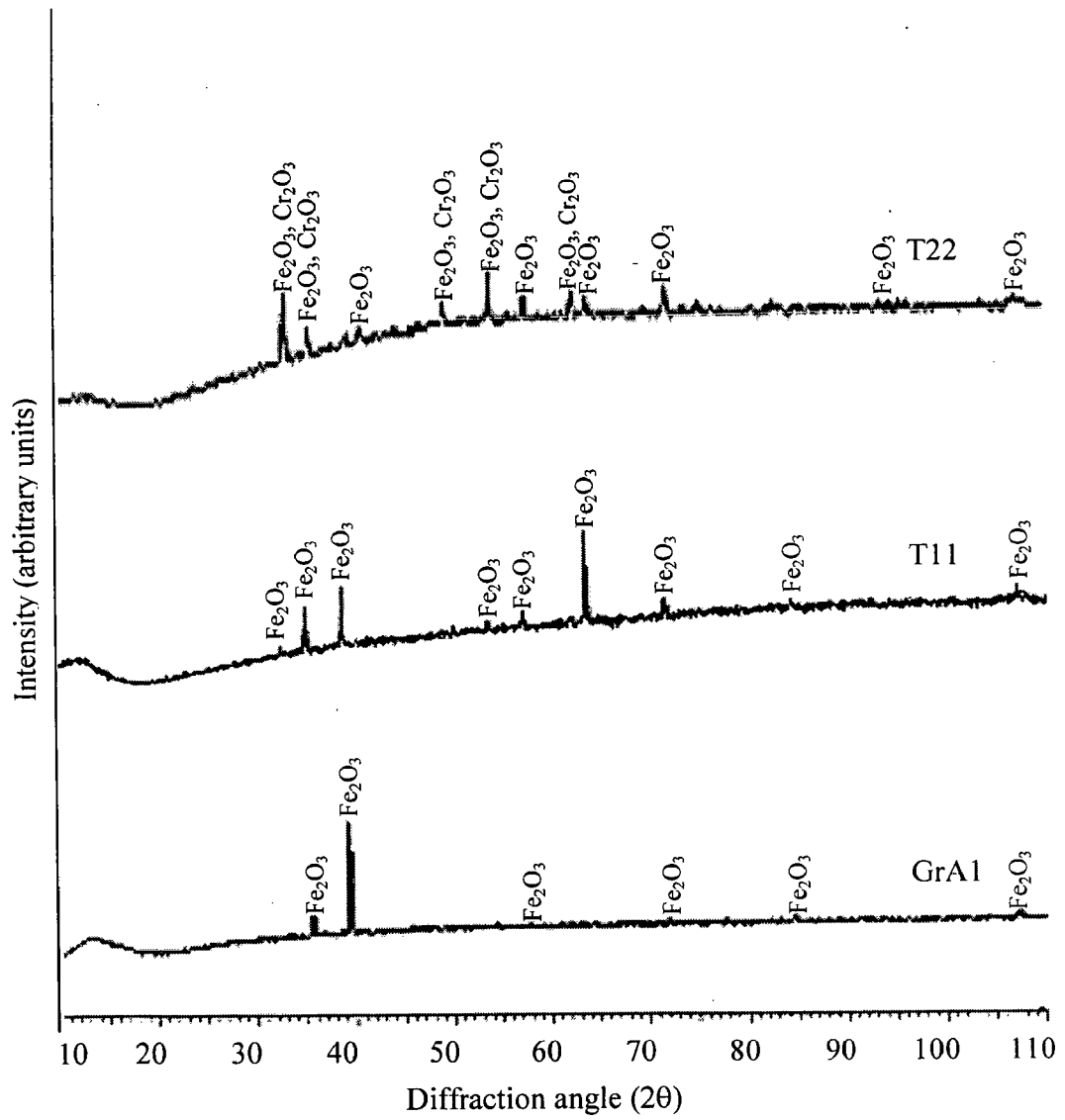
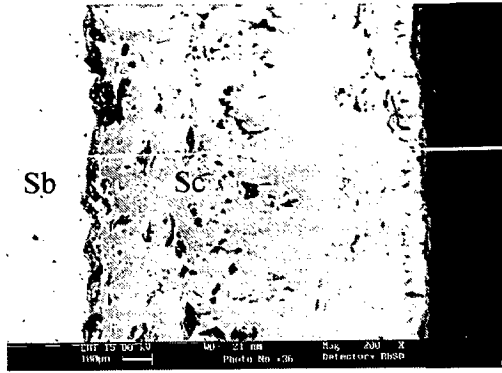
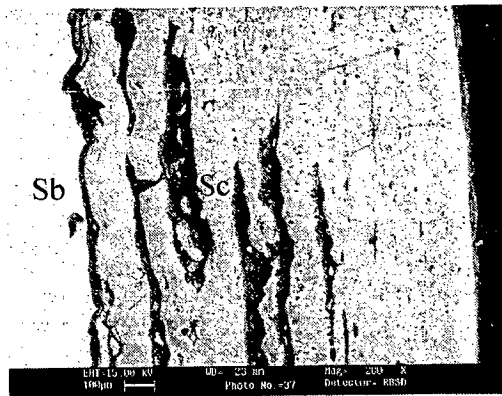


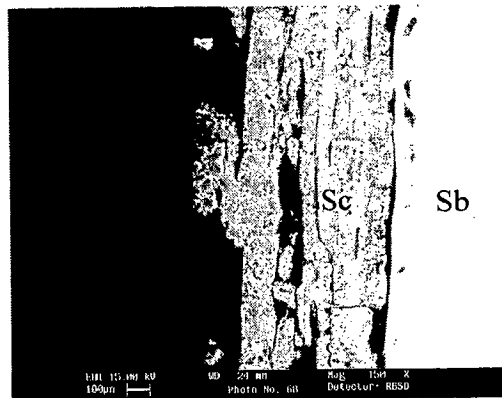
Fig. 5.4: X-ray diffraction profiles for GrA1, T11 and T22 boiler steels subjected to cyclic oxidation in air at 900°C for 50 cycles.



(a)



(b)



(c)

Fig. 5.5: SEM backscattered image of the cross-section of unwelded steels after cyclic oxidation in air at 900°C for 50 cycles (a) GrA1, 200X (b) T11, 200X (c) T22, 50X.

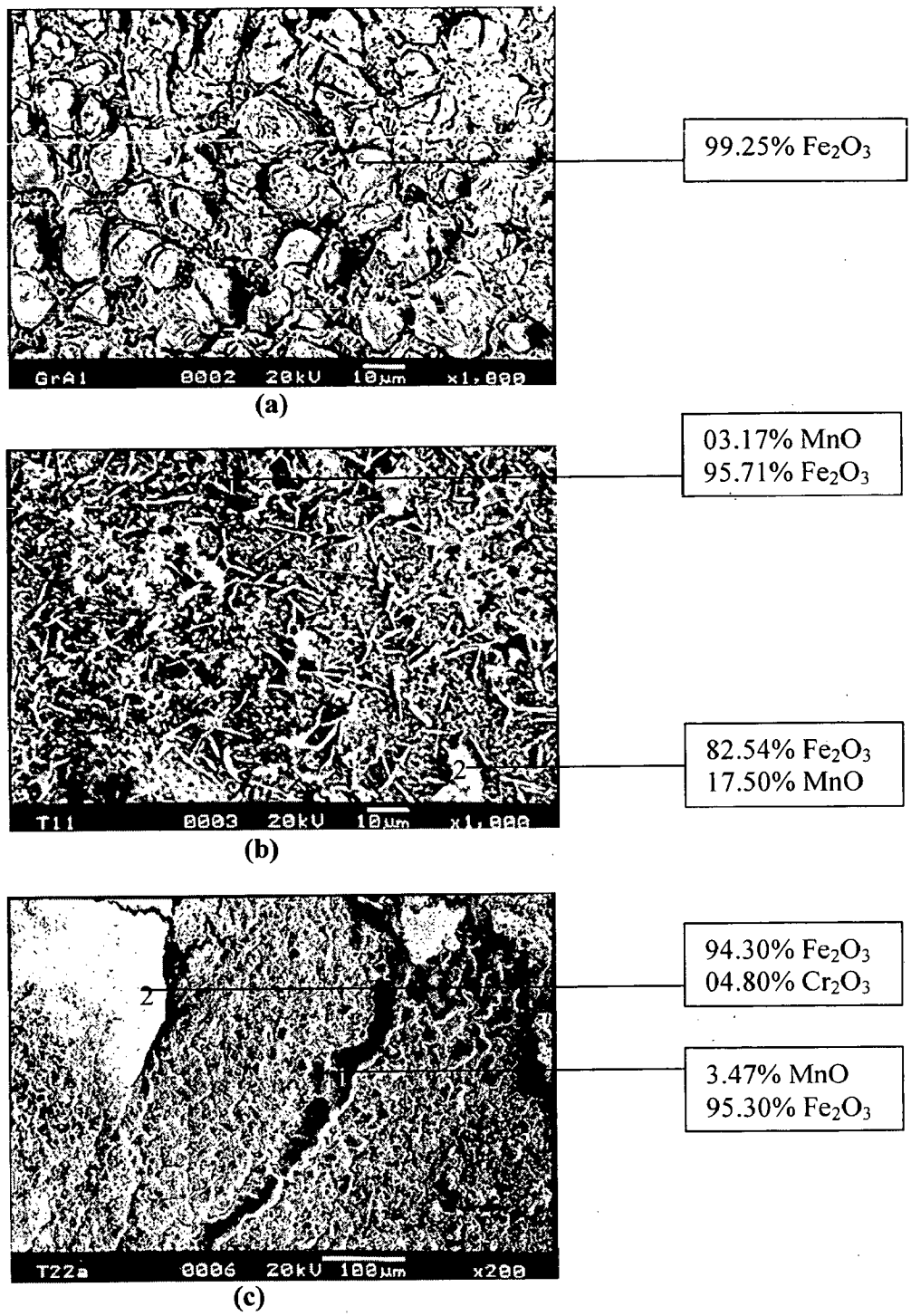


Fig. 5.6: SEM micrographs showing surface scale morphology and EDAX analysis for unwelded boiler steels oxidized in air at 900 °C for 50 cycles (a) GrA1, 1000X (b) T11, 1000X (c) T22, 200X.

5.1.2 SMAW WELDMENT

5.1.2.1 Visual Examination

Macrographs for oxidized SMAW weldment in GrA1, T11 and T22 steel for 50 cycles in air at 900°C are shown in Fig. 5.7. The surface appearance for welded GrA1 steel was smooth and no cracks are apparent. But the weld regions seen black in colour during 14th cycle and some little cracks seem after 27th cycle. Whereas for the other two welded steels occurrence of large number of cracks have been observed in the oxidized samples. For welded T22 steel the spalling started to appear just after 4th cycle. The new oxide scale seems to have grown in this void and which led to cracks and spalling of the top scale. In case of welded T11 steel cracks have been observed during 36th cycle. Through these cracks some oxides dark grey in colour appeared to be protruding out. The colour of oxide scale for all the three samples is dark grey having very small greenish look in the early stage of experimentation. After few cycles the colour of oxide scale turned blackish gray as shown in Fig 5.7.

5.1.2.2 Thermogravimetric Data

Fig. 5.8 shows the variation of weight gain as a function of time. The cumulative weight gain for welded T22 type of steel is almost linear. The spalling has also been observed on this steel proved to be least effective as the total weight gain is approximately to the weight gain for unwelded steel. The welded T22 steel has showed higher weight gain than other two welded steels. The weight gain (mg/cm²) after exposure of 50 cycles is around 185.354, 123.582 and 248.157 for welded GrA1, T11 and T22 steels respectively than that of unwelded steels. The maximum resistance to the oxidation at 900°C has been provided by unwelded T22 steel. The oxidation behaviour for welded GrA1, T11 and T22 steels is almost parabolic in nature as shown by Fig. 5.9. The value of parabolic rate constant, K_p ($10^{-8} \text{ g}^2 \text{ cm}^{-4} \text{ s}^{-1}$) for these welded steels is 20.365 (GrA1), 8.832 (T11) and 36.447 (T22).

5.1.2.3 X-ray Diffraction Analysis

The X-ray diffractograms for SMAW weldment in steels after cyclic oxidation in air for 50 cycles at 900°C are shown in Fig. 5.10. All the welded oxidized steels have indicated the formation of similar phases. The main phases analyzed by XRD analysis are Cr₂O₃, Fe₂O₃. In case of T11 steel the main phases Fe₂O₃ with MnO.

5.1.2.4 Scale Thickness Measurement

The oxide scale thickness for SMAW weldment in steels was measured from the BSEI shown in Fig. 5.11 after oxidation in air for 50 cycles at 900°C. Although the welded T22 steel as indicated thick scale formation yet it is about 1.75 times of that for unwelded steel. The minimum scale thickness has been measured for GrA1 type of SMAW weldment in steel which is around 1.2 times of that for welded T22 steel. The average values of weld regions in SMAW weldment of steels oxide scale thickness are 1.110, 1.250 and 1.333 mm for GrA1, T11 and T22 steels respectively. Whereas the average values of HAZ in SMAW weldment of steels oxide scale thickness are 1.196, 1.373 and 1.386 mm for GrA1, T11 and T22 steels respectively.

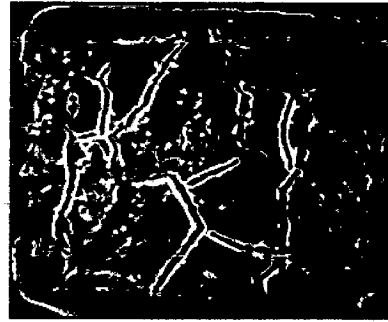
5.1.2.5 SEM/EDAX Analysis

5.1.2.5.1 Surface Morphology

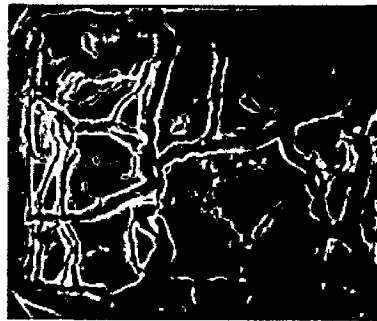
SEM micrograph Fig. 5.12 (a) for weld region of SMAW weldment in GrA1 steel indicates more oxidation along boundary of ferrite phases. The oxide scale mainly contains oxides of Fe. The top scale contains larger amount of iron oxide (99.44%) as compared to boundary region having 99.11% iron oxide. Whereas the oxide scale of HAZ region consists of mainly iron oxide (99.01%) with small amount of MnO (0.65%) at Point 2 in Fig. 5.12 (b). In case of T11 steel the weld region indicates the spalled region contains amount of Fe₂O₃ (91.23%) and MnO (8.25%) as compared to top scale having 99.14% iron oxide Fig. 5.12 (c). whereas the oxide scale of HAZ region consists of Fe₂O₃ (96.23%) with MnO (2.14%) and SiO₂ (1.25%) at point 1 top scale. The inner scale mainly indicates the iron oxide (99.01%) and MnO (1.97%) at point 2 Fig. 5.12 (d). The SEM micrograph for weld region of SMAW weldment in T22 steel Fig. 5.12 (e) indicates that the scale has developed cracks and from the inside Fe₂O₃ has oozed out. The main top scale is rich in iron oxide 97.96% with MnO (1.95%) point 2. The inner scale having Fe₂O₃ (95.41%) and MnO (3.40%) point 1. The oxide scale of HAZ region of this weldment in T22 steel consists of MnO with main phase Fe₂O₃ (96.78%) at point 2, whereas at point 1 it was only 95.57% with MnO and Cr₂O₃ Fig. 5.12 (f).



(a)



(b)



(c)

Fig. 5.7: Macrographs of the corroded SMAW weldments of (a) GrA1, (b) T11 and (c) T22 steels subjected to cycle oxidation in air at 900 °C for 50 cycles.

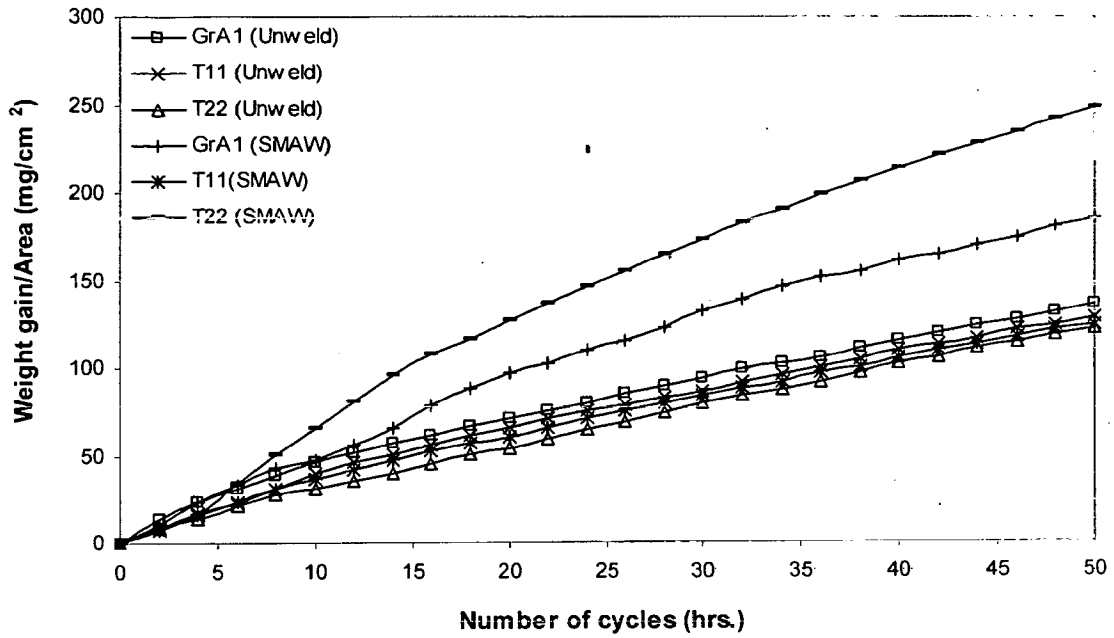


Fig. 5.8: Weight gain plot for unwelded and SMAW weldment of different steels exposed to air at 900 °C for 50 cycles.

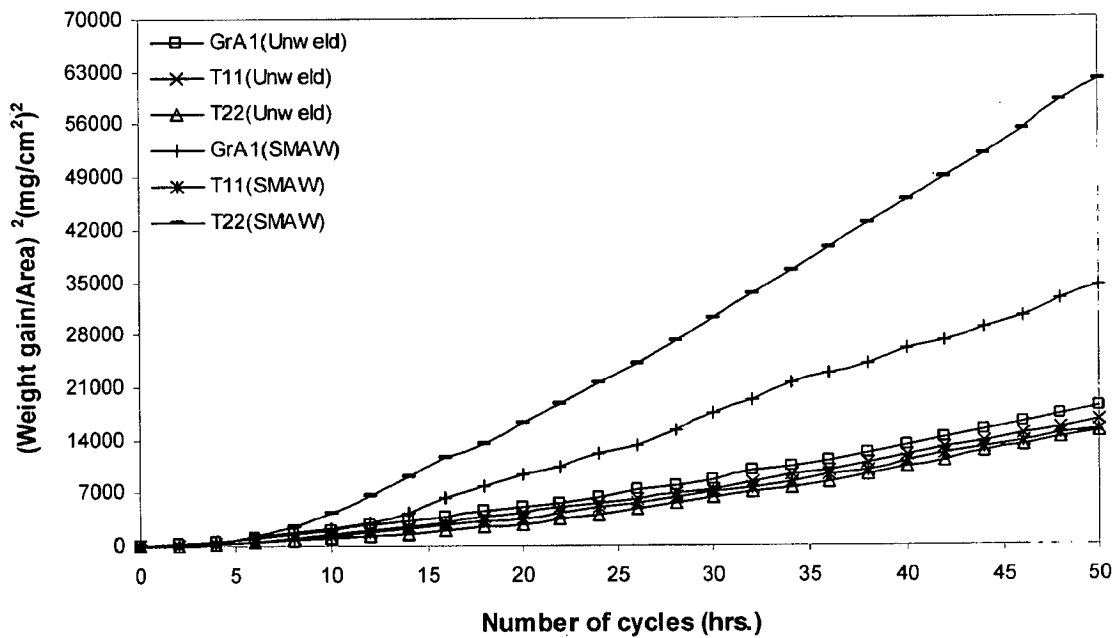


Fig. 5.9: Weight gain square (mg^2/cm^4) plot for unwelded and SMAW weldment of different steels exposed to air at 900 °C for 50 cycles.

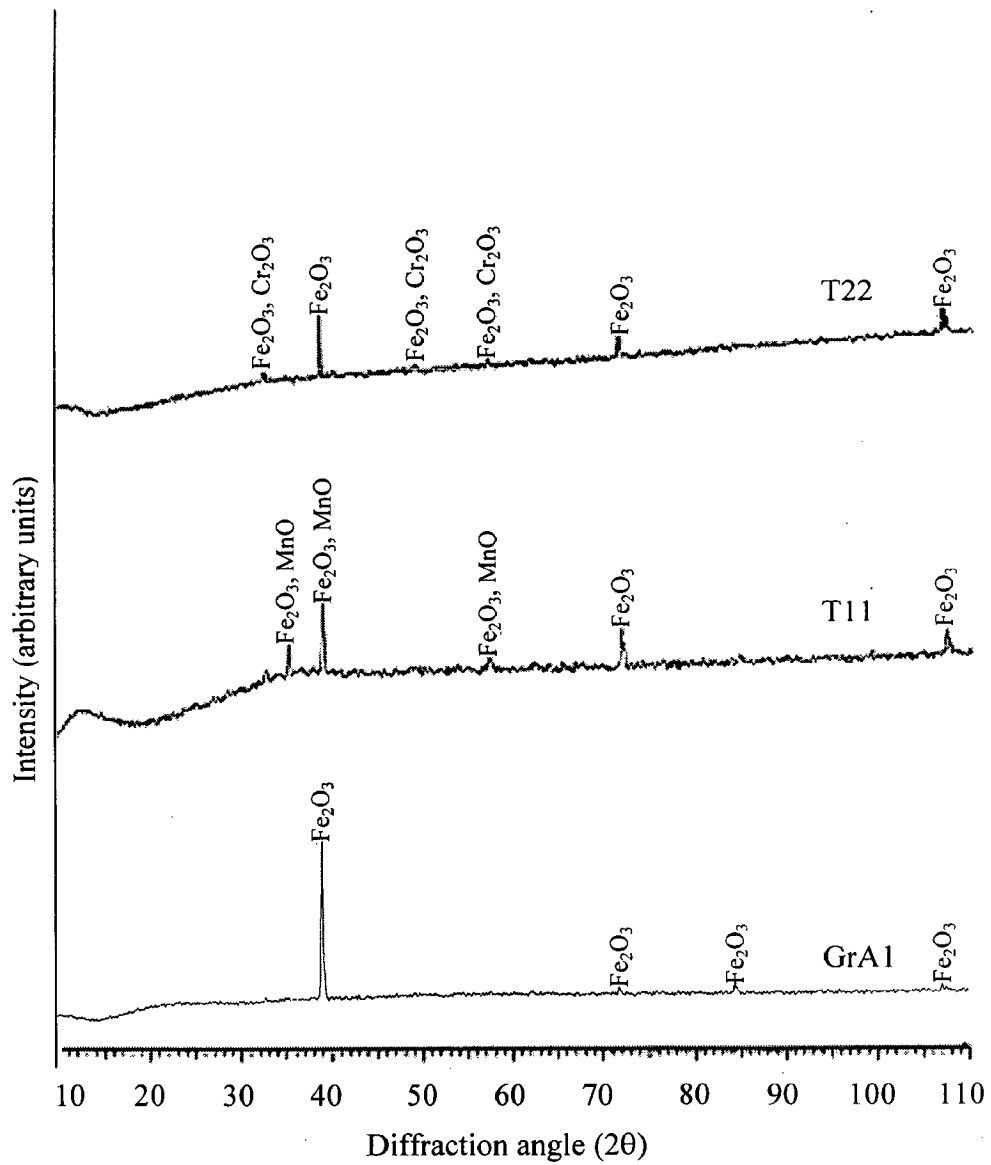


Fig. 5.10: X- ray diffraction profiles for corroded SMAW weldment in GrA1, T11 and T22 boiler steels subjected to cycle oxidation in air at 900 °C for 50 cycles.

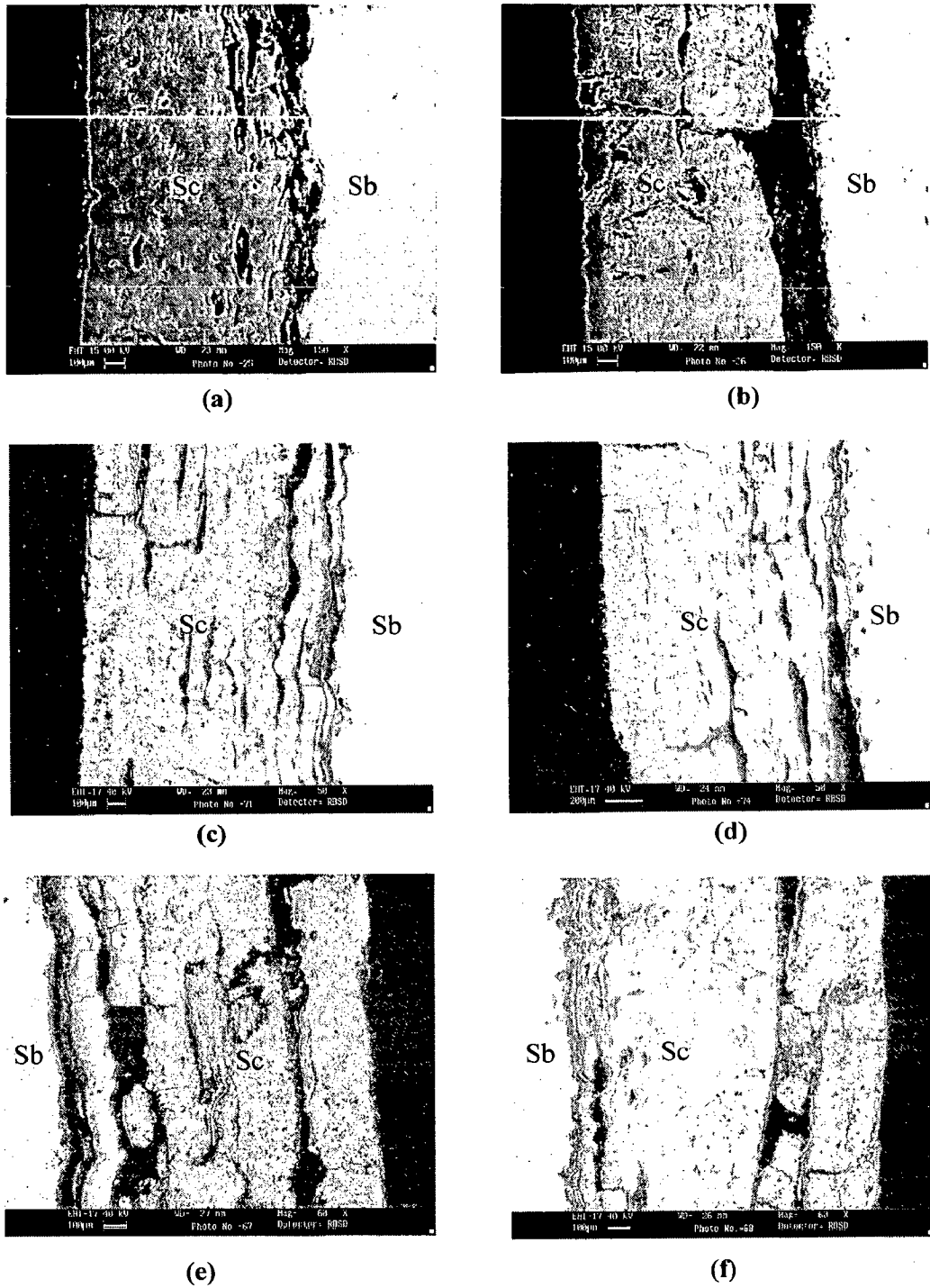


Fig. 5.11: SEM back scattered image of cross section for SMAW weldment in (a) GrA1 (weld),150X (b) GrA1 (HAZ), 150X (c) T11 (weld), 50X (d) T11 (HAZ), 50X (e) T22 (weld), 60X (f) T22 (HAZ), 60X steels after cyclic oxidation in air at 900 °C for 50 cycles.

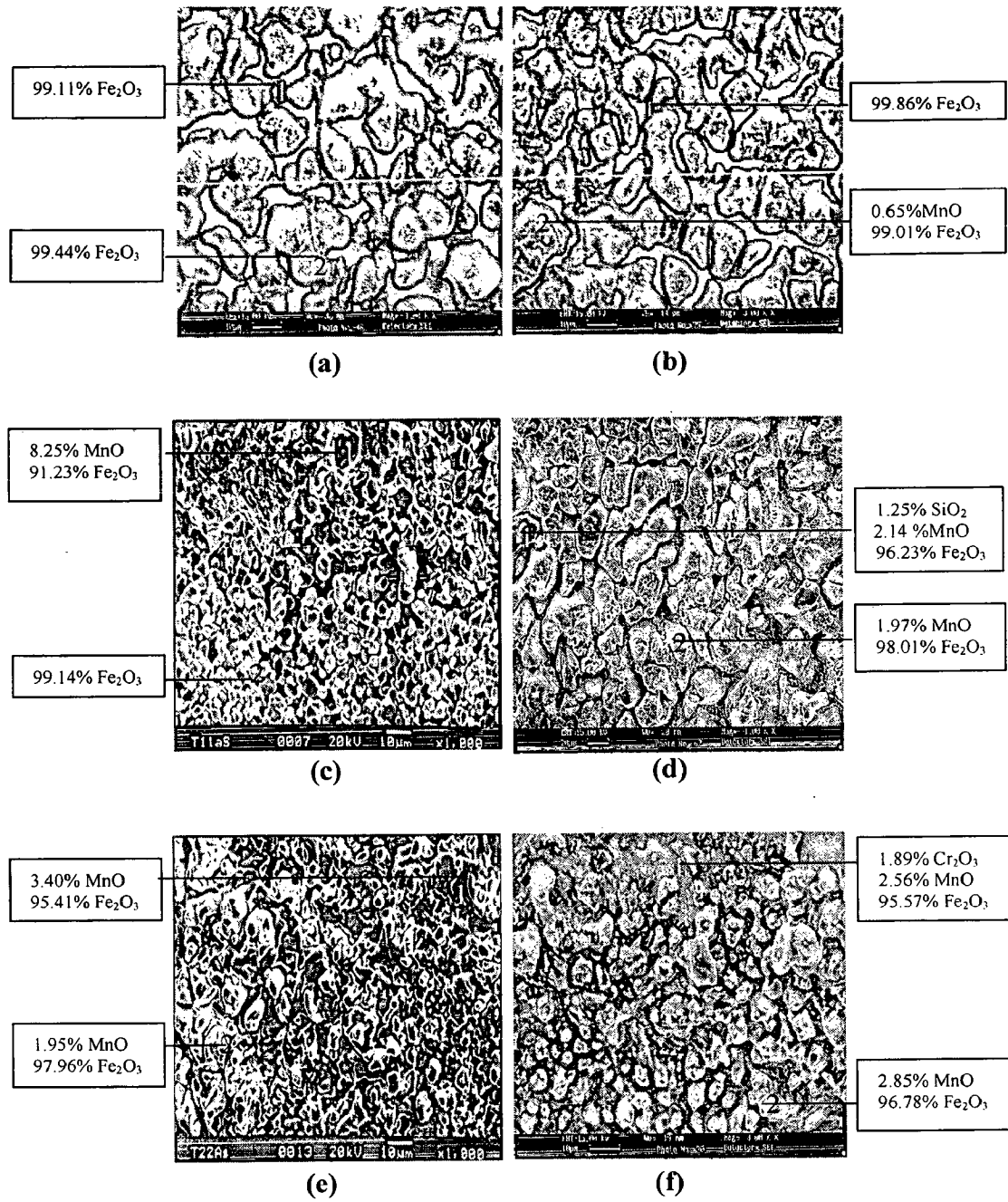


Fig.5.12: SEM micrographs showing surface scale morphology and EDAX analysis for SMAW weldment of different steels in air at 900 °C for 50 cycles (a) GrA1 (weld, 1000X (b) GrA1 (HAZ), 3000X (c) T11 (weld), 1000X (d) T11 (HAZ), 1000X (e) T22 (weld), 1000 X (f) T22 (HAZ), 3000X.

5.1.3 TIG WELDMENT

5.1.3.1 Visual Examination

The colour of oxide scale during initial cycles for this weldment was blackish grey and turned light black after 34th cycle in GrA1 steel. The macrographs after cyclic oxidation for 50 cycles at 900 °C for this weldment are as shown in Fig. 5.13. For TIG weldment in GrA1 and T11 steels the cracks in the oxide scale had started appearing during 30th and 26th cycle respectively. The weld region appeared black colour during 2nd cycle for T11 whereas it seems during 6th cycle of T22 steel. The width of cracks was comparatively more in case of welded T22 steel. Oxide protrusions, blackish dark grey in colour have been observed through these cracks.

5.1.3.2 Thermogravimetric Data

Cumulative weight change (mg/cm^2) variation as a function of time expressed in number of cycles for TIG weldment in steels is shown in Fig. 5.14. It can be inferred from the plot that welded T11 and unwelded T22 steel showed good resistance to oxidation. T22 as welded steel has shown more weight gain and indicated almost linear behaviour and its weight change is nearly 1.32 times more than the same welded T11 steel. The behaviour of welded T22 steel has followed the parabolic law from 22nd cycles. Its parabolic rate constant (K_p) is $20.371 \times 10^{-8} \text{ g}^2 \text{ cm}^{-4} \text{ s}^{-1}$. The parabolic behaviour has been followed by welded GrA1 and T11 steels as shown in Fig. 5.15 with parabolic rate constant, K_p values 13.074 and $8.348 \times 10^{-8} \text{ g}^2 \text{ cm}^{-4} \text{ s}^{-1}$ respectively.

5.1.3.3 X-ray Diffraction Analysis

All the welded steels after oxidation in air at 900 °C for 50 cycles have reported the formation of common phases. As could be seen in Fig. 5.16 the prominent phases analysed through XRD analysis for TIG weldment steels are Fe_2O_3 , Cr_2O_3 , and Fe_3O_4 . The XRD diffractogram for welded T11 steel has revealed weak peaks of Cr_2O_3 with Fe_2O_3 . In the oxide scale of welded T22 steel the common phase is Fe_2O_3 with Cr_2O_3 and Fe_3O_4 .

5.1.3.4 Scale Thickness Measurement

The scale thicknesses measured from the back scattered electron images (Fig. 5.17) for weld region of TIG weldment in GrA1, T11 and T22 steels oxidised in air at 900°C are 0.704, 1.080 and 1.095 mm respectively. Whereas the scale thicknesses measured from the back scattered electron images for HAZ region of TIG weldment in GrA1, T11 and T22

steels oxidized in air at 900 °C are 0.843, 0.795 and 0.940 mm respectively. Penetration of reacting species is more for welded T22 steel .The cross sectional image for the oxide scale of HAZ region in T11 steel indicates cracks right through scale. Whereas the oxide scale debonding at substrate/scale interface is evident from Fig. 5.17 (a), (b) and (e), (f) for GrA1 and T22 steels respectively .

5.1.3.5 SEM/EDAX Analysis

5.1.3.5.1 Surface morphology

The SEM micrograph for weld region of TIG weldment in GrA1 steel Fig. 5.18 (a) after oxidation indicates a scale rich in Fe_2O_3 (99.60%) as revealed by EDAX. Oxide protrusions from inside consisting mainly of Fe_2O_3 (99.83%) are indicated point 1. The EDAX analysis revealed the oxide scale on HAZ region consists of iron oxide Fe_2O_3 (96.59% and SiO_2 (2.56%) at point 2, whereas the black portion (Point 1) consists of 99.20% Fe_2O_3 with small amount of MnO (0.56%) Fig. 5.18 (b).

SEM micrograph Fig. 5.18 (c) for weld region of TIG welded T11 steel after cyclic oxidation shows iron rich scale containing some amount of MnO (2.22%) point 2. The EDAX analysis inside the crack (point 1) indicates the presence of SiO_2 , Cr_2O_3 and MnO with the main phase is Fe_2O_3 (91.07%). The EDAX analysis of oxide scale of HAZ region of same steel is consists of mainly little higher amount of Fe_2O_3 (98.10%) than weld region Fig. 5.18 (d). The oxide scale of weld region shown in Fig. 5.18 (e) for the same welded T22 steel oxidized after TIG weldment indicates massive scale having cracks. The inner scale consists of mainly iron oxides with little amount of MnO (1.20%) and Cr_2O_3 (2.60%) point 1. Whereas the upper scale containing MnO (1.22%) and Cr_2O_3 (1.28%) with main oxide Fe_2O_3 point 2. The EDAX analysis of HAZ region in this steel indicates the Fe_2O_3 (97.55%) with little amount of Cr_2O_3 (1.58%) at point 1 (black portion), whereas the white portion consists of Cr_2O_3 (2.47%) with main phase of iron oxide (96.75%) at point 2 in Fig. 5.18 (f).

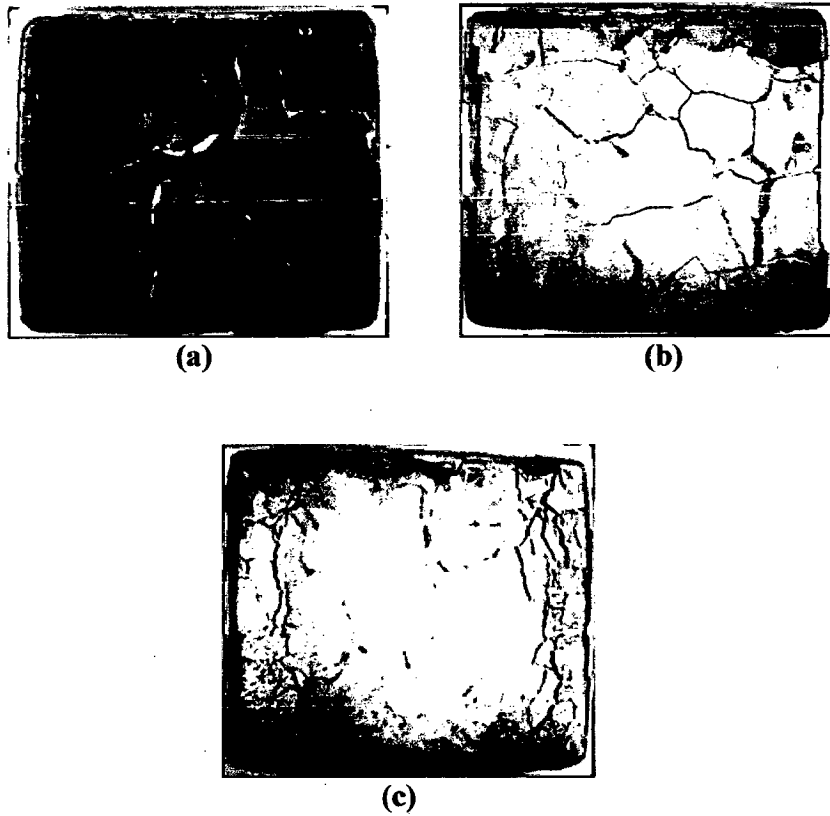


Fig. 5.13: Macrographs of TIG weldment in (a) GrA1, (b) T11 and (c) T22 steels subjected to cycle oxidation in air at 900 °C for 50 cycles.

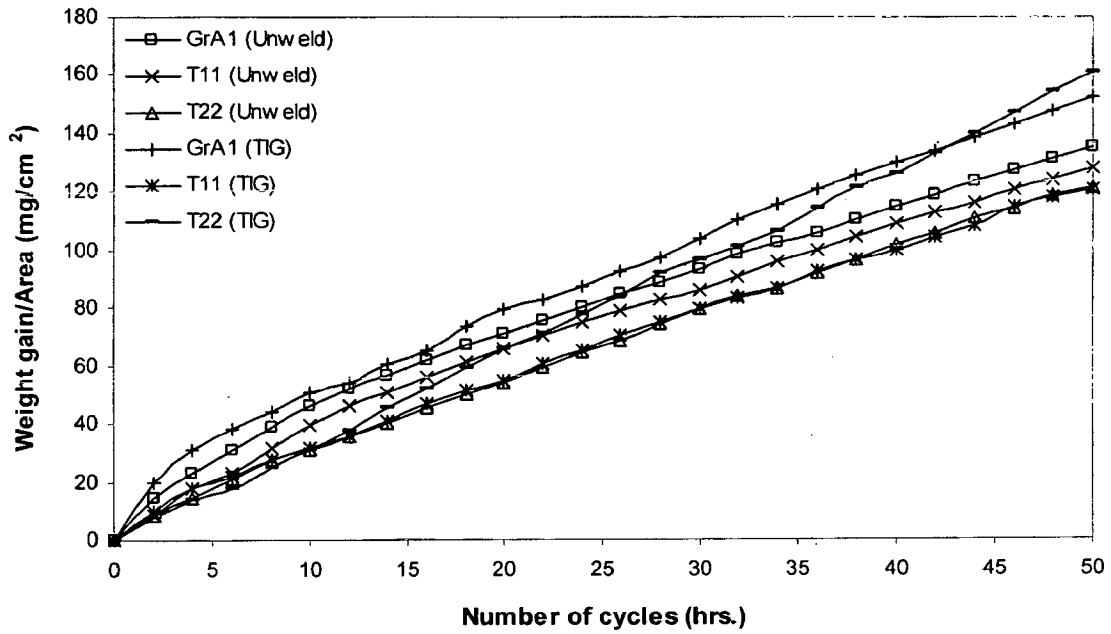


Fig. 5.14: Weight gain plot for unwelded and TIG weldment of the different steels exposed to air at 900 °C for 50 cycles.

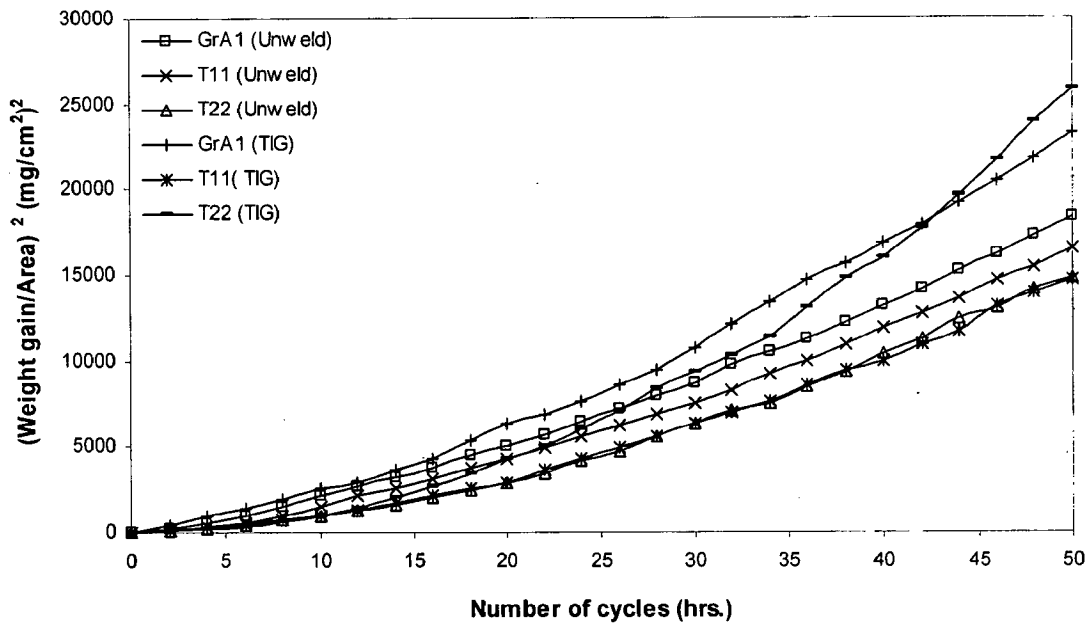


Fig. 5.15: Weight gain square (mg²/cm⁴) plot for TIG Weldment of the different steels exposed to air at 900 °C for 50 cycles.

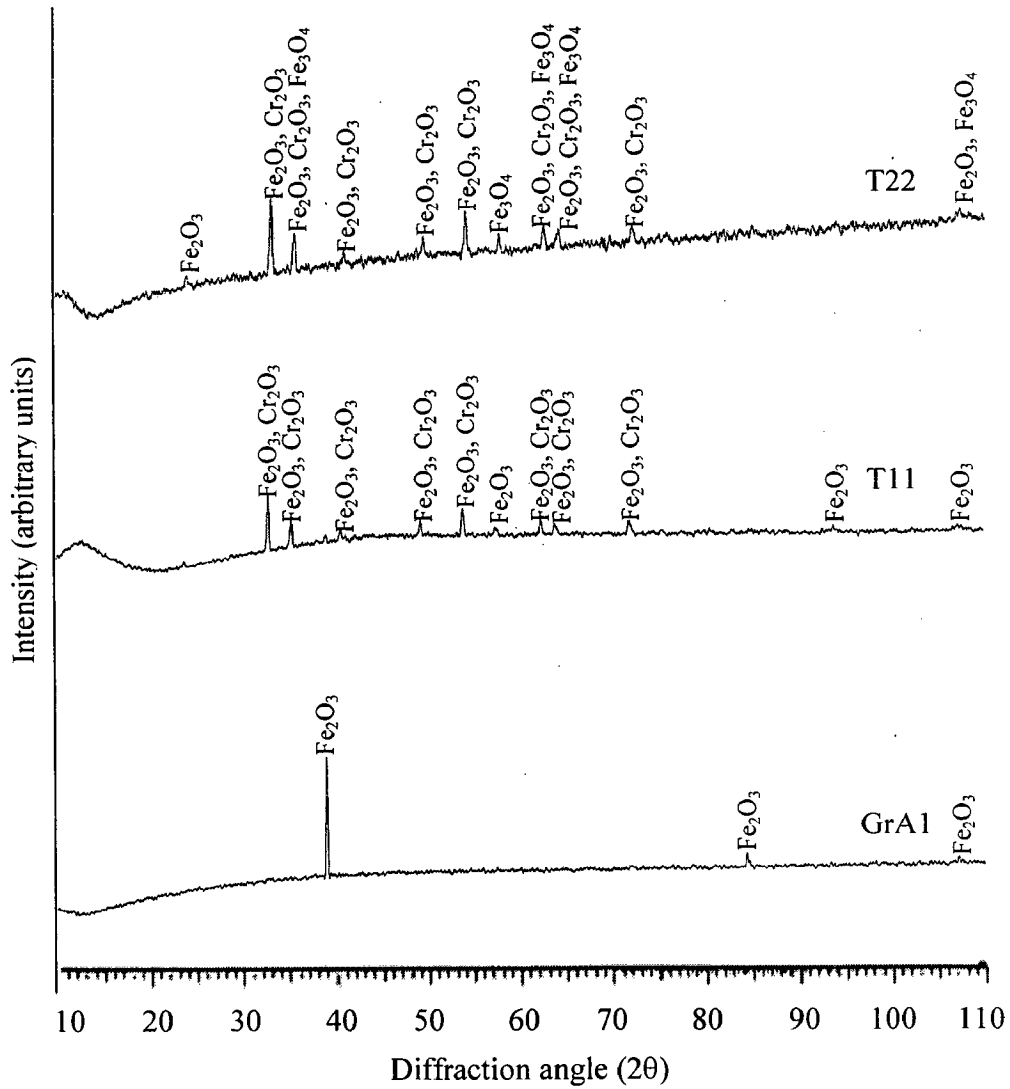
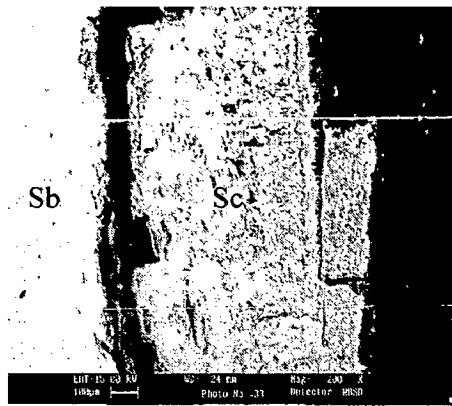
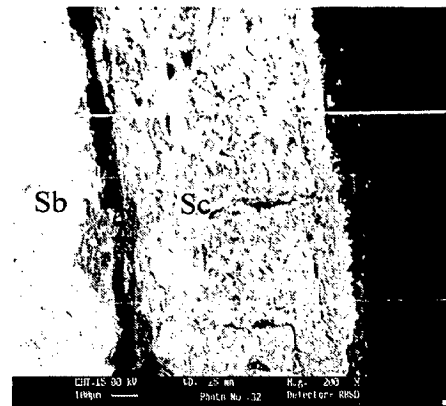


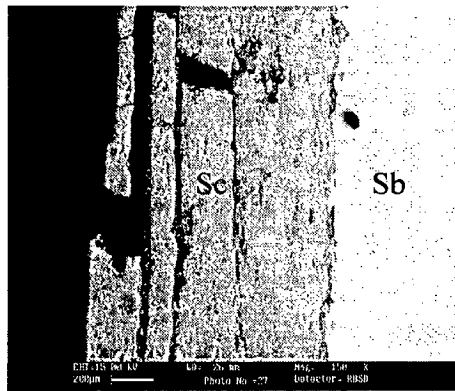
Fig. 5.16: X-ray diffraction profiles for corroded TIG weldment in GrA1, T11 and T22 boiler steels subjected to cyclic oxidation in air at 900 °C for 50 cycles.



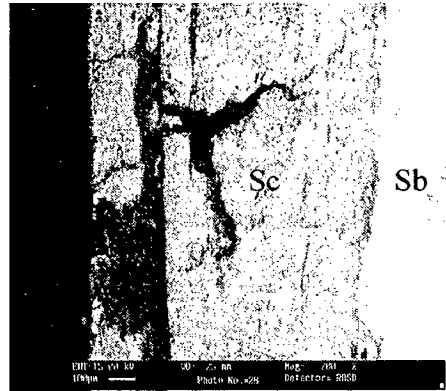
(a)



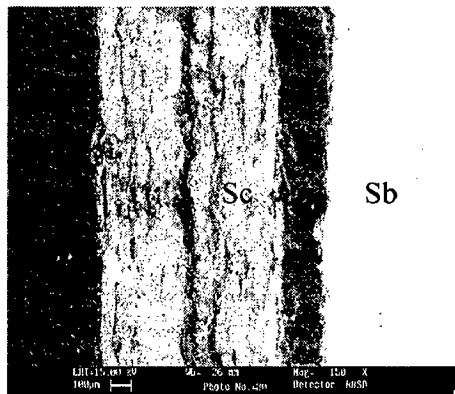
(b)



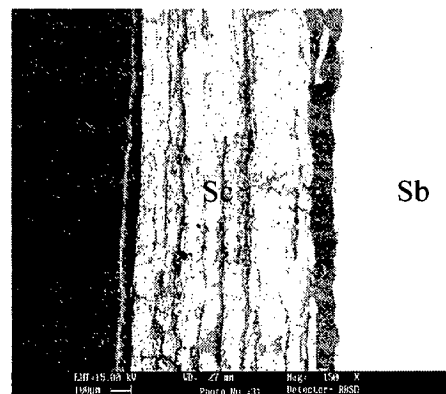
(c)



(d)



(e)



(f)

Fig. 5.17: SEM back scattered image of cross section for TIG weldment steels after cyclic oxidation in air at 900 °C for 50 cycles (a) GrA1 (weld), 200X (b) GrA1 (HAZ), 200X (c) T11(weld), 150X and (d) T11 (HAZ), 150X (e) T22 (weld), 150X (f) T22 (HAZ), 150X.

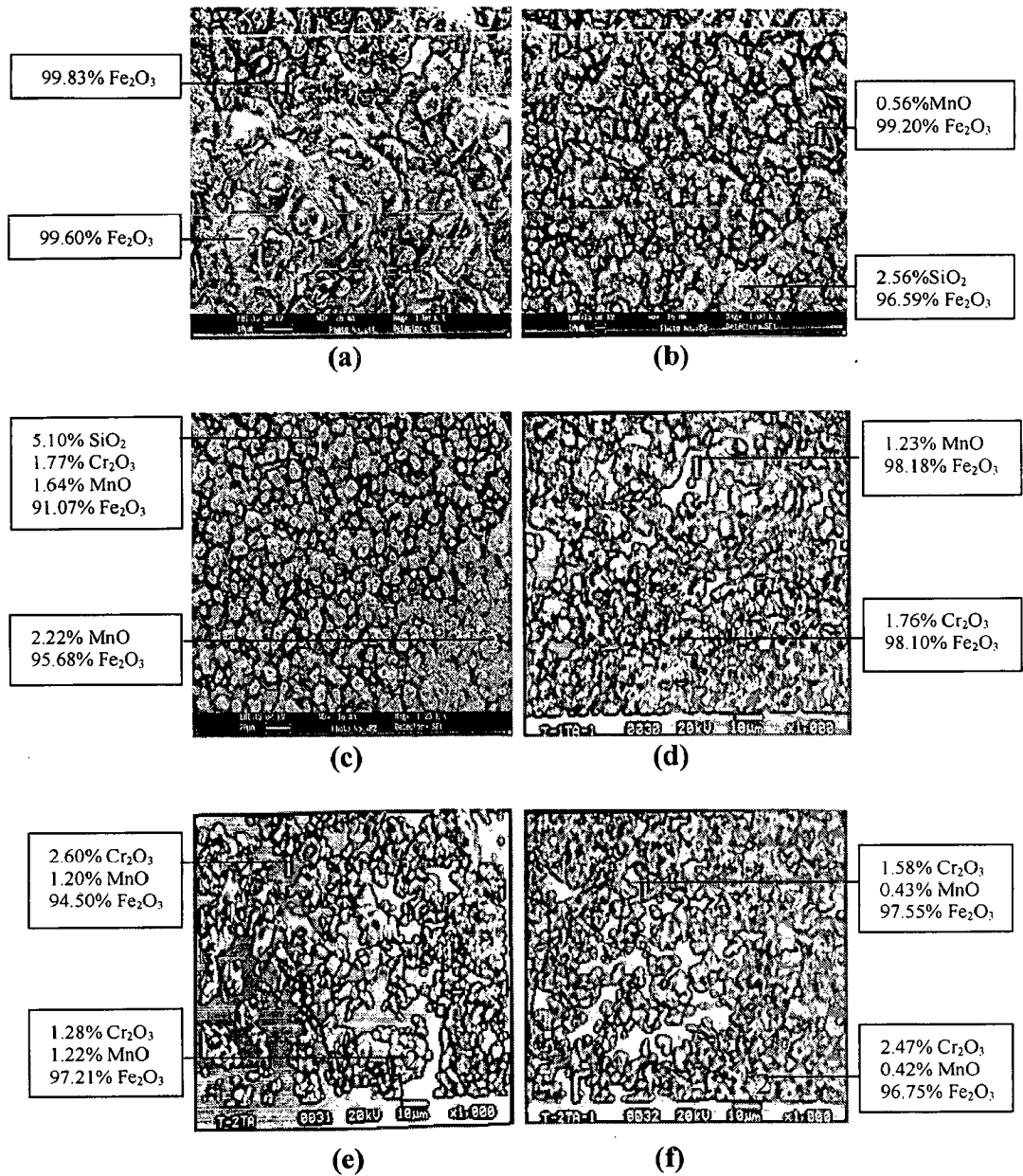


Fig. 5.18: Surface morphology and EDAX analysis for TIG weldment of the different steels oxidized in air at 900 °C for 50 cycles (a) GrA1 (weld), 1000X (b) GrA1 (HAZ), 1000X (c) T11 (weld), 1000X (d) T11 (HAZ), 1000K (e) T22 (weld), 1000X (f) T22 (HAZ), and 1000 X.

PART (B) OXIDATION STUDIES OF DIFFERENT REGIONS OF WELDMENTS IN AIR ENVIRONMENT

This part of chapter 5 deals with the critical examination of corrosion products and the behaviour of different regions of weldments in steels when subjected to high temperature cyclic oxidation in air at 900°C for 50 cycles. The samples were visually examined at the end of each cycle during study. Efforts have been made to understand the mechanism of corrosion.

The corrosion products were analyzed with XRD and SEM/EDAX. The results for different regions of weldment in steels have been reported under different subheadings. In view of the thermogravimetric data for the each base steel is reported along with the each region of the weldments. The parabolic rate constants and scale thicknesses have been evaluated.

5.2 Results

5.2.1 Different Regions of SMAW Weldment i. e. the Base Metal, HAZ and Weld Metal exposed to Air at 900 °C for 50 cycles in GrA1 Steel

5.2.1.1 Visual Examination

The macrographs for different regions of SMAW weldment in GrA1 steel oxidized in air at 900 °C for 50 cycles are shown in Fig. 5.19. The colour of weld metal is blackish grey during 1st cycle and started turning dark blackish blue in 7th cycle of oxidation. During experimentation the blackness of the oxide scale seemed to be increasing. No cracks were visible but very small oxide protrusions developed during last five cycles. Whereas minimum spalling was observed in case of HAZ region during 14th cycle. The colour of oxide scale seems as blackish blue during 16th cycle. The cracks in the scale of HAZ had appeared in the middle of surface of specimen after 33rd cycle.

5.2.1.2 Thermogravimetric Data

Thermogravimetric measurements taken throughout the total number of cycles are plotted relative to the number of cycles with an aim to understand the kinetics of oxidation. Figure 5.20 gives the variation of weight gain per unit area as a function of number of cycles. Whereas in Fig. 5.21 the square of weight gain per unit area has been plotted as a function of time expressed in number of cycles to confirm the parabolic behaviour of the different regions of SMAW weldment. It can be inferred from Fig. 5.20 that the HAZ showed less weight gain

as compared to base metal and weld metal. Among the different regions of SMAW weldment in GrA1 steel although maximum weight gain is observed for the base metal which is around 1.8 times of that for the HAZ. The weight gain for all the regions of the weldment is same during first twelve cycles and increase in the weight gain was only noticed for base metal after 12th cycles and shown slight variation from parabolic rate law. The calculated values of parabolic rate constant (K_p) for weld metal and HAZ are 5.558 and $3.102 \times 10^{-8} \text{ g}^2 \text{ cm}^{-4} \text{ s}^{-1}$ respectively.

5.2.1.3 X-ray Diffraction Analysis

The XRD analysis for base metal, weld metal and HAZ regions of SMAW weldment in GrA1 steel after exposure to air at 900 °C for 50 cycles is shown in Fig. 5.22 and these diffractograms has almost similar phases for all the regions. As obvious from the composition all the regions have indicated the formation of iron oxide (Fe_2O_3).

5.2.1.4 Scale Thickness Measurement

SEM back scattered images for different regions of SMAW weldment in GrA1 steel after oxidation in air at 900 °C for 50 cycles are shown in Fig. 5.23. The first look at Fig. 5.5 (a) micrograph for base metal reveals thick scale. Scale thickness on the base metal is almost 1.33 times more than that on the HAZ which has indicated thinnest scale among all the regions. The average values of scale thickness measured from BSEI for base metal, weld metal and HAZ regions are 1.1, 0.866 and 0.822 mm respectively. More voids and internal oxidation are seemed in the oxide scale along the cross section in all the three regions. Debonding of oxide scale at the metal/scale interface was observed in the oxidized weld metal specimen.

5.2.1.5 SEM/EDAX Analysis

5.2.1.5.1 Surface Morphology

SEM/EDAX analysis of the oxide scale developed on the surfaces of different regions of SMAW weldment in GrA1 steel is shown in Fig. 5.24. The EDAX analysis of scale for weld metal indicates that the scale mainly consisted of Fe_2O_3 (99.97%) Fig. 5.24 (a). The spalled region indicates that the subscale which is rich in Fe. SEM indicates that the upper scale for HAZ is also mainly iron oxide along with small amount of MnO at point 2. The scale which seems to have oozed out from surface is mainly consisting of Fe_2O_3 (99.98%) point 1 Fig. 5.24 (b).

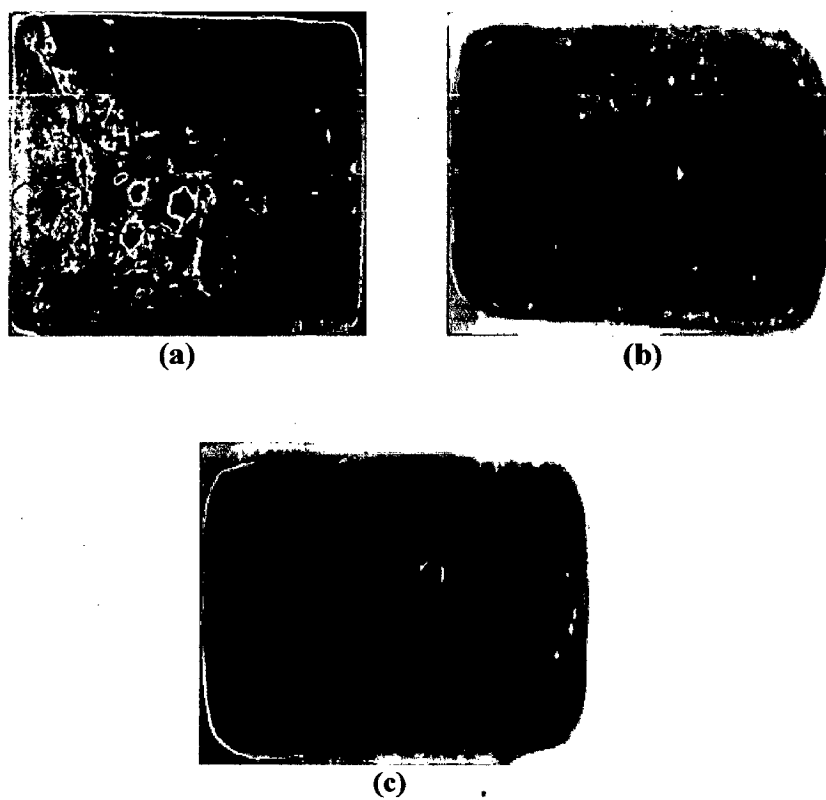


Fig. 5.19: Macrographs of different regions of SMAW weldments in GrA1 steel subjected to cyclic oxidation in air at 900 °C for 50 cycles (a) Base Metal, (b) Weld Metal and (c) HAZ.

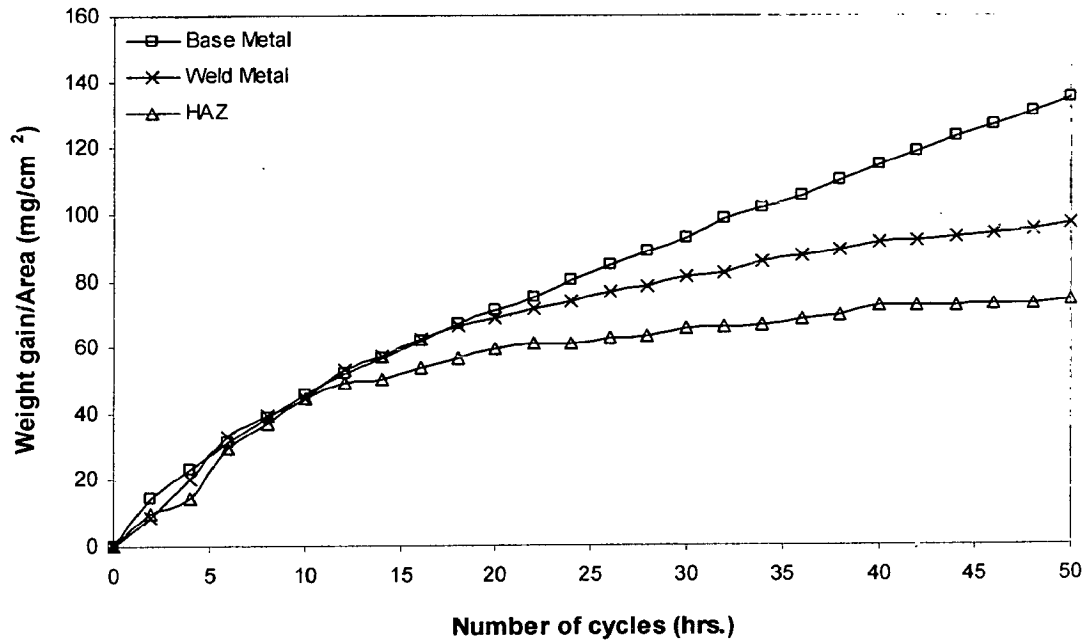


Fig. 5.20: Weight gain plot for different regions of SMAW weldment in GrA1 steel exposed to air at 900 °C for 50 cycles.

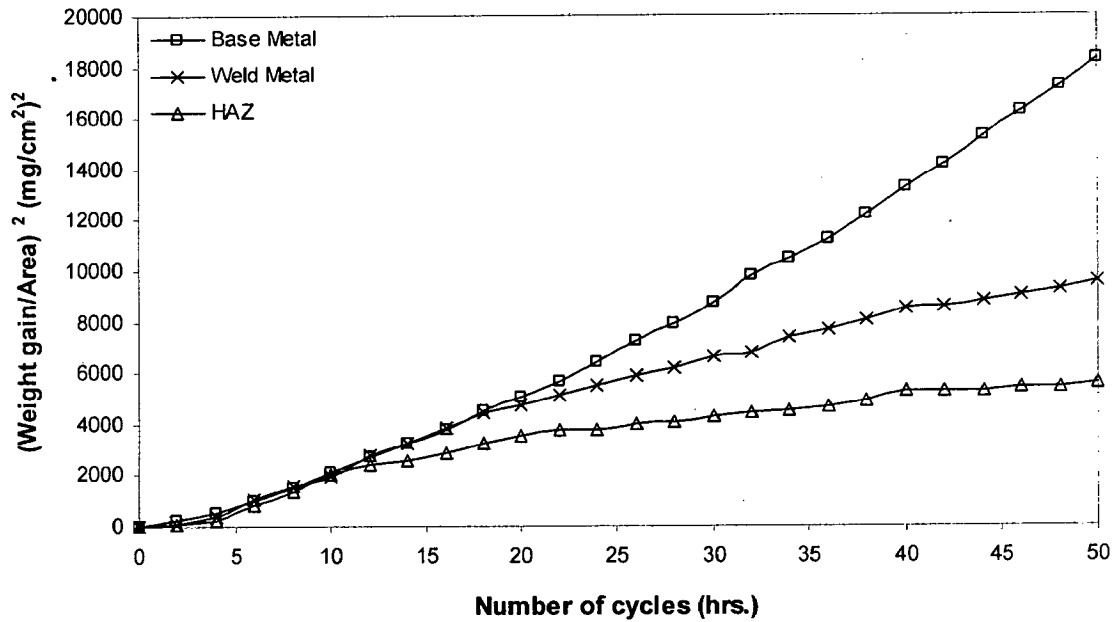


Fig. 5.21: Weight gain square (mg²/cm⁴) plot for different regions of SMAW weldment in GrA1 steel exposed to air at 900 °C for 50 cycles.

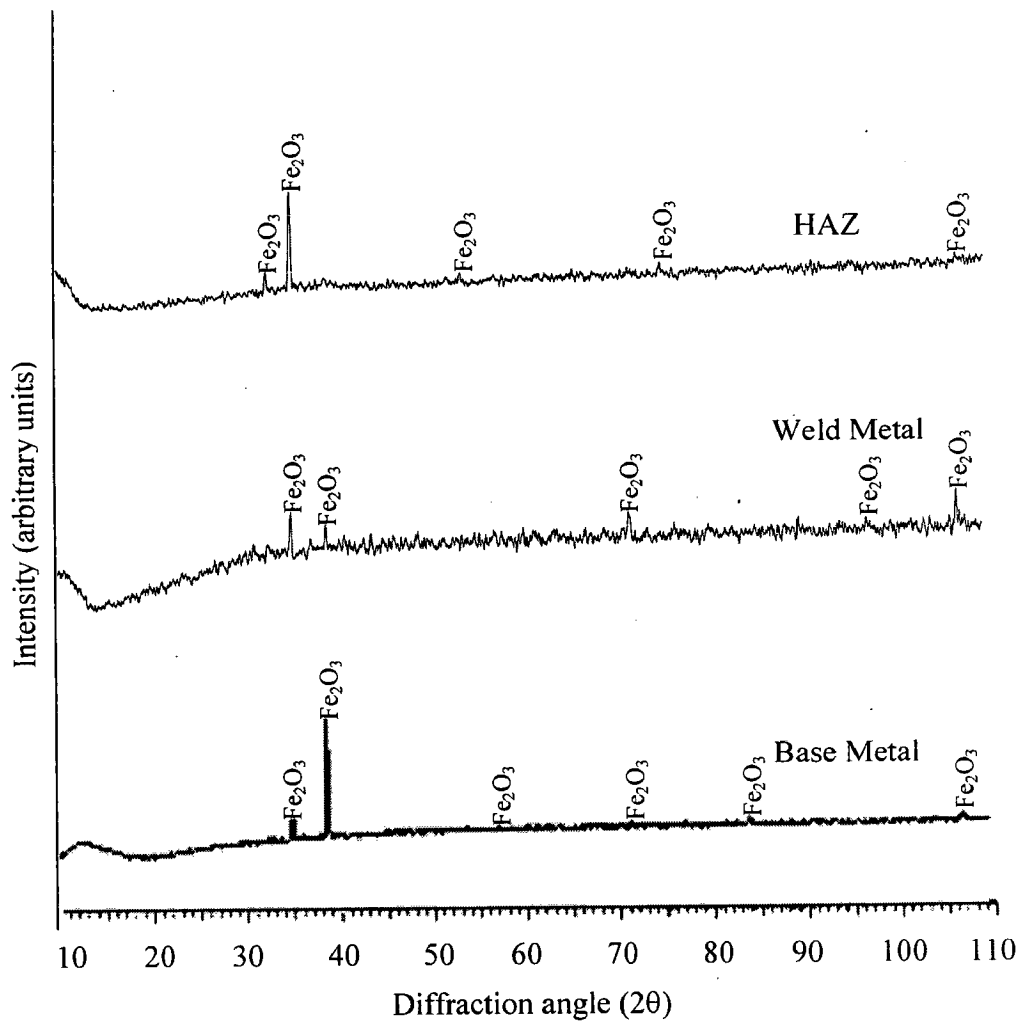
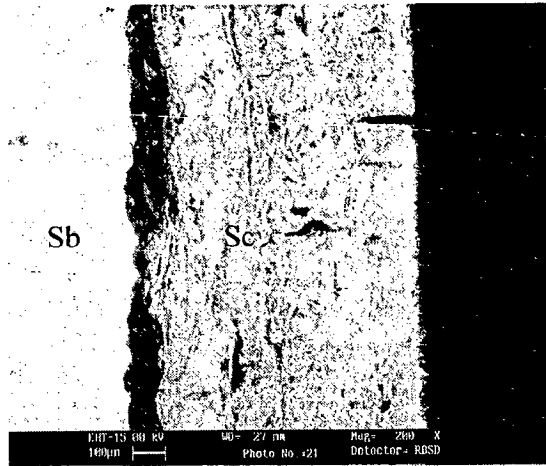
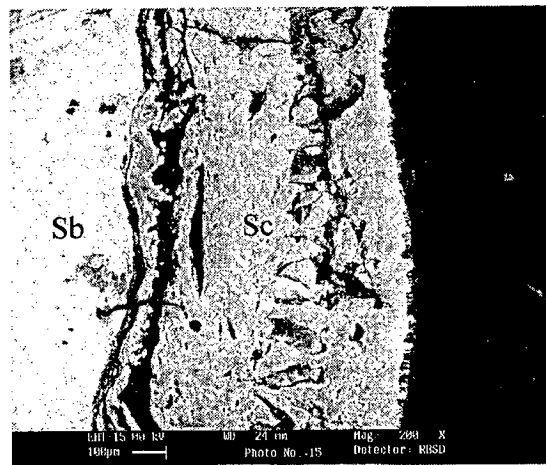


Fig. 5.22: X-ray diffraction profiles for different regions of SMAW weldment in GrA1 steel exposed to air at 900 °C for 50 cycles.

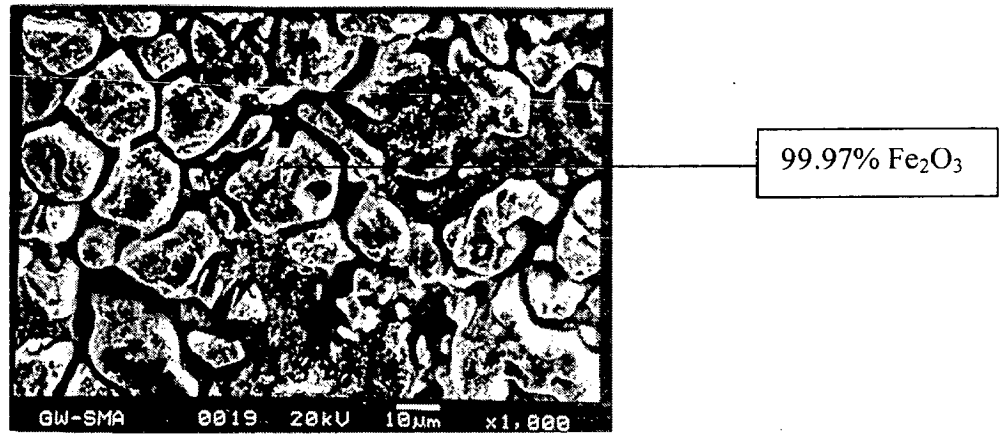


(a)

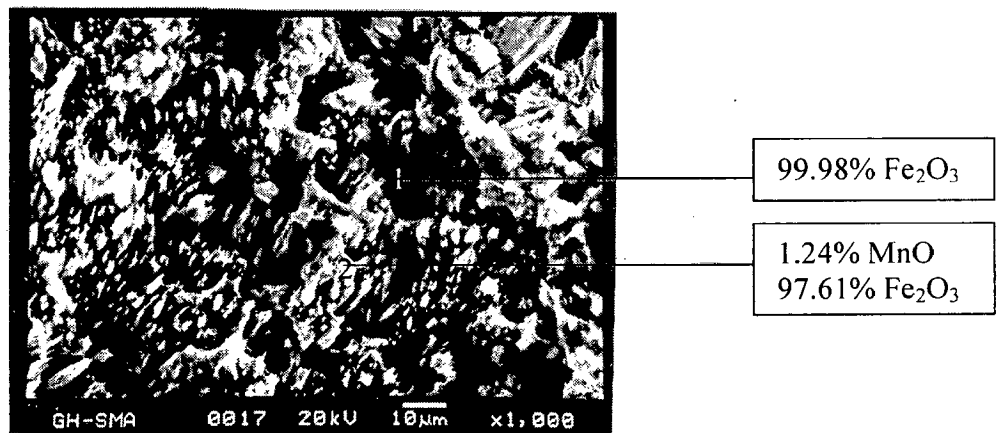


(b)

Fig. 5.23: SEM back scattered image of the cross section of different regions of SMAW weldment in GrA1 steel exposed to air at 900 °C for 50 cycles (a) Weld Metal, 200X (b) HAZ, 200X.



(a)



(b)

Fig. 5.24: Surface morphology and EDAX analysis for different regions of SMAW weldment in GrA1 steel exposed to air at 900 °C for 50 cycles (a) Weld Metal, 1000X and (b) HAZ, 1000X.

5.2.2 Different Regions of SMAW Weldment i. e. the Base Metal, HAZ and Weld Metal exposed to Air at 900 °C for 50 cycles in T11 Steel

5.2.2.1 Visual Examination

During cyclic study the colour of scale for base metal and weld metal was light grey during first few cycles and turned to dark grey after fifth cycle. In case of HAZ the colour of scale in the starting was black which was continuous up to the last cycle. In case of base metal the spalling and sputtering started just after 4th cycle. Where as minimum spalling was observed in case of HAZ. The cracks in the oxide scale for weld metal appeared after 25th cycle. Morphology of the oxide scale for steels after 50 cycles of oxidation is shown in Fig. 5.25. The scale formed on HAZ is of uniform thickness and has blackish white spot appearance in middle of the surface. Where as irregular and fragile scale is observed for base metal in Fig. 5.25 (a) showing spalled areas.

5.2.2.2 Thermogravimetric Data

The plots of cumulative weight gain (mg/cm^2) as a function of time (number of cycles) for base metal, weld metal and HAZ at 900 °C in air upto 50 cycles is shown in Fig. 5.26. Extensive spalling and sputtering has limited the study upto 50 cycles. The plot for all the regions shows a same weight gain during the first six cycles followed by gradual weight gain. The amount of the spalled scale has also been incorporated in weight gain measurements. The total weight gain at the end of 50 cycles for base metal, weld metal and HAZ is 128.387, 67.792, and 78.701 mg/cm^2 respectively. The $(\text{weight gain}/\text{unit area})^2$ plot against number of cycles Fig. 5.27 further confirms that parabolic law is followed by all the three regions. The values of parabolic rate constant, K_p ($10^{-8} \text{ g}^2 \text{ cm}^{-4} \text{ s}^{-1}$) are 9.384, 2.469 and 3.344 for base metal, weld metal and HAZ respectively.

5.2.2.3 X-ray Diffraction Analysis

The XRD analysis for base metal, weld metal and HAZ regions after exposure to air at 900 °C for 50 cycles is shown in Fig. 5.28 and these diffractograms has almost similar phases for all the regions. As obvious from the composition all the regions have indicated the formation of iron oxide (Fe_2O_3). Where as big peaks of Fe_3O_4 along with Fe_2O_3 are indicated in the oxide scale of weld metal.

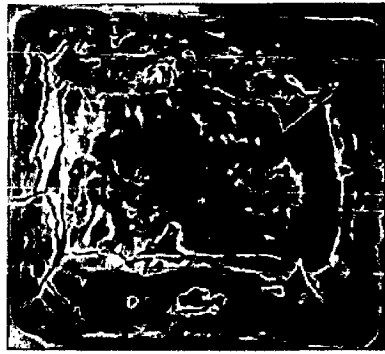
5.2.2.4 Scale Thickness Measurement

The scale thickness after cyclic oxidation in air at 900 °C for SMAW weldment in T11 steel was measured from the back scattered SEM image shown in Fig. 5.29. The average identified scale thickness for weld metal and HAZ is 0.618 mm and 0.726 mm respectively. The maximum scale thickness among the regions of SMAW weldment was measured for base metal which is 1.289 mm and around two times more than the scale thickness for weld metal. Oxide scale is debonding at the oxide scale/metal interface for weld metal and HAZ.

5.2.2.5 SEM/EDAX Analysis

5.2.2.5.1 Surface Morphology

SEM/EDAX analysis for weld metal as given in Fig. 5.30 (a) indicates that top scale is mainly of Fe₂O₃ (99.24%). Whereas inner scale mainly contains Fe₂O₃ (97.99%) along with SiO₂ (1.51%). SEM micrograph for the top scale of HAZ shown in Fig. 5.30 (b) indicates formation of massive scale consisting mainly iron oxides Fe₂O₃ (99.80%). The inner scale shows iron oxide 99.12%.



(a)



(b)



(c)

Fig. 5.25: Macrographs of different regions of SMAW weldments in T11 steel subjected to cyclic oxidation in air at 900 °C for 50 cycles (a) Base Metal, (b) Weld Metal and (c) HAZ.

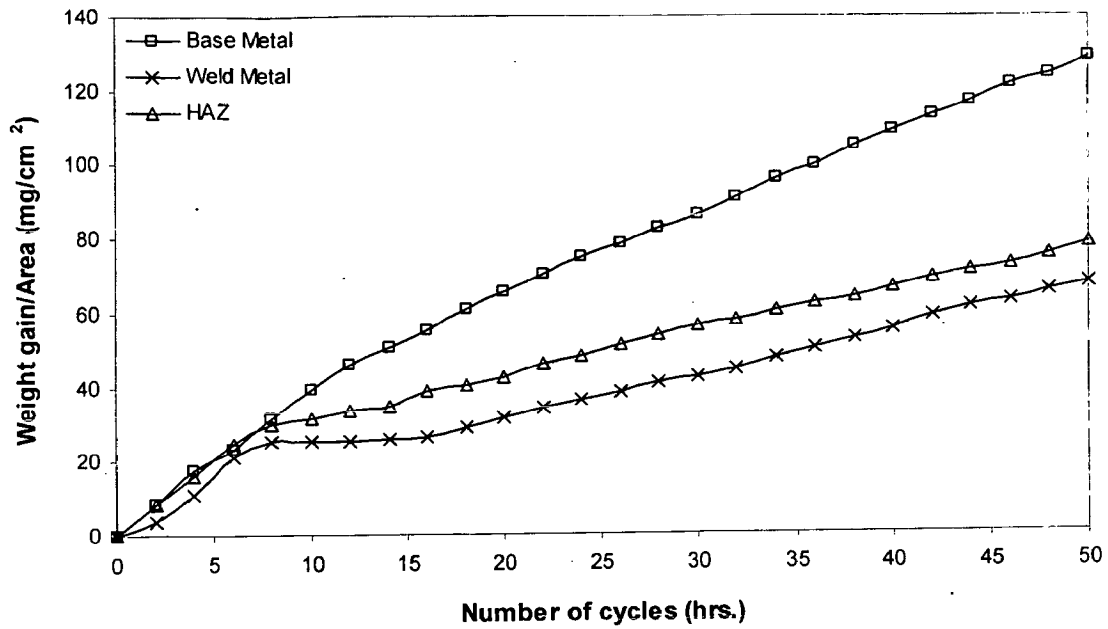


Fig. 5.26: Weight gain plot for different regions of SMAW weldment in T11 steel exposed to air at 900 °C for 50 cycles.

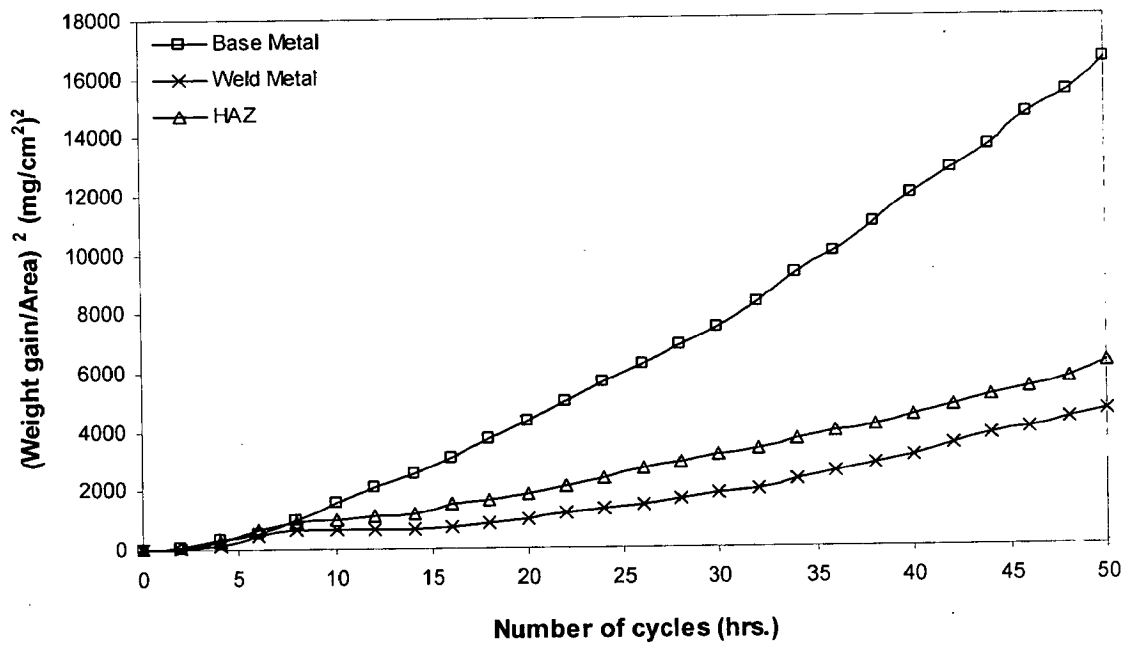


Fig. 5.27: Weight gain square (mg²/cm⁴) plot for different regions of SMAW weldment in T11 steel exposed to air at 900 °C for 50 cycles.

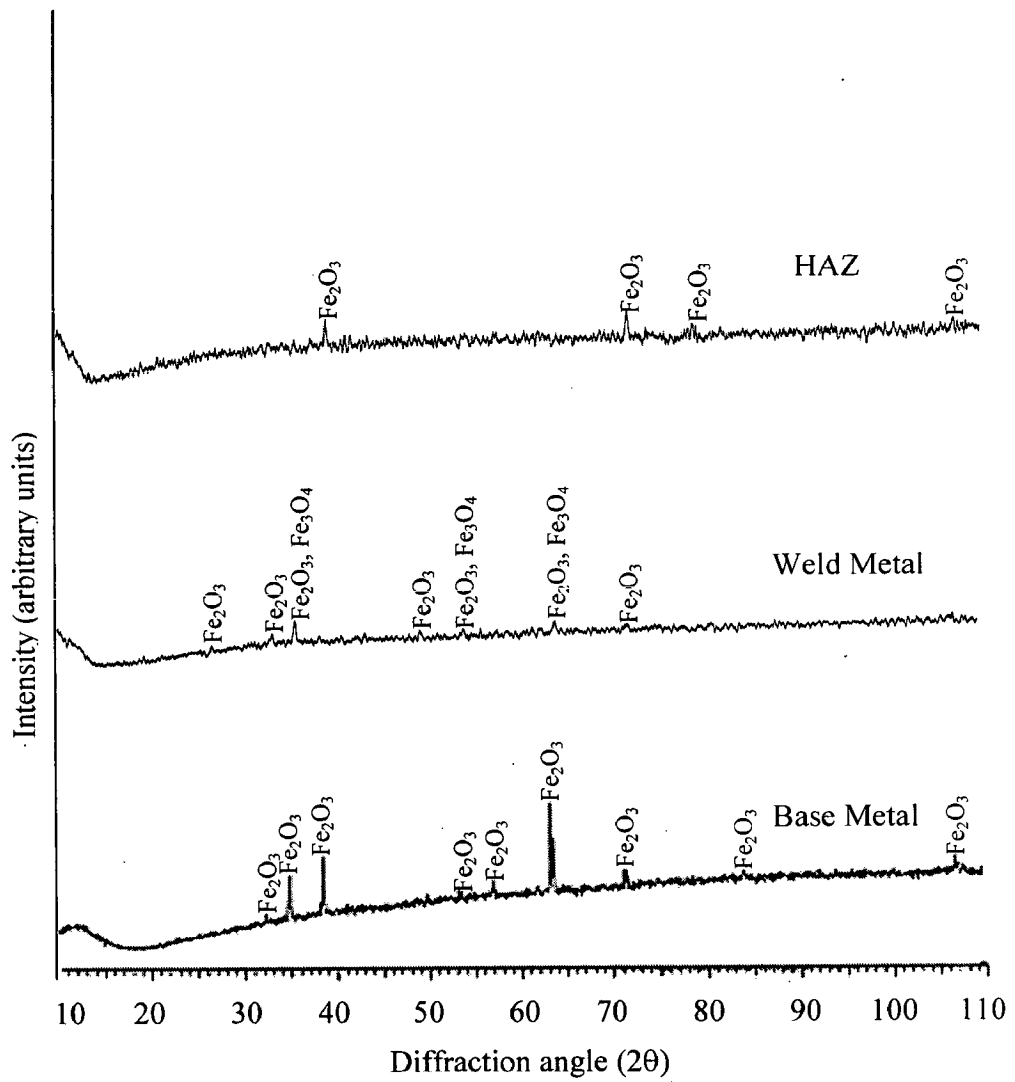
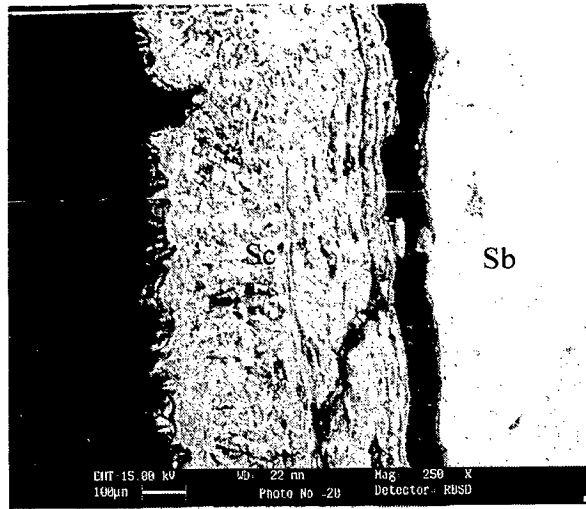
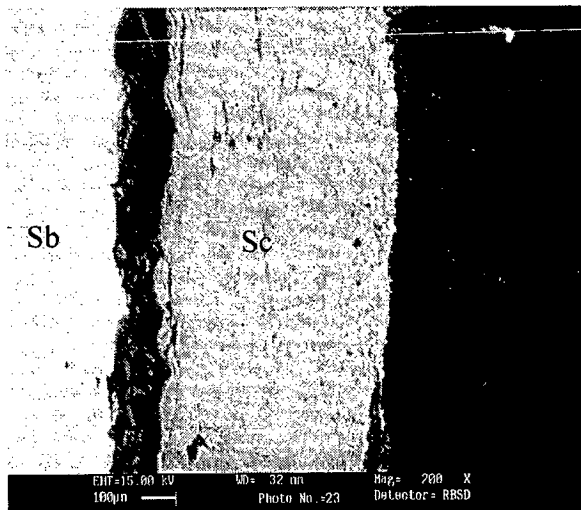


Fig. 5.28: X-ray diffraction profiles for different regions of SMAW weldment in T11 steel exposed to air at 900 °C for 50 cycles.

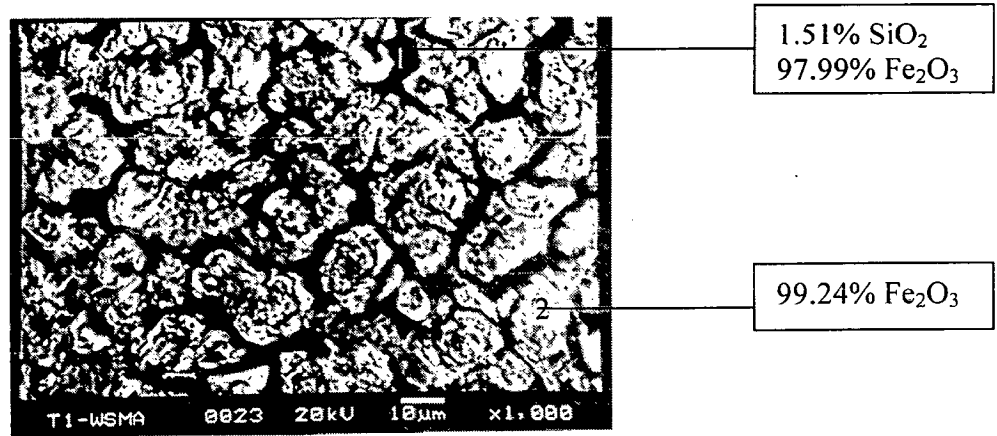


(a)

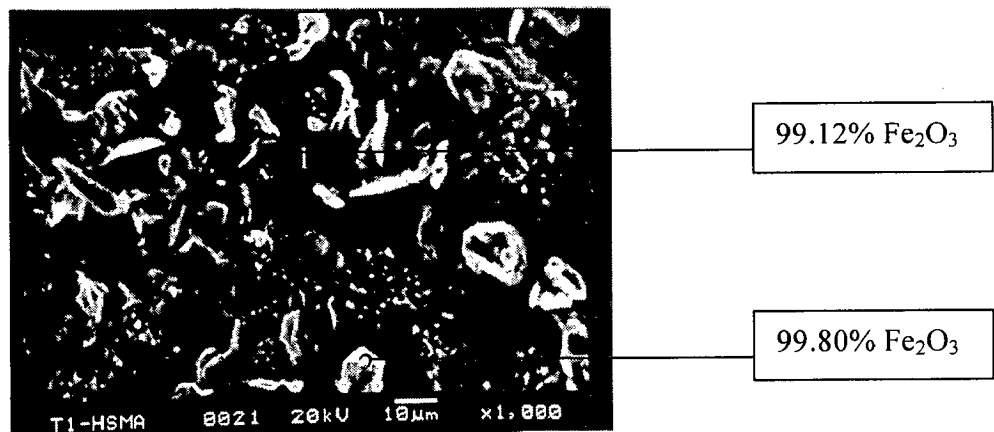


(b)

Fig. 5.29: SEM back scattered image of the cross section of different regions of SMAW weldment in T11 steel exposed to air at 900 °C for 50 cycles (a) Weld Metal, 200X (b) HAZ, 250X.



(a)



(b)

Fig. 5.30: Surface morphology and EDAX analysis of the scale on different regions of SMAW weldment in T11 steel exposed to air at 900 °C for 50 cycles (a) Weld Metal, 1000X and (b) HAZ, 1000X.

5.2.3 Different Regions of SMAW Weldment i. e. Base Metal, HAZ and Weld Metal exposed to Air 900 °C for 50 cycles in T22 Steel

5.2.3.1 Visual Examination

The colour of scale for weld metal was blackish grey during first few cycles and turned to blackish brown during 14th cycle. Cracking and spalling started just after 30th cycle. Where as minimum spalling was observed in case of base metal. The width of cracks in the oxide scale of weld metal increase with the increasing of cycle. In case of HAZ cracking and spalling had appeared after 10th cycle. Lustrous blackish grey colour scale was noticed for HAZ. Morphology of the oxide scale for steels after 50 cycles of oxidation is shown in Fig. 5.31. The scale formed on HAZ is of uniform thickness and has dull appearance.

5.2.3.2 Thermogravimetric Data

The weight gain/area for the three regions of SMAW weldment in T22 steel is plotted against number of cycles in Fig. 5.32. It can be inferred from the plots that after 4th cycle HAZ specimen showed more weight gain/unit area throughout exposure. The weld metal specimen showed lesser weight gain than HAZ and base metal. All the three specimen showed parabolic behaviour. The values of parabolic rate constant, K_p for base metal, weld metal and HAZ are 8.515, 4.859 and $9.826 \times 10^{-8} \text{ g}^2 \text{ cm}^{-4} \text{ s}^{-1}$ respectively in Fig. 5.33. The HAZ region has indicated slight variation from the parabolic rate law and its parabolic rate constant K_p is almost double than that of weld metal.

5.2.3.3 X-ray Diffraction Analysis

The XRD analysis for different regions of SMAW weldment in T22 steel after exposure to air at 900 °C for 50 cycles is shown in Fig. 5.34 and these diffractograms has almost similar phases for all the regions. Extra phase MnO with Fe_2O_3 was observed for weld metal.

5.2.3.4 Scale Thickness Measurement

SEM back scattered images for different regions of SMAW weldment in T22 steel after oxidation in air at 900 °C for 50 cycles are shown in Fig. 5.35. The oxide scale image on base metal reveals slightly thick scale. The average values of scale thickness measured from BSEI

for base metal, weld metal and HAZ regions are 0.763, 0.689 and 0.735 mm respectively. Cracks were seen in cross-section of oxide scale of weld metal whereas in case of HAZ the oxide scale was debonding at the oxide/metal interface

5.2.3.5 SEM/EDAX Analysis

5.2.3.5.1 Surface Morphology

SEM micrograph of the scale formed after 50 cycles of oxidation in air at 900 °C for weld metal indicates a scale containing distorted grains. EDAX analysis indicates the formation of mainly iron oxide along with MnO (5.17%) point 2. whereas at the inner scale has higher concentration of MnO (10.30%), SiO₂ (1.24%) with main scale Fe₂O₃ (87.42%) point 1 in Fig. 5.36 (a).

In case of HAZ SEM micrograph it can be inferred that more oxidation was seen along the grain boundary of coarse grain. EDAX analysis reveals that the scale consist of Fe₂O₃ (96.96%) and MnO (2.45%) at point 1. The coarse grain indicates the presence of Fe₂O₃ with little amount of MnO (1.50%) point 2 in micrograph of Fig. 5.36 (b).

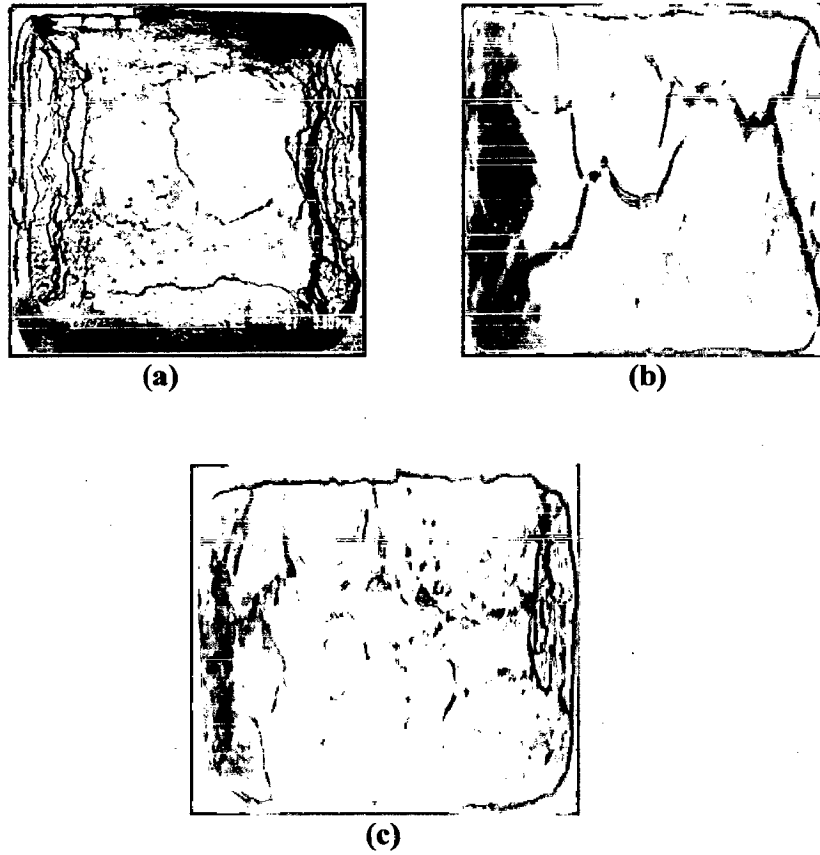


Fig. 5.31: Macrographs of different regions of SMAW weldment in T22 steel subjected to cyclic oxidation in air at 900 °C for 50 cycles (a) Base Metal, (b) Weld Metal and (c) HAZ.

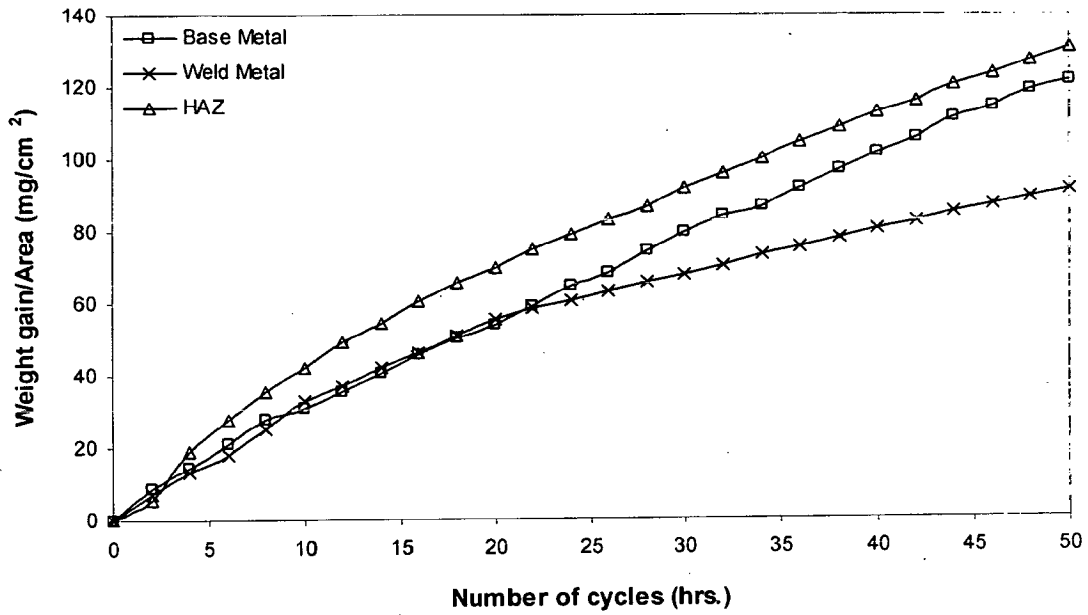


Fig. 5.32: Weight gain plot for different regions of SMAW weldment in T22 steel exposed to air at 900 °C for 50 cycles.

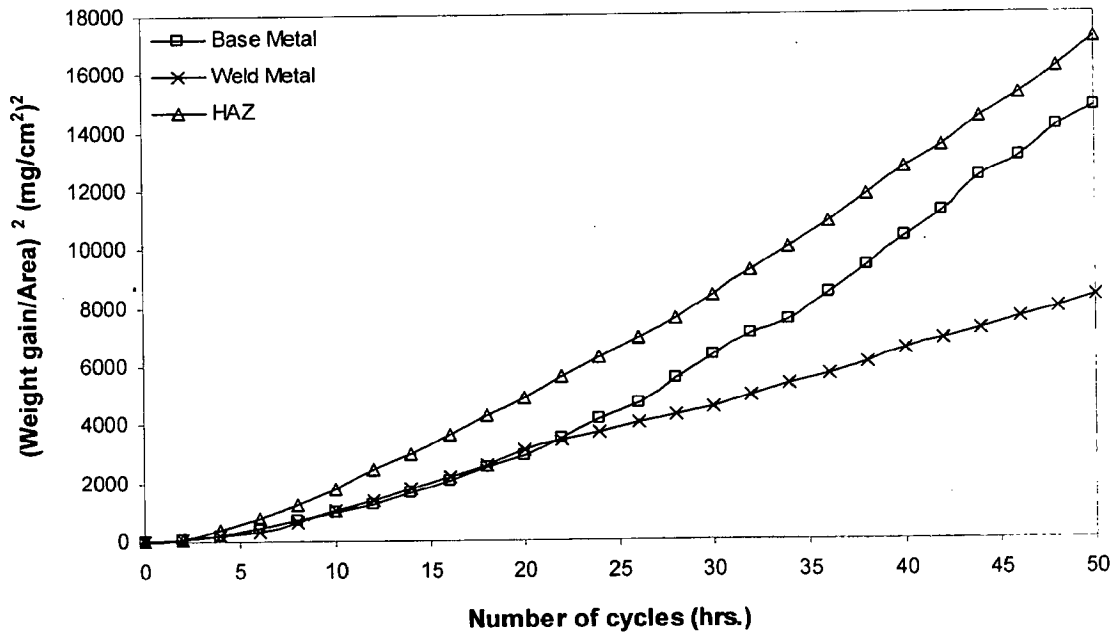


Fig. 5.33: Weight gain square (mg²/cm⁴) plot for different regions of SMAW weldment in T22 steel exposed to air at 900 °C for 50 cycles.

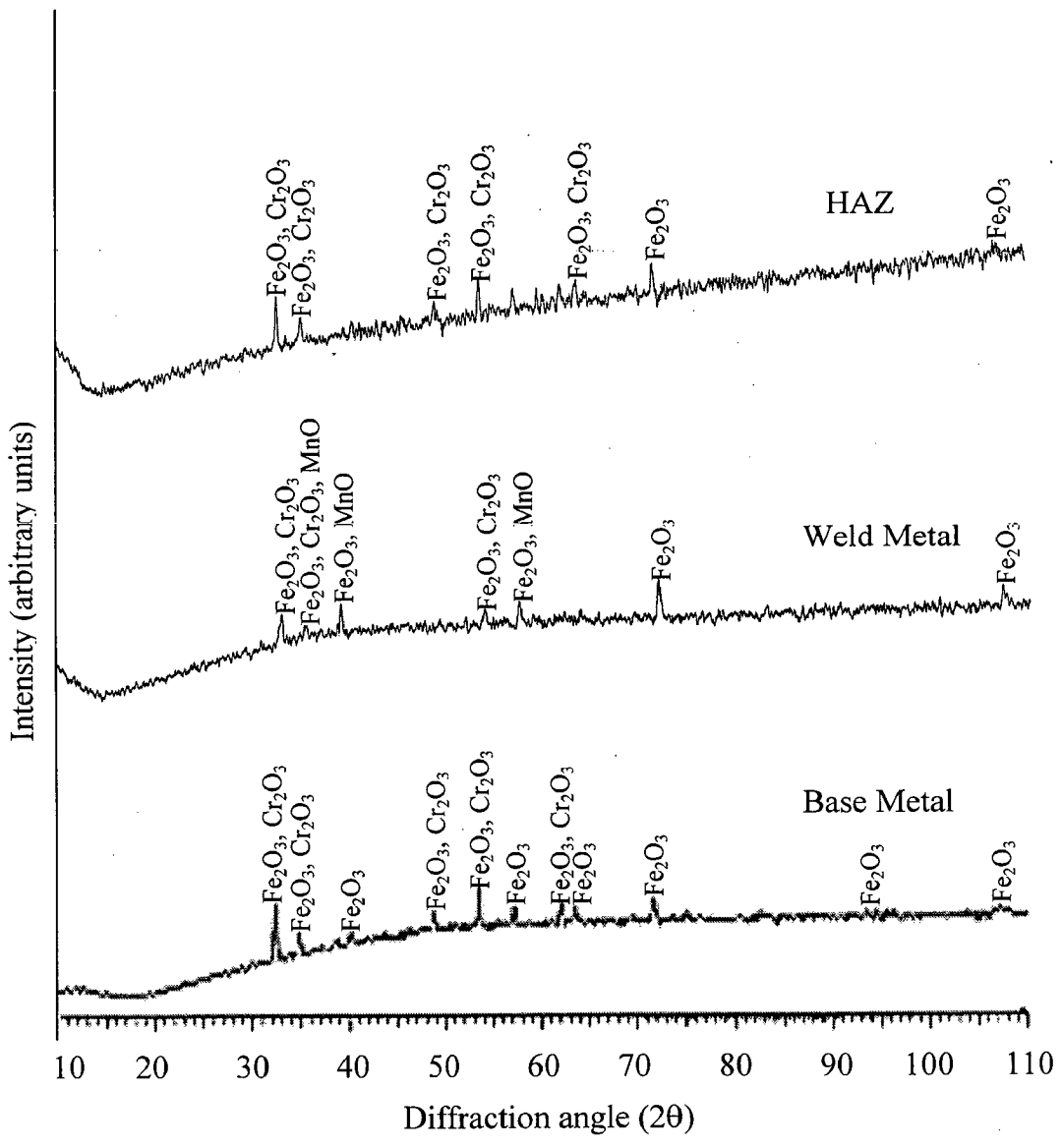
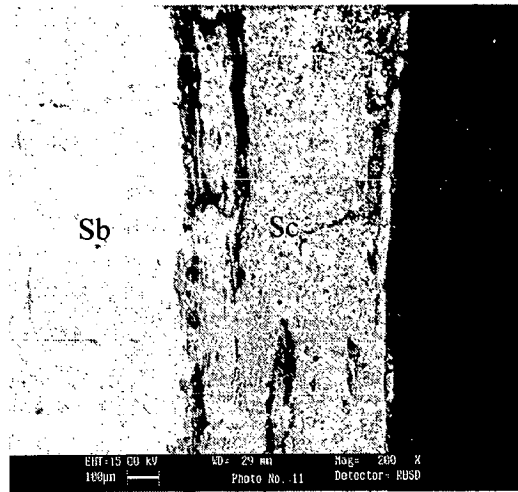
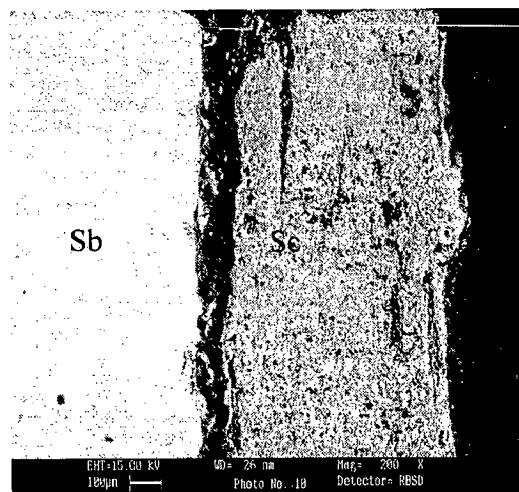


Fig. 5.34: X-ray diffraction profiles for different regions of SMAW weldment in T22 steel exposed to air at 900 °C for 50 cycles.

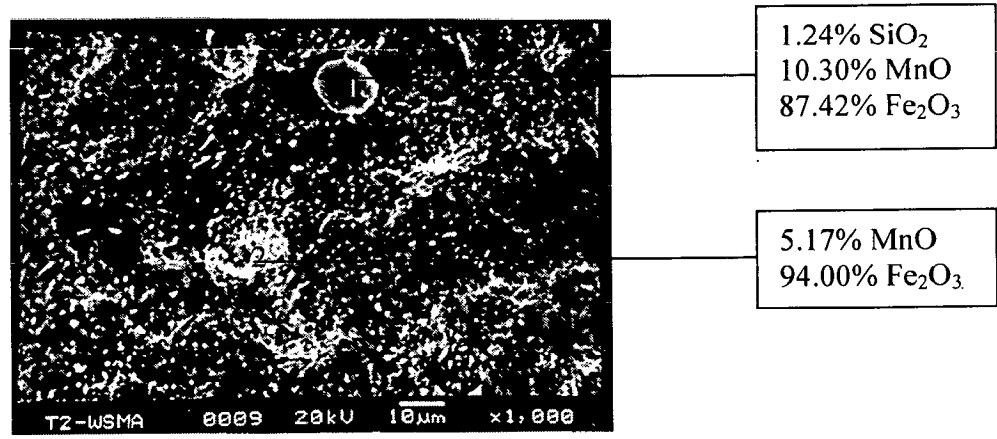


(a)

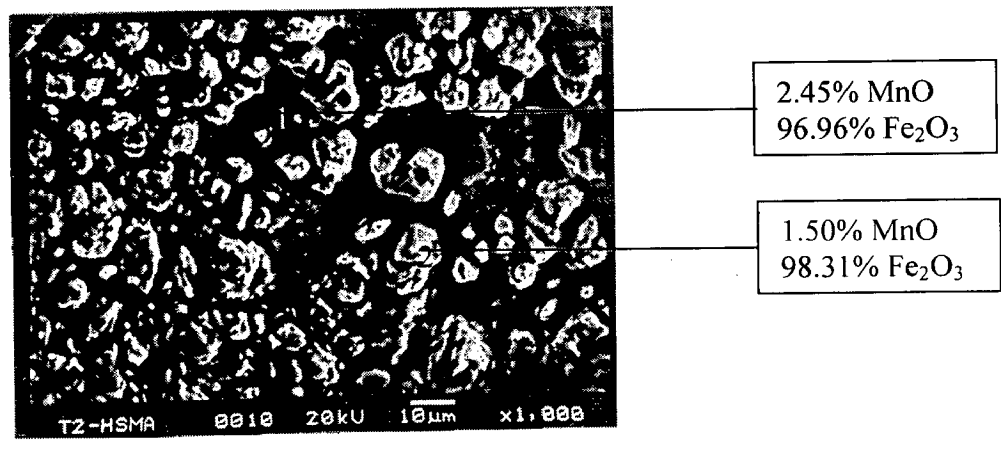


(b)

Fig. 5.35: SEM back scattered image of the cross section of different regions of SMAW weldment in T22 steel exposed to air at 900 °C for 50 cycles (a) Weld Metal, 200X (b) HAZ, 200X.



(a)



(b)

Fig. 5.36: SEM micrographs showing surface morphology and EDAX analysis for different regions of SMAW weldment in T22 steel exposed to air at 900°C for 50 cycles (a) Weld Metal, 1000X and (b) HAZ, 1000X.

5.2.4 Different Regions of TIG Weldment i. e. the Base Metal, HAZ and Weld Metal exposed to Air at 900 °C for 50 cycles in GrA1 Steel

5.2.4.1 Visual Examination

The colour of oxide scale during initial cycles for this weldment was blackish grey in weld metal. A spot of yellow colour was seen at the surface as shown in Fig. 5.37 (b). Spalling was observed during 6th cycle. No cracking was observed in the oxide scale of weld metal. In case of HAZ the colour of oxide scale was seen black. Cracks started appearing just after 6th cycle. Little spalling was observed during 10th and 23rd cycle. The scale formed on HAZ is of uniform thickness and seems to be black in colour.

5.2.4.2 Thermogravimetric Data

The plots of cumulative weight gain (mg/cm^2) as a function of time (number of cycles) for different regions of TIG weldment in GrA1 steel at 900 °C in air upto 50 cycles are shown in Fig. 5.38. The plot for all the regions shows a large weight gain during the first few cycles followed by gradual weight gain. The amount of the spalled scale has also been incorporated in weight gain measurements. The total weight gain at the end of 50 cycles for base metal, weld metal and HAZ is 135.275, 139.797 and 145.053 mg/cm^2 respectively. The (weight gain/unit area)² plot against number of cycles Fig. 5.39 further confirms that parabolic law is followed by all the three regions. The values of parabolic rate constant, K_p ($10^{-8} \text{ g}^2 \text{ cm}^{-4} \text{ s}^{-1}$) are 10.282, 10.927 and 11.656 for base metal, weld metal and HAZ regions respectively.

5.2.4.3 X-ray Diffraction Analysis

The XRD analysis for different regions of TIG weldment in GrA1 steel after exposure to air at 900 °C for 50 cycles is shown in Fig. 5.40 and these diffractograms reveals similar phases for all the regions. As obvious from the composition all the regions have indicated the formation of iron oxide (Fe_2O_3). Where as strong peaks of Fe_2O_3 are indicated in the oxide scale of base metal.

5.2.4.4 Scale Thickness Measurement

The scale thickness was measured from SEM back scattered images for different regions of TIG weldment in GrA1 steel as shown in Fig. 5.41. Very thick oxide scale was identified in case of HAZ and was around 1.68 times more than the scale thickness measured for weld metal. The scale thickness values are 1.1, 0.812 and 1.37 mm for base metal, weld metal and HAZ respectively.

5.2.4.5 SEM/EDAX Analysis

5.2.4.5.1 Surface Morphology

SEM micrograph of the scale formed after 50 cycles of oxidation in air at 900°C for different regions of TIG weldment in GrA1 steel indicates a scale containing distorted grains. EDAX analysis indicates the formation of mainly iron oxide, Fig. 5.42 (a). The micrograph of top surface of the scale in case of weld metal indicates intergranular cracking. EDAX analysis shows the presence of mainly Fe₂O₃ (99.12%) at point 1, whereas it is Fe₂O₃ (99.39%) at point 2. In case of HAZ inner scale contains some amount of SiO₂ (10.52%), P₂O₅ (1.23%) along with main scale Fe₂O₃ (87.96%) point 1 in micrograph of Fig. 5.42 (b), whereas the top scale mainly consists Fe₂O₃ (98.57%) with SiO₂ (1.27%).

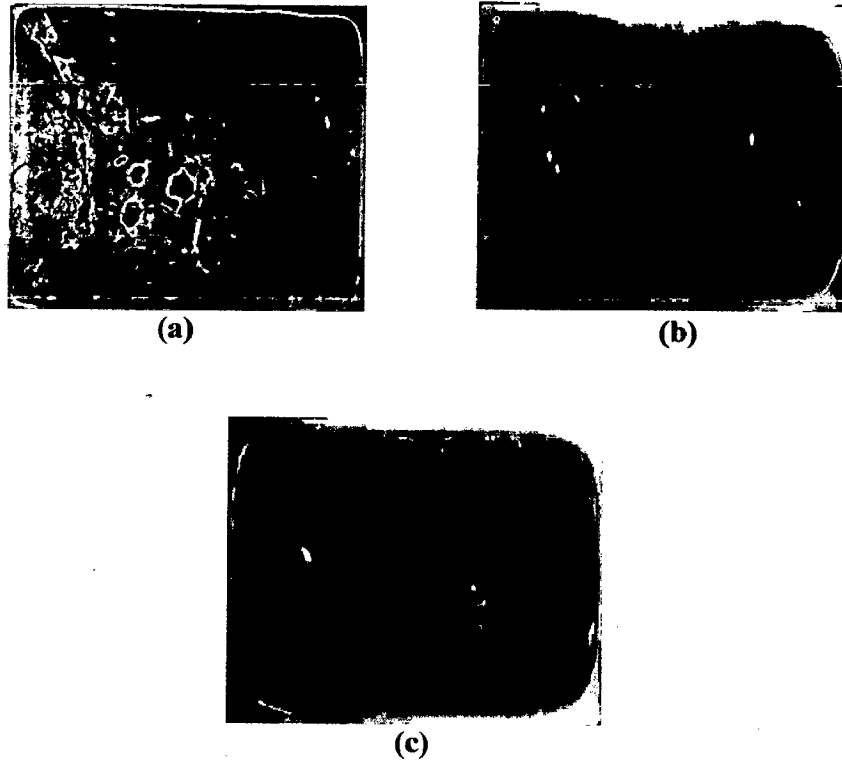


Fig. 5.37: Macrographs of different regions of TIG weldments in GrA1 steel subjected to cyclic oxidation in air at 900 °C for 50 cycles (a) Base Metal, (b) Weld Metal and (c) HAZ.

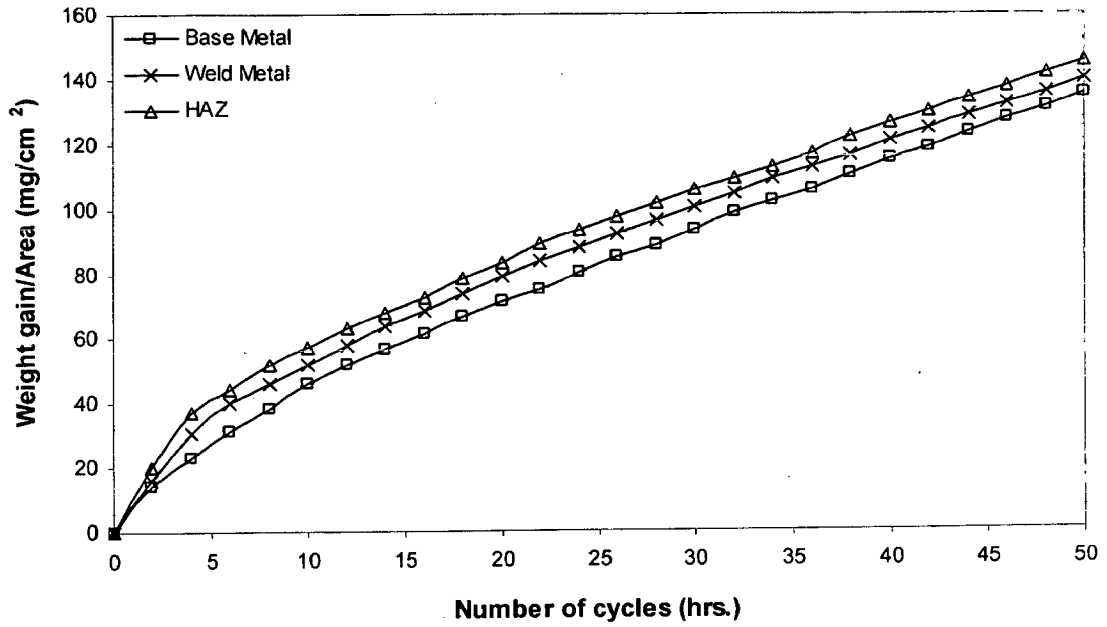


Fig. 5.38: Weight gain plot for different regions of TIG weldment in GrA1 steel exposed to air at 900 °C for 50 cycles.

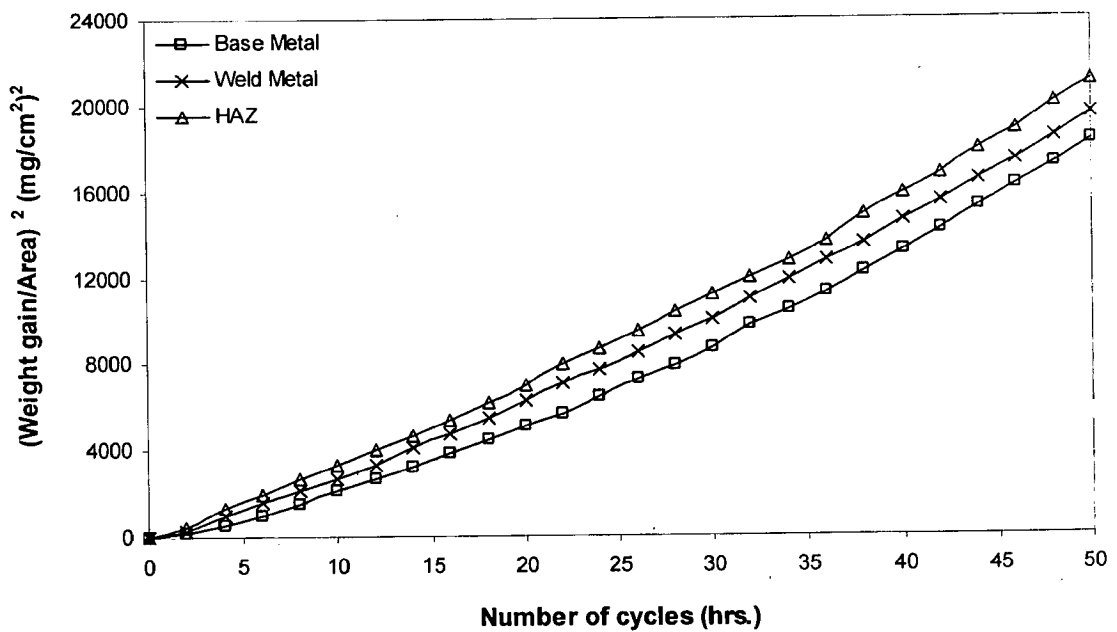


Fig. 5.39: Weight gain square (mg²/cm⁴) plot for different regions of TIG weldment in GrA1 steel exposed to air at 900 °C for 50 cycles.

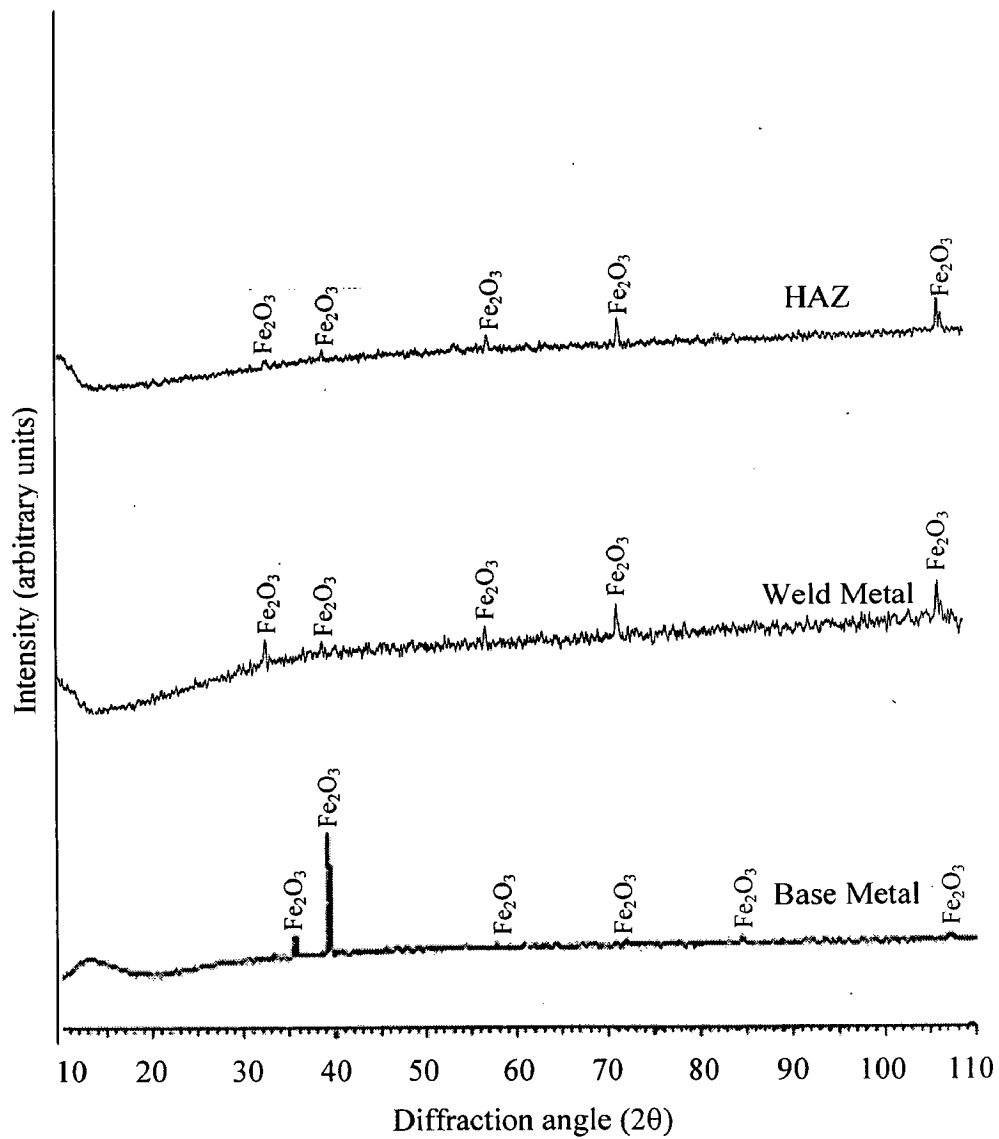
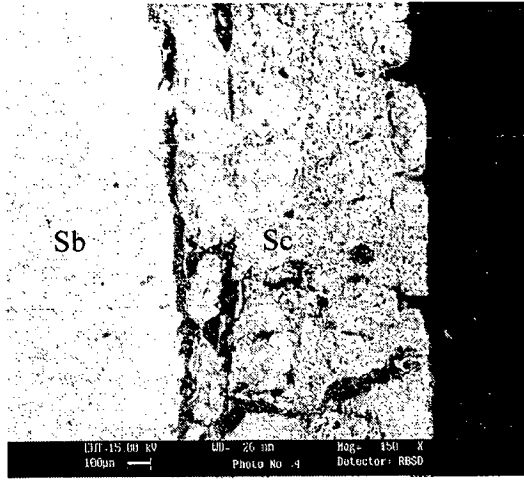
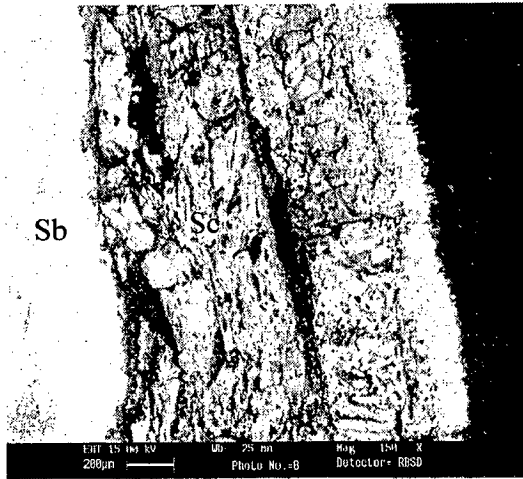


Fig. 5.40: X-ray diffraction profiles for different regions of TIG weldment in GrA1 steel exposed to air at 900 °C for 50 cycles.

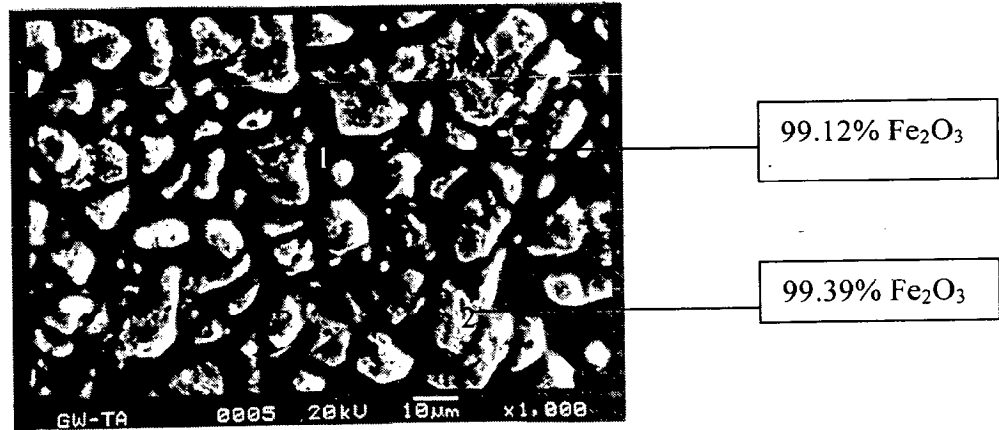


(a)

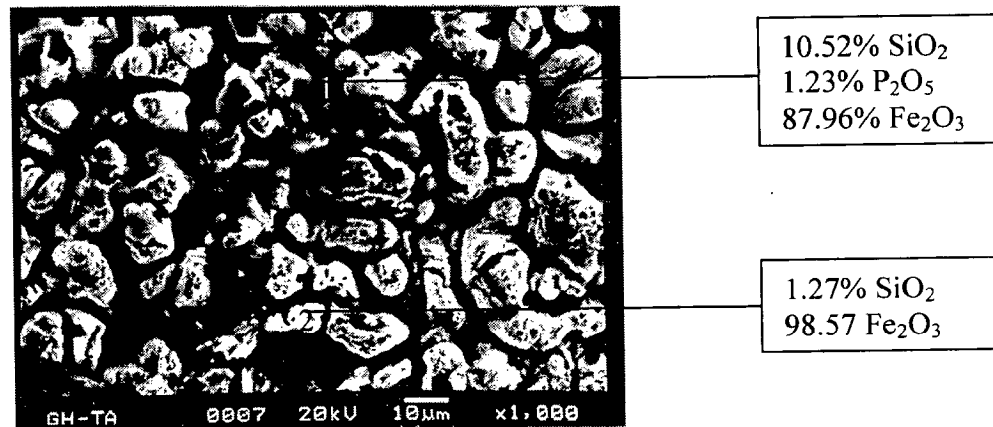


(b)

Fig. 5.41: SEM back scattered image of the cross section of different regions of TIG weldment in GrA1 steel exposed to air at 900 °C for 50 cycles (a) Weld Metal, 150X (b) HAZ, 150X.



(a)



(b)

Fig. 5.42: SEM micrographs showing the surface morphology and EDAX analysis for different regions of TIG weldment in GrA1 steel exposed to air at 900 °C for 50 cycles (a) Weld Metal, 1000X and (b) HAZ, 1000X.

5.2.5 Different Regions of TIG Weldment i. e. the Base Metal, HAZ and Weld Metal exposed to Air at 900 °C for 50 cycles in T11 Steel

5.2.5.1 Visual Examination

Macrographs for oxidized of different regions of TIG weldment in T11 steel for 50 cycles in air at 900°C are shown in Fig. 5.43. The oxide scale of opposite surface was spalled during 50th cycle while it is same as the edges for weld metal, similar condition was observed in case of HAZ specimen. Little spalling was seen during 5th cycle in blackish gray scale on weld metal. Some minute cracks are seems after 30th cycle in weld metal. In case of HAZ cracking started just after 8th cycle and little spalling was observed during 17th cycle. In the end of experiment the scale got removed from one surface of weld metal and HAZ as shown in Fig. 5.43 (b) & (c).

5.2.5.2 Thermogravimetric Data

Fig. 5.44 shows the variation of weight gain as a function of time. The cumulative weight gain for base metal is more as compared to weld metal and HAZ. The plot shows a large weight gain during first few cycles for weld metal than HAZ. The total weight gain (mg/cm^2) after exposure of 50 cycles is around 128.387, 112.845 and 121.138 for base metal, weld metal and HAZ regions respectively. The maximum resistance to the oxidation at 900°C has been provided by weld metal. The oxidation behaviour for different regions of TIG weldment in T11 steel is almost parabolic in nature as shown by Fig. 5.45. The value of parabolic rate constant, K_p ($10^{-8} \text{ g}^2 \text{ cm}^{-4} \text{ s}^{-1}$) for these 9.384 (base metal), 6.962 (weld metal) and 8.323 (HAZ).

5.2.5.3 X-ray Diffraction Analysis

The XRD analysis for base metal, weld metal and HAZ regions after exposure to air at 900°C for 50 cycles is shown in Fig. 5.46 and these diffractograms has almost similar phases for all the regions. As obvious from the composition all the regions have indicated the formation of iron oxide (Fe_2O_3). Where as some peaks of Cr_2O_3 , Fe_3O_4 along with Fe_2O_3 are indicated in the oxide scale of HAZ. In case of weld metal Fe_3O_4 with Fe_2O_3 are indicated.

5.2.5.4 Scale Thickness Measurement

The oxide scale thickness for different regions of TIG weldment in T11 steel was measured from the BSEI shown in Fig. 5.47 after oxidation in air for 50 cycles at 900°C. Although the weld metal has indicated a thick scale formation. The scale was debonding at the oxide /metal interface in case of weld metal and HAZ. More cracks were observed along the cross-section of oxide scale of HAZ. The average values of oxide scale thickness in base metal, weld metal and HAZ regions are 1.289, 1.334 and 1.05 mm respectively.

5.2.5.5 SEM/EDAX Analysis

5.2.5.5.1 Surface Morphology

SEM micrograph of the scale formed after 50 cycles of oxidation in air at 900°C for weld metal indicates a scale containing distorted grains. EDAX analysis indicates the formation of top scale mainly iron oxide with MnO (2.44%), whereas the spalled area contains SiO₂ (9.49%), P₂O₅ (1.21%), MnO (2.80%) with main phase Fe₂O₃ (85.64%) point 1 Fig. 5.48 (a). The EDAX analysis of top surface of the scale in case of HAZ indicates mainly Fe₂O₃ (99.54%) at point 2, whereas inner scale shows the presence of little amount of SiO₂ (1.06%) with Fe₂O₃ (98.23%) in the scale at the point 1 in micrograph of Fig. 5.48 (b).

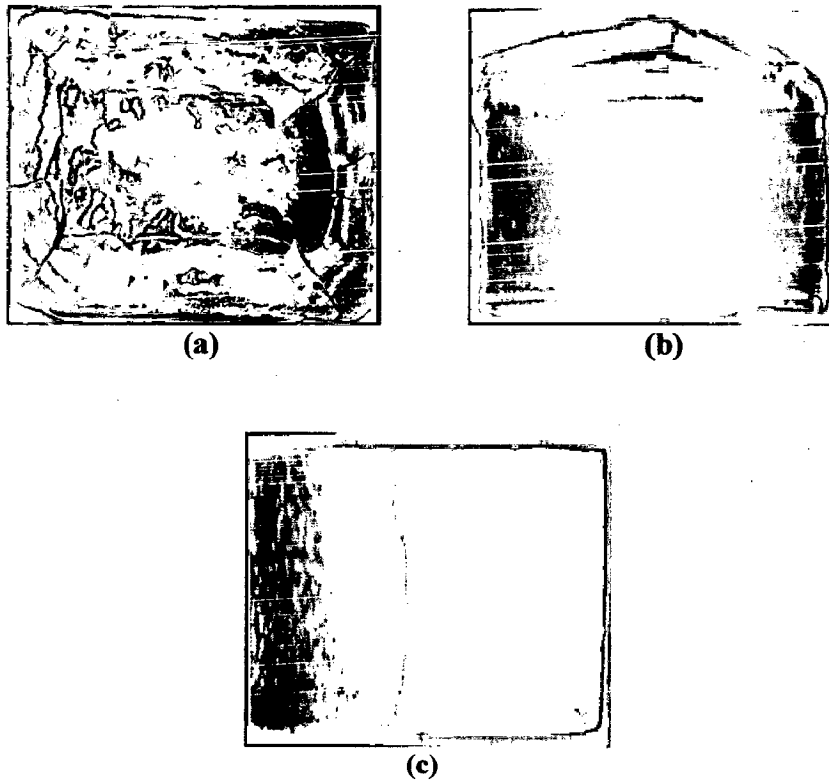


Fig. 5.43: Macrographs of different regions of TIG weldments in T11 steel subjected to cyclic oxidation in air at 900 °C for 50 cycles (a) Base Metal, (b) Weld Metal and (c) HAZ.

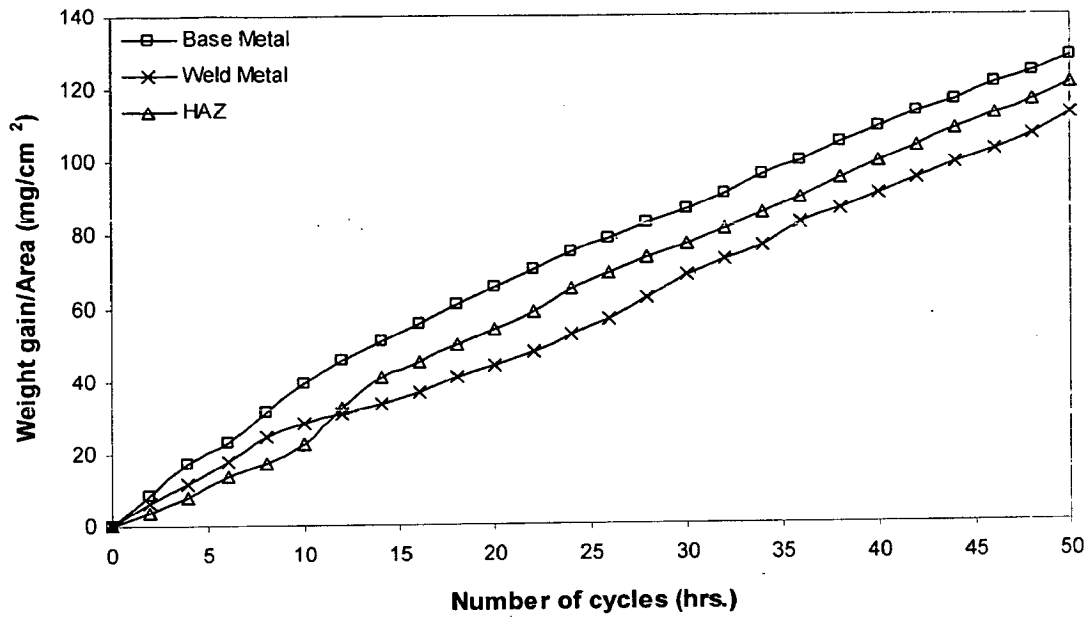


Fig. 5.44: Weight gain plot for different regions of TIG weldment in T11 steel exposed to air at 900 °C for 50 cycles.

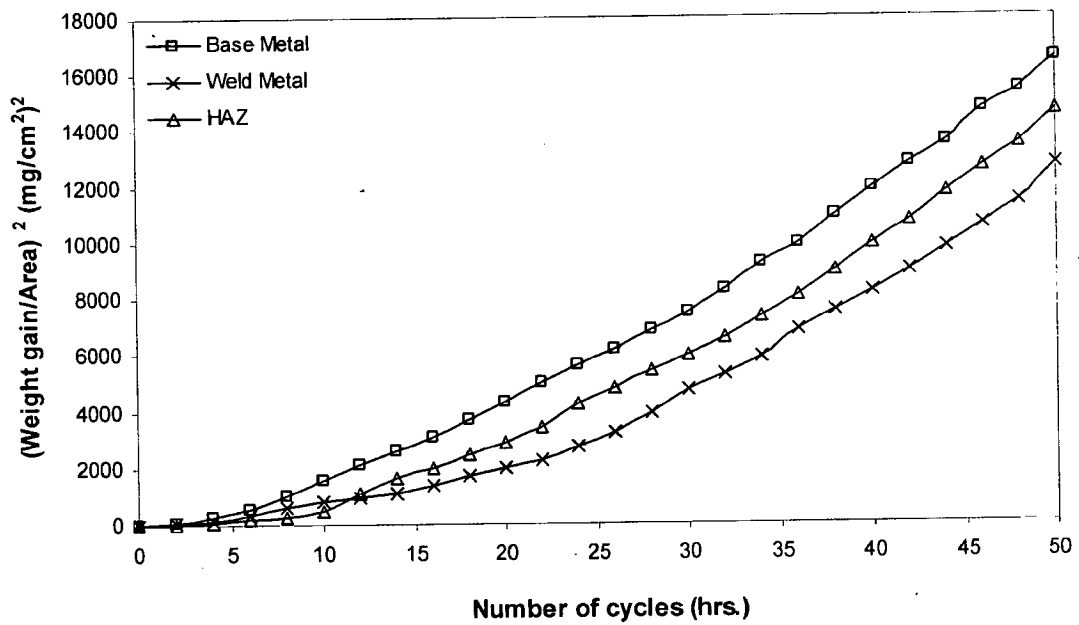


Fig. 5.45: Weight gain square (mg²/cm⁴) plot for different regions of TIG weldment in T11 steel exposed to air at 900 °C for 50 cycles.

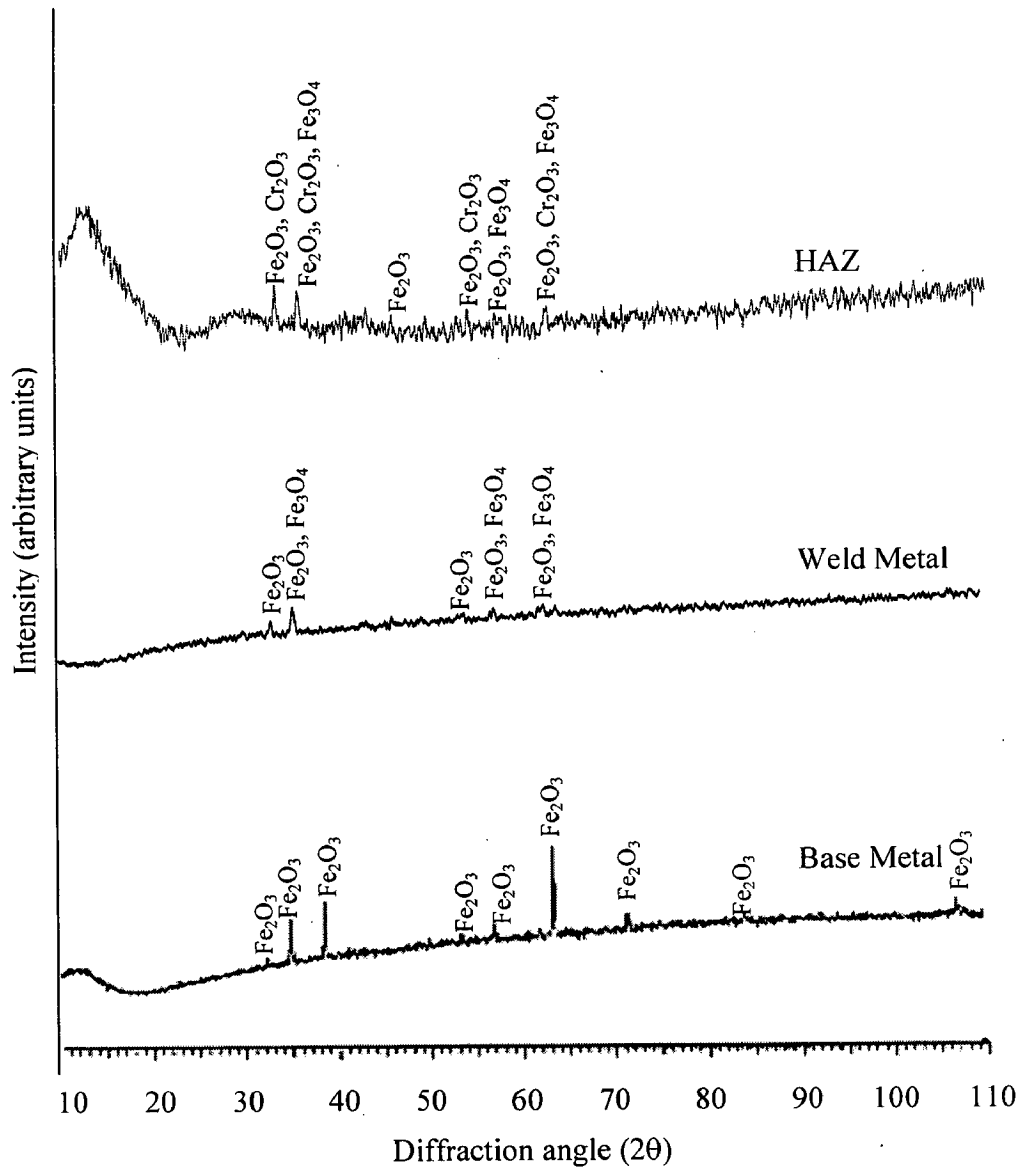
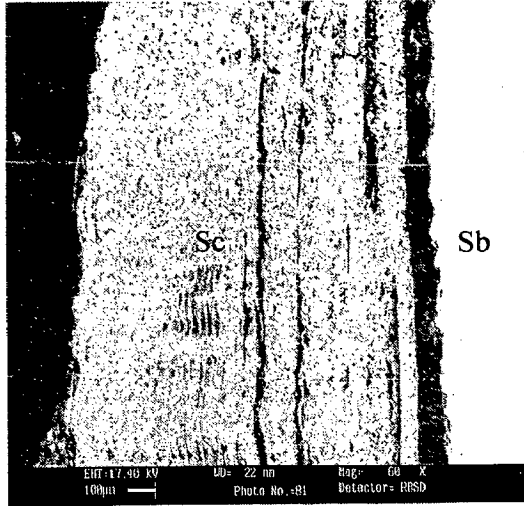
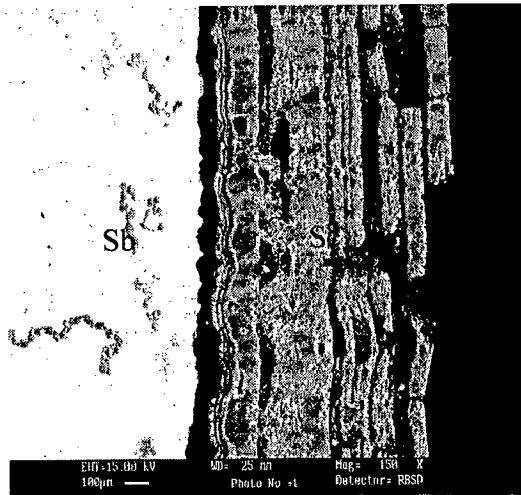


Fig. 5.46: X-ray diffraction profiles for different regions of TIG weldment in T11 steel exposed to air at 900 °C for 50 cycles.

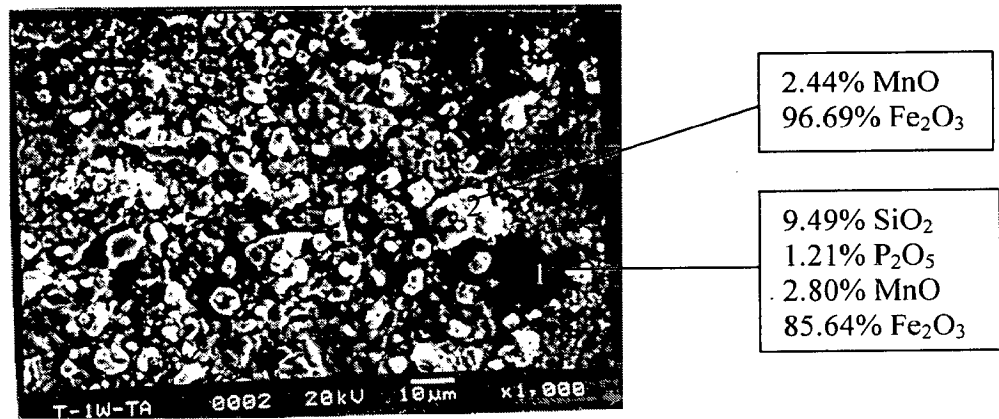


(a)

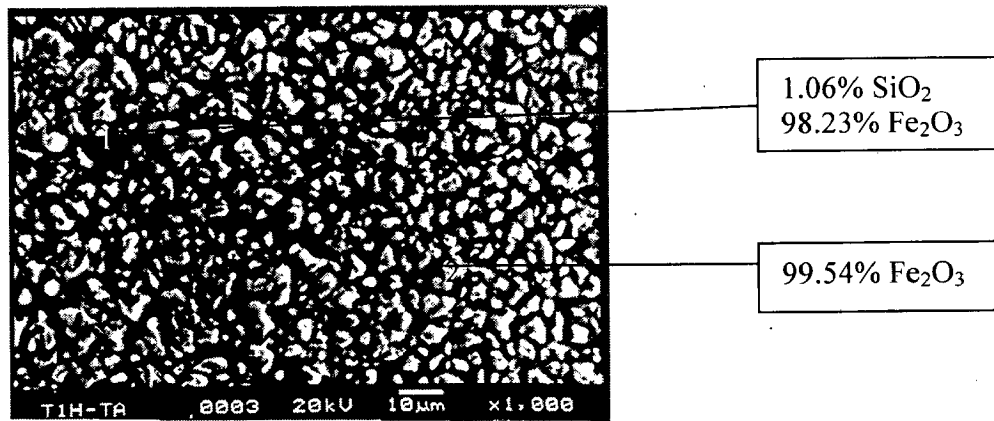


(b)

Fig. 5.47: SEM back scattered image of cross section of the different regions of TIG weldment in T11 steel exposed to air at 900 °C for 50 cycles (a) Weld Metal, 60X (b) HAZ, 150X.



(a)



(b)

Fig. 5.48: SEM micrographs showing surface morphology and EDAX analysis for different regions of TIG weldment in T11 steel exposed to air at 900 °C for 50 cycles (a) Weld Metal, 1000X and (b) HAZ, 1000X.

5.2.6 Different Regions of TIG Weldment i. e. the Base metal, HAZ and Weld Metal exposed to Air at 900 °C for 50 cycles in T22 Steel

5.2.6.1 Visual Examination

The colour of oxide scale during initial cycles oxidation for different regions of TIG weldment in T22 steel was blackish grey and turned light blackish brown after subsequent cycles. The macrographs after cyclic oxidation for 50 cycles at 900°C for different regions are as shown in Fig. 5.49. For the weld metal the cracks in the oxide scale had started appearing during 30th cycle and spalling observed just after 32nd cycle. In case of HAZ specimen, the cracking and spalling appeared during 8th and 17th cycle respectively. Oxide scale had dull appearance and spalled at edges of weld metal. More cracks were seen on the surface of oxide scale of HAZ as compared to that on the weld metal.

5.2.6.2 Thermogravimetric Data

The plots of cumulative weight gain (mg/cm^2) as a function of time (number of cycles) for different regions of TIG weldment in T22 steel at 900°C in air upto 50 cycles are shown in Fig. 5.50. Extensive spalling and sputtering has limited the study upto 50 cycles. The plot for all the steels shows same weight gain upto the 8th cycles followed by gradual weight gain. The amount of the spalled scale has also been incorporated in weight gain measurements. The total weight gain at the end of 50 cycles for base metal, weld metal and HAZ regions is 121.61, 175.021 and 185.402 mg/cm^2 respectively. The $(\text{weight gain}/\text{unit area})^2$ plot against number of cycles Fig. 5.51 further confirms that parabolic law is slightly changed for weld metal and HAZ regions. The values of parabolic rate constant, K_p ($10^{-8} \text{ g}^2 \text{ cm}^4 \text{ s}^{-1}$) are 8.515, 17.107 (upto 37th cycles) and 19.752 (40th cycles) for base metal, weld metal and HAZ respectively.

5.2.6.3 X-ray Diffraction Analysis

The XRD analysis for different regions of TIG weldment in T22 steel after exposure to air at 900°C for 50 cycles is shown in Fig. 5.52 and these diffractograms has almost similar phases of iron oxide (Fe_2O_3) with Cr_2O_3 for all the three regions. Where as weak peaks of Fe_3O_4 , Cr_2O_3 along with Fe_2O_3 are indicated in the oxide scale of HAZ.

5.2.6.4 Scale Thickness Measurement

The scale thickness was measured from SEM back scattered images as shown in Fig. 5.53. A little thicker oxide scale was identified in case of HAZ and was around 1.09 times more than the scale thickness measured for base metal. The scale thickness values are 0.763, 0.8 and 0.831mm for the base metal, weld metal and HAZ respectively. In case of weld metal the scale debonding was observed at the oxide/metal interface. Cracks across the scale formed on the weld metal.

5.2.6.5 SEM/EDAX Analysis

5.2.6.5.1 Surface Morphology

SEM micrograph of the scale formed after 50 cycles of oxidation in air 900°C for different regions of TIG weldment in T22 steel is shown in Fig. 5.54. EDAX analysis of oxide weld metal indicates the top scale mainly consists of Fe₂O₃ (93.81%) along with Cr₂O₃ (4.48%) and MnO (1.45%) point 2, whereas the inner scale contains SiO₂ (7.12%), Cr₂O₃ (3.38%) and MnO (2.14%) along with main oxide Fe₂O₃ (87.36%) point 1 Fig 5.54 (a). SEM micrograph of HAZ indicates coarse grains. The HAZ EDAX analysis indicates the top scale mainly consists of iron oxide (97.88%). The cracks in the scale contained Fe₂O₃ (89.09%) and MnO (9.28%) as shown in Fig. 5.54 (b).

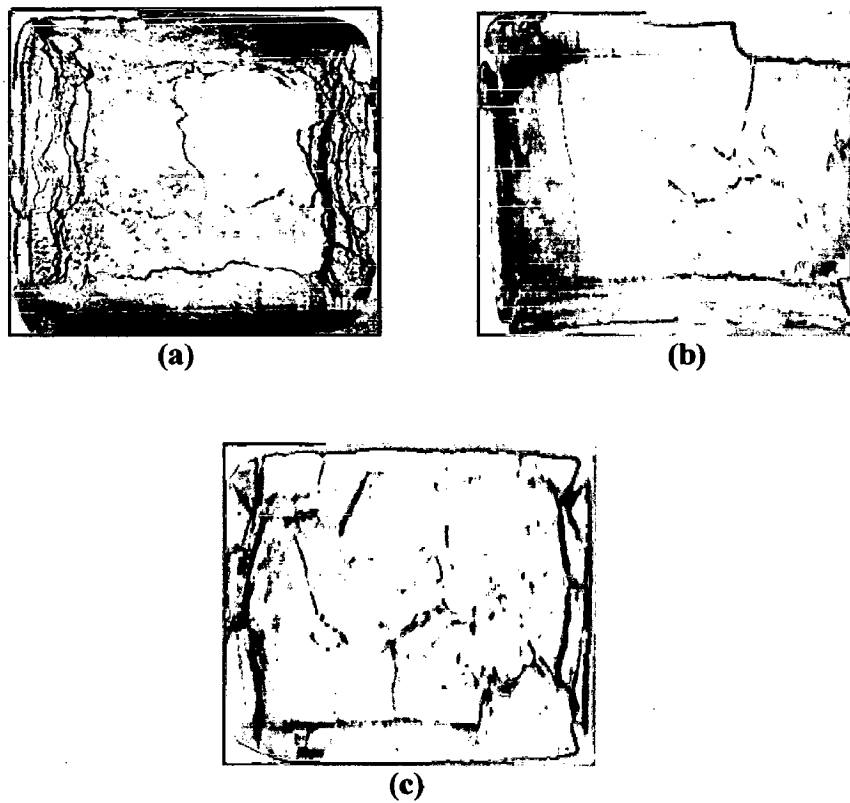


Fig. 5.49: Macrographs of different regions of TIG weldments in T22 steel subjected to cyclic oxidation in air at 900 °C for 50 cycles (a) Base Metal, (b) Weld Metal and (c) HAZ.

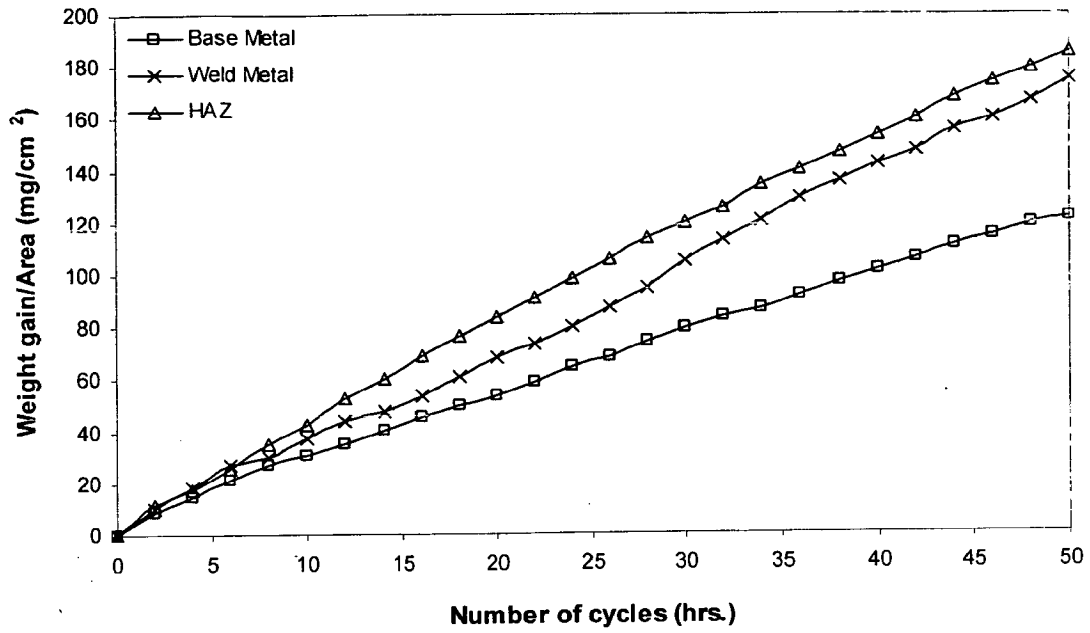


Fig. 5.50: Weight gain plot for different regions of TIG weldment in T22 steel exposed to air at 900 °C for 50 cycles.

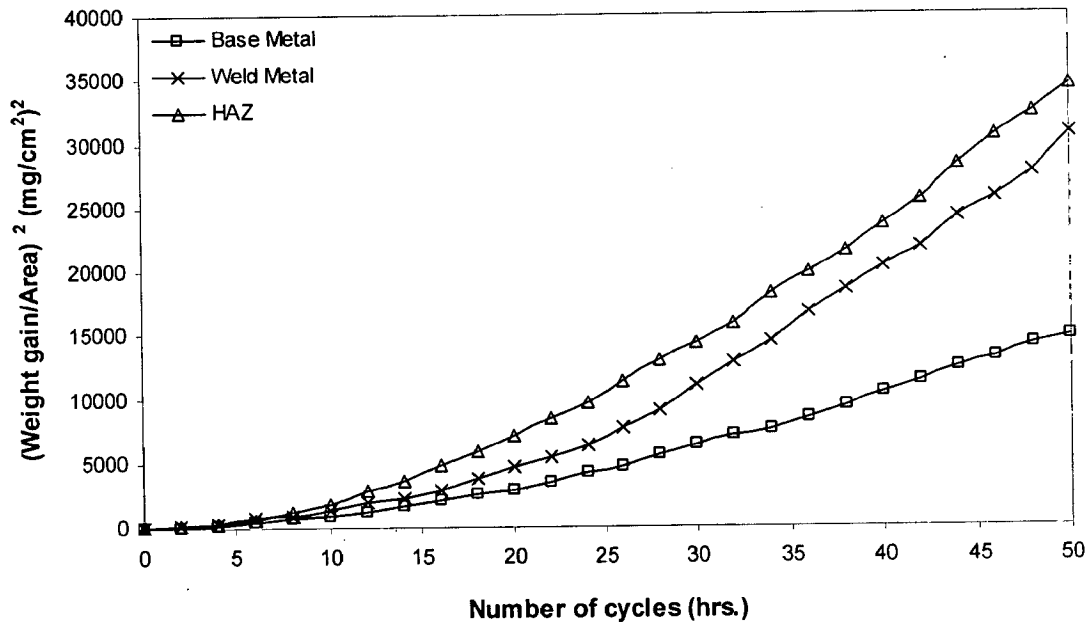


Fig. 5.51: Weight gain square (mg²/cm⁴) plot for different regions of TIG weldment in T22 steel exposed to air at 900 °C for 50 cycles.

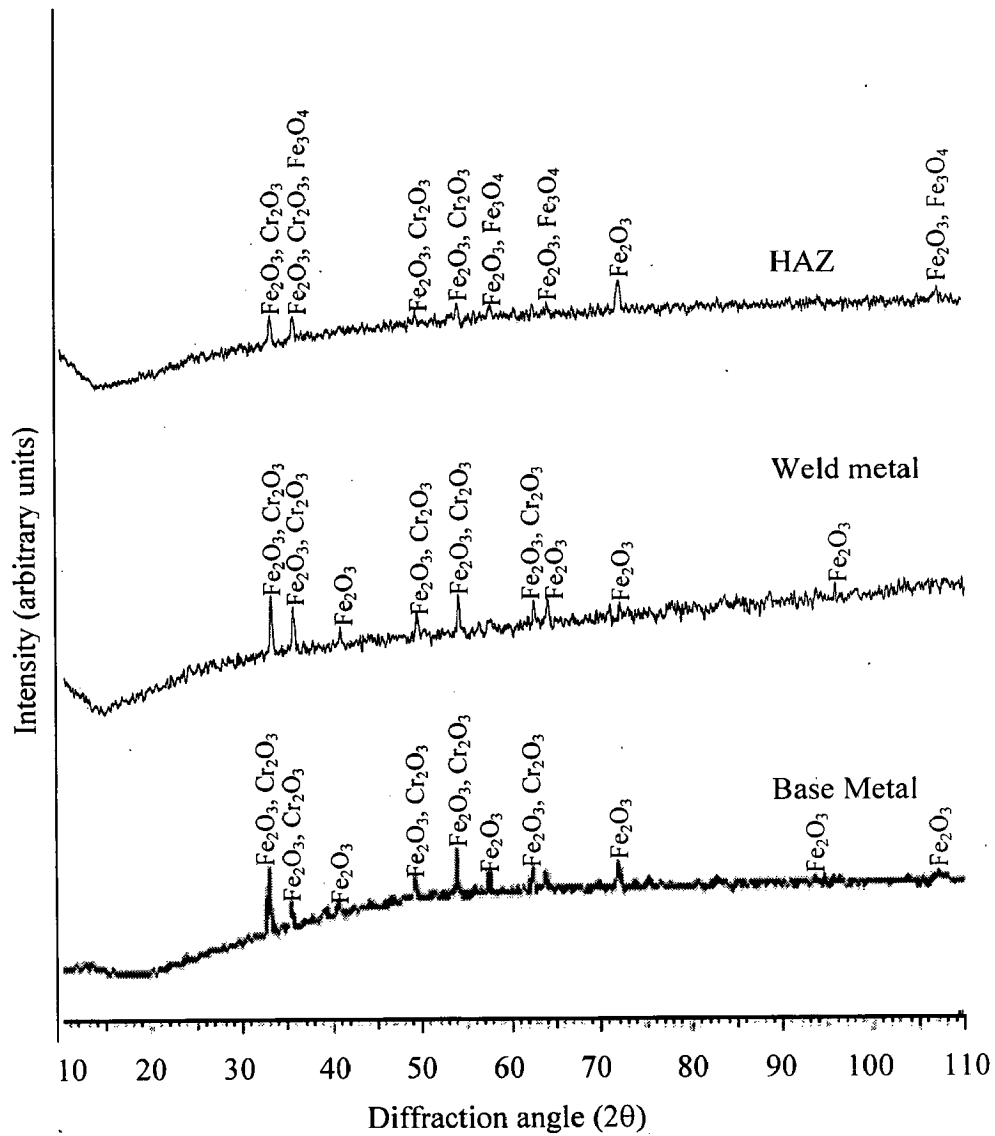
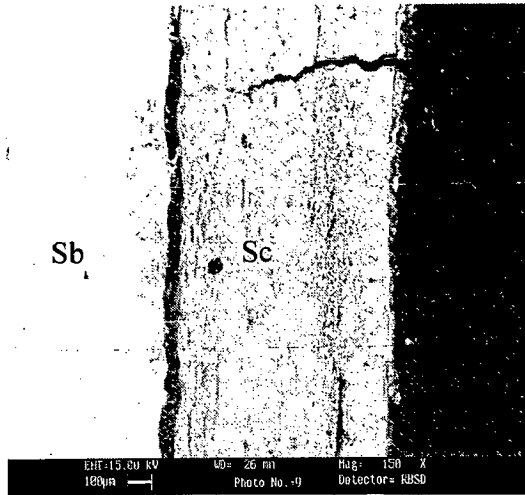
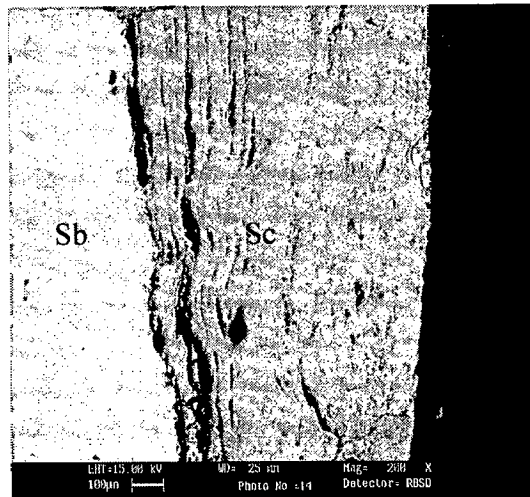


Fig. 5.52: X-ray diffraction profiles for different regions of TIG weldment in T22 steel exposed to air at 900 °C for 50 cycles.

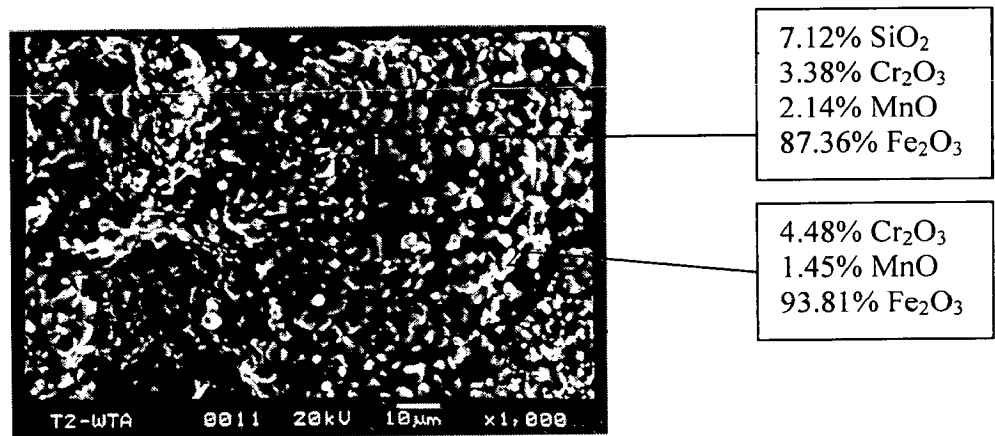


(a)

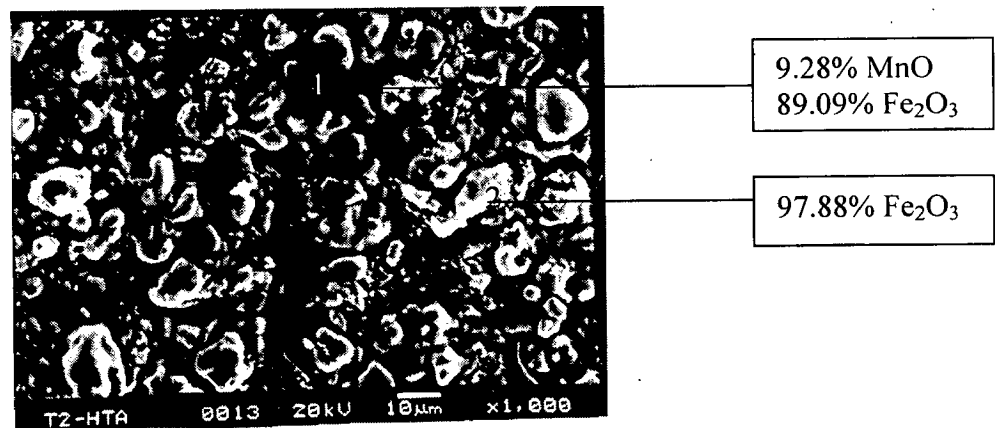


(b)

Fig. 5.53: SEM back scattered image of cross section of different regions of TIG weldment in T22 steel exposed to air at 900 °C for 50 cycles (a) Weld Metal, 150X (b) HAZ, 200X.



(a)



(b)

Fig.5.54: SEM micrographs showing surface morphology and EDAX analysis for different regions of TIG weldment in T22 steel exposed to air at 900 °C for 50 cycles (a) Weld Metal, 1000X and (b) HAZ, 1000X.

5.3 SUMMARY OF RESULTS

The results of oxidation studies in air for weldments, different regions of weldment and unwelded steels are summarized in Table 5.1 to understand the comparative behaviour of weldment and different regions of weldment in steels.

Table 5.1: Summary of the results for weldments, different regions of weldments and unwelded steels oxidized in air at 900 °C for 50 cycles.

Base steel	Weldment	Scale thickness (mm)	Weight gain mg/cm ²	K _p (10 ⁻⁸ g ² cm ⁻⁴ s ⁻¹)	XRD analysis	Remarks
GrA1	Base Metal	1.1	135.275	10.282	Fe ₂ O ₃	Spalling is indicated. Scale cracked during 25 th cycle.
	SMAW weldment	1.110 (weld) 1.196 (HAZ)	185.354	20.365	Fe ₂ O ₃	Weld regions appeared shining black during fist few cycles. Little cracks appeared after 27 th cycle.
	TIG weldment	0.704 (weld) 0.843 (HAZ)	152.480	13.074	Fe ₂ O ₃	Colour of oxide scale appeared black after 34 th cycle. Cracks appeared during 30 th Cycle.
	Weld metal (SMAW)	0.866	97.720	5.558	Fe ₂ O ₃	Colour of oxide scale scale dark blackish blue. No crack appeared. Oxide protrusion appeared last five cycle.
	HAZ (SMAW)	0.822	74.760	3.102	Fe ₂ O ₃	Spalling indicated during 14 th cycle. Cracks appeared during 33 rd cycle in the middle of surface. Oxide protrusions appeared in this cycle.
	Weld metal (TIG)	0.812	139.797	10.927	Fe ₂ O ₃	Blackish blue spot seems on surface. Spalling appeared during 6 th cycle. No cracks appeared.
	HAZ (TIG)	1.370	145.053	11.656	Fe ₂ O ₃	Oxide scale appeared black. Little spalling appeared during 23 rd cycle. Cracks appeared after 6 th cycle.
T11	Base Metal	1.289	128.387	9.384	Fe ₂ O ₃	Spalling indicated. Scale is lustrous.
	SMAW weldment	1.250 (weld) 1.373 (HAZ)	123.582	8.832	Fe ₂ O ₃ and MnO	Cracks appeared during 36 th Cycle. Spalling indicated.
	TIG weldment	1.080 (weld) 0.795 (HAZ)	121.170	8.348	Fe ₂ O ₃ and Cr ₂ O ₃	Weld region appeared black during 1 st cycle. Cracks appeared during 26 th Cycle.
	Weld metal (SMAW)	0.618	67.792	2.469	Fe ₂ O ₃ Fe ₃ O ₄	Cracks appeared during 25 th Cycle. Spalling indicated.

	HAZ (SMAW)	0.726	78.701	3.344	Fe ₂ O ₃	Colour of oxide scale appeared black in colour. Spalling indicated. No Cracks appeared.
	Weld metal (TIG)	1.334	112.845	6.962	Fe ₂ O ₃ and Fe ₃ O ₄	Intense spalling indicated at one surface: Cracks appeared during 30 th cycle.
	HAZ (TIG)	1.050	121.138	8.323	Fe ₂ O ₃ , Cr ₂ O ₃ and Fe ₃ O ₄	Intense Spalling indicated at one surface. Cracks appeared during 8 th cycle.
T22	Base Metal	0.763	121.610	8.515	Fe ₂ O ₃ , Cr ₂ O ₃	Intense spalling and sputtering indicated just after 4 th cycle. Scale is fragile.
	SMAW weldment	1.333 (weld) 1.386 (HAZ)	248.157	36.447	Fe ₂ O ₃ and Cr ₂ O ₃	Spalling indicated. Cracks appeared after 4 th cycle. Oxide scale appeared dull.
	TIG weldment	1.095 (weld) 0.940 (HAZ)	160.839	20.371 The behavior was parabolic from 22 nd to 50 th cycle)	Fe ₂ O ₃ , Cr ₂ O ₃ and Fe ₃ O ₄	Weld region appeared shining black during 6 th cycle. More cracks indicated. Oxide protrusion appeared. Scale was fragile and indicated some spalling.
	Weld metal (SMAW)	0.689	91.231	4.859	Fe ₂ O ₃ and Cr ₂ O ₃	Blackish brown colour seems during 14 th cycle. Cracking and spalling after 30 th cycle.
	HAZ (SMAW)	0.735	130.881	9.826	Fe ₂ O ₃ and Cr ₂ O ₃	Cracks and spalling appeared during 10 th cycle. Oxide scale appeared dull and lustrous blackish gray.
	Weld metal (TIG)	0.8	175.021	17.107 (The behavior was not parabolic from 38 th to 50 th cycle)	Fe ₂ O ₃ and Cr ₂ O ₃	Spalling indicated after 32 nd Cycle. Cracks appeared during 30 th Cycle. Dull appearance of oxide scale at edges.
	HAZ (TIG)	0.831	185.401	19.752 Upto 40 th cycle	Fe ₂ O ₃ and Cr ₂ O ₃	Cracks appeared during 8 th cycle. Spalling indicated during 17 th cycle.

5.4 DISCUSSION

5.4.1 Unwelded Steels

The oxidation resistance in air is slightly more for T11 and T22 type of steel as compared to GrA1 steel. The three types of boiler steels almost follow parabolic oxidation rate law. The XRD analysis has revealed mainly the presence Fe_2O_3 in the scale of all the three steels along with weak peaks of Cr_2O_3 in the scale of T22 steel. However the presence of chromium oxide as revealed by the surface scale XRD analysis for T22 steel may perhaps be due to spalling of top Fe_2O_3 layer of the scale. Fe_2O_3 formation has also been reported by Lai (1990), where he has observed upper layer of Fe_2O_3 for iron-chromium alloys. Author has further reported that alloys having 2% chromium could only form the oxides of chromium along with iron oxide in the innermost layer. Similar findings are revealed by the EDAX analysis in the present study also where presence of chromium in the scale has been indicated for T22 type of boiler steels, Fig. 5.6 (c). Presence of only iron oxide in the scale of GrA1 steel has further been confirmed by EDAX. EDAX analysis confirmed the upper scale of Fe_2O_3 with small amount of MnO for T11, whereas for T22 steels which is followed by subscale where Fe_2O_3 and Cr_2O_3 are coexisting. This can be attributed to depletion of iron from substrate to form oxides in the upper scale thereby leaving behind chromium rich pockets which further get oxidized to form oxides of chromium in the inner scale. This is supported by the findings Sidhu (2003A).

The minimum weight gain values for T11 and T22 steels as compared to GrA1 steel may be attributed to the presence of chromium up to 0.91% for T11 and 2.64% for T22 steels and similar to the findings of Lai (1990) who observed significant increase in the oxidation resistance for 0.5% Mo containing steels by increasing chromium from 1 to 9%. The spalling as observed in case of T11 and T22 steel may also be contributed by the presence of molybdenum in the steels. Chatterjee et al (2001) have suggested that during initial oxidation Fe is oxidized and the oxide scale is protective in nature. With progress of oxidation Mo becomes enriched at the alloy interface, leading to the formation of an inner layer of molten MoO_3 (m. p. 795°C) which penetrates along the alloy-scale interface. This liquid oxide disrupts and dissolves the protective oxide scale, causing the alloy to suffer catastrophic oxidation (Lai, 1990). Chatterjee et al (2001) also suggested that molybdenum is less noble than the other alloying elements. MoO_3 will be reduced to a lower oxide of molybdenum or even to molybdenum. Simultaneously MoO_3 may exert dissolving action on other oxides, such as Fe_2O_3 and Cr_2O_3 and this fluxing may further get accelerated by the enthalpy of formation of Fe_2O_3 and Cr_2O_3 which tends to increase the temperature at the alloy-scale interface.

5.4.2 SMAW Weldment

The welded T11 steel has showed more resistance to oxidation in air and its weight gain values are lesser than base T11 steel. This steel weldment followed the parabolic rate law of oxidation. The value of parabolic rate constant for welded T11 steel is one fourth of that of similarly welded T22 type of steel. Whereas severe oxidation was observed in case of welded T22 steel. The sequence of oxidation rate based on weight gain per unit area values for the welded steel after 50 cycles of oxidation is:

$$T22 > GrA1 > T11$$

The oxidation resistance of welded T11 steel might be due to the oxides of iron along with MnO as indicated by the XRD analysis as well as the surface EDAX analysis. The formation of main oxide Fe_2O_3 in upper scale for SMAW weldment in 2.25Cr-1Mo (T22) steel has also been reported by Raman (1999). Fe_2O_3 might be formed due to the interdiffusion of oxygen and interaction with the metal. Internal oxidation, development of cracks and spallation has been observed for all the welded steel. Development of cracks in the oxide scale on the weldment may be attributed due to the mismatch in thermal coefficient of expansion of scale and substrate.

The phenomena of cracking of the scale of SMAW weldment may also be contributed by presence of Mo in two of the substrate steels namely T22 and T11 which contains 1.06 and 0.51% Mo respectively. Mo forms MoO_3 which has melting point of $795^{\circ}C$ at alloy scale interface as suggested by Lai (1990) and Chatterjee et al (2001) in case of substrate alloy.

5.4.3 TIG Weldment

The corrosion rate of TIG welded steels as inferred from the weight gain data given in Fig. 5.14 seems to be more than that of the unwelded steels in case of T11. Similarly total weight gain value for welded GrA1 steel after 50 cycles of oxidation at $900^{\circ}C$ is 1.125 times more than that for unwelded steel. The more weight gain is also indicated for welded T22 steel, its final weight gain value is around 1.3 times more than that for similar type of unwelded steel. The oxidation rate (total weight gain values after 50 cycles of oxidation) of TIG weldment in boiler steels followed the sequence.

$$T22 > GrA1 > T11$$

The indication of Fe_2O_3 , Cr_2O_3 , MnO and Fe_3O_4 peaks in the scale of welded steels are confirmed by the XRD analysis.

The results of XRD are in accordance with the surface EDAX analysis. In case of welded GrA1 and T11 steels the Fe_2O_3 is the main constituent, whereas top scale is richer in iron oxide.

5.4.4 Different Regions of SMAW and TIG Weldment in GrA1 Steel

From the weight gain values it can be inferred that the HAZ has shown better resistance to oxidation for the SMAW weldment. The XRD analysis revealed the mainly oxides of iron of all the regions that is also in accordance with the surface EDAX analysis. The visual observation has indicated lower extent of cracking for HAZ in case of TIG weldment as compared to SMAW weldment, whereas more cracks were noticed for base metal. The sequence of oxidation in terms of weight gain per unit area for different regions of SMAW and TIG weldment in steel is as follows:

Base metal > Weld metal > HAZ for SMAW weldment

HAZ > Weld metal > Base metal for TIG weldment

In case of SMAW weldment the more-protective inner scales which formed on both the weld metal and the HAZ, resulted in a limited inward diffusion of oxygen ions, and hence a less extensive internal oxidation. A less-protective inner scale formed in the case of the base metal, presumably permitted a greater inward diffusion of oxygen ions, thus facilitating a greater concentration of oxygen available for reaction with the iron. More rapid diffusion of oxygen ions through the base metal scale caused extensive internal oxidation and formation of a subscale zone densely populated with internal precipitates.

5.4.5 Different Regions of SMAW and TIG Weldment in T11 Steel

The XRD analysis revealed the oxides of iron Fe_2O_3 along with Fe_3O_4 . The visual observation has indicated lower extent of cracking scale in the different regions in case of TIG weldment as compared to SMAW weldment. The intense spallation of scale on weld and HAZ specimens were only noticed in the 50th cycle in case of TIG welding. The spalled material has been identified by the EDAX analysis to be mainly iron oxide along with SiO_2 and MnO as shown in Fig. 5.48 (a).

From the weight gain values it can be inferred that the weld metal has shown better resistance the oxidation. The sequence of oxidation in terms of weight gain for different region of SMAW and TIG weldment in steel is as follows:

Base metal > HAZ > weld metal for both SMAW and TIG weldments

It can be inferred from the weight gain data that corrosion rates of different regions of SMAW weldment in T11 type of steels are comparable to each other. HAZ region showed the more weight gain values than that of weld metal in both the process the reason may be carbide precipitation as indicated by higher hardness which has led to depletion of chromium thereby weakening protection against oxidation.

5.4.6 Different Regions of SMAW and TIG Weldment in T22 Steel

It can be inferred from the weight gain data that corrosion rates of different regions of SMAW weldment in T22 type of steels are comparable to each other. HAZ region showed the more weight gain values in both the process, the reason may be the absence of Cr oxide in the inner scale of HAZ.

The XRD analysis revealed the oxides of iron along with Cr_2O_3 . The visual observation has indicated lower extent of cracking in the scale of different regions of TIG weldment as compared to SMAW weldment. The material from the cracks has been identified by the EDAX analysis and found to be mainly iron oxide with MnO in the scale of HAZ (TIG) as shown in Fig. 5.54 (b).

From the weight gain values it can be inferred that the weld metal has developed better to resistance to oxidation in case of SMAW weldment. The sequence of oxidation in air in terms of weight gain for different region of SMAW and TIG weldment in steels is as follows:

HAZ > Base metal > weld metal for SMAW weldment

HAZ > weld metal > Base metal for TIG weldment

The higher oxidation rate of the HAZ and the formation of a thicker scale over it may be attributed to absence of a protective inner scale of Fe-Cr oxides, due to the non-availability of free Cr in this region Fig. 5.54 (b), as also suggested by Raman and Gnanamoorthy, 1993.

PART (A) HOT CORROSION STUDIES OF UNWELDED STEEL AND WELDMENTS IN MOLTEN SALT ENVIRONMENT

This part deals with the critical examination of corrosion products and the behaviour of unwelded steels and weldments when subjected to hot corrosion at 900°C under the thin coat of molten salt (Na_2SO_4 -60% V_2O_5). The samples were visually examined at the end of each cycle for any change in the colour, luster, adherence of scale to the substrate and spalling tendency. The weight change measurements were made at the end of each cycle. Efforts have also been made to understand the mechanism of corrosion wherever possible.

The corrosion products were analysed with the help of XRD, SEM/EDAX and EPMA. The results for unwelded steels and weldments have been reported under different subheadings. In view of comparison the thermogravimetric data of each welding process is plotted along with the unwelded steels. The parabolic rate constants and scale thicknesses values have been evaluated after 50 cycles of exposure.

6.1 RESULTS

6.1.1 Unwelded Steels

6.1.1.1 Visual Examination

Fig. 6.1 shows the macrographs of the corroded specimens of unwelded GrA1, T11 and T22 steel after exposure in Na_2SO_4 - 60% V_2O_5 environment at 900°C for 50 cycles. The colour of substrate steels turned dull grey from dark brown during first cycle. For GrA1 base steel the sky grey colour scale appeared on the surface from 7th cycle onward which was fragile and started spalling. Exfoliation of the top scale was observed from 29th cycle onward. Scale cracked around 39th cycle and there was gradual increase in the width of cracks for every subsequent cycle.

In case of T11 base steel dark black shining spots were noticed on the surface after first cycle. The scale was lustrous and started cracking during 36th cycle. Spalling and increase in the width of cracks was observed in the remaining cycles. It can be seen from the macrograph Fig.

6.1(c) that intense spalling was there for T22 steel. Whereas fragile and dark grey colour scale was observed for T22 base steel. Intense spalling was observed through out the experimentation. As soon as subscale forms the top layer of scale spalled away from it and the separated multiple layers overlapping each other were seen.

6.1.1.2 Thermogravimetric Data

Weight gain per unit area expressed in mg/cm^2 is plotted as a function of time expressed in number of cycles for oxidised GrA1, T11 and T22 base steels and is shown in Fig. 6.2. T22 steel showed the maximum weight gain where T11 steel showed better resistance to given aggressive environment. Enormous increase in the weight gain for T22 steel was observed in the given molten salt as compared to its weight gain values in air at the same temperature and is more than double that of in air and the minimum weight gain was noticed for T11 type of steel. Weight gain square (mg^2/cm^4) plotted as a function of time (number of cycles) is shown in Fig. 6.3, from where it can be inferred that all the three base steels followed almost parabolic behaviour. The parabolic rate constants K_p in $10^{-8} \text{ g}^2 \text{ cm}^{-4} \text{ s}^{-1}$ for GrA1, T11 and T22 steels are 49.394, 10.416 and 76.233 respectively. The parabolic rate constant of T22 base steel is larger than the other two base steels and is around 7.3 times of that for T11 steel.

6.1.1.3 X-ray Diffraction Analysis

The X-ray diffractograms of the scale for GrA1, T11 and T22 base steels after exposure to molten salt ($\text{Na}_2\text{SO}_4\text{-60}\%\text{V}_2\text{O}_5$) at 900°C for 50 cycles are shown in Fig. 6.4. In the given environment all the steels have Fe_2O_3 as the main constituent of scale (Fig. 6.4). In addition to this Fe_3O_4 peaks were observed for GrA1 type of steel. Where as continuous and intense spalling was observed during oxidation of T22 type of steel and so XRD of the spalled scale was taken which indicated the presence of Fe_2O_3 and Cr_2O_3 .

6.1.1.4 Scale Thickness Measurement

The samples were cut across the cross-section after exposure to molten salt at 900°C for 50 cycles and mounted. The scale thickness values were measured from SEM back scattered images shown in Fig. 6.5. The oxide scale thickness could not be measured for T22 steel due to intense spalling and sputtering. The SEM micrograph shows the fragile and cracked scale for T11 and GrA1 base steel. The scale thickness for GrA1 base steel is 2.177 mm which is around 1.88 times the oxide scale thickness of T11 base steel (1.157 mm).

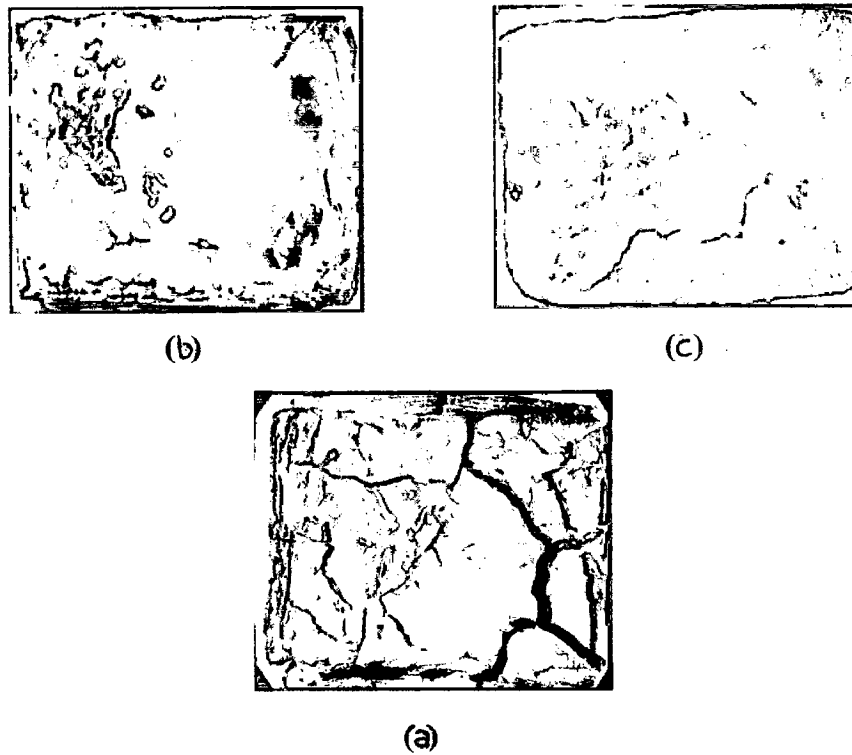


Fig. 6.1: Macrographs of unwelded steels subjected to cyclic hot corrosion in Na_2SO_4 - $60\%\text{V}_2\text{O}_5$ at 900°C for 50 cycles (a) GrA1, (b) T11 and (c) T22.

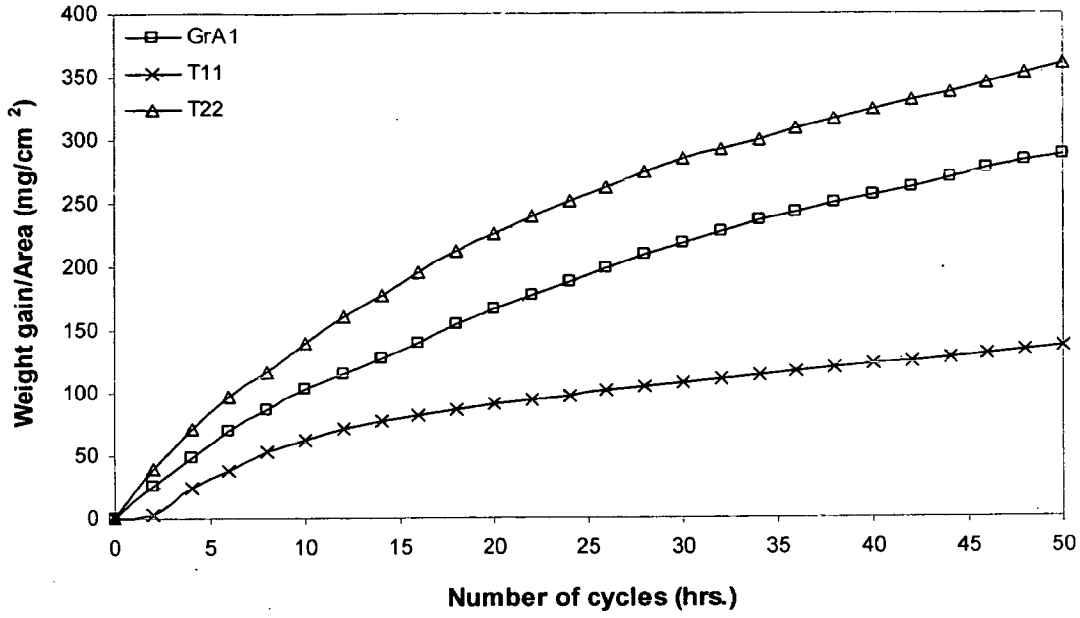


Fig. 6.2: Weight gain plot for un welded steels exposed to Na_2SO_4 -60% V_2O_5 at 900°C for 50 cycles.

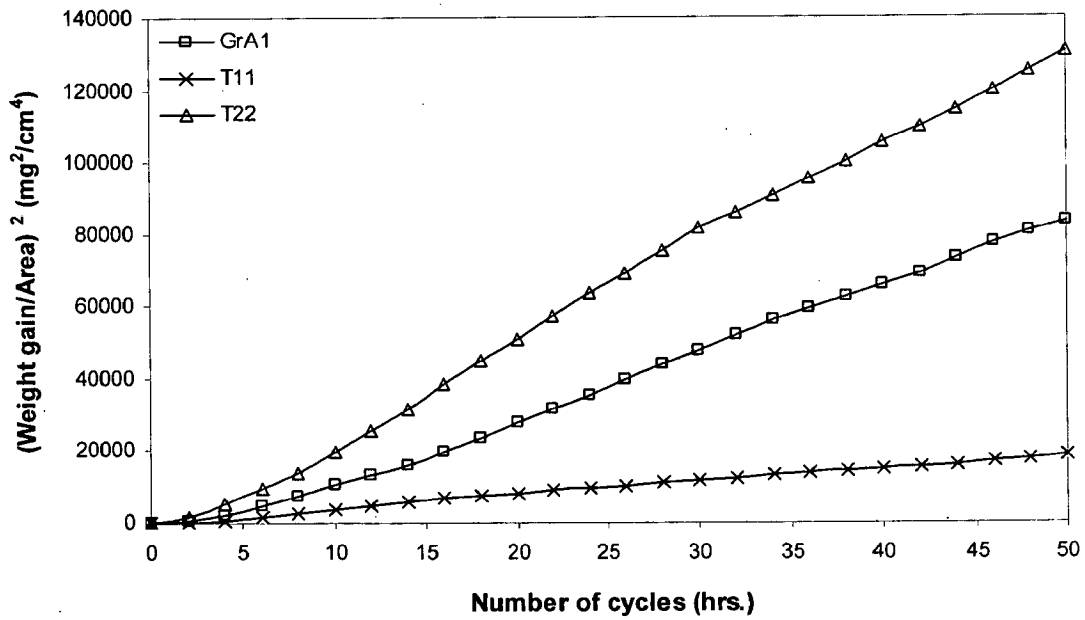


Fig. 6.3: Weight gain square (mg^2/cm^4) plot for un welded steels exposed to Na_2SO_4 -60% V_2O_5 at 900°C for 50 cycles.

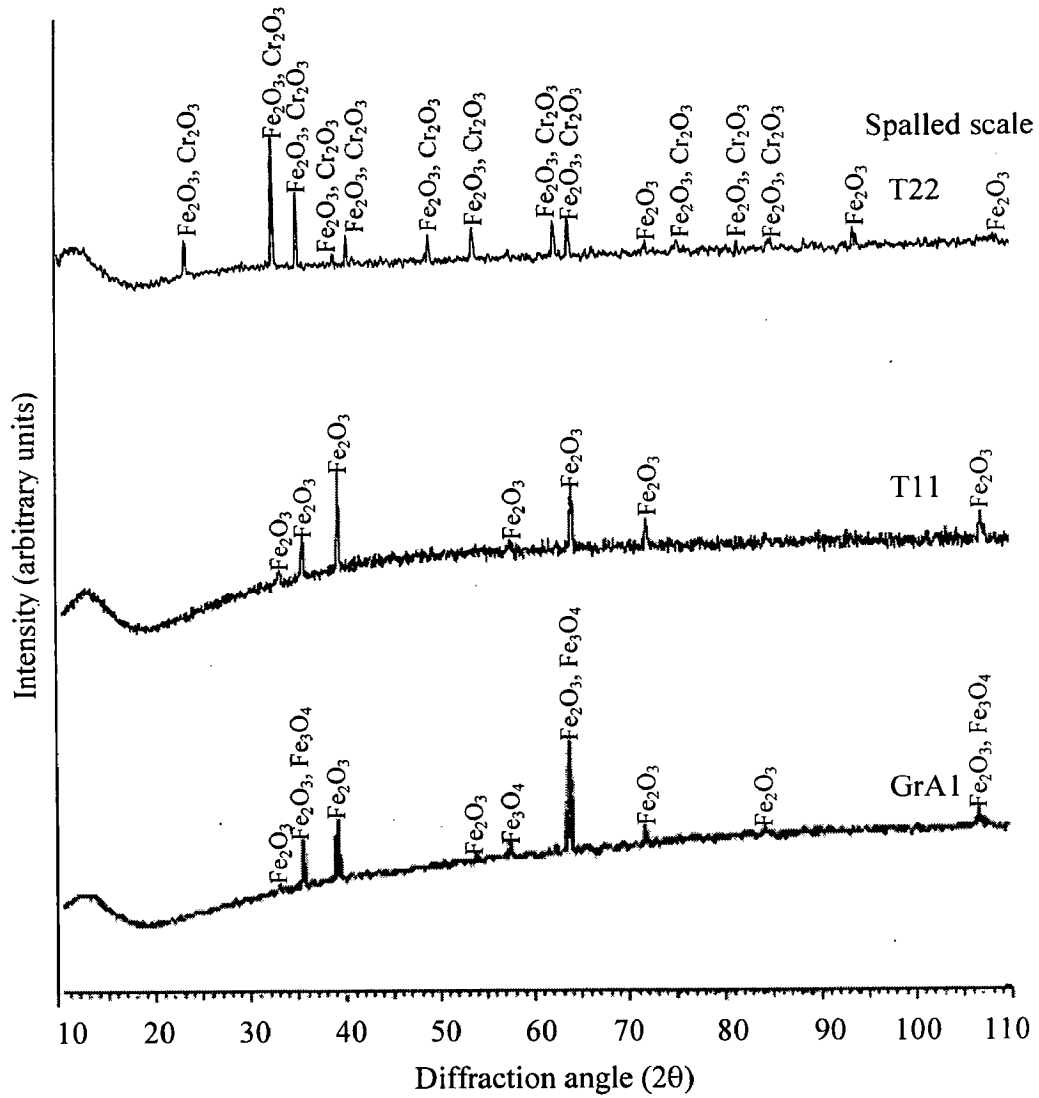
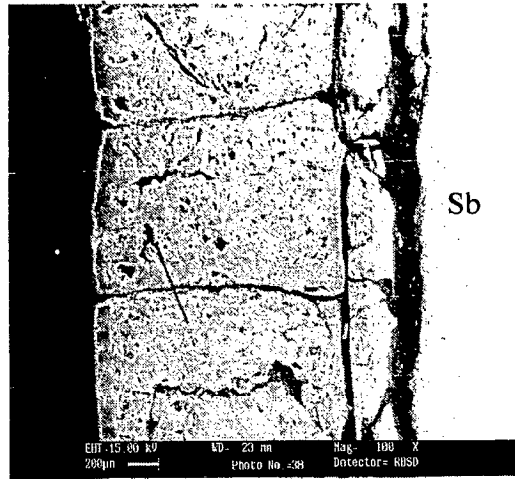
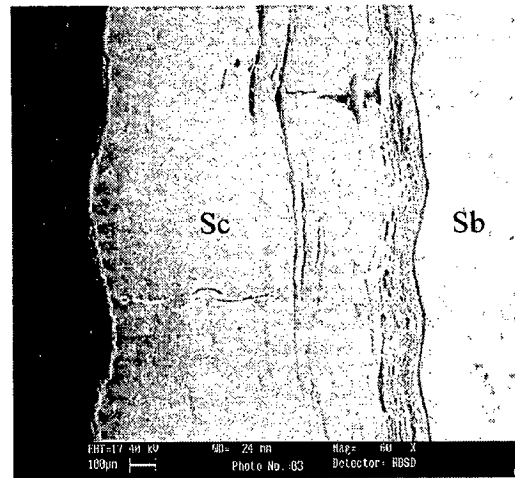


Fig. 6.4: X-ray diffraction profiles for unwelded GrA1, T11 and T22 boiler steels subjected to cyclic oxidation in Na₂SO₄ - 60% V₂O₅ at 900°C for 50 cycles.

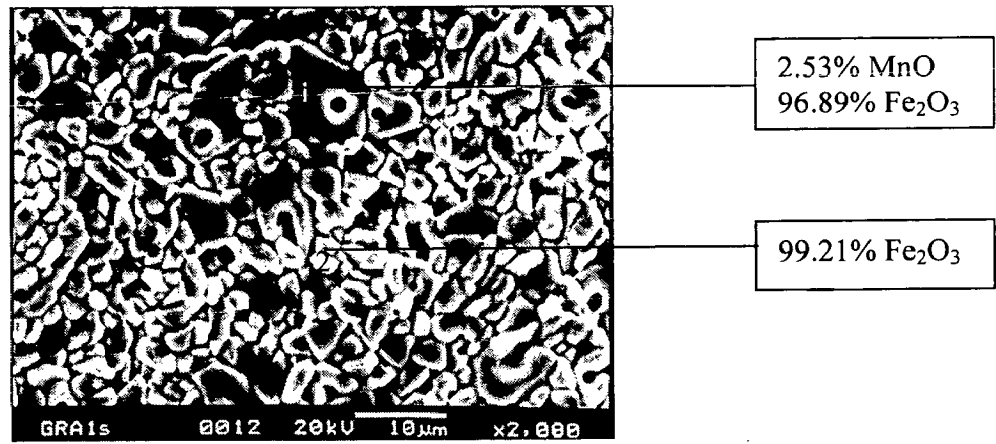


(a)

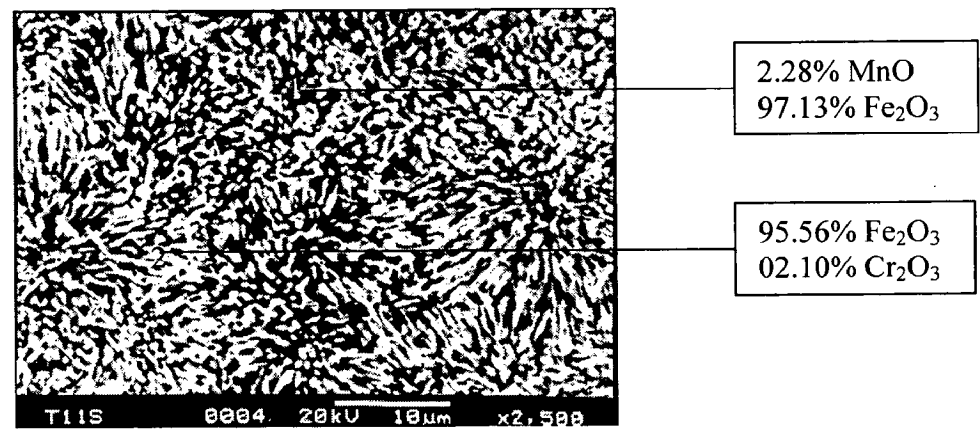


(b)

Fig. 6.5: SEM back scattered image of the cross section of unwelded steels after cyclic hot corrosion in $\text{Na}_2\text{SO}_4\text{-60\%V}_2\text{O}_5$ at 900°C for 50 cycles (a) GrA1, 100X (b) T11, 60X



(a)



(b)

Fig. 6.6: SEM micrographs showing surface scale morphology and EDAX analysis for boiler steels oxidized in $\text{Na}_2\text{SO}_4\text{-60\%V}_2\text{O}_5$ at 900°C for 50 cycles (a) GrA1, 2000X (b) T11, 2500X.

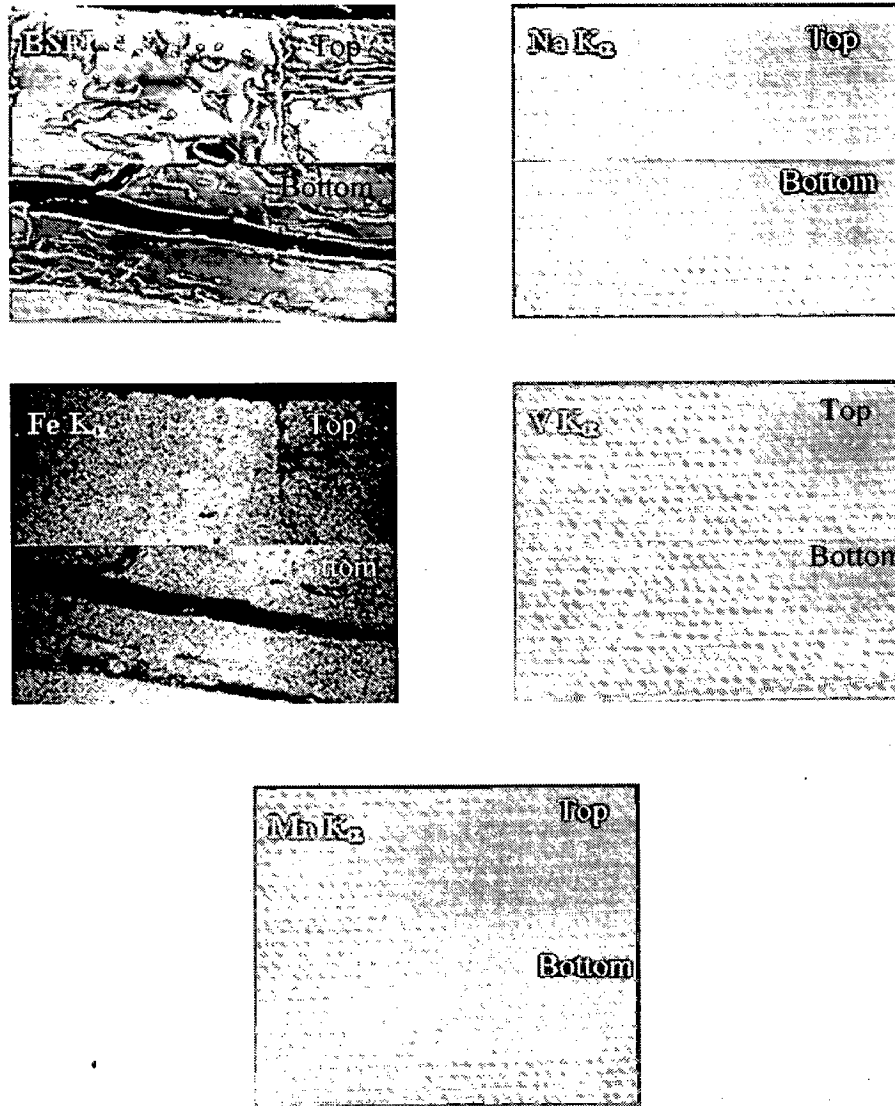


Fig. 6.7: BSEI and X-ray mapping of the cross-section of GrA1 boiler steel subjected to cyclic oxidation in $\text{Na}_2\text{SO}_4 - 60\% \text{V}_2\text{O}_5$ at 900°C for 50 cycles, 200X.

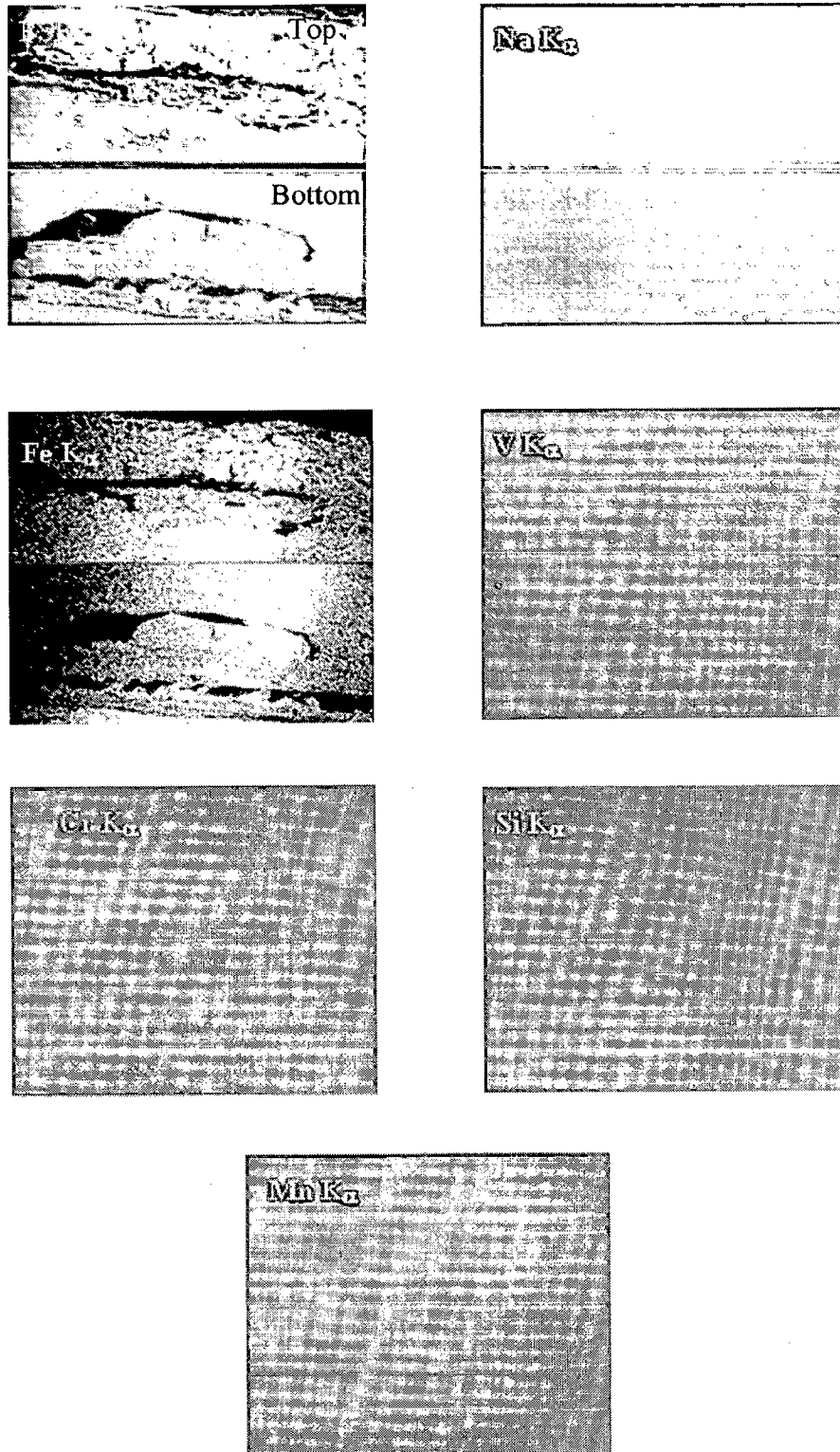


Fig. 6.8: BSEI and X-ray mapping of the cross-section of T11 boiler steel subjected to cyclic oxidation in $\text{Na}_2\text{SO}_4 - 60\% \text{V}_2\text{O}_5$ at 900°C for 50 cycles, 200X.

6.1.1.5 SEM/EDAX Analysis

6.1.1.5.1 Surface Morphology

The SEM micrograph of the GrA1 base steel exposed to Na_2SO_4 -60% V_2O_5 environment at 900°C given in Fig. 6.6 (a) indicates the formation of predominantly Fe_2O_3 scale. The top scale indicates spalling but the remaining subscale consists of Fe_2O_3 with MnO (2.53%). Whereas SEM micrograph and EDAX analysis after cyclic hot corrosion at 900°C for T11 base steel is shown in Fig. 6.6 (b). The top scale is mainly Fe_2O_3 and has some amount of the Cr_2O_3 (2.10%). Spalled region contains Fe_2O_3 with MnO (2.28%).

6.1.1.6 EPMA Analysis

The X-ray maps of GrA1 steel after exposure in Na_2SO_4 -60% V_2O_5 at 900°C for 50 cycles shown in Fig. 6.7 indicate formation of a thick scale of Fe. V is present through out the scale in very small amount.

EPMA micrograph Fig.6.8, for T11 steel indicates thick scale containing mainly of Fe throughout the scale. Vanadium and sodium is distributed throughout the scale in lower concentration. Irregular streaks of chromium are indicated in the inner scale near to the metal/scale interface. Minute amount of Si and Mn is also present in the scale.

6.1.2 SMAW WELDMENT

6.1.2.1 Visual Examination

The macrograph for the corroded surfaces of GrA1, T11 and T22 steels weldment by SMAW are shown in Fig. 6.9. It was observed that for all the welded steels, the colour of the scale surface turned blackish gray from dark brown during first cycle.

In case of welded GrA1 steel the oxide protrusions, dark black shining spots were observed on the surface of weld regions after first cycle. Spalling of oxide scale started during the 7th cycle. Even little cracks were found on 29th cycles, colour of the scale was blackish gray after 50th cycles. In case of welded T11 steel dark black shining spots were observed in the scale on weld regions during 10th cycle. The scale of welded T11 steel started cracking during 12th cycle and oozing out of oxides from these cracks were observed during the remaining cycles. Whereas in case of welded T22 steel the scale cracked in the middle of surface just after 1st cycle and after that there was increase in the number and width of these cracks. During 27th cycle a drastic increase in the number of cracks for this steel has been observed and some material from the inside was seen to be coming out through these cracks. Intense spalling of oxide scale was indicated by welded T22 steel.

6.1.2.2 Thermogravimetric Data

Weight gain (mg/cm^2) data plotted with time expressed in number of cycles for unwelded and SMAW weldments in GrA1, T11 and T22 steels is given in Fig. 6.10. It can be inferred from the plots that the weight gain for welded T22 steel is very much higher as compared to welded T11 and GrA1 steels. The total weight gain after 50 cycles for this welded steel is around 2.4 times more than that of welded T11 steel and 2.8 times for T11 unweld steel. Unwelded T11 steel showed the least weight gain as compared to welded steels. Welded T22 steel has shown proportionately less resistance to hot corrosion. Welded GrA1, T11 and T22 steels followed the parabolic behaviour as can be inferred from the square of weight change (mg^2/cm^4) plotted with number of cycles in Fig. 6.11. The parabolic rate constants (K_p in $10^{-8} \text{ g}^2 \text{ cm}^{-4} \text{ s}^{-1}$) for these welded steels are 31.686 (GrA1), 13.186 (T11) and 84.372 (T22).

6.1.2.3 X-ray Diffraction Analysis

The X-ray diffractograms for the corroded surfaces of SMAW weldment in steels after cyclic studies in molten salt are shown in Fig. 6.12. All the corroded steels weldment indicated the formation of major phase Fe_2O_3 . The phases revealed by XRD analysis are Fe_2O_3 in case of GrA1 steel weldment while T11 and T22 showed Fe_2O_3 , Fe_3O_4 and Fe_2O_3 , Cr_2O_3 , Fe_3O_4 respectively.

6.1.2.4 Scale Thickness Measurement

SEM back scattered images across the cross-sections of SMAW weldment in GrA1, T11 and T22 steels after hot corrosion for 50 cycles at 900°C are shown in Fig. 6.13. Micrograph shows fragile scale for welded T22 steel whereas scale with through cracks is seen over the HAZ region is seen for welded GrA1 steel. The average scale thickness values measured for weld region of SMAW weldment in GrA1, T11 and T22 steels are 1.190, 0.975 and 1.955 mm respectively. Whereas average scale thickness measured for HAZ of SMAW weldment from backscattered images is 1.297, 0.994 and 1.862 mm for GrA1, T11 and T22 steel respectively. Minimum scale thickness is indicated by welded T11 steel.

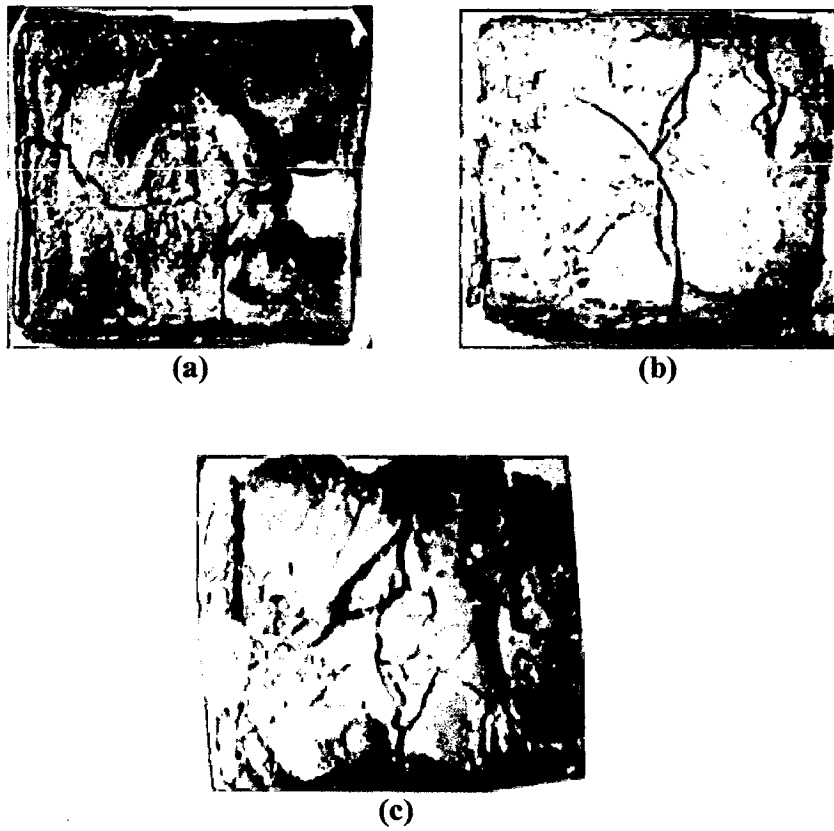


Fig. 6.9: Macrographs of SMAW weldment steels subjected to cyclic hot corrosion in $\text{Na}_2\text{SO}_4\text{-60\%V}_2\text{O}_5$ at 900°C for 50 cycles (a) GrA1 (b) T11 and (c) T22.

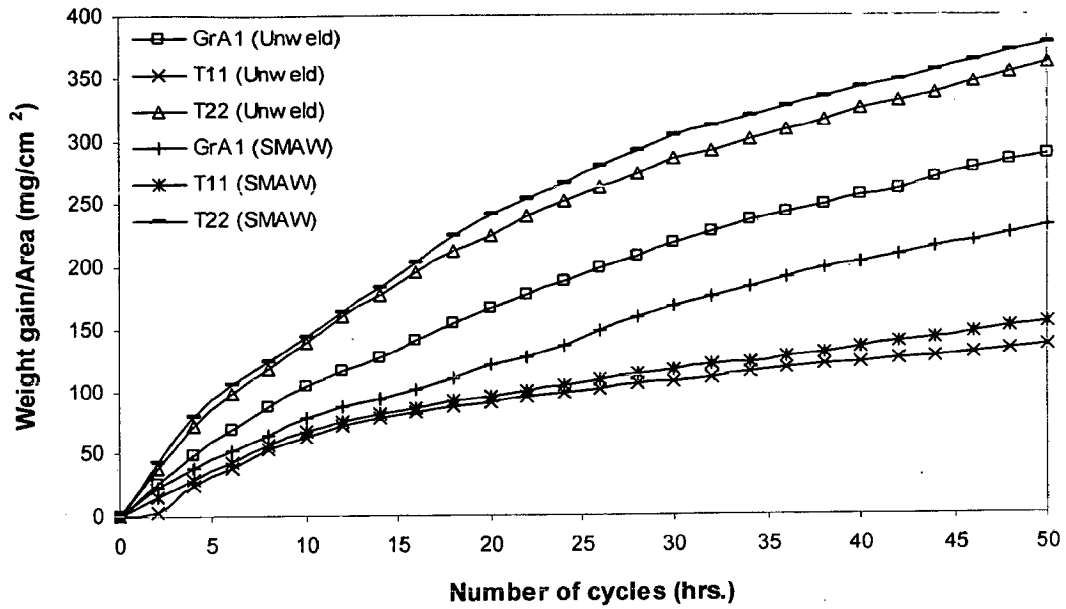


Fig. 6.10: Weight gain plot for unwelded and SMAW weldment steels exposed to Na_2SO_4 - $60\%\text{V}_2\text{O}_5$ at 900°C for 50 cycles.

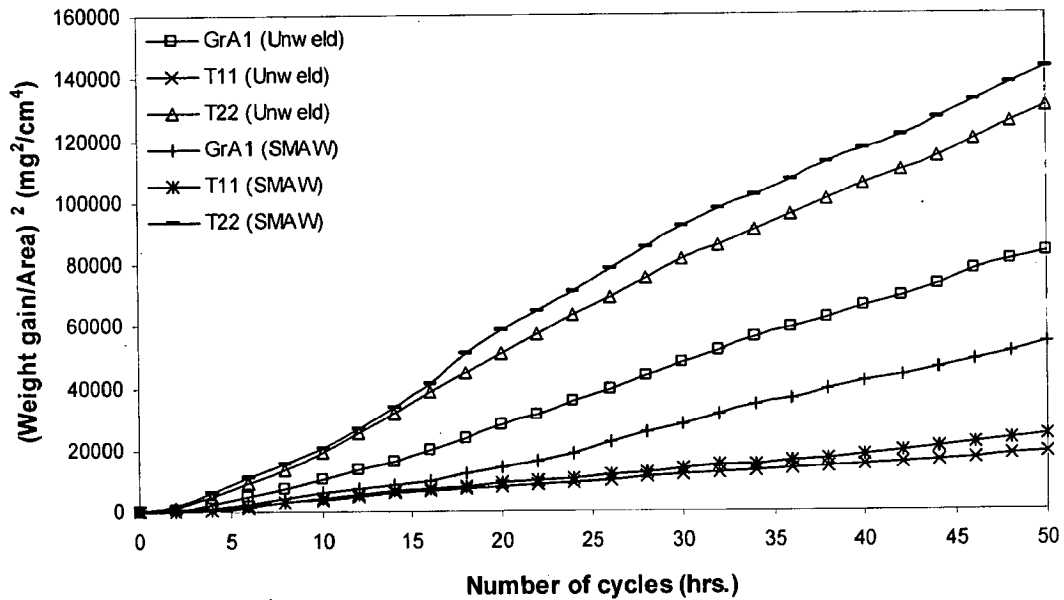


Fig. 6.11: Weight gain square (mg^2/cm^4) plot for unwelded and SMAW weldment steels exposed to Na_2SO_4 - $60\%\text{V}_2\text{O}_5$ at 900°C for 50 cycles.

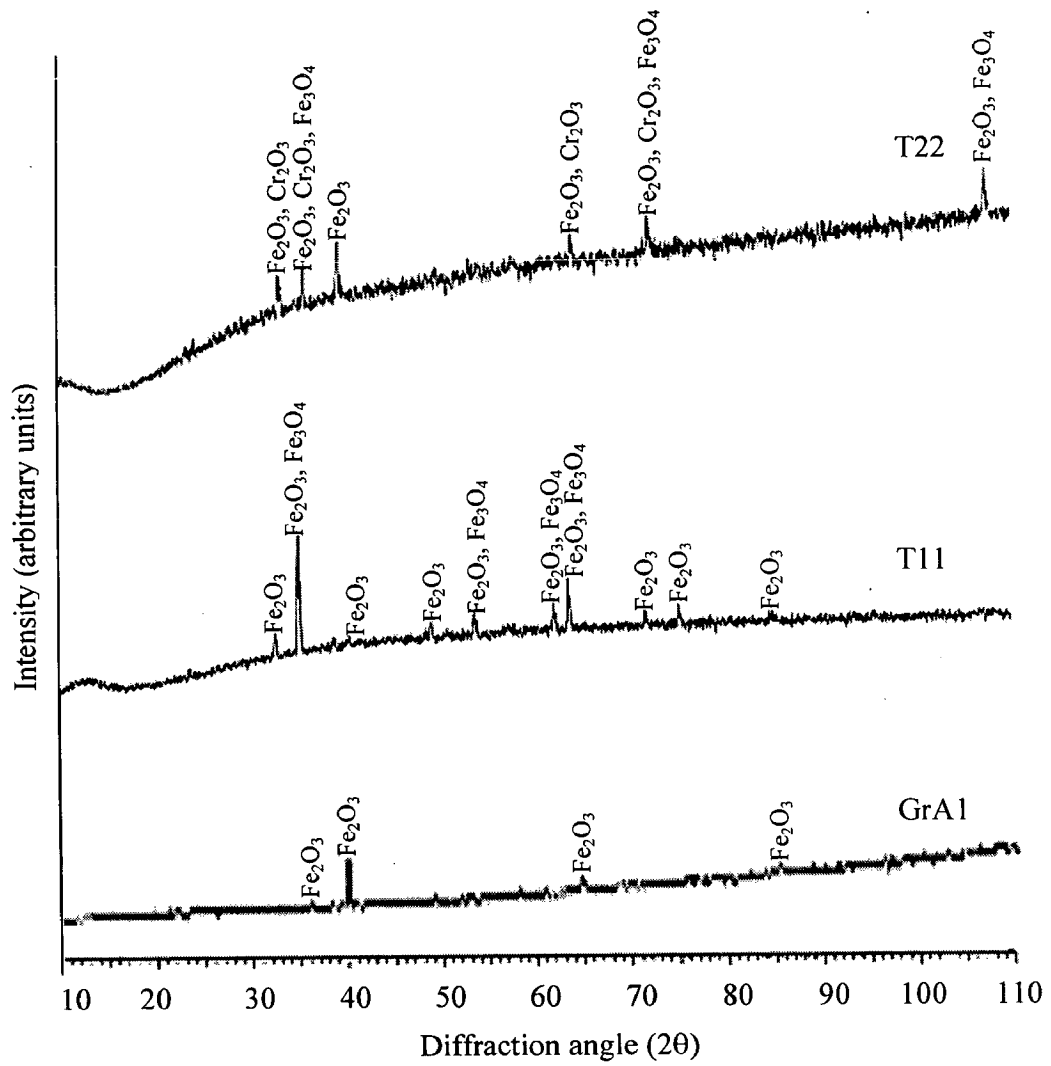


Fig. 6.12: X-ray diffraction profiles for SMAW weldment in GrA1, T11 and T22 boiler steels exposed to Na₂SO₄ -60%V₂O₅ at 900°C for 50 cycles.

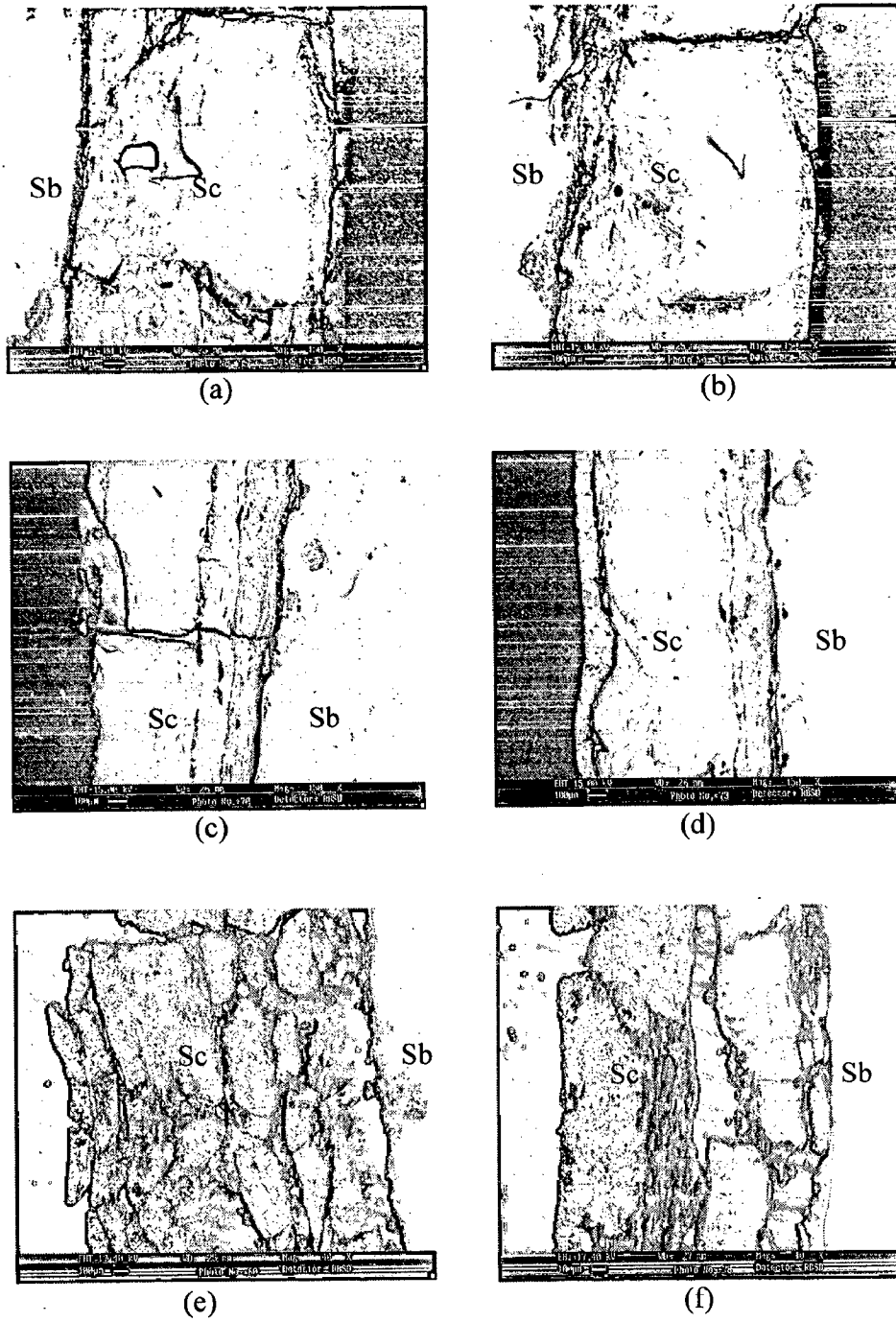


Fig. 6.13: SEM back scattered image of the cross section of SMAW weldment steels exposed to Na_2SO_4 -60% V_2O_5 at 900°C for 50 cycles. (a) GrA1 (weld), 150X. (b) GrA1 (HAZ), 150X (c) T11 (weld), 150X (d) T11 (HAZ), 150X (e) T22 (weld), 40X (f) T22 (HAZ, 40X.

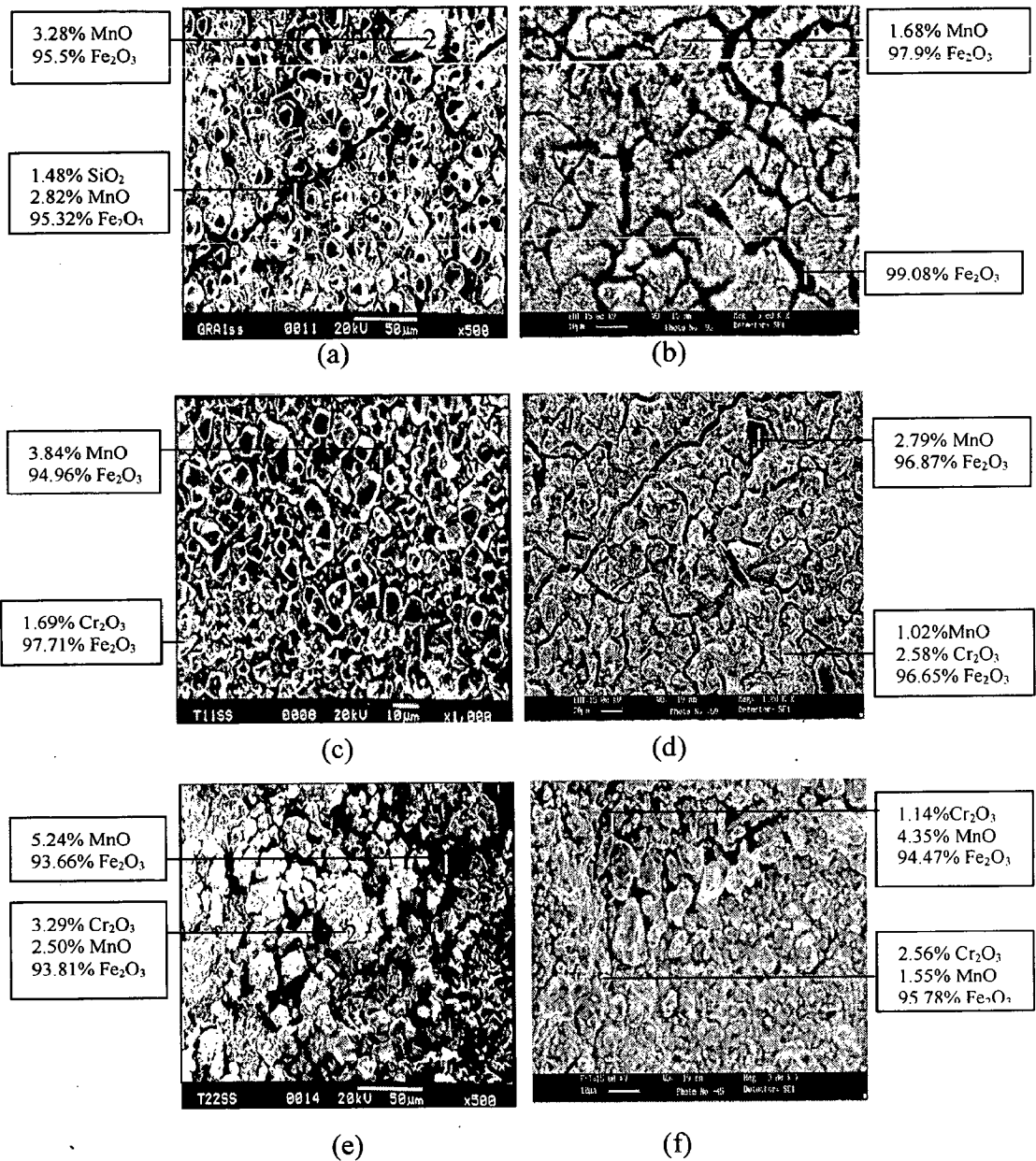


Fig. 6.14: SEM micrographs showing surface scale morphology and EDAX analysis for SMAW weldment in boiler steels in Na_2SO_4 -60% V_2O_5 at 900°C for 50 cycles (a) GrA1 (weld), 500X (b) GrA1 (HAZ), 3000X (c) T11 (weld), 1000X (d) T11 (HAZ), 1000X (e) T22 (weld), 500X (f) T22 (HAZ), 3000X.

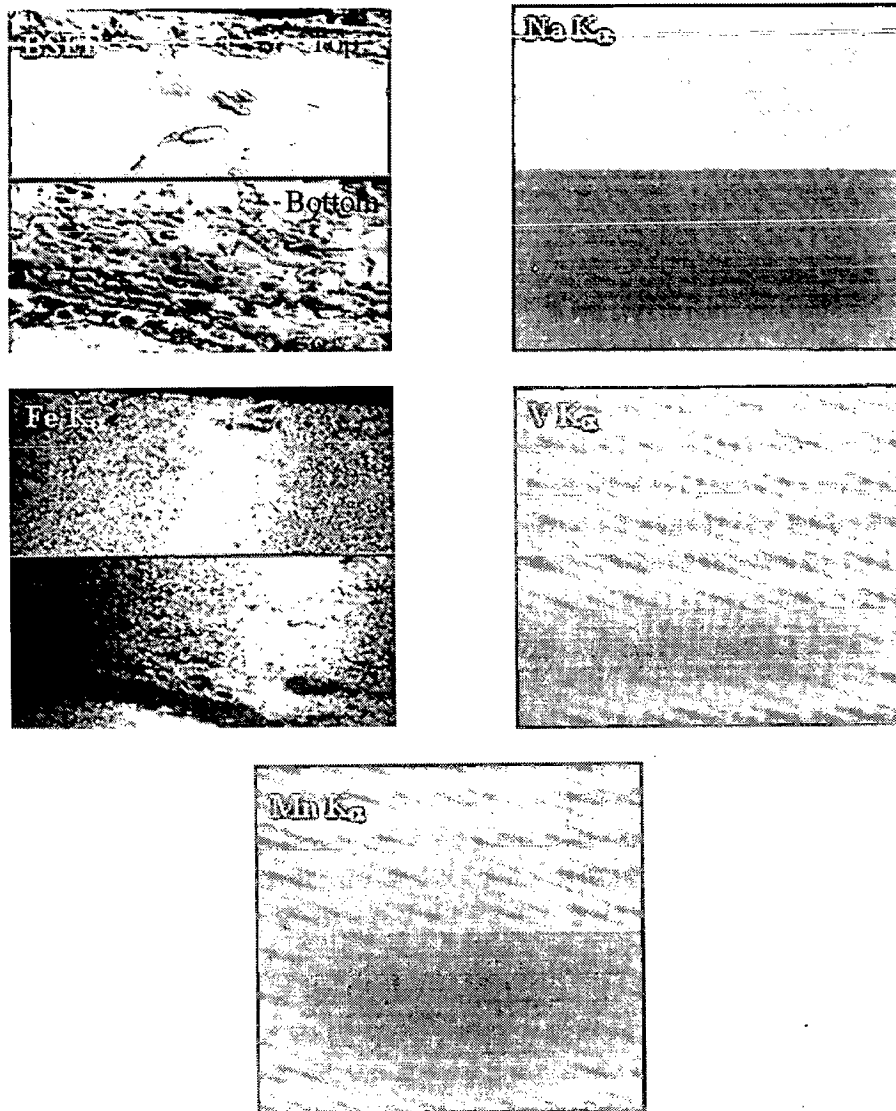


Fig. 6.15: BSEI and X-ray mapping of the cross-section of weld zone of SMAW weldment in GrA1 boiler steel subjected to cyclic oxidation in $\text{Na}_2\text{SO}_4 - 60\% \text{V}_2\text{O}_5$ at 900°C for 50 cycles, 200X.

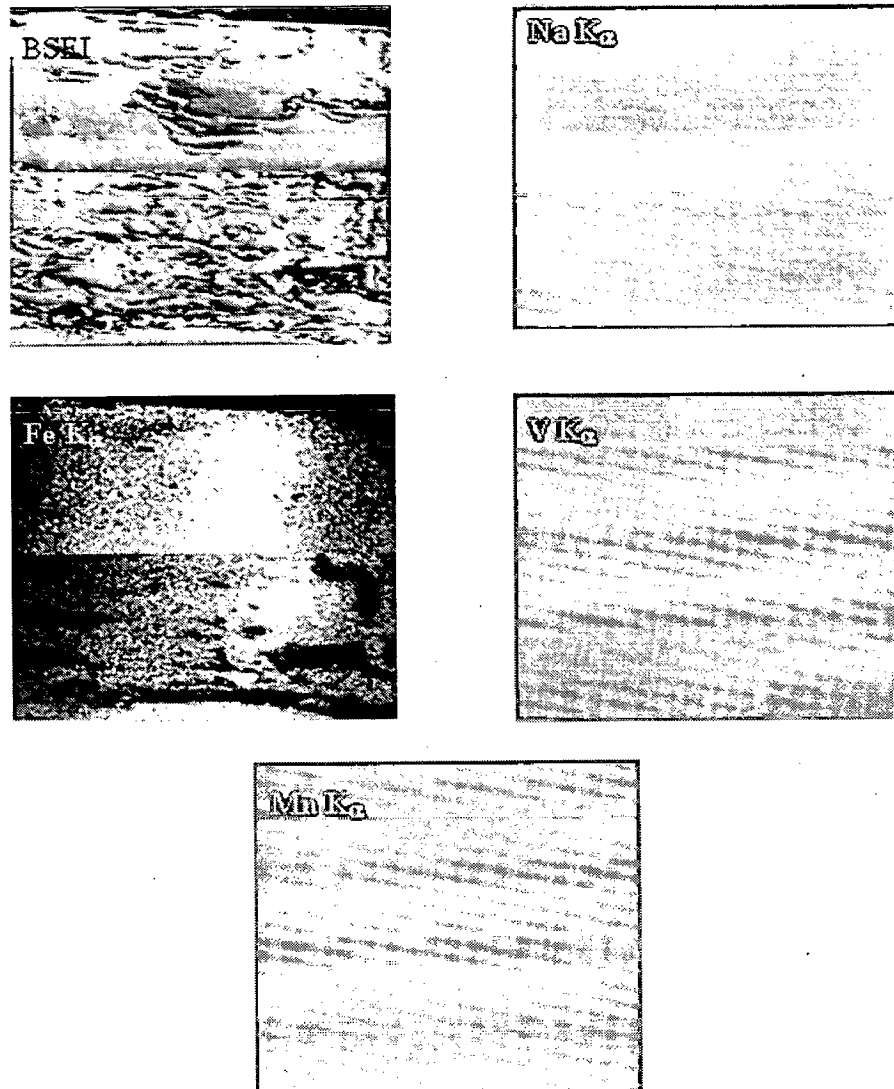


Fig. 6.16: BSEI and X-ray mapping of the cross-section of HAZ of SMAW weldment in GrA1 boiler steel subjected to cyclic oxidation in Na_2SO_4 - 60% V_2O_5 at 900°C for 50 cycles, 200X.

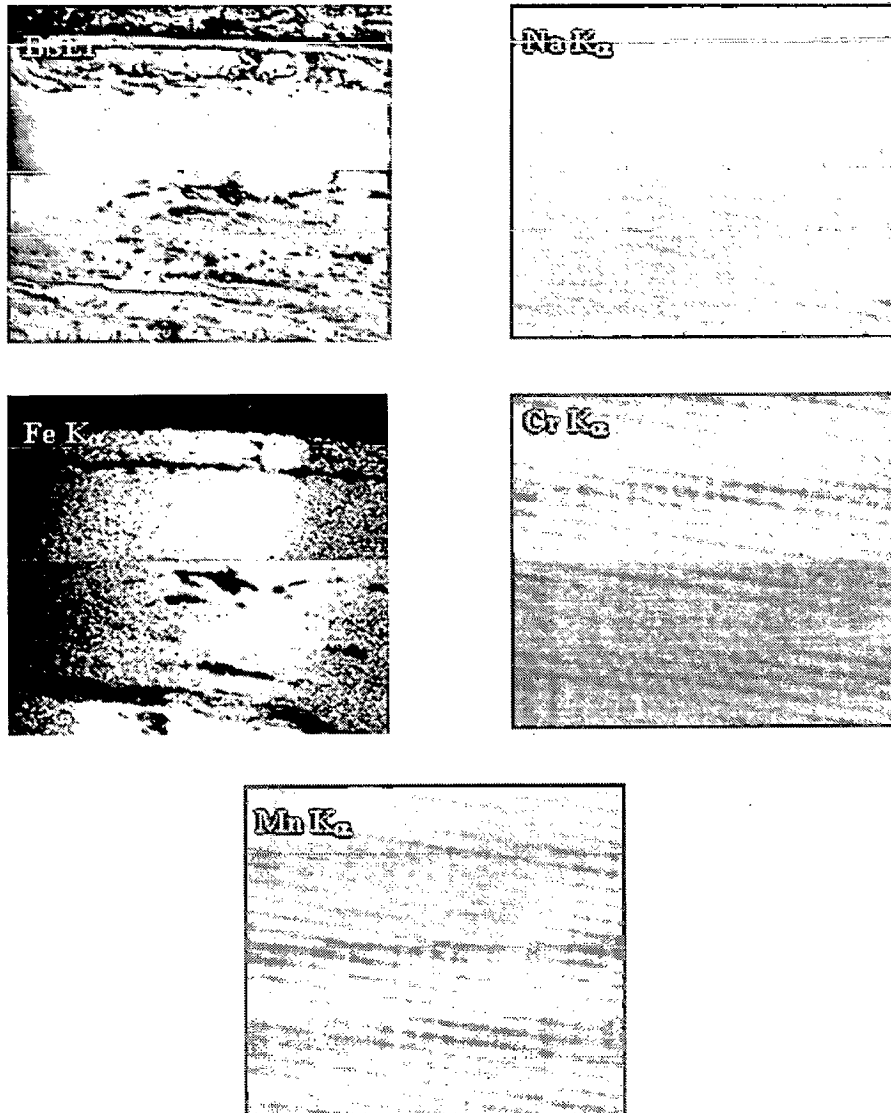


Fig. 6.17: BSEI and X-ray mapping of the cross-section of weld zone of SMAW weldment in T11 boiler steel subjected to cyclic oxidation in Na_2SO_4 - 60% V_2O_5 at 900°C for 50 cycles, 200X.

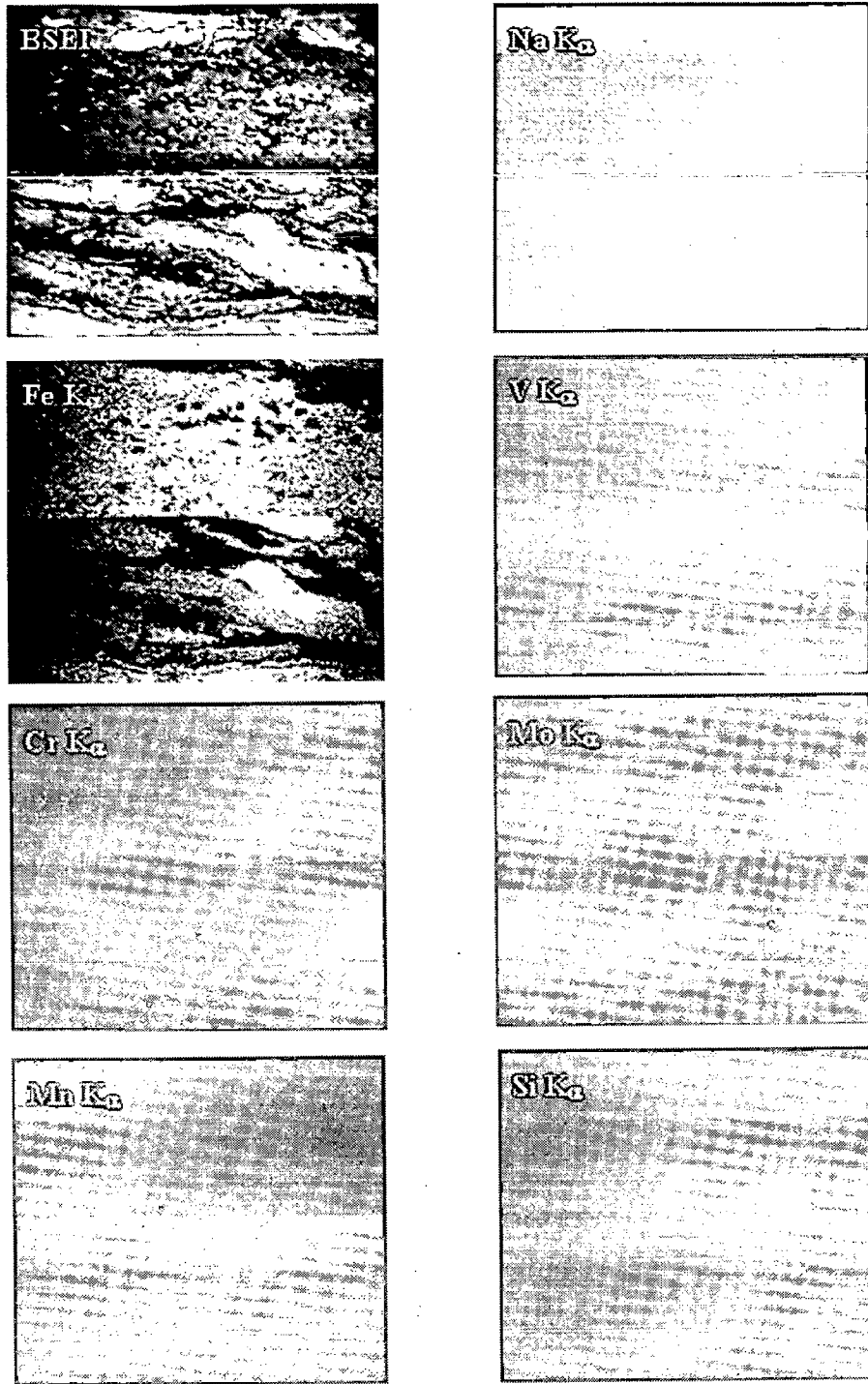


Fig. 6.18: BSEI and X-ray mapping of the cross-section of weld zone of SMAW weldment in T22 boiler steel subjected to cyclic oxidation in $\text{Na}_2\text{SO}_4 - 60\% \text{V}_2\text{O}_5$ at 900°C for 50 cycles, 200X.

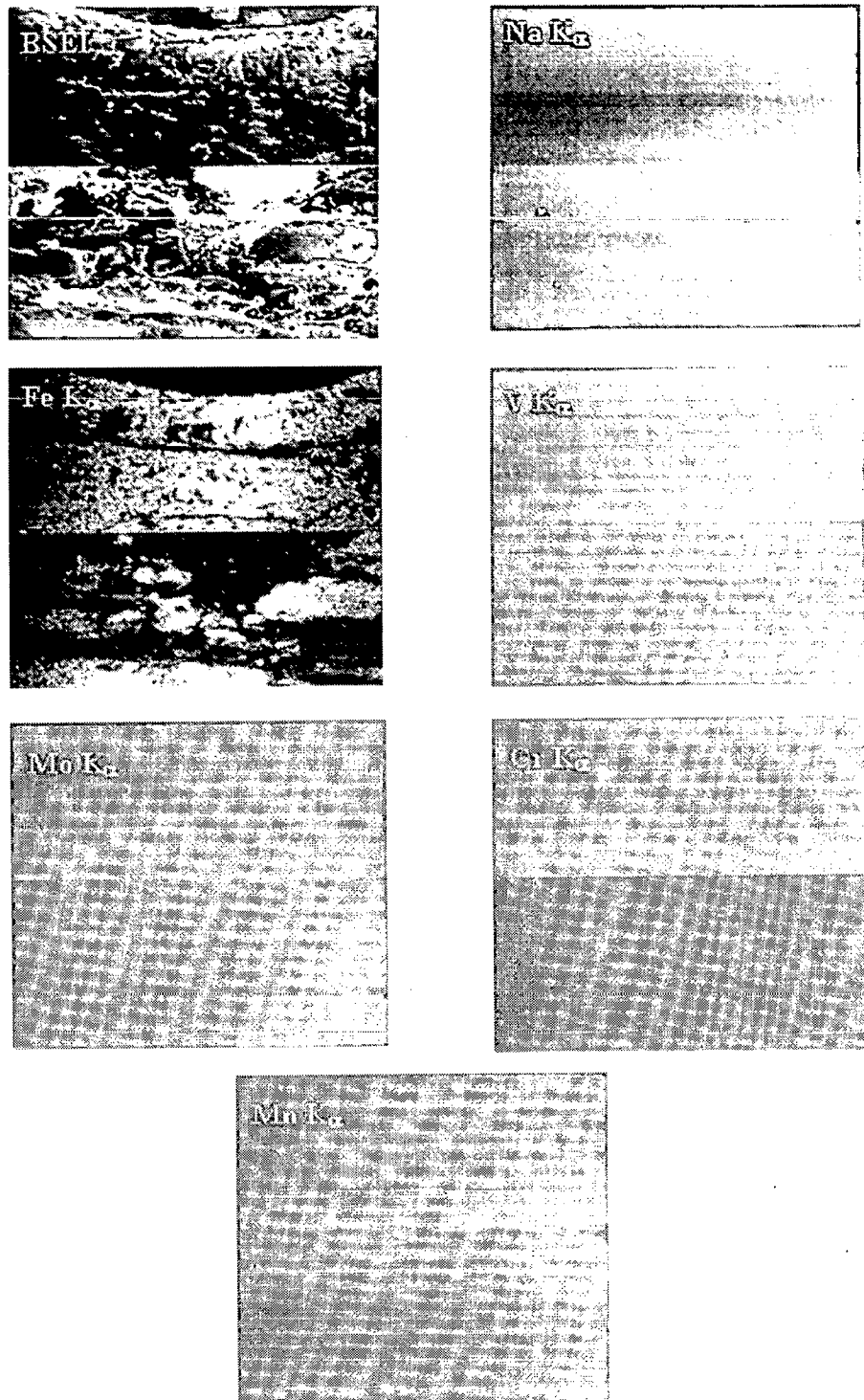


Fig. 6.19: BSEI and X-ray mapping of the cross-section of HAZ of SMAW weldment in T22 boiler steel subjected to cyclic oxidation in Na_2SO_4 - 60% V_2O_5 at 900°C for 50 cycles, 200X.

6.1.2.5 SEM/EDAX Analysis

6.1.2.5.1 Surface Morphology

SEM micrograph and EDAX analysis for SMAW weldment in steels after hot corrosion in molten salt for 50 cycles at 900°C are given in Fig. 6.14. SEM of the top surface for weld region of SMAW weldment in GrA1 steel after hot corrosion indicates the cracking of the scale as evident from Fig. 6.14 (a). The top scale was consisting of Fe₂O₃ and MnO (point 1) whereas in side the cracks oxides were appeared to be mainly of Fe₂O₃, MnO and SiO₂ (point 2). The top scale of HAZ region indicates the spalled portion consist of iron oxide Fe₂O₃ (99.08%) in Fig. 6.14 (b).

The SEM/EDAX analysis for weld region of welded T11 steel also indicates the top scale mainly consists of Fe₂O₃ and Cr₂O₃. The spalled region contains mainly Fe₂O₃ with small amounts of MnO (3.84%) Fig. 6.14 (c). Whereas the scale on HAZ region was containing of MnO (1.02%), Cr₂O₃ (2.58%) and Fe₂O₃ (96.65%) as can be seen from Fig 6.14 (d).

The surface SEM for weld region of welded T22 steel shown in Fig. 6.14 (e) indicates a scale with nodules growing from inside. It has cracked from the middle. Scale is mainly of Fe₂O₃ (93.81%) having small percentage of Cr₂O₃ (3.29%) and MnO (2.50%). The nodular growth which is oozing out of the openings in the scale contains mainly Fe₂O₃ (93.66%) with little amount of MnO (5.24%) point (2). Whereas the HAZ region contains cracks and EDAX analysis revealed the scale mainly consists of Fe₂O₃ with Cr₂O₃ and MnO of inner scale at point 1. The top scale contain Cr₂O₃ (2.56%), MnO (1.55%) with Fe₂O₃ as main oxide at point 2 in Fig. 6.14 (f).

6.1.2.6 EPMA Analysis

The EPMA for welded GrA1 steel as shown in Fig. 6.15, where Fe is mainly present. Vanadium is also present in the scale.

The EPMA of the cross-section of corroded weld region in T11 steel weldment indicates that scale is mainly consisting of Fe with very small concentration of Mn (Fig. 6.16). Na is seen existing at one point in the top scale. In case of HAZ region of T11 steel weldment Fe is only the main element.

The EPMA of weld region of T22 steel weldment indicates that scale Fe is main element with Cr streaks present at bottom of scale. While little amounts of V and Mo seen in the scale. In case of HAZ of T22 steel weldments Na scattered at the bottom scale with main scale Fe. Cr was seen in little amounts at some place in this oxide scale.

6.1.3 TIG Weldment

6.1.3.1 Visual Examination

The colour of scale during first cycle turned blackish gray for all the welded steels and up to the end of cyclic study (Fig. 6.20). Oxide protrusion dark blackish grey in colour appeared from the beneath for all the welded steels. For TIG welded GrA1 and T11 steels minor cracks appeared in the scale of weld regions during 5th and 8th cycles respectively. Whereas in case of same weldment in T22 steel the cracks and spalling in the scale appeared after 4th cycle and was comparatively more in number having substantial width. More spalling was also noticed for this type of welded steel from 13th cycle. Scale on the welded regions was seen as slightly black in colour during 2nd cycle.

6.1.3.2 Thermogravimetric Data

Weight change (mg/cm^2) variation as a function of time expressed in number of cycles for TIG weldment in steels after hot corrosion in Na_2SO_4 -60% V_2O_5 at 900°C for 50 cycles are as shown in Fig. 6.21. TIG welded T22 steel showed lesser weight gain as compared to unwelded specimens in the given molten salt environment.

The behaviour for TIG welded GrA1, T11 and T22 steels was almost parabolic with parabolic rate constants, K_p is 47.731, 15.797 and $57.738 \times 10^{-8} \text{ g}^2 \text{ cm}^{-4} \text{ s}^{-1}$ respectively as shown in Fig. 6.22. Although welded T22 steel showed higher weight gain as compared to other two types of welded steels yet it is around 1.8 times of the weight gain value of welded T11 steel.

Welded T11 steel when exposed to molten salt after TIG weldment showed slightly less resistance to hot corrosion than same unwelded steel. But welded and unwelded GrA1 steel showed the approximately same weight gain.

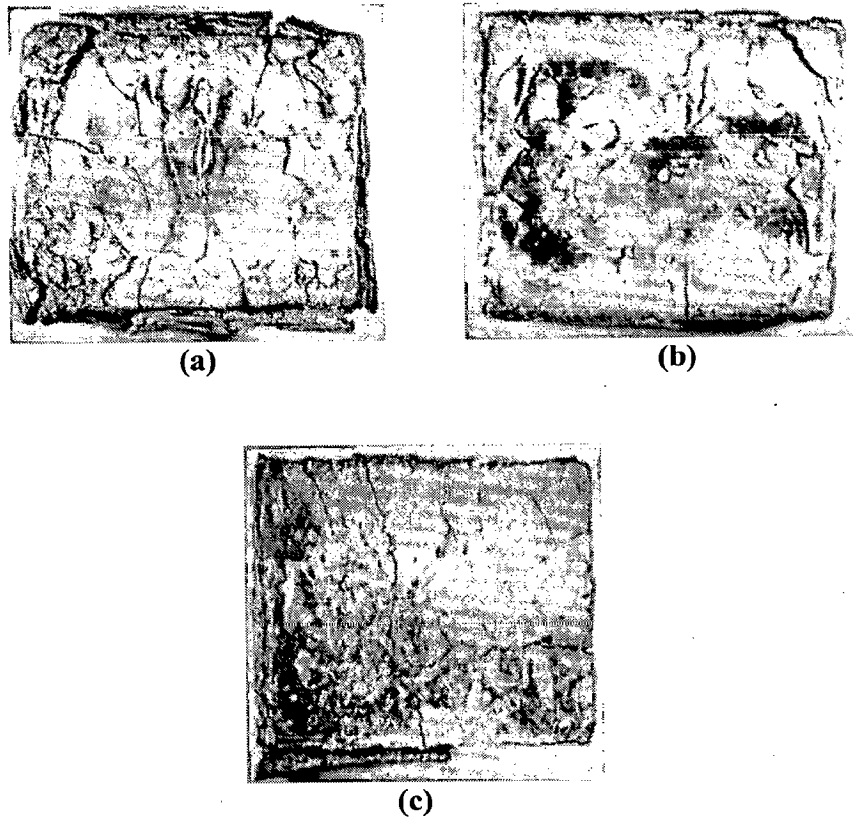


Fig. 6.20: Macrographs of TIG weldment steels subjected to cyclic hot corrosion in Na_2SO_4 -60% V_2O_5 at 900°C for 50 cycles (a) GrA1, (b) T11 and (c) T22.

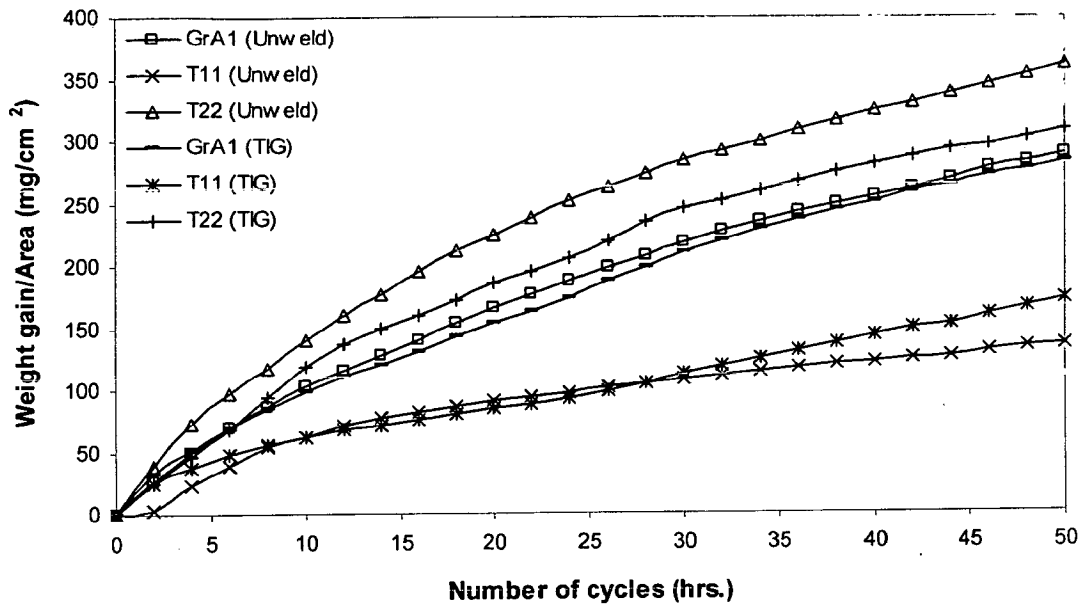


Fig. 6.21: Weight gain plot for unwelded and TIG weldment GrA1, T11 and T22 boiler steels exposed to Na_2SO_4 -60% V_2O_5 at 900°C for 50 cycles.

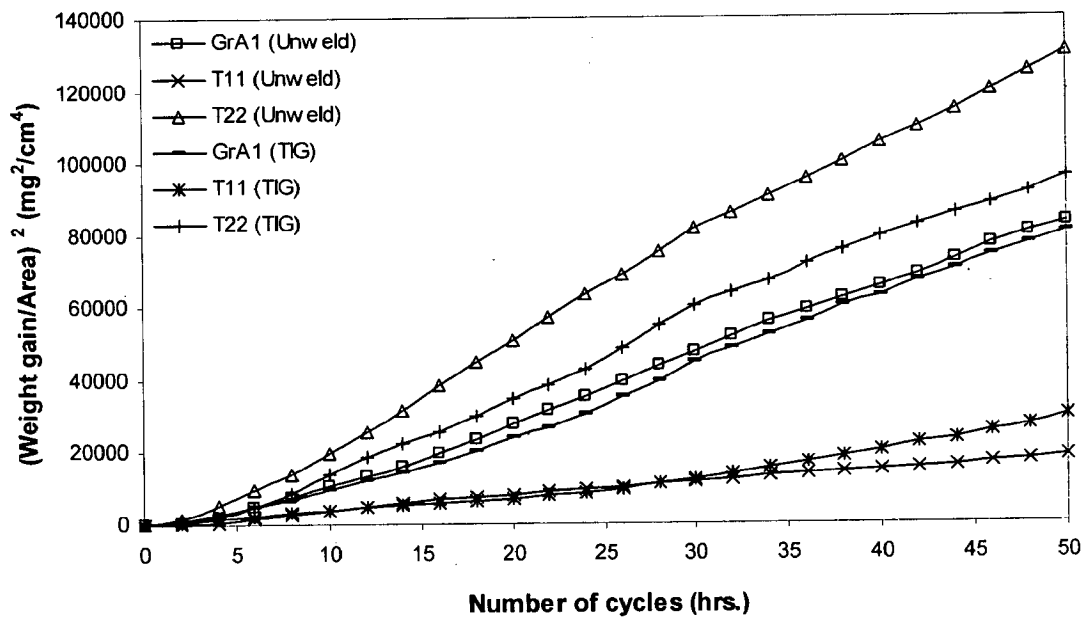


Fig. 6.22: Weight gain square (mg^2/cm^4) plot for unwelded and TIG weldment in GrA1, T11 and T22 boiler steels exposed to Na_2SO_4 -60% V_2O_5 at 900°C for 50 cycles.

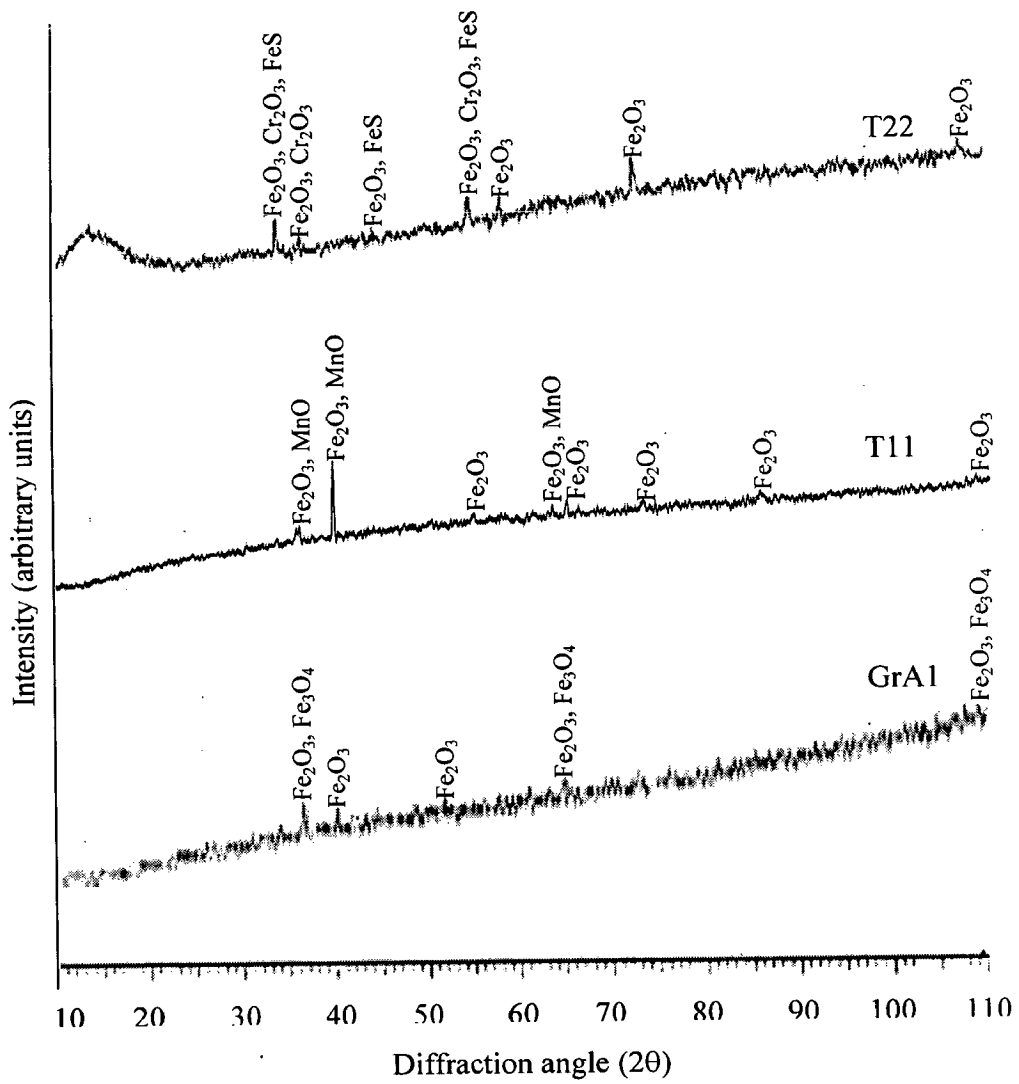


Fig. 6.23: X-ray diffraction profiles for TIG weldment in GrA1, T11 and T22 boiler steels exposed to Na₂SO₄ -60%V₂O₅ at 900°C for 50 cycles.

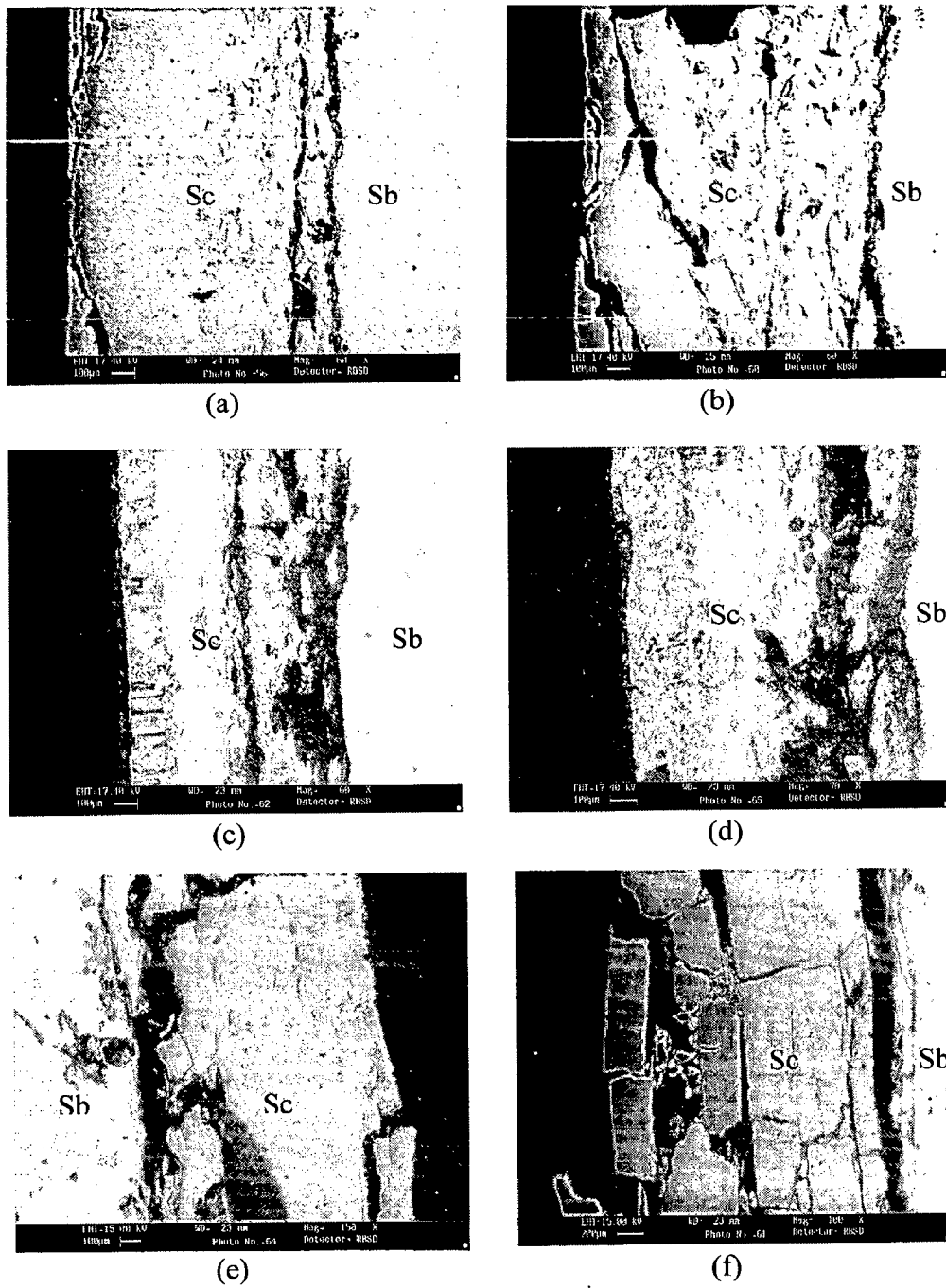


Fig. 6.24: SEM back scattered image of the cross section of TIG weldment in GrA1, T11 and T22 boiler steels exposed to Na_2SO_4 -60% V_2O_5 at 900°C for 50 cycles.(a) GrA1(weld), 60X (b) GrA1(HAZ), 60X (c) T11(weld), 60X (d) T11(HAZ), 70X (e) T22 (weld), 150X (f) T22 (HAZ), 100X.

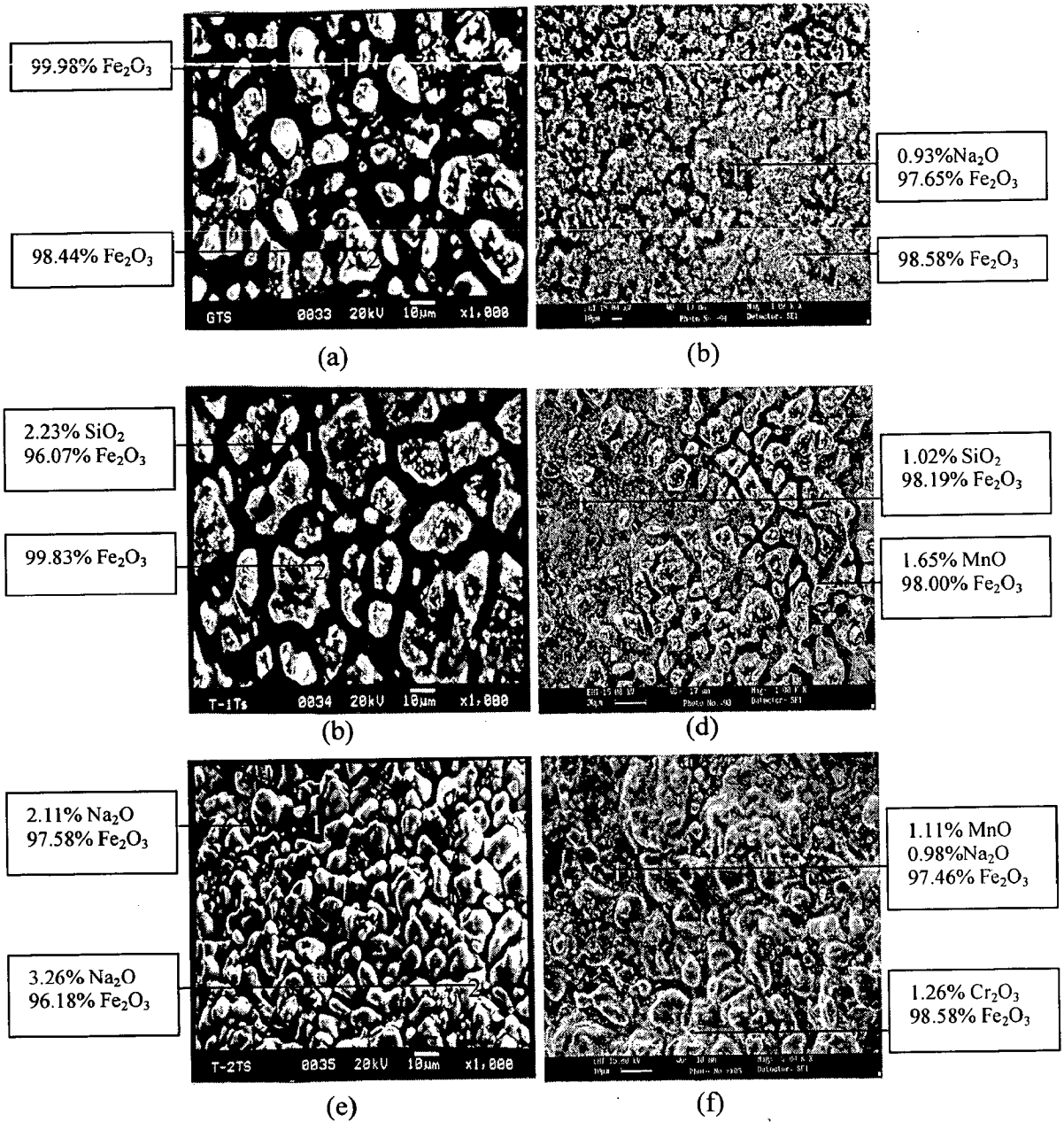


Fig 6.25: SEM micrographs showing surface scale morphology and EDAX analysis for TIG weldment steels in Na₂SO₄ - 60% V₂O₅ at 900°C for 50 cycles (a) GrA1 (weld), 1000X (b) GrA1 (HAZ), 1000X (c) T11 (weld), 1000X (d) T11 (HAZ), 2000X (e) T22 (weld), 1000 X (f) T22 (HAZ), and 3000X.

6.1.3.3 X-ray Diffraction Analysis

The XRD profile of the scale of welded steels after hot corrosion in molten salt at 900°C for 50 cycles shows Fe₂O₃ common phases for all the steels as could be seen in Fig. 6.23. In GrA1 steel phases are Fe₂O₃ with Fe₃O₄. Extra phases were observed in welded T22 steel were Cr₂O₃ with FeS. TIG Welded T11 steel when exposed to the given environment showed the formation of Fe₂O₃ along with MnO.

6.1.3.4 Scale Thickness Measurement

Backscattered electron images across the cross-section of TIG weldment in GrA1, T11 and T22 steels after cyclic hot corrosion are shown in Fig. 6.24. Average scale thickness measured of weld regions of TIG weldment from these backscattered images is 1.092, 0.893 and 1.242 mm for GrA1, T11 and T22 steels respectively. Whereas average scale thickness measured for HAZ of TIG weldment from backscattered images is 1.228, 1.793 and 2.274 mm for GrA1, T11 and T22 steel respectively. The oxide scale thickness of weld region of welded T22 steel is 1.4 times more than that of welded T11 steel.

6.1.3.5 SEM/EDAX Analysis

6.1.3.5.1 Surface Morphology

The weld region of TIG welded GrA1 steel after hot corrosion in the molten salt at 900°C after 50 cycles as shown in Fig. 6.25 (a), (b) indicated only Fe₂O₃ as well as on the HAZ. In case of TIG welded T11 steel, SEM micrograph of weld showed the top scale mainly Fe₂O₃ (99.83%) point 1 whereas inner oxide scale contains Fe₂O₃ (96.07%) with small amounts of SiO₂ (2.23%) point 2 Fig. 6.25 (c). The oxidized HAZ consists of mainly Fe₂O₃ with small amount of MnO (1.65%) in top scale at point 2. The inner scale indicates the mainly iron oxide Fe₂O₃ (98.19%) with SiO₂ (1.02%) point 1 in Fig. 6.25 (d).

SEM micrograph for weld region of welded T22 steel after hot corrosion indicates granular scale with outward growth as shown in Fig 6.25 (e). In this case the top scale consists mainly of Fe₂O₃ (96.18%) with little amounts of Na₂O (3.26%) whereas the inner scale has been identified as Fe₂O₃ (97.58%) with Na₂O (2.11%). The scale on HAZ of this weldment consists of spalled scale of Fe₂O₃ (97.46%) with 1.11% MnO and 0.96% Na₂O at Point 1, whereas the top scale indicates the Cr₂O₃ with the main phase of Fe₂O₃ (98.58%) at point 2 Fig. 6.25 (f).

6.1.3.6 EPMA Analysis

Elemental X-ray mapping for weld region of TIG weldment in GrA1 steel after hot corrosion in molten salt at 900°C for 50 cycles shown in Fig 6.26 indicates the formation of scale containing mainly iron and vanadium. Vanadium band is present at middle and bottom of the scale. Where as in HAZ regions of TIG weldment in GrA1 steel contains mainly iron with slightly V and Na. Vanadium is present in upper oxide scale and Na scattered in the whole scale as can be seen in Fig. 6.27.

EPMA for the cross-section of weld region of TIG weldment in T11 steel corroded in the given environment shows granular attack (Fig. 6.28). Oxide scale contains mainly Fe with some Na, Vanadium and chromium. Vanadium and sodium is present throughout the scale in low concentration. Chromium is also indicated in middle and bottom of the scale particularly at the interface of oxide scale and metal. In case of HAZ regions of TIG weldments in T11 steel corroded contains Fe, Na, V and Cr. Na and V are in the same position as that of weld regions but slightly change found in Cr. Cr is present in bottom of the scale also (Fig. 6.29).

The EPMA for corroded cross-section of weld region of TIG weldment in T22 steel (Fig. 6.30) shows scale consisting mainly of iron with small concentration of Cr, Mo and V. The chromium concentration increases in the middle of scale which is present as layer as streaks. Very small concentration of Mo was found in bottom. HAZ region of weldment in T22 steel contains only iron and chromium. Vanadium is also present in bottom scale reaches through the cracks which is the cause to increase oxidation (Fig. 6.31).

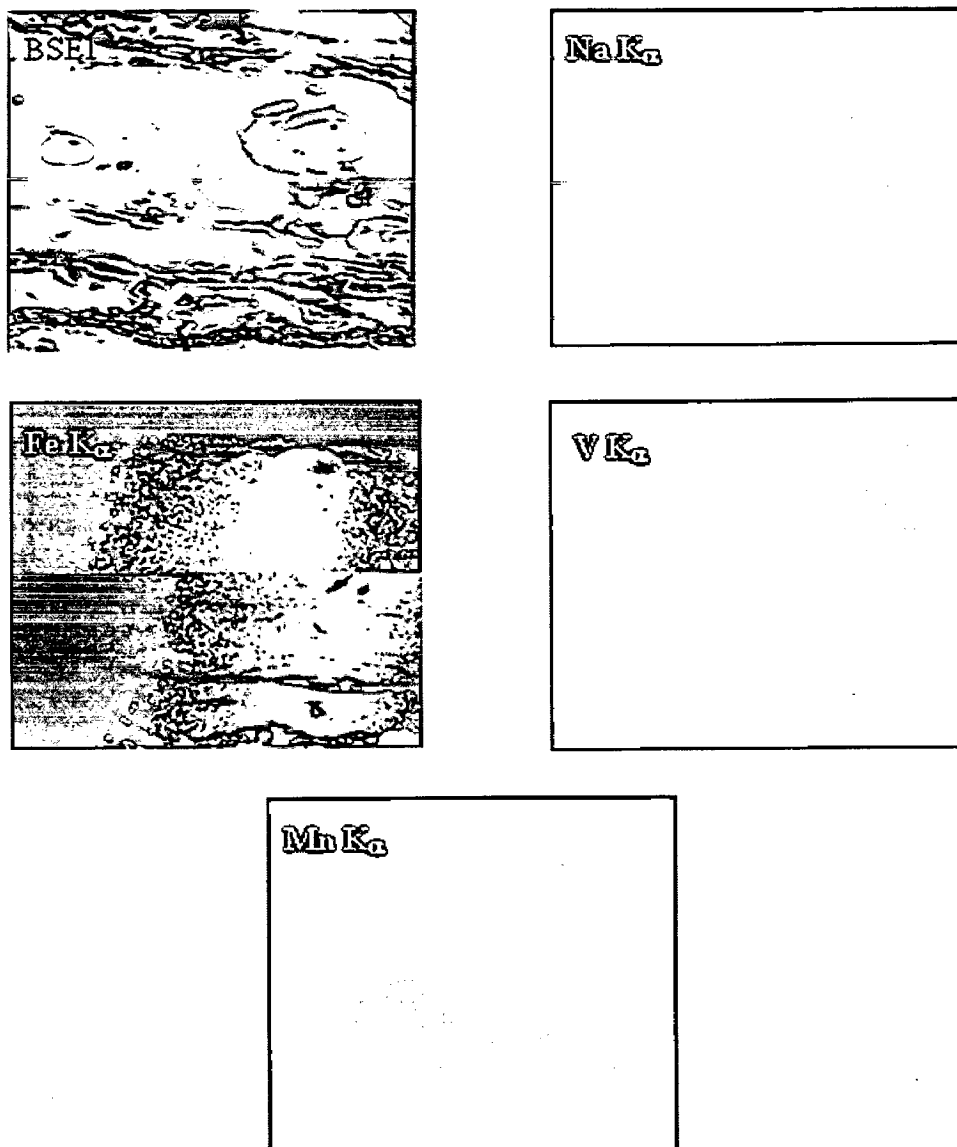


Fig. 6.26: BSEI and X-ray mapping of the cross-section of weld region of TIG weldment in GrA1 boiler steel subjected to cyclic oxidation in Na₂SO₄- 60% V₂O₅ at 900°C for 50 cycles, 200X.

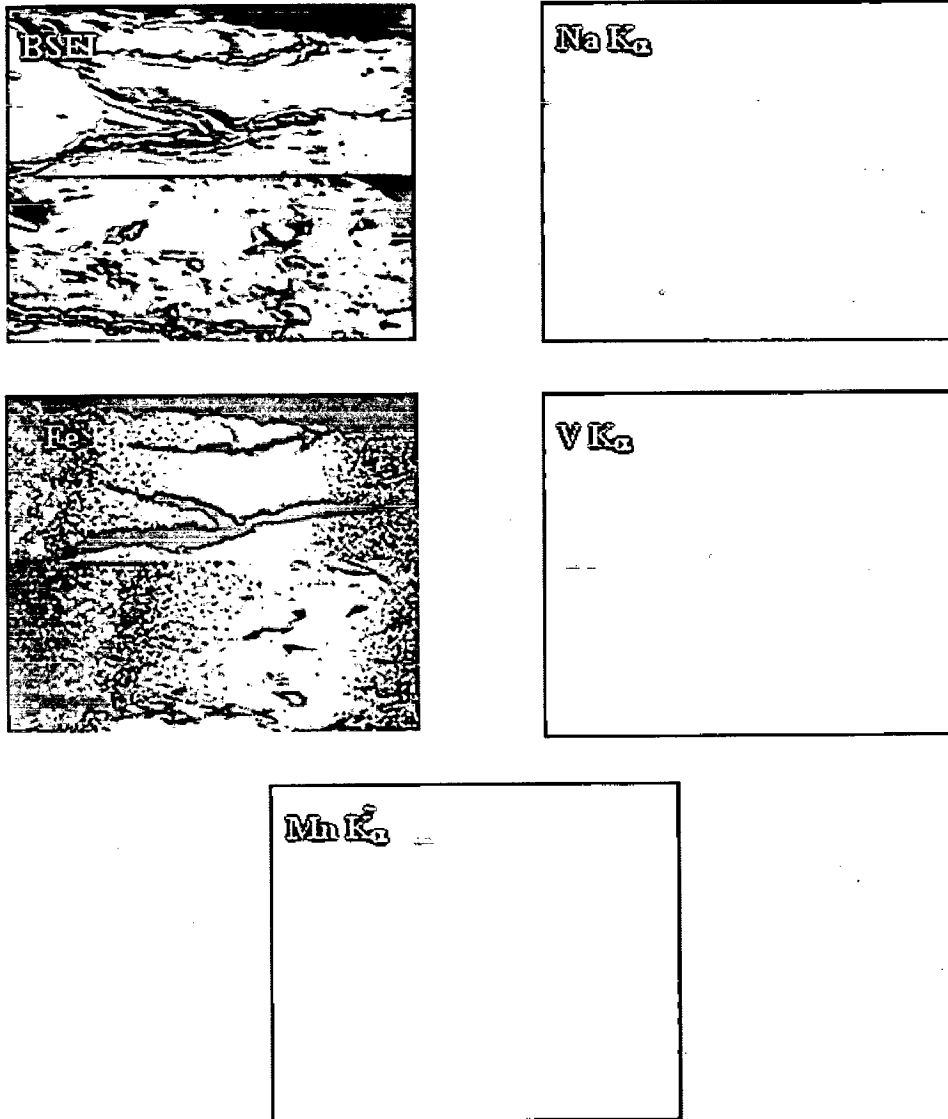


Fig. 6.27: BSEI and X-ray mapping of the cross-section of HAZ of TIG weldment in GrA1 boiler steel subjected to cyclic oxidation in Na₂SO₄- 60% V₂O₅ at 900°C for 50 cycles, 200X.

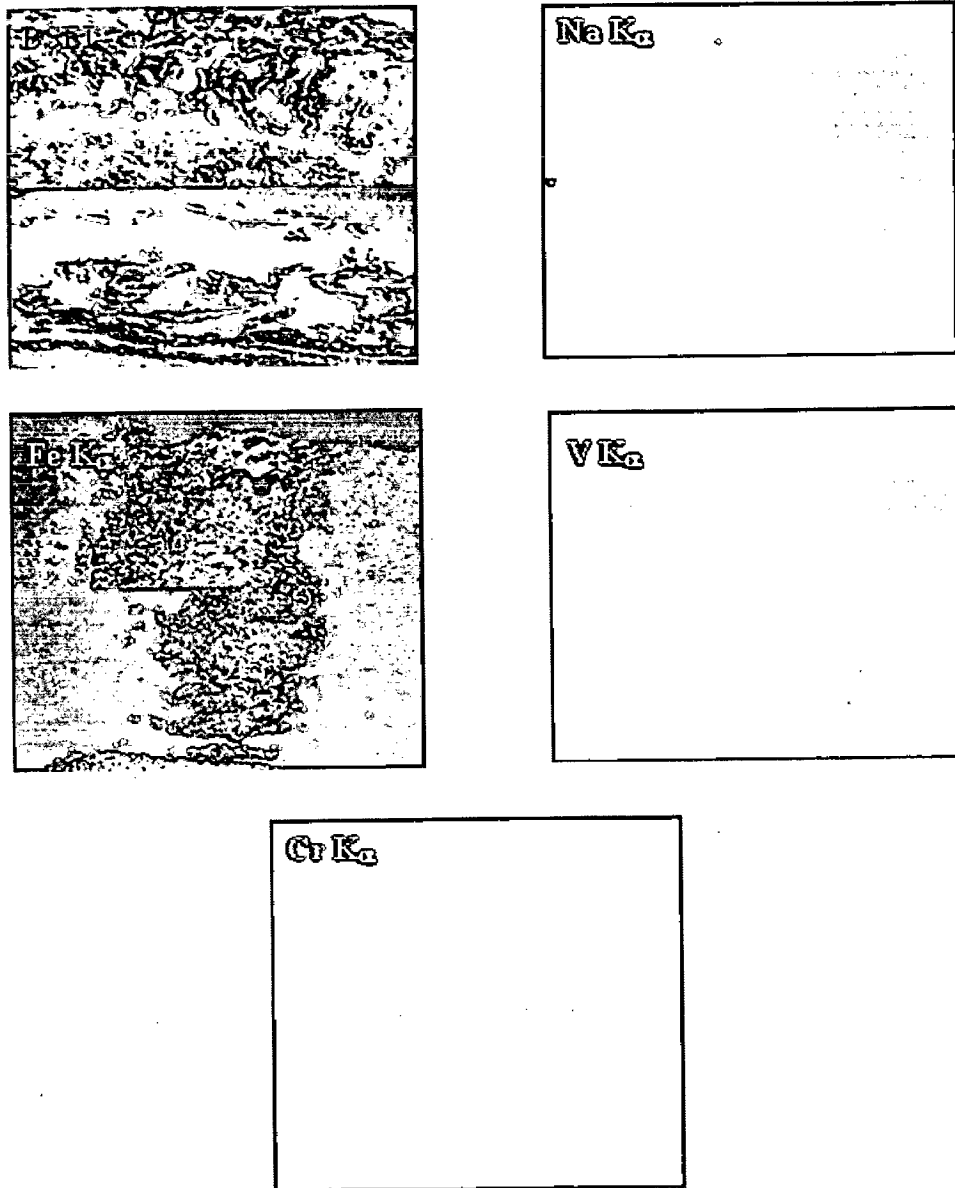


Fig. 6.28: BSEI and X-ray mapping of the cross-section of weld regions of TIG weldment in T11 boiler steel subjected to cyclic oxidation in Na_2SO_4 -60% V_2O_5 at 900°C for 50 cycles, 200X.

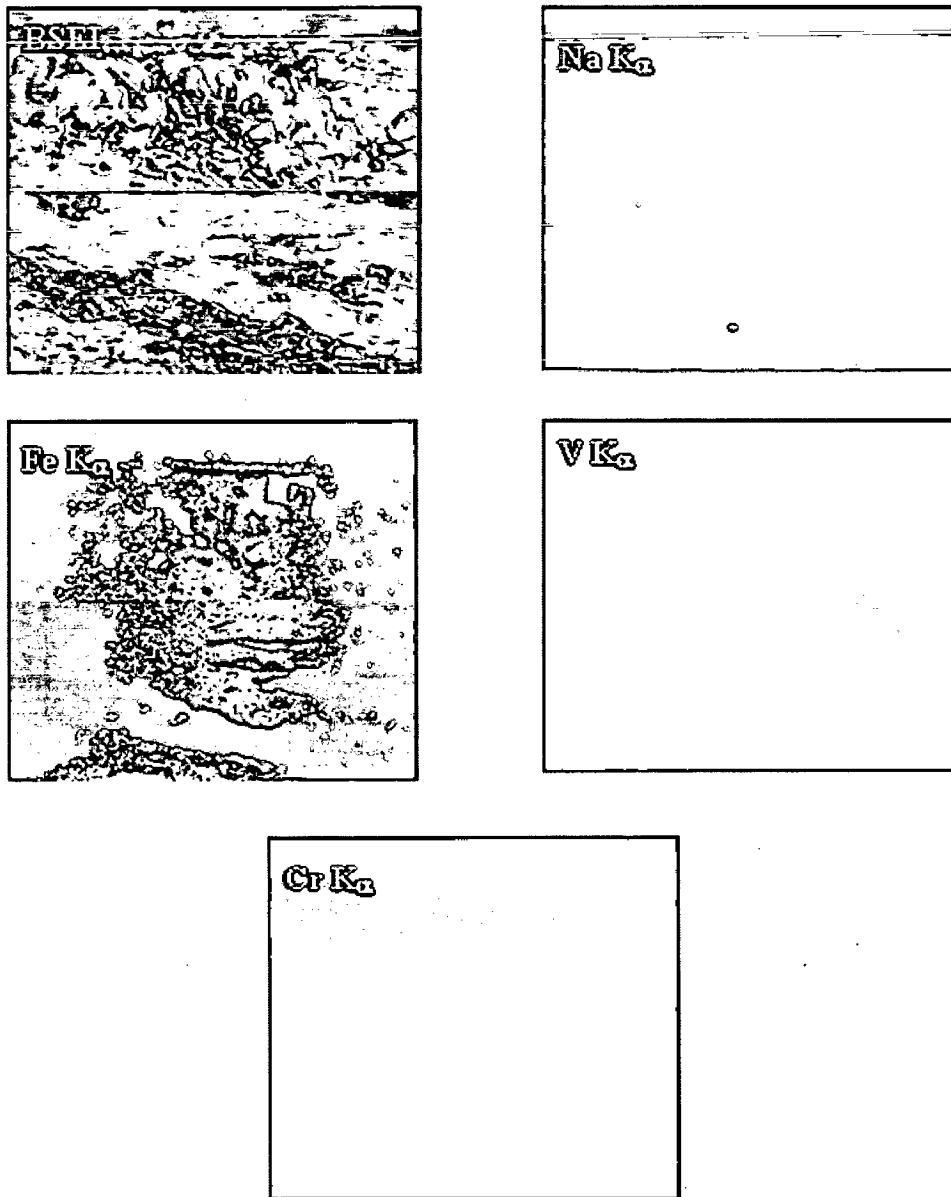


Fig. 6.29: BSEI and X-ray mapping of the cross-section of HAZ regions of TIG weldment in T11 boiler steel subjected to cyclic oxidation in Na_2SO_4 - 60% V_2O_5 at 900°C for 50 cycles, 200X.

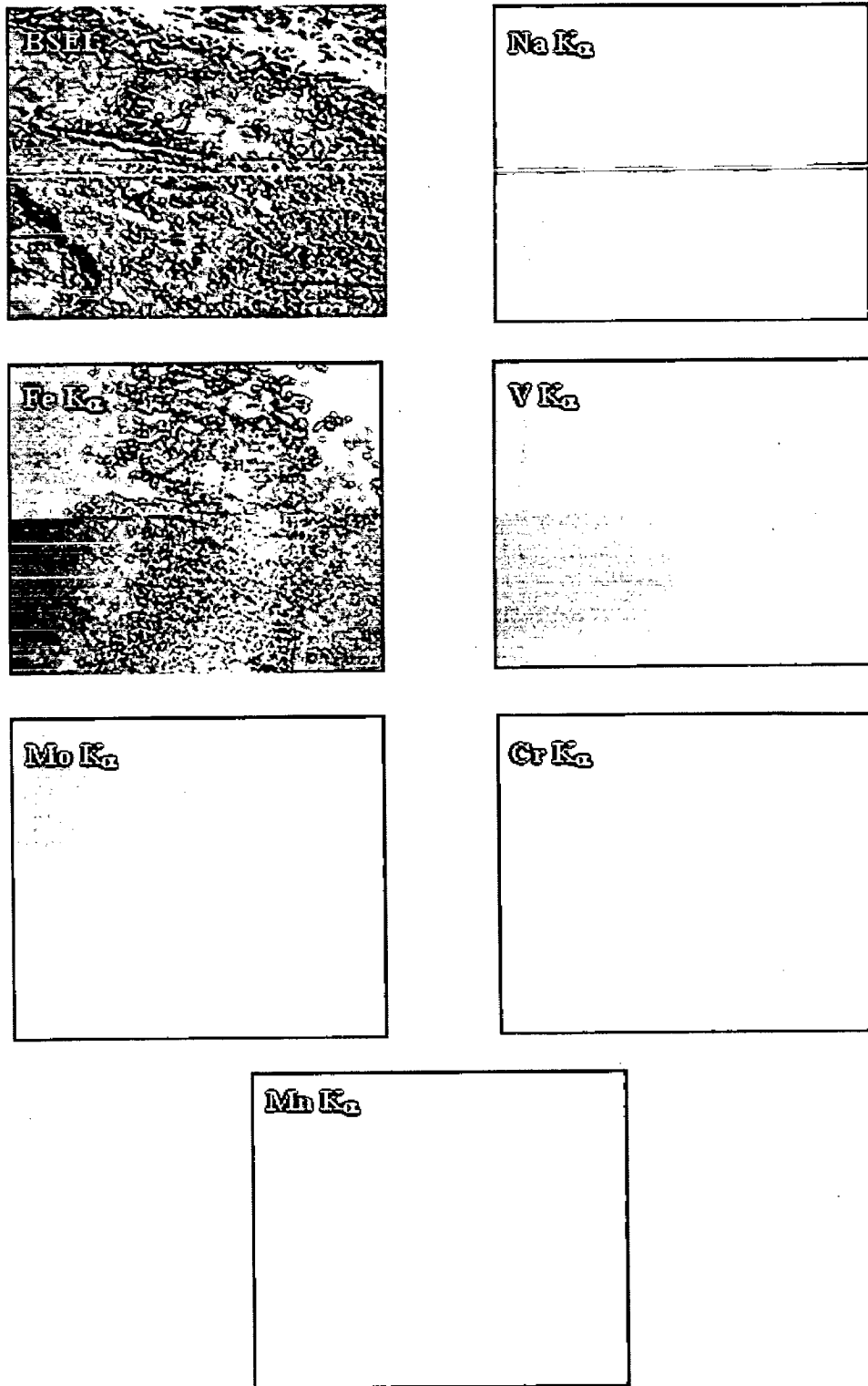


Fig. 6.30: BSEI and X-ray mapping of the cross-section of weld regions of TIG weldment in T22 boiler steel subjected to cyclic oxidation in $\text{Na}_2\text{SO}_4 - 60\% \text{V}_2\text{O}_5$ at 900°C for 50 cycles, 200X.

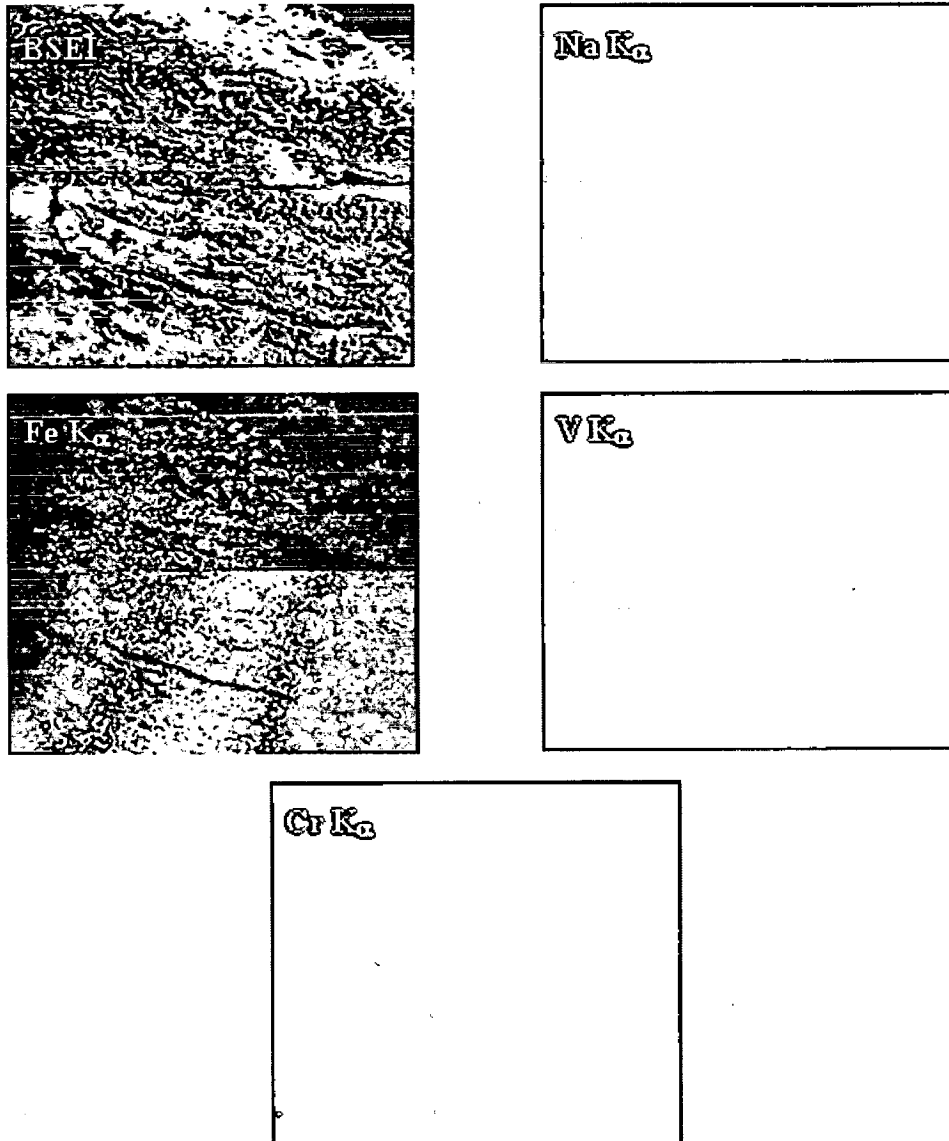


Fig. 6.31: BSEI and X-ray mapping of the cross-section of HAZ regions of TIG weldment in T22 boiler steel subjected to cyclic oxidation in Na_2SO_4 - 60% V_2O_5 at 900°C for 50 cycles, 200X.

PART (B) HOT CORROSION STUDIES ON DIFFERENT REGIONS OF STEEL WELDMENTS IN MOLTEN SALT ENVIRONMENT

This part of chapter 6 deals with the critical examination of corrosion products and the behaviour of different regions of steels weldments when subjected to high temperature cyclic oxidation in Na_2SO_4 -60% V_2O_5 at 900°C for 50 cycles. The samples were visually examined at the end of each cycle during study. Efforts have been made to understand the mechanism of corrosion.

The corrosion products were analysed with XRD, SEM/EDAX and EPMA. The results for different regions of weldment in steels have been reported under different subheadings. In view of the thermogravimetric data for the each base metal is reported along with the each regions of the weldment. The parabolic rate constants and scale thicknesses have been evaluated.

6.2 RESULTS

6.2.1 Different Regions of SMAW Weldment i.e. Base Metal, Weld Metal and HAZ exposed to Molten Salt at 900°C in GrA1 Steel

6.2.1.1 Visual Examination

Macro morphology of the oxide scale for different regions of SMAW weldment after hot corrosion in Na_2SO_4 -60% V_2O_5 at 900°C for 50 cycles is shown in Fig. 6.32. For base metal the sky grey colour scale appeared on the surface from 5th cycle onward which was fragile and started spalling. Exfoliation of the top scale was observed from 30th cycle onward. Scale cracked around 36th cycle and there was gradual increase in the width of cracks for every subsequent cycle. Whereas in case of weld metal black colour scale appeared on the whole surface from the 1st cycle itself and spalling was observed from the beneath during 22nd cycle. Similarly appearance of blackish colour in the oxide scale of HAZ was noticed from the 1st cycle. Little spalling of oxide scale in HAZ has appeared around 15th cycle. Significant cracks were seen in the oxide scale of HAZ from 42nd cycle onward.

6.2.1.2 Thermogravimetric Data

Weight change expressed in mg/cm^2 has been plotted in Fig. 6.33 as a function of time expressed in number of cycles for the weld metal, base metal and HAZ regions of SMAW weldment in GrA1 steel. Total weight gain after 50 cycles of hot corrosion for base metal is almost 3.4 times more than the total weight gain value of HAZ in GrA1 steel. Although the weight gain value of base metal is around 2.8 times more than that of weld metal.

The $(\text{weight gain/unit area})^2$ plot against number of cycles Fig. 6.34 further confirms that parabolic law is followed by all the three regions. The values of parabolic rate constant, K_p ($10^{-8} \text{ g}^2 \text{ cm}^{-4} \text{ s}^{-1}$) are 49.394, 6.055 and 4.148 for base metal, weld metal and HAZ respectively.

6.2.1.3 X-ray Diffraction Analysis

X-ray diffraction analysis for corroded base metal, weld metal and HAZ is shown in Fig. 6.35 and these diffractograms has almost similar phases for all the regions. As obvious from the composition all the regions have indicated the formation of iron oxide (Fe_2O_3). Where as intense peaks of Fe_2O_3 along with Fe_3O_4 are indicated in the oxide scale of the base metal.

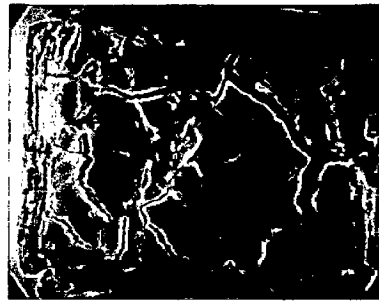
6.2.1.4 Scale Thickness Measurement

Scanning electron back scattered micrographs for different regions of SMAW weldment in GrA1 steel after hot corrosion in molten salt at 900°C for 50 cycles are shown in Fig. 6.36. Very thick oxide scale was identified in case of base metal and was around 2.6 times more than the scale thickness measured for HAZ. The oxide scale thickness values for base metal, weld metal and HAZ are 2.177, 0.9 and 0.821 mm respectively.

6.2.1.5 SEM/EDAX Analysis

6.2.1.5.1 Surface Morphology

SEM morphology and EDAX analysis for different regions of SMAW weldment in GrA1 steel after cyclic hot corrosion are shown in Fig. 6.37. The oxide scale of weld metal contains nodules both large and small in size as can be seen in Fig. 6.37(a). The composition of the top scale is mainly Fe_2O_3 (96.41%) and MnO (3.28%) whereas inner scale contains Fe_2O_3 (91.34%) with Na_2O (2.60%), MnO (2.82%), SiO_2 (1.30% and S (1.12%). SEM micrograph Fig. 6.37 (b) for HAZ in steel also indicates the formation of similar types of oxides contains Fe_2O_3 (97.11%), MnO (1.23%) and Na_2O (1.16%) at point 2. The grain boundary are rich in Fe_2O_3 (96.98%) and MnO (2.31%) point 1.



(a)



(b)



(c)

Fig. 6.32: Macrographs of different regions of SMAW weldments in GrA1 steel subjected to cyclic hot corrosion in Na_2SO_4 -60% V_2O_5 at 900°C for 50 cycles (a) Base Metal, (b) Weld Metal and (c) HAZ.

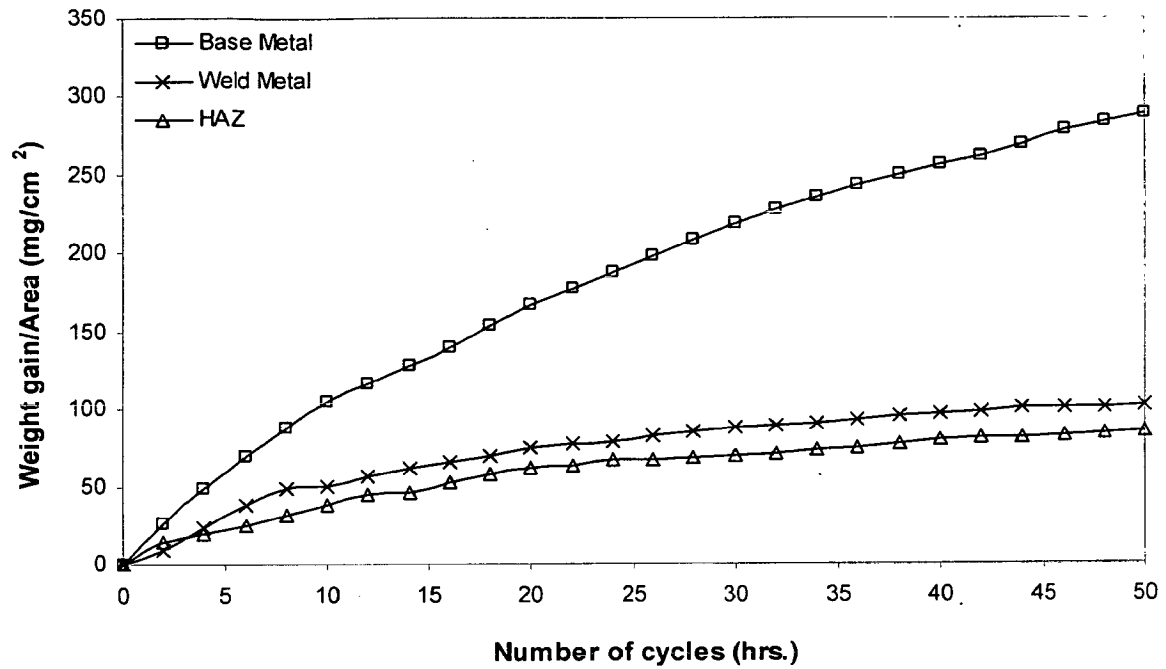


Fig. 6.33: Weight gain plot for different regions of SMAW weldment in GrA1 steels exposed to $\text{Na}_2\text{SO}_4\text{-60}\%\text{V}_2\text{O}_5$ at 900°C for 50 cycles.

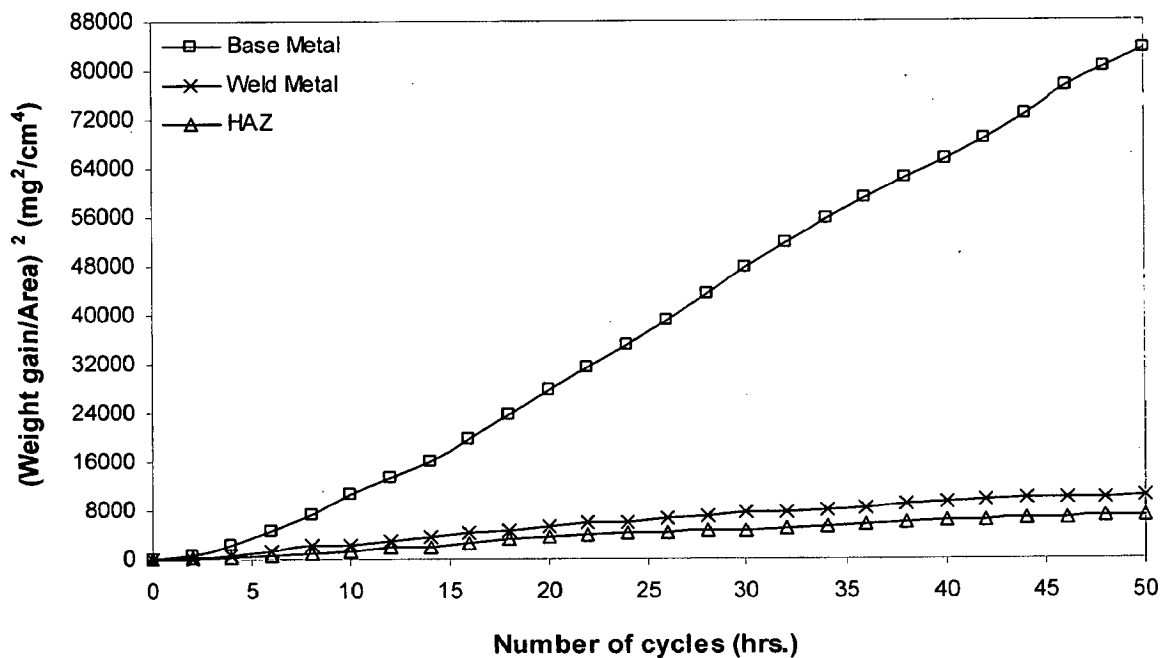


Fig. 6.34: Weight gain square (mg^2/cm^4) plot for different regions of SMAW weldment in GrA1 steel exposed to cyclic hot corrosion in $\text{Na}_2\text{SO}_4\text{-60}\%\text{V}_2\text{O}_5$ at 900°C for 50 cycles.

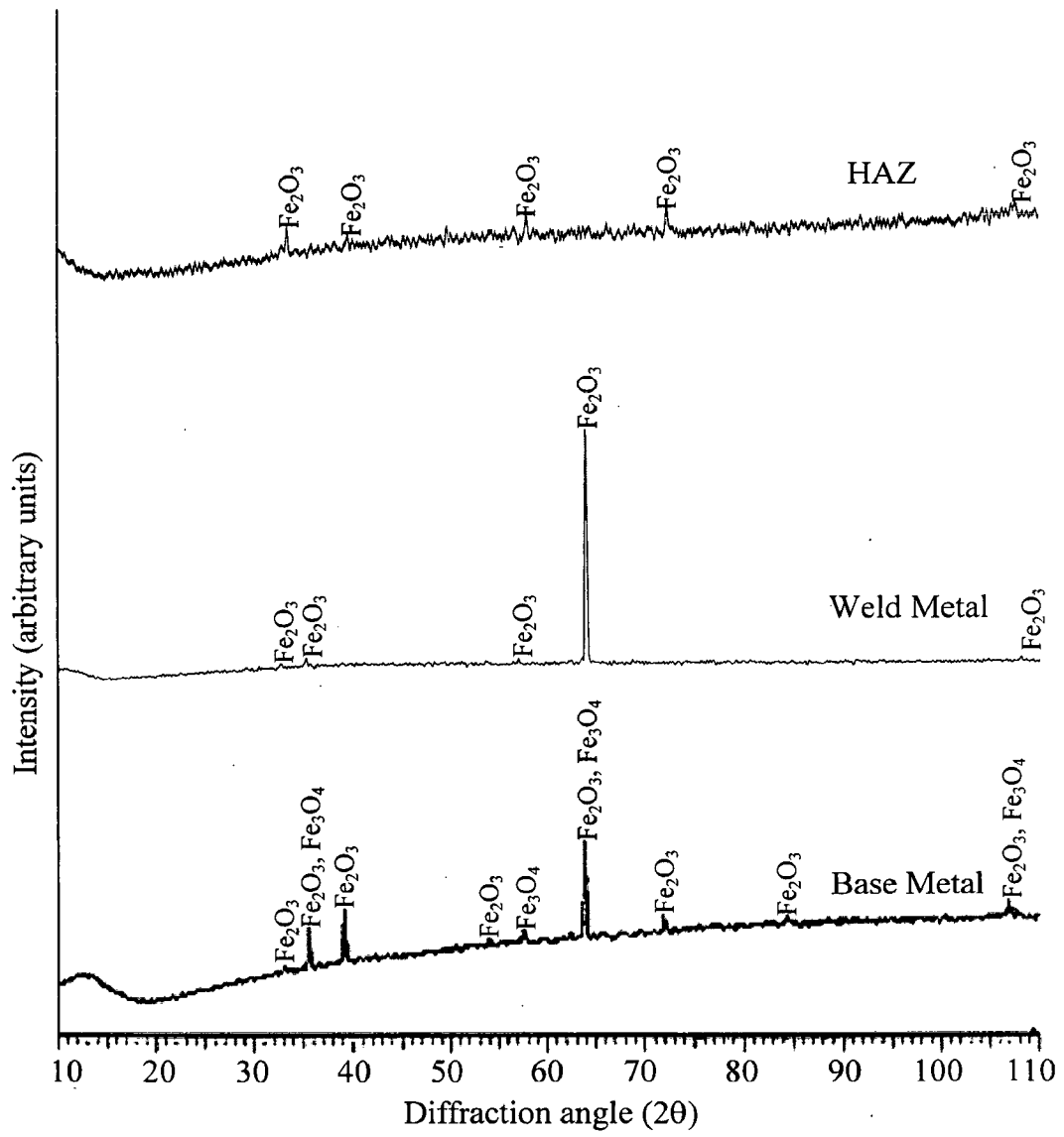
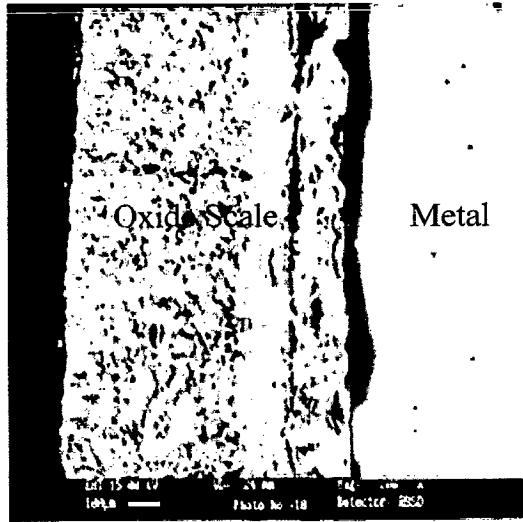
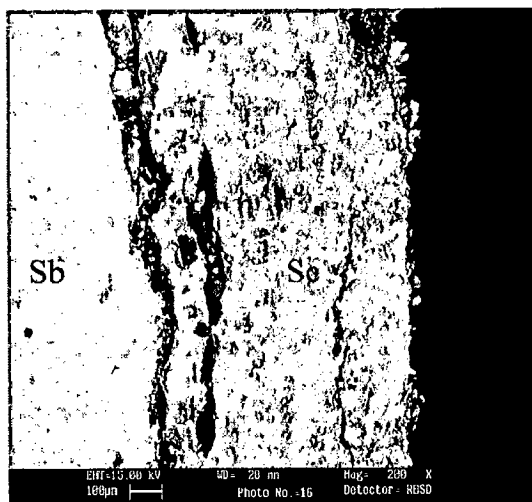


Fig. 6.35: X-ray diffraction profiles for different regions of SMAW weldment in GrA1 steel exposed to cyclic hot corrosion in Na₂SO₄-60%V₂O₅ at 900°C for 50 cycles.



(a)



(b)

Fig. 6.36: SEM back scattered image of the cross section of different regions of SMAW weldment in GrA1 steel exposed to cyclic hot corrosion in $\text{Na}_2\text{SO}_4\text{-60\%V}_2\text{O}_5$ at 900°C for 50 cycles (a) Weld Metal, 200X (b) HAZ, 200X.

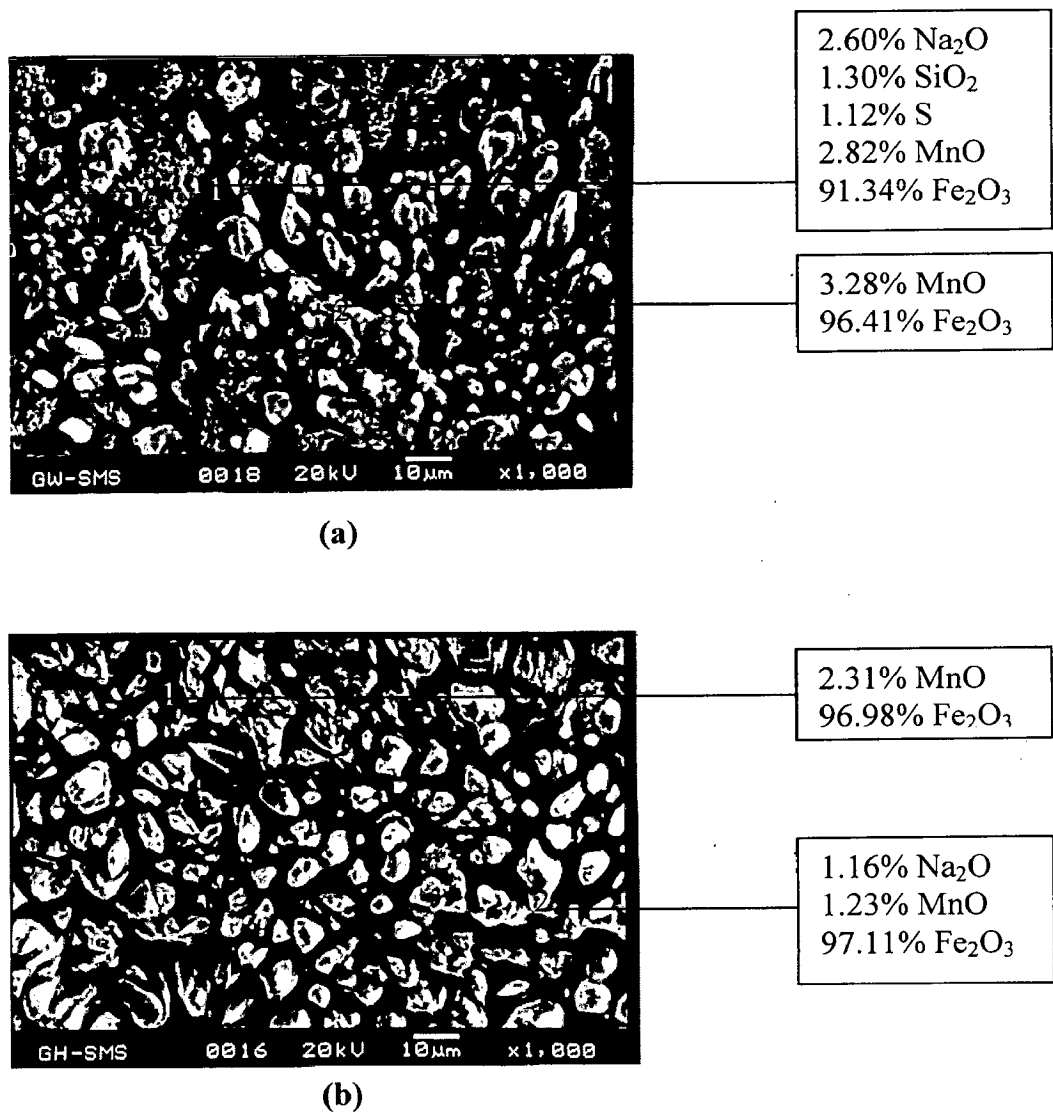


Fig. 6.37: Surface morphology and EDAX analysis for different regions of SMAW weldment in GrA1 steel exposed to Na₂SO₄ -60% V₂O₅ at 900°C for 50 cycles (a) Weld Metal, 1000X and (b) HAZ, 1000X.

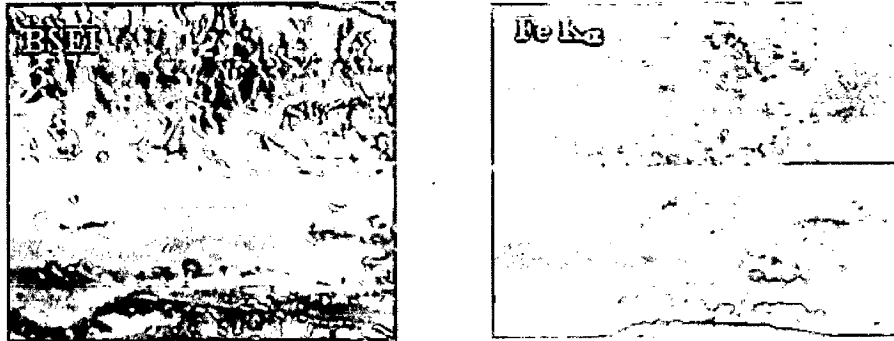


Fig. 6.38: BSEI and X-ray mapping of the cross-section of weld metal of SMAW weldment in GrA1 steel subjected to cyclic oxidation in Na_2SO_4 -60% V_2O_5 at 900°C for 50 cycles, 200X.

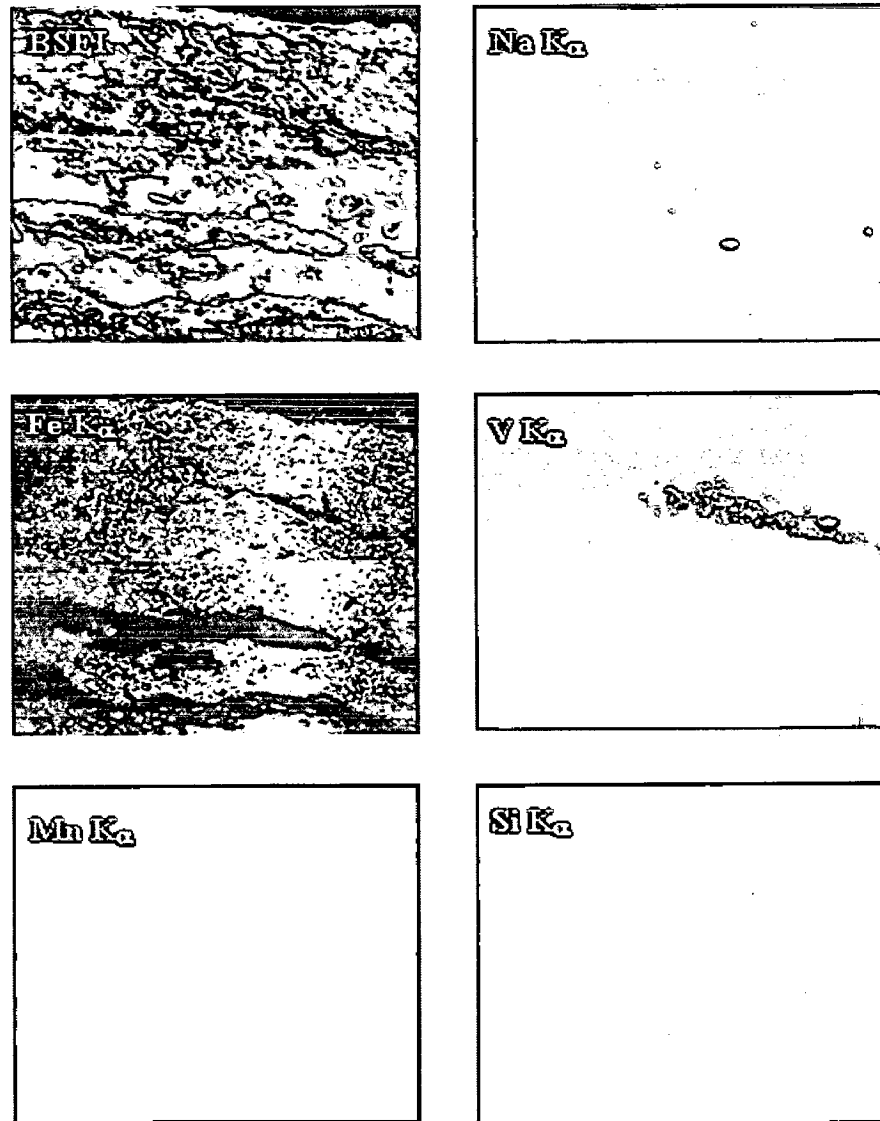


Fig. 6.39: BSEI and X-ray mapping of the cross-section of HAZ of SMAW weldment in GrA1 steel subjected to cyclic oxidation in Na_2SO_4 -60% V_2O_5 at 900°C for 50 cycles, 200X.

6.2.1.6 EPMA Analysis

The EPMA of the cross-section of the exposed specimen (weld metal) Fig. 6.38 indicates mainly presence of iron in the upper and lower part of the scale with internal oxidation formed near the interface of metal and oxide. The EPMA analysis for the exposed cross-section of HAZ is shown in Fig. 6.39. EPMA indicates the scale mainly consists of oxides of iron with some vanadium, sodium, Mn and Si. Concentration of Vanadium is more in upper scale where as sodium is scattered in both scale equally. Little amount of Mn was also found in the scale.

6.2.2 Different Regions of SMAW Weldment i.e. Base Metal, Weld Metal and HAZ exposed to Molten Salt at 900°C in T11 Steel

6.2.2.1 Visual Examination

Macro morphology of the oxide scale for base metal, weld metal and HAZ regions of SMAW weldments after hot corrosion in Na_2SO_4 -60% V_2O_5 at 900°C for 50 cycles is shown in Fig. 6.40. For weld metal upto 5th cycle the colour of scale turned completely to dark blackish grey. Whereas purplish look appeared in the scale during 42nd cycle and disappeared latter on. Similarly appearance of black colour in the oxide scale of HAZ was noticed from the beginning and remains same in the whole experiment. Little spalling of oxide scale at the edges has appeared around 37th cycle for HAZ. Whereas in case of weld metal scale cracked and started spalling after 29th cycle and there was significant increase in the number of cracks as well as increase in width of these cracks upto 39th cycle. Oxides, light blackish grey in colour started oozing out from the edges below through these cracks after 42nd cycle.

6.2.2.2 Thermogravimetric Data

Weight change (mg/cm^2) variation as a function of time expressed in number of cycles for SMAW weldment in T11 steel after hot corrosion in Na_2SO_4 -60% V_2O_5 at 900°C for 50 cycles are as shown in Fig. 6.41. HAZ regions showed lesser weight gain as compared to base metal and weld metal specimens in the given molten salt environment. The total weight gain (mg/cm^2) for base metal, weld metal and HAZ regions at the end of 50 cycles is 135.801, 144.532 and 93.787 respectively. Extensive spalling and sputtering has limited the study upto 50 cycles. The plot for all the three regions of the steel weldment shows same weight gain during the first few cycles. The behaviour for base metal, weld metal and HAZ regions was almost parabolic with parabolic rate constants; K_p is 10.416, 11.608 and $4.575 \times 10^{-8} \text{ g}^2 \text{ cm}^{-4} \text{ s}^{-1}$ respectively as shown in Fig. 6.42.

6.2.2.3 X-ray Diffraction Analysis

The XRD analysis for different regions of SMAW weldment in T11 steel after exposure to $\text{Na}_2\text{SO}_4\text{-60}\%\text{V}_2\text{O}_5$ at 900°C for 50 cycles is shown in Fig. 6.43 and these diffractograms has almost similar phases for all the three regions. As obvious from the composition all the regions have indicated the formation of iron oxide (Fe_2O_3). Where as some strong peaks of Fe_2O_3 along with MnO are indicated in the oxide scale of weld metal and HAZ.

6.2.2.4 Scale Thickness Measurement

The scale thickness was measured from SEM back scattered images as shown in Fig. 6.44. Very thick oxide scale was identified in case of base metal and was around 1.27 times more than the scale thickness measured for weld metal. The scale thickness values are 1.157, 0.905 and 0.993 mm for base metal, weld metal and HAZ regions respectively. Wider internal oxidation was found in case of HAZ than weld metal.

6.2.2.5 SEM/EDAX Analysis

6.2.2.5.1 Surface Morphology

SEM micrograph of the scale formed after 50 cycles of hot corrosion in molten salt at 900°C for different regions of SMAW weldment in T11 steel are shown in Fig. 6.45. The micrograph of top surface of the scale in case of weld metal indicates intergranular cracking. EDAX analysis shows the presence of little amount of MnO (2.83%) in the scale at point 2 in micrograph of Fig. 6.45 (a). The subscale has less content of MnO (2.42%) with main phase being Fe_2O_3 (96.36%) point 1. Whereas in case of HAZ inner scale is mainly Fe_2O_3 (94.93%) with MnO (1.58%), Na_2O (2.50%) at point 1. At point 2 on micrograph in Fig. 6.45 (b) presence of Fe_2O_3 (43.60%) with MoO_3 (11.98%), Na_2O (38.14%), SiO_2 (4.79%) and P_2O_5 (1.13%).

6.2.2.6 EPMA Analysis

The EPMA of the cross-section of the exposed weld metal specimen (SMAW weldment in T11 steel) Fig. 6.46 indicates mainly presence of iron in the whole of the scale, some sodium has diffused into scale through the cracks. There is presence of very thin irregular layer of Cr just above the metal in the lower oxide scale.

EPMA shows the thick scale for HAZ where iron is present throughout the scale (Fig. 6.47). Na is seen in the lower scale where the more cracks are present in the scale. Concentration of Mn is very small in the scale.

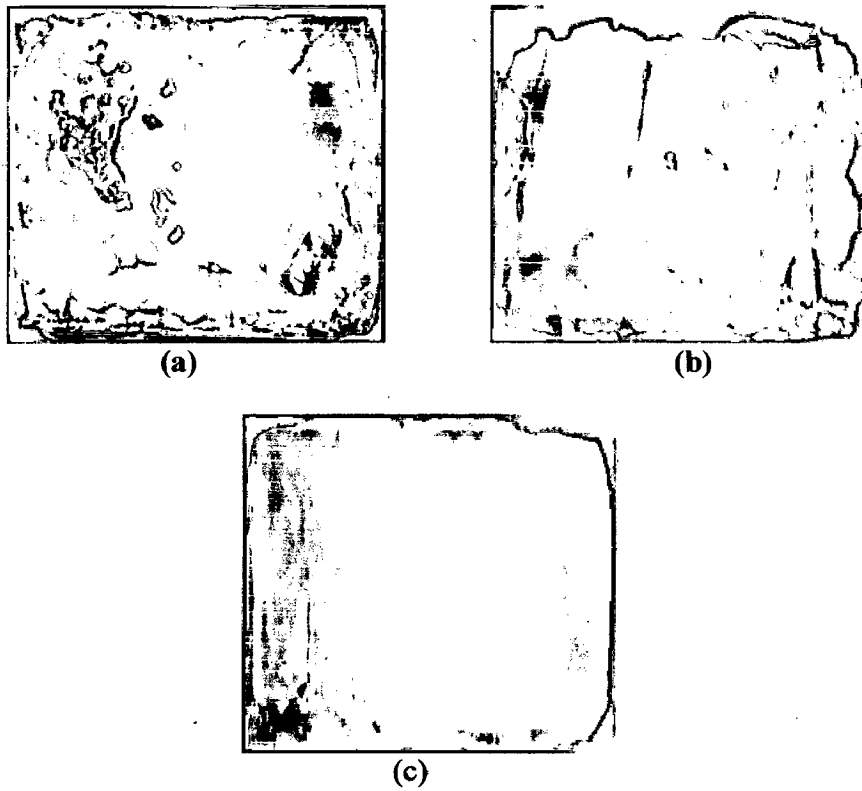


Fig. 6.40: Macrographs of different regions of SMAW weldments in T11 steel subjected to cyclic hot corrosion in $\text{Na}_2\text{SO}_4\text{-60\%V}_2\text{O}_5$ at 900°C for 50 cycles (a) Base Metal, (b) Weld Metal and (c) HAZ.

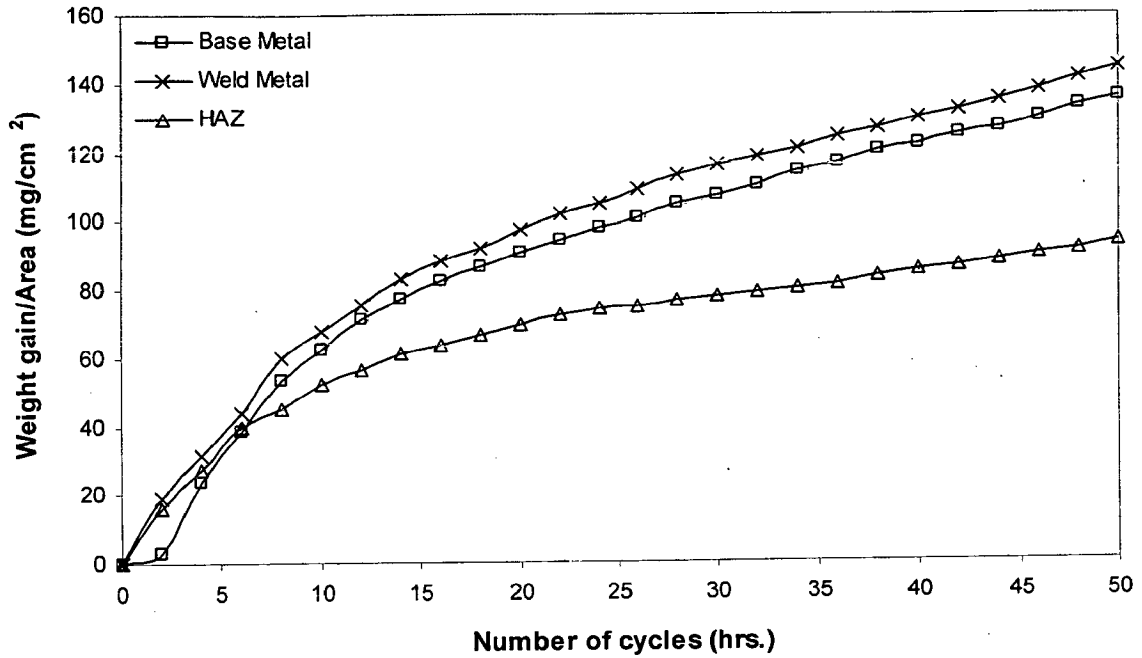


Fig. 6.41: Weight gain plot for different regions of SMAW weldment in T11 steels exposed to $\text{Na}_2\text{SO}_4\text{-60}\%\text{V}_2\text{O}_5$ at 900°C for 50 cycles.

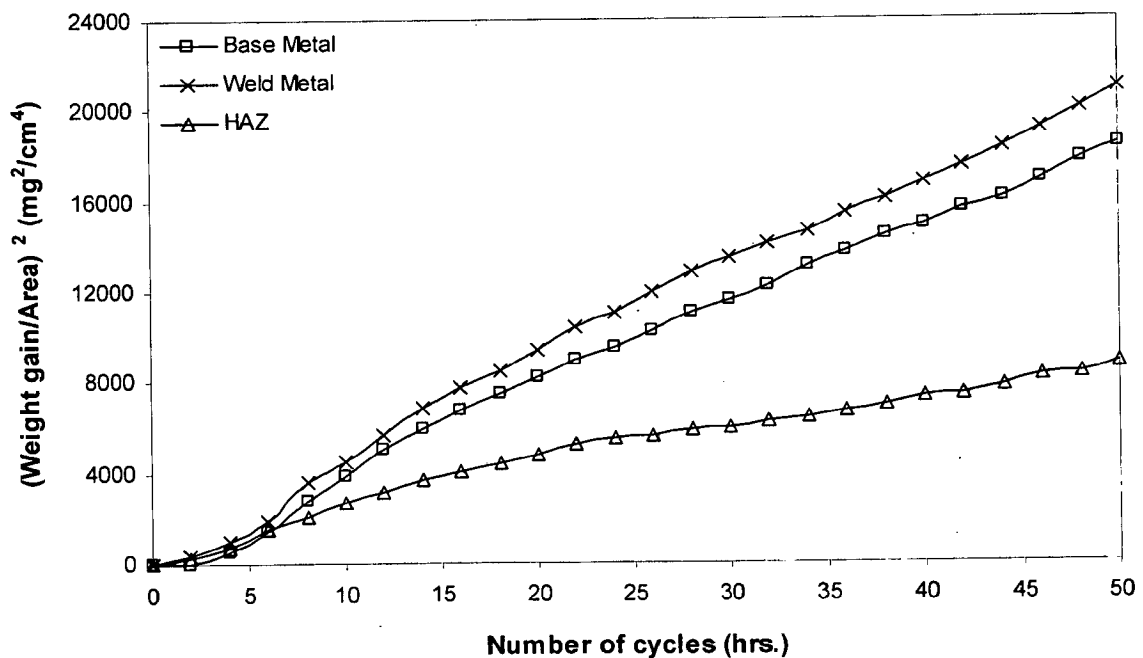


Fig. 6.42: Weight gain square (mg^2/cm^4) plot for different regions of SMAW weldment in T11 steel exposed to cyclic hot corrosion in $\text{Na}_2\text{SO}_4\text{-60}\%\text{V}_2\text{O}_5$ at 900°C for 50 cycles.

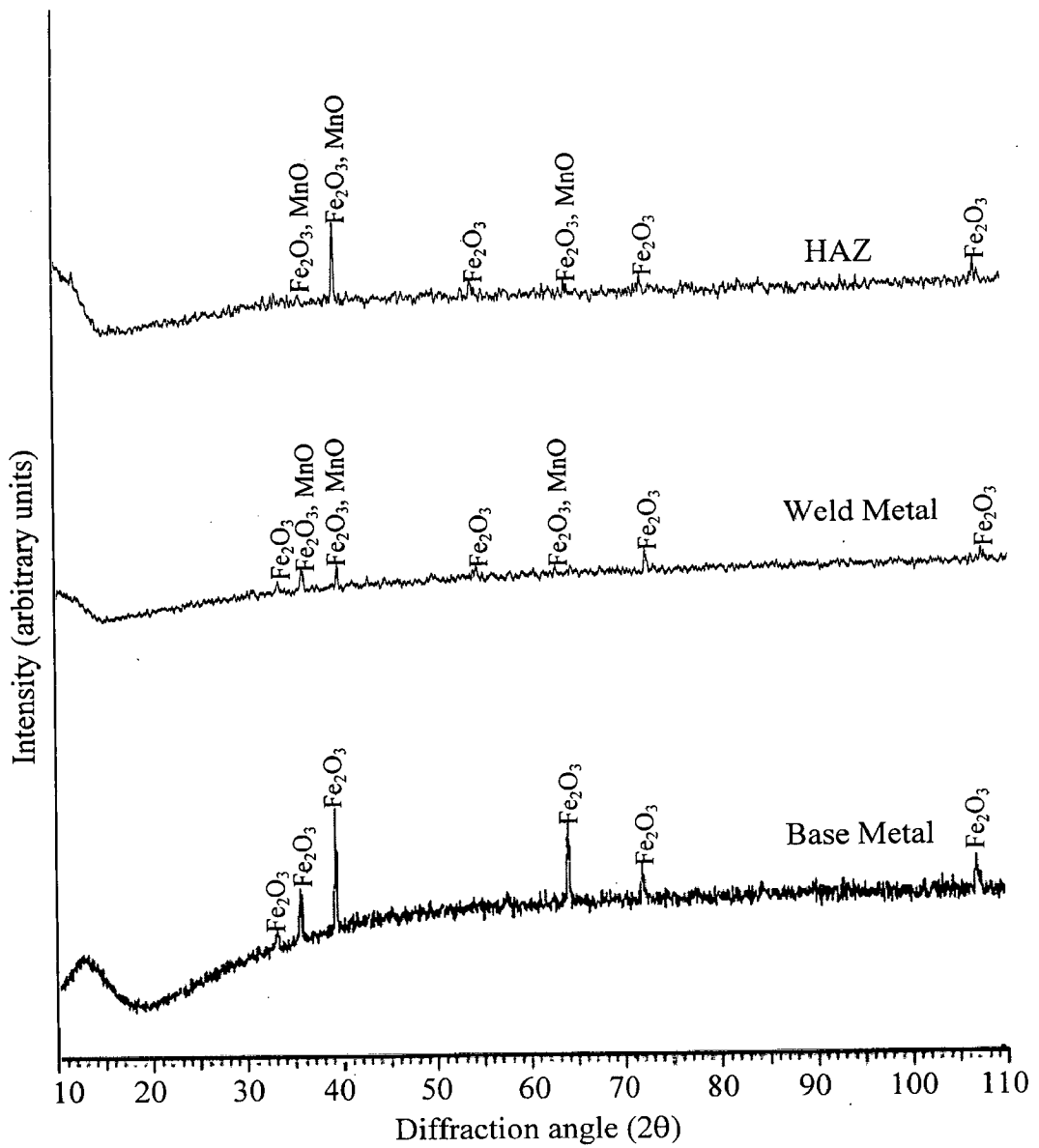
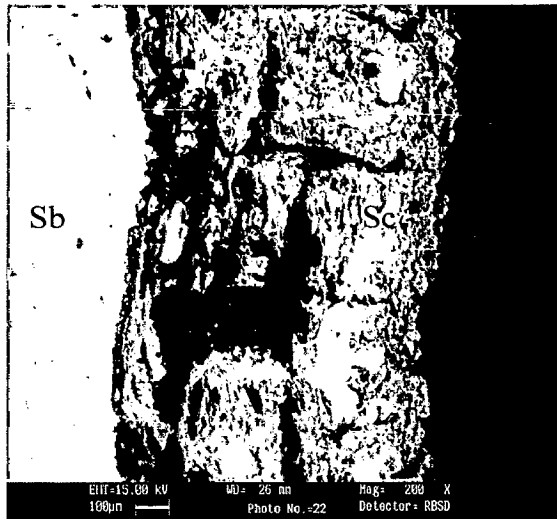
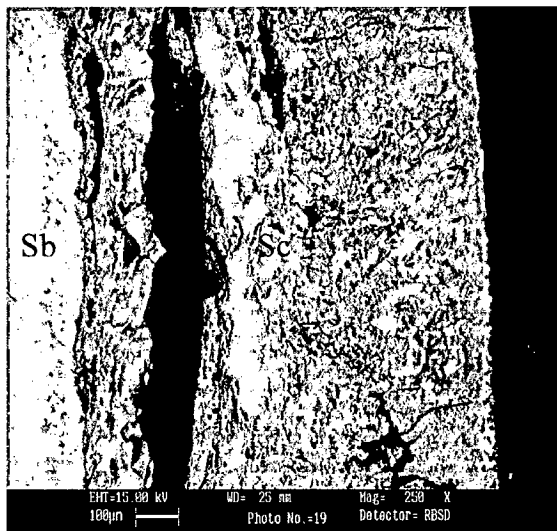


Fig. 6.43: X-ray diffraction profiles for different regions of SMAW weldment in T11 steel exposed to cyclic hot corrosion in Na₂SO₄-60%V₂O₅ at 900°C for 50 cycles.

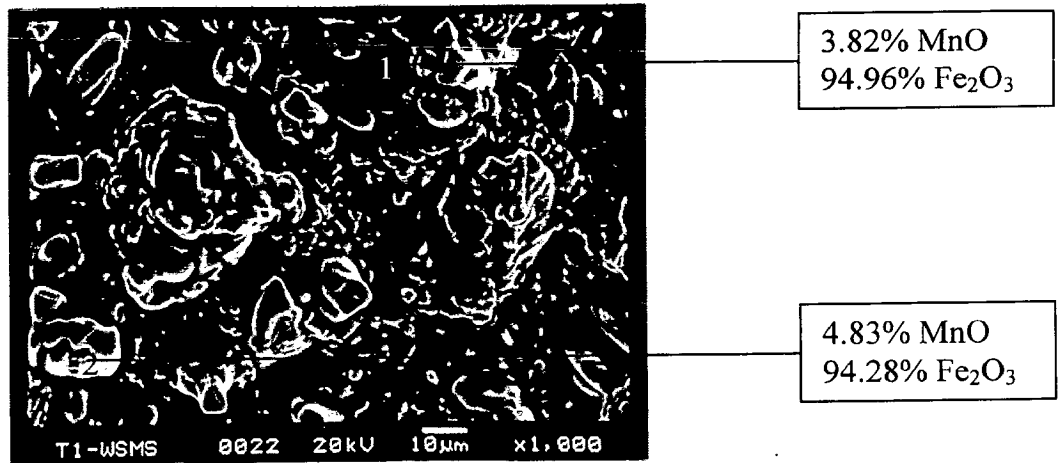


(a)

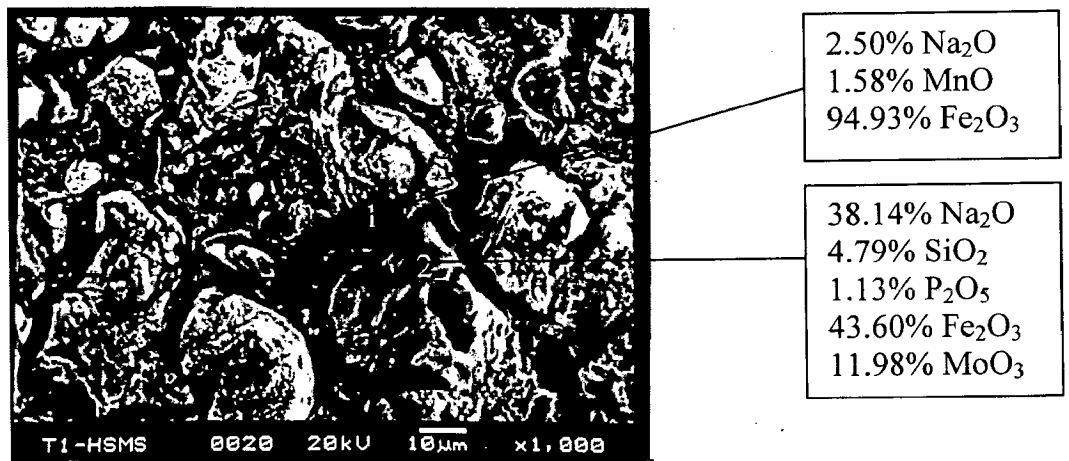


(b)

Fig. 6.44: SEM back scattered image of the cross section of different regions of SMAW weldment in T11 steel exposed to cyclic hot corrosion in $\text{Na}_2\text{SO}_4\text{-60\%V}_2\text{O}_5$ at 900°C for 50 cycles (a) Weld Metal, 200X (b) HAZ, 250X.



(a)



(b)

Fig. 6.45: SEM micrographs showing surface morphology and EDAX analysis for different regions of SMAW weldment in T11 steel exposed to Na₂SO₄ -60% V₂O₅ at 900°C for 50 cycles (a) Weld Metal, 1000X and (b) HAZ, 1000X.

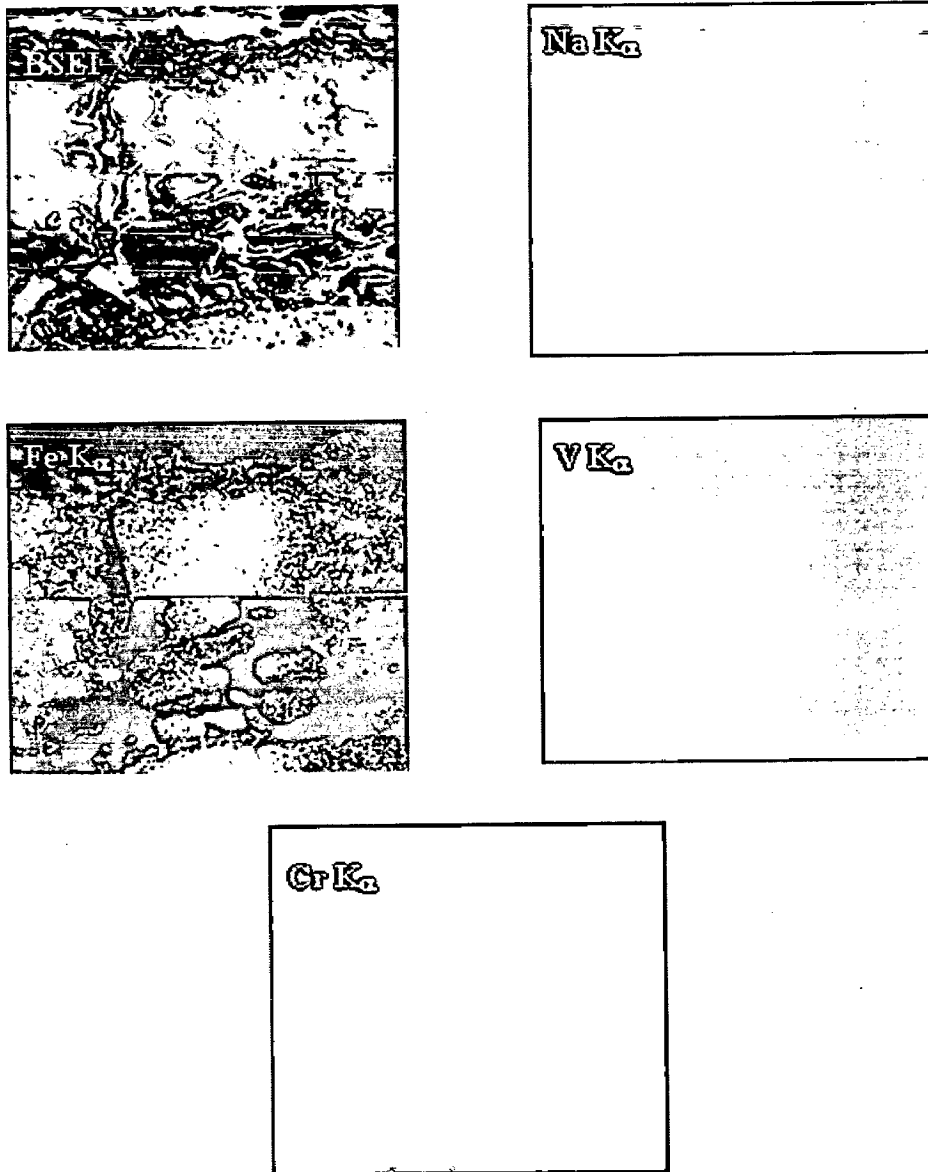


Fig. 6.46: BSEI and X-ray mapping of the cross-section of weld metal of SMAW weldment in T11 steel subjected to cyclic oxidation in Na_2SO_4 -60% V_2O_5 at 900°C for 50 cycles, 200X.

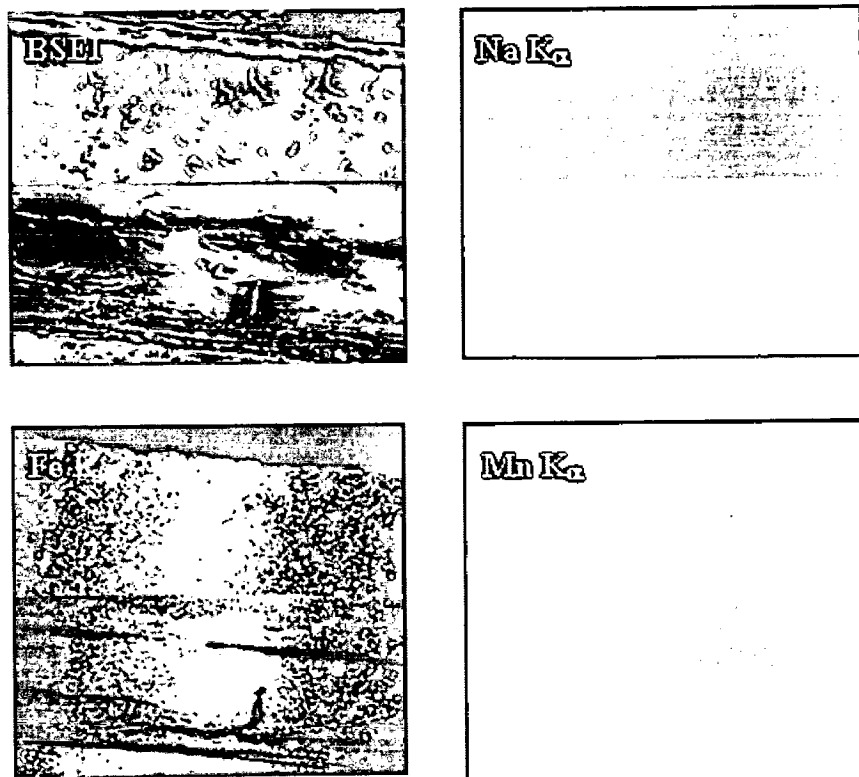


Fig. 6.47: BSEI and X-ray mapping of the cross-section of HAZ of SMAW weldment in T11 steel subjected to cyclic oxidation in Na_2SO_4 -60% V_2O_5 at 900 °C for 50 cycles, 200X.

6.2.3 Different Regions of SMAW Weldment i.e. Base Metal, Weld Metal and HAZ exposed to Molten Salt at 900°C in T22 Steel

6.2.3.1 Visual Examination

Surface macrographs for different regions of SMAW weldment in T22 steel are shown in Fig. 6.48. The colour of surface of all samples after exposure changed from blackish gray to blackish brown colour and thereafter up to the end of the study all the samples retained in this colour. In case of weld metal some spalling of scale was indicated in the form of very small particles from 10th cycle on ward. Little increase in spalling was observed during 16th cycle. Very small cracks were observed in the scale around 33rd cycle. Little oxide protrusions from the beneath were noticed during last four cycles.

In case of HAZ the spalling started after 8th cycle. Oxide scale cracked at surface and edges just after 28th cycle and slight increase in the number and width of these cracks has been seen for the subsequent cycles. Material from the inside oozed out through these cracks.

6.2.3.2 Thermogravimetric Data

The weight gain/unit area for the different regions of SMAW weldment in T22 steel is plotted as a function of time expressed in number of cycles in Fig. 6.49. Base metal show more weight gain as compared to weld metal and HAZ specimens in the given molten salt environment. Total weight gain of base metal is 2.93 times more than that of weld metal. These regions have followed the parabolic rate law with parabolic rate constants (K_p) 76.233, 9.388 and $14.818 \times 10^{-8} \text{ g}^2 \text{ cm}^{-4} \text{ s}^{-1}$ for base metal, weld metal and HAZ respectively (Fig. 6.50).

6.2.3.3 X-ray Diffraction Analysis

The X-ray diffractograms for base metal, weld metal and HAZ regions after cyclic hot corrosion in Na_2SO_4 -60% V_2O_5 at 900°C are shown in Fig. 6.51. Identical phases have been revealed in the surface scale of all the three regions. The XRD analysis revealed the formation of weak peaks of MnO, Cr_2O_3 along with iron oxide (Fe_2O_3) as main phase for HAZ.

6.2.3.4 Scale Thickness Measurement

SEM back scattered micrographs for the corroded cross-sections of weld metal and HAZ steel are shown in Fig. 6.52. The scale thickness values are 1.104 and 0.931 mm for weld metal and HAZ respectively. The scale of base metal which has completely undergone spalling and cracking and so its thickness can not be estimated.

6.2.3.5 SEM/EDAX Analysis

6.2.3.5.1 Surface Morphology

After hot corrosion the top scale of weld metal consists of MnO (4.06%), SiO₂ (0.94%) and Fe₂O₃ (94.82%) as shown by SEM/EDAX analysis Fig. 6.53 (a). It has cracks running across the scale and EDAX analysis of these cracks indicates of Fe₂O₃ (92.86%) and MnO (6.12%) point 1. SEM of the HAZ corroded in Na₂SO₄-60%V₂O₅ environment indicated a massive scale having a large crack running through it as evident from Fig. 6.53 (b). The EDAX of the top scale indicates mainly Fe₂O₃ (95.43%) along with Cr₂O₃ (2.86%) and MnO (1.26%). Whereas inner scale presented in Fig. 6.53 (b) shows massive scale along with indication of oozing out of some material through the cracks in the scale. The material that has oozed out from inside is mainly Fe₂O₃ (90.78%) with MnO (5.00%), Cr₂O₃ (2.22%) and SiO₂ (1.36%).

6.2.3.6 EPMA Analysis

The Elemental X-ray mapping of corroded cross-section of weld metal exposed to Na₂SO₄-60%V₂O₅ environment at 900°C indicates mainly iron rich layer at through out of the scale (Fig. 6.54). Where sodium and vanadium are scattered in both of scale but little higher concentration present near to the oxide/metal interface. Chromium is present in very small concentration near substrate metal. Elemental X-ray maps for the corroded cross-section of HAZ shown in Fig. 6.55 indicate the distribution of elements in the scale almost identical to the weld metal. Little higher concentration of chromium is present in top and bottom scale as a thin layer. Whereas Mo and Mn are also present in the scale. Vanadium seems more in bottom scale.

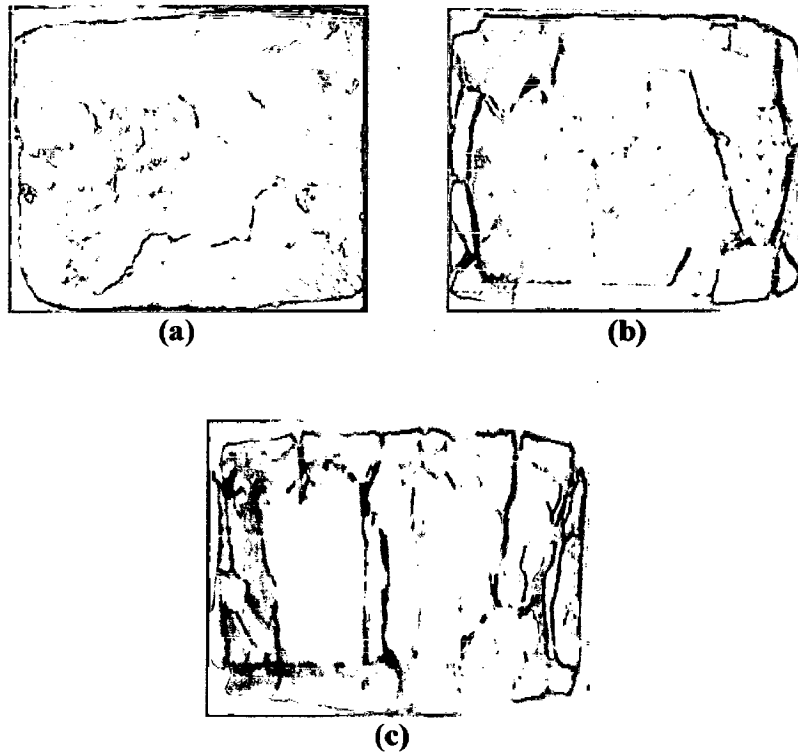


Fig. 6.48: Macrographs of different regions of SMAW weldments in T22 steel subjected to cyclic hot corrosion in $\text{Na}_2\text{SO}_4\text{-60}\%\text{V}_2\text{O}_5$ at 900°C for 50 cycles (a) Base Metal, (b) Weld Metal and (c) HAZ.

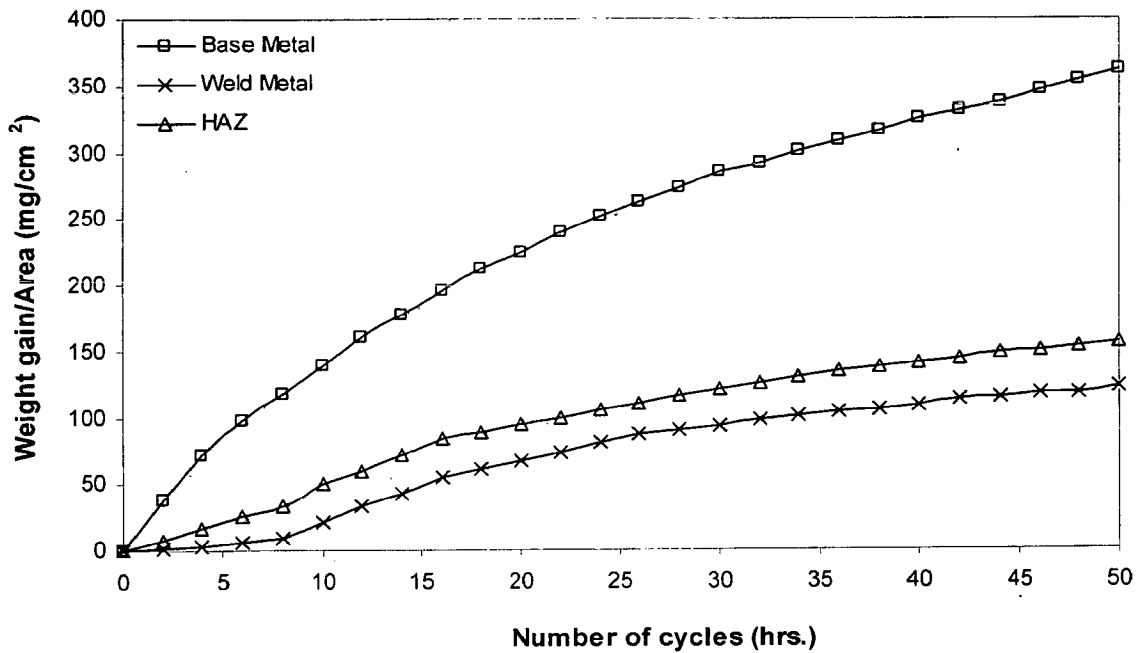


Fig. 6.49: Weight gain plot for different regions of SMAW weldment in T22 steels exposed to $\text{Na}_2\text{SO}_4\text{-60\%V}_2\text{O}_5$ at 900°C for 50 cycles.

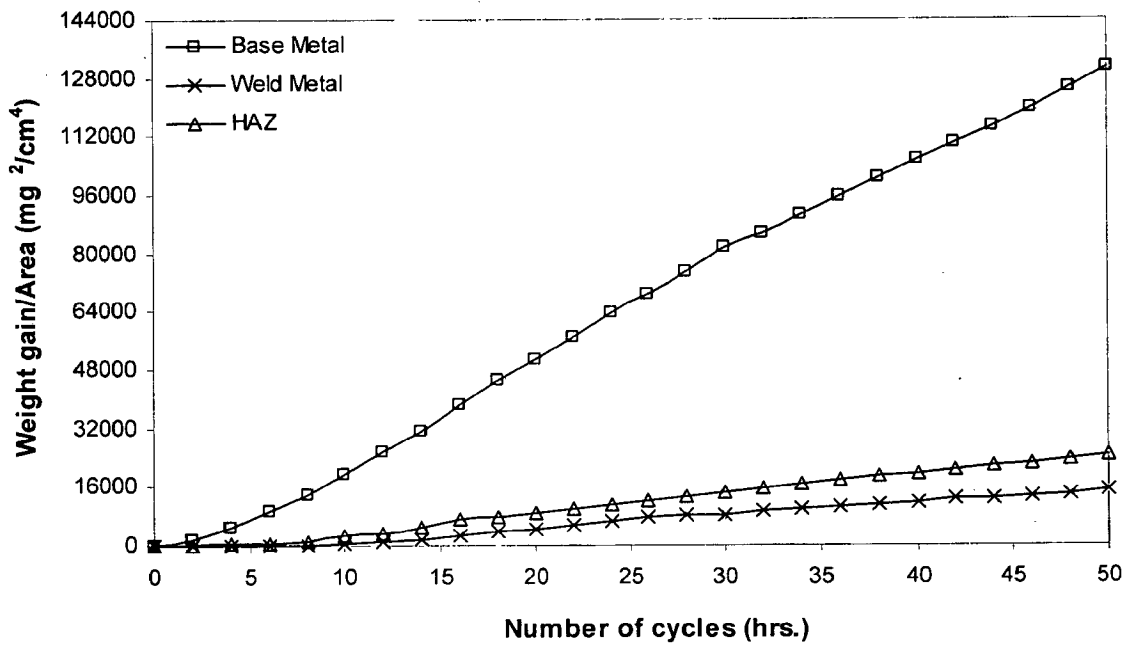


Fig. 6.50: Weight gain square (mg^2/cm^4) plot for different regions of SMAW weldment in T22 steel exposed to cyclic hot corrosion in $\text{Na}_2\text{SO}_4\text{-60\%V}_2\text{O}_5$ at 900°C for 50 cycles.

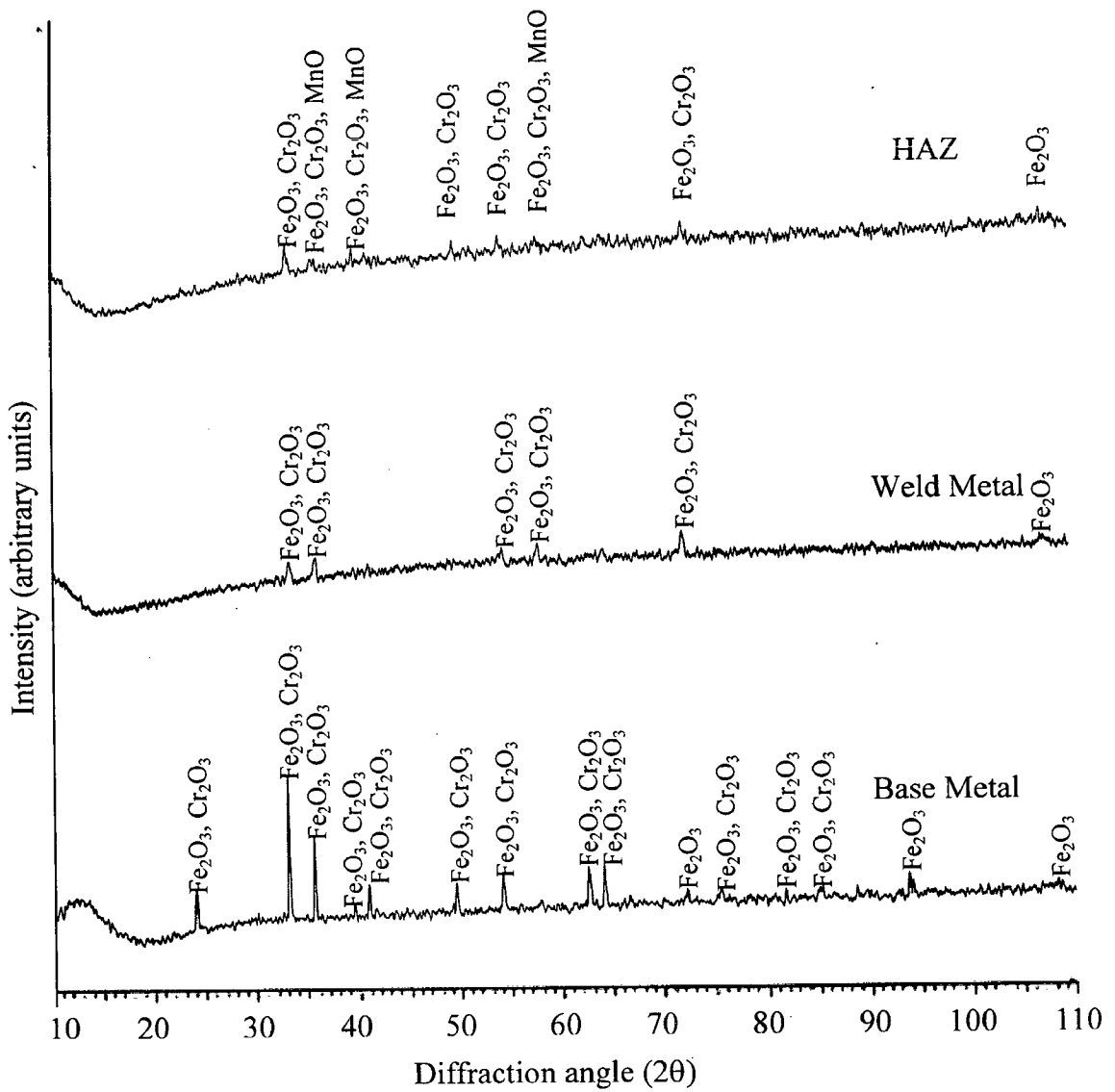
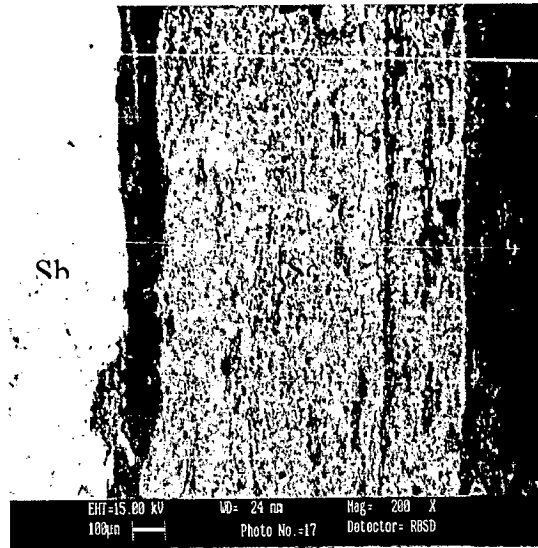
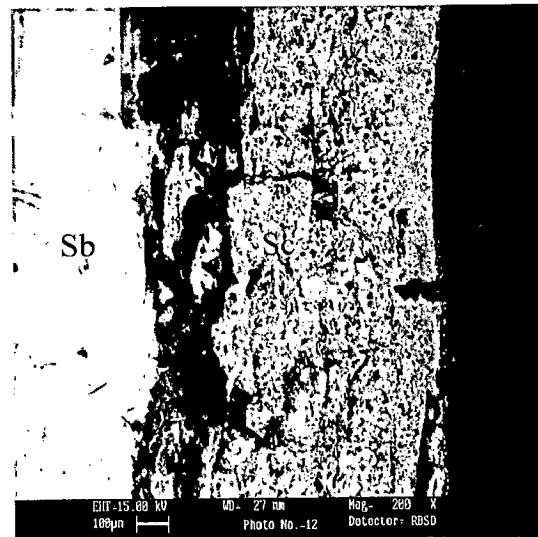


Fig. 6.51: X-ray diffraction profiles for different regions of SMAW weldment in T22 steel exposed to cyclic hot corrosion in Na₂SO₄-60%V₂O₅ at 900°C for 50 cycles.

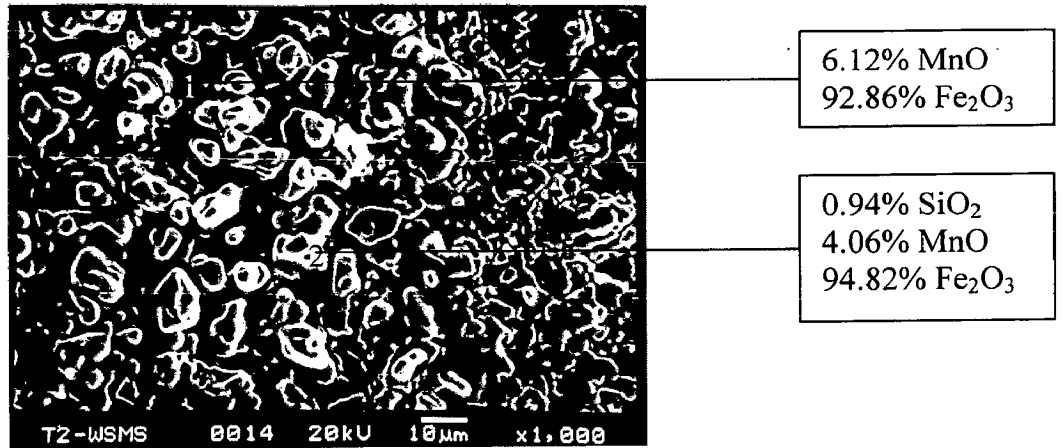


(a)

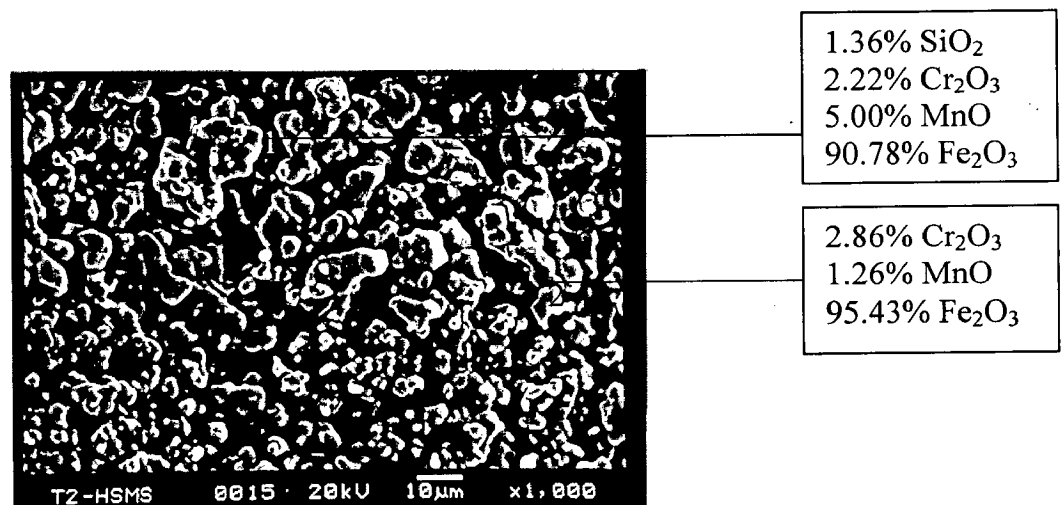


(b)

Fig. 6.52: SEM back scattered image of the cross section of different regions of SMAW weldment in T22 steel exposed to cyclic hot corrosion in $\text{Na}_2\text{SO}_4\text{-60\%V}_2\text{O}_5$ at 900°C for 50 cycles (a) Weld Metal, 200X (b) HAZ, 200X.



(a)



(b)

Fig. 6.53: SEM morphology showing surface morphology and EDAX analysis for different regions of SMAW weldment in T22 steel exposed to cyclic hot corrosion in Na₂SO₄-60%V₂O₅ at 900°C for 50 cycles (a) Weld metal, 1000X (b) HAZ, 1000X.

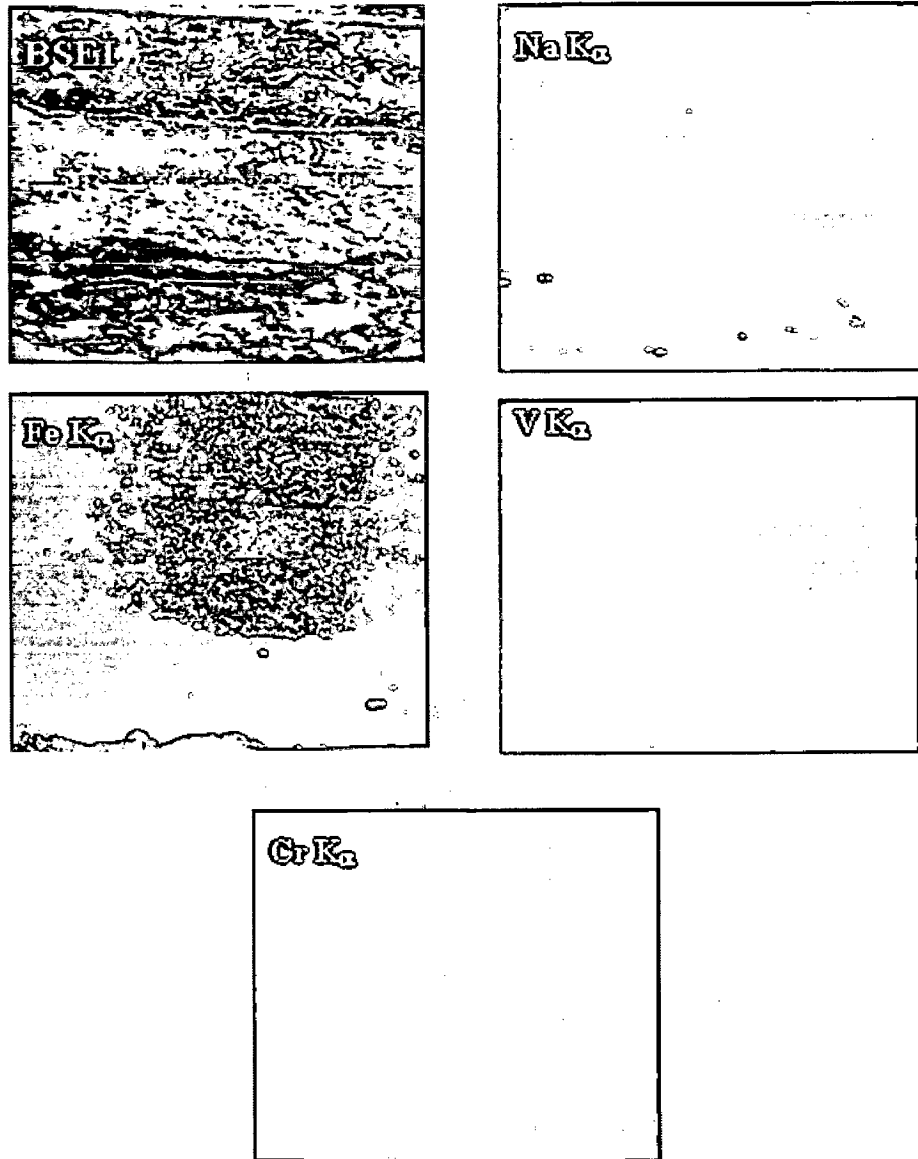


Fig. 6.54: BSEI and X-ray mapping of the cross-section of weld metal of SMAW weldment in T22 steel subjected to cyclic oxidation in Na₂SO₄ -60% V₂O₅ at 900°C for 50 cycles, 200X.

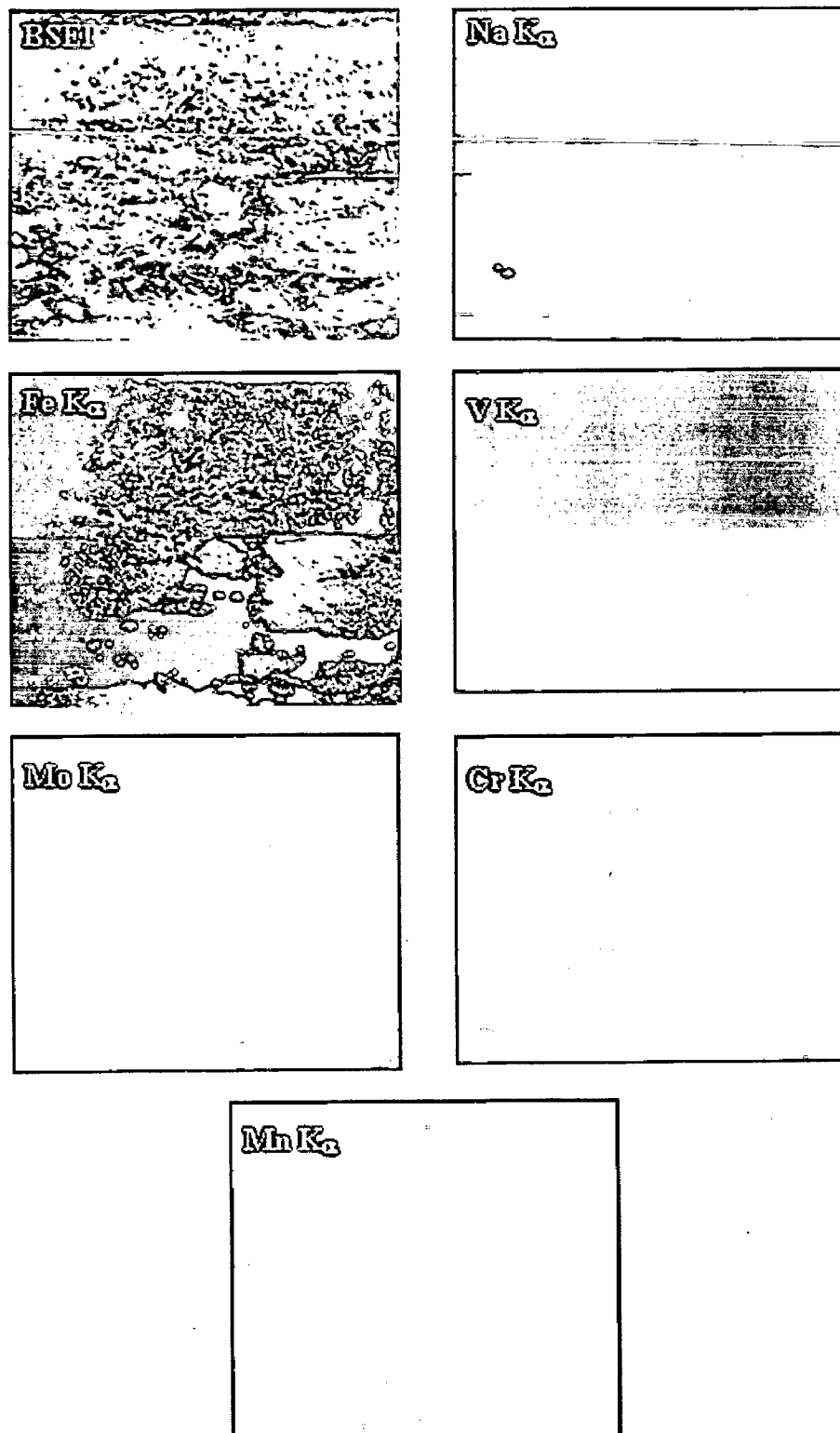


Fig. 6.55: BSEI and X-ray mapping of the cross-section of HAZ of SMAW weldment in T22 steel subjected to cyclic oxidation in Na_2SO_4 -60% V_2O_5 at 900°C for 50 cycles, 200X.

6.2.4 Different Regions of TIG Weldment i.e. Base Metal, Weld Metal and HAZ exposed to Molten Salt at 900°C in GrA1 Steel

6.2.4.1 Visual Examination

Macro morphology of the oxide scale for different regions of TIG weldment in GrA1 steel after hot corrosion in $\text{Na}_2\text{SO}_4\text{-60\%V}_2\text{O}_5$ at 900°C for 50 cycles is shown in Fig. 6.56. For weld metal the colour of scale was completely black. Cracks were observed during 14th cycle. Significant increase in the number of cracks as well as its width on surface and edges were noticed during 27th cycle. Little spalling was observed after 25th cycle.

In case of HAZ the colour of scale seems black during 1st cycle and it turned into blackish gray with increasing cycle. Spalling and cracking were observed during 14th cycle. Oxides have oozed out to the surface from beneath.

6.2.4.2 Thermogravimetric Data

Weight change expressed in mg/cm^2 has been plotted in Fig. 6.57 as a function of time expressed in number of cycles for the weld metal and HAZ along with base metal. The base metal seems to be more weight gain than weld metal and is only around 1.55 times of that for weld metal.

The square of total weight gain values per unit area (mg^2/cm^4) is plotted in Fig. 6.58, to understand the behaviour of corrosion for different regions of TIG weldment in GrA1 steel. The different regions followed the parabolic rate law for the whole range of cyclic study with parabolic rate constant (K_p) of 49.394, 20.335 and $22.531 \times 10^{-8} \text{ g}^2 \text{ cm}^{-4} \text{ s}^{-1}$ for base metal, weld metal and HAZ respectively.

6.2.4.3 X-ray Diffraction Analysis

The XRD profile of the scale of different regions of TIG weldment in GrA1 steel after hot corrosion in molten salt at 900°C for 50 cycle shows common phases for all the samples as could be seen in Fig. 6.59. Fe_3O_4 was also observed along with Fe_2O_3 for weld metal and base metal.

6.2.4.4 Scale Thickness Measurement

Backscattered electron images across the cross-section of weld metal and HAZ after cyclic hot corrosion are shown in Fig. 6.60. Very thick oxide scale was identified in case of

base metal which is around 1.4 times more than that on HAZ. Average scale thickness measured from these backscattered images is 2.177, 1.9 and 1.555 mm for base metal, weld metal and HAZ regions respectively. Small cracks were seen along the cross-section of oxide scale on the weld metal.

6.2.4.5 SEM/EDAX Analysis

6.2.4.5.1 Surface Morphology

Spongy scale is indicated with cracks running through it weld metal after hot corrosion in the molten salt at 900°C after 50 cycles as shown in Fig. 6.61 (a). The spalling has been observed. The top scale mainly contains oxides of Fe with small amounts of S (5.83%). At the cracks scale has been identified only as Fe₂O₃ (99.45%).

SEM micrograph for HAZ after hot corrosion indicates granular scale as shown in Fig 6.61 (b). In this case the top scale consists mainly of Fe₂O₃ (99.07%). Inner scale mainly consists of Na₂O (1.61%), MnO (0.96%) and Fe₂O₃ (96.75%).

6.2.4.6 EPMA Analysis

Elemental X-ray mapping for weld metal after hot corrosion in molten salt at 900°C for 50 cycles indicates the formation of scale containing mainly iron. Na and V are present at bottom scale. There is presence of silicon at some places as in pockets in the scale. Very small concentration of Mn is distributed in the scale. Scale seems have more cracks near to the metal/oxide interface as can be seen in Fig. 6.62.

EPMA for the cross-section of HAZ after hot corrosion in the given environment shows only iron as main element. Big voids forms in the middle of the oxide scale Fig. 6.63.

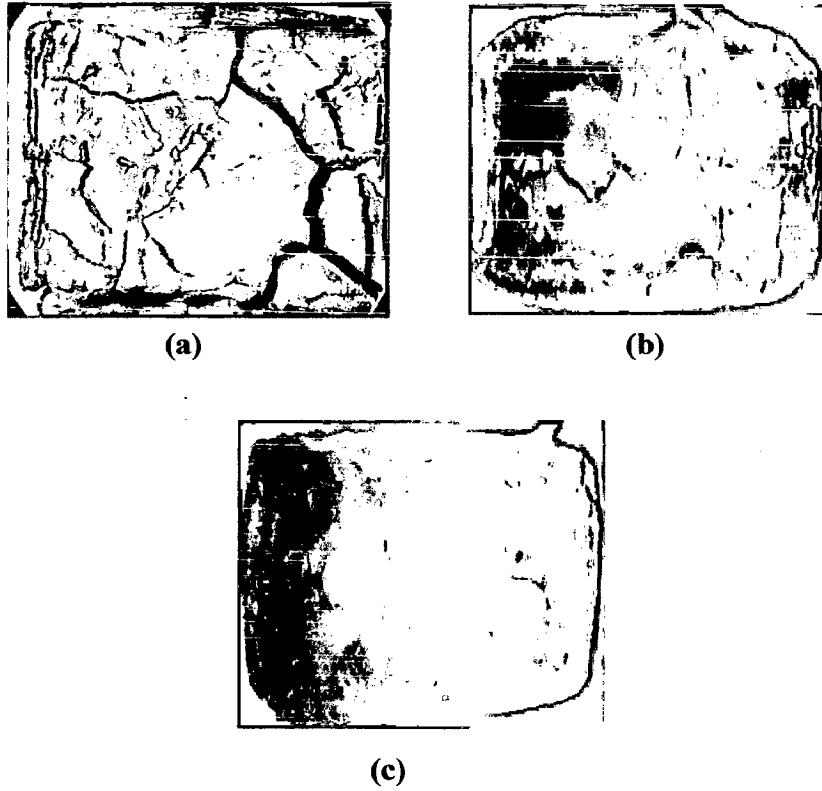


Fig. 6.56: Macrographs of different regions of TIG weldments in GrA1 steel subjected to cyclic hot corrosion in Na_2SO_4 -60% V_2O_5 at 900°C for 50 cycles (a) Base Metal, (b) Weld Metal and (c) HAZ.

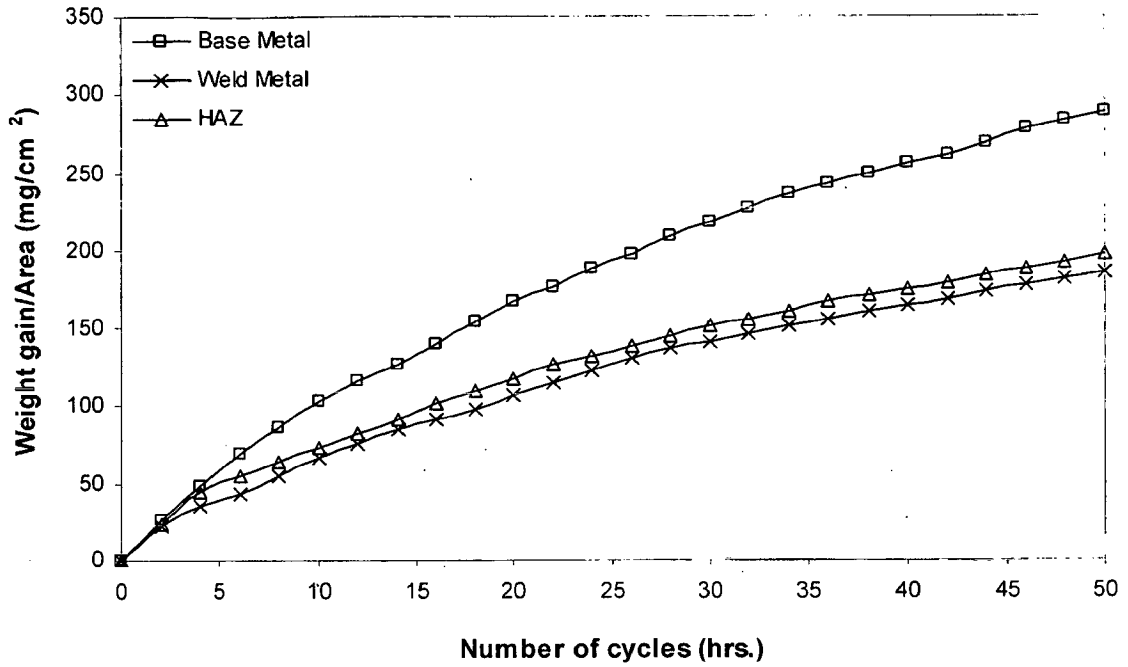


Fig. 6.57: Weight gain plot for different regions of TIG weldment in GrA1 steels exposed to $\text{Na}_2\text{SO}_4\text{-60}\%\text{V}_2\text{O}_5$ at 900°C for 50 cycles.

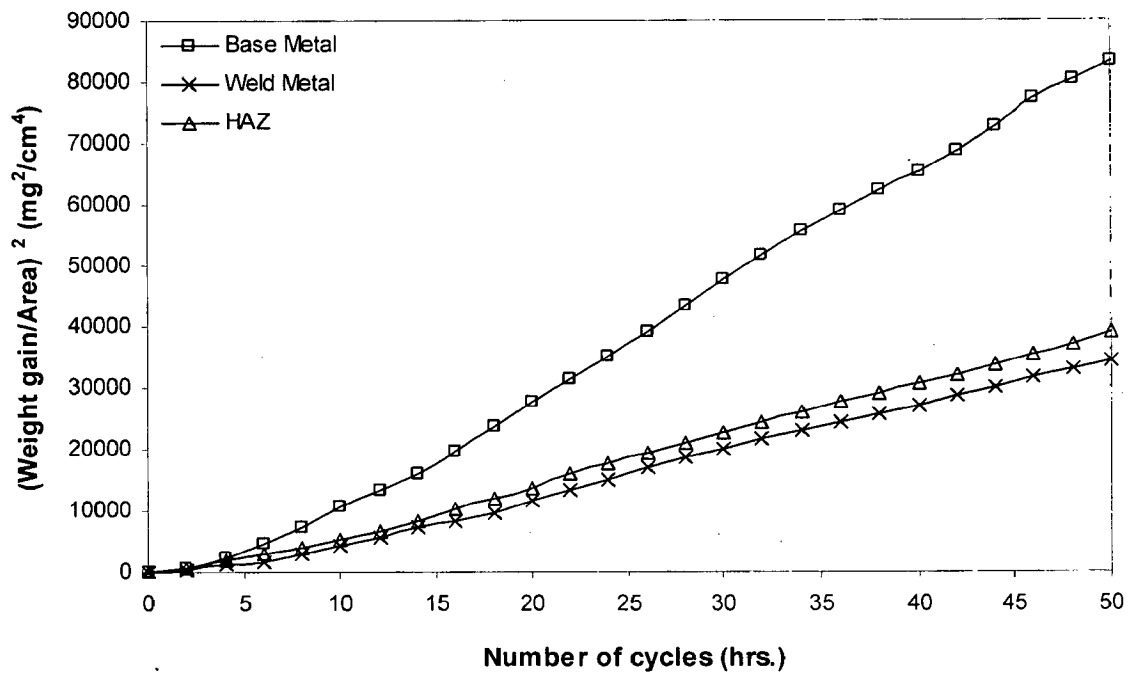


Fig. 6.58: Weight gain square (mg^2/cm^4) plot for different regions of TIG weldment in GrA1 steel exposed to cyclic hot corrosion in $\text{Na}_2\text{SO}_4\text{-60}\%\text{V}_2\text{O}_5$ at 900°C for 50 cycles.

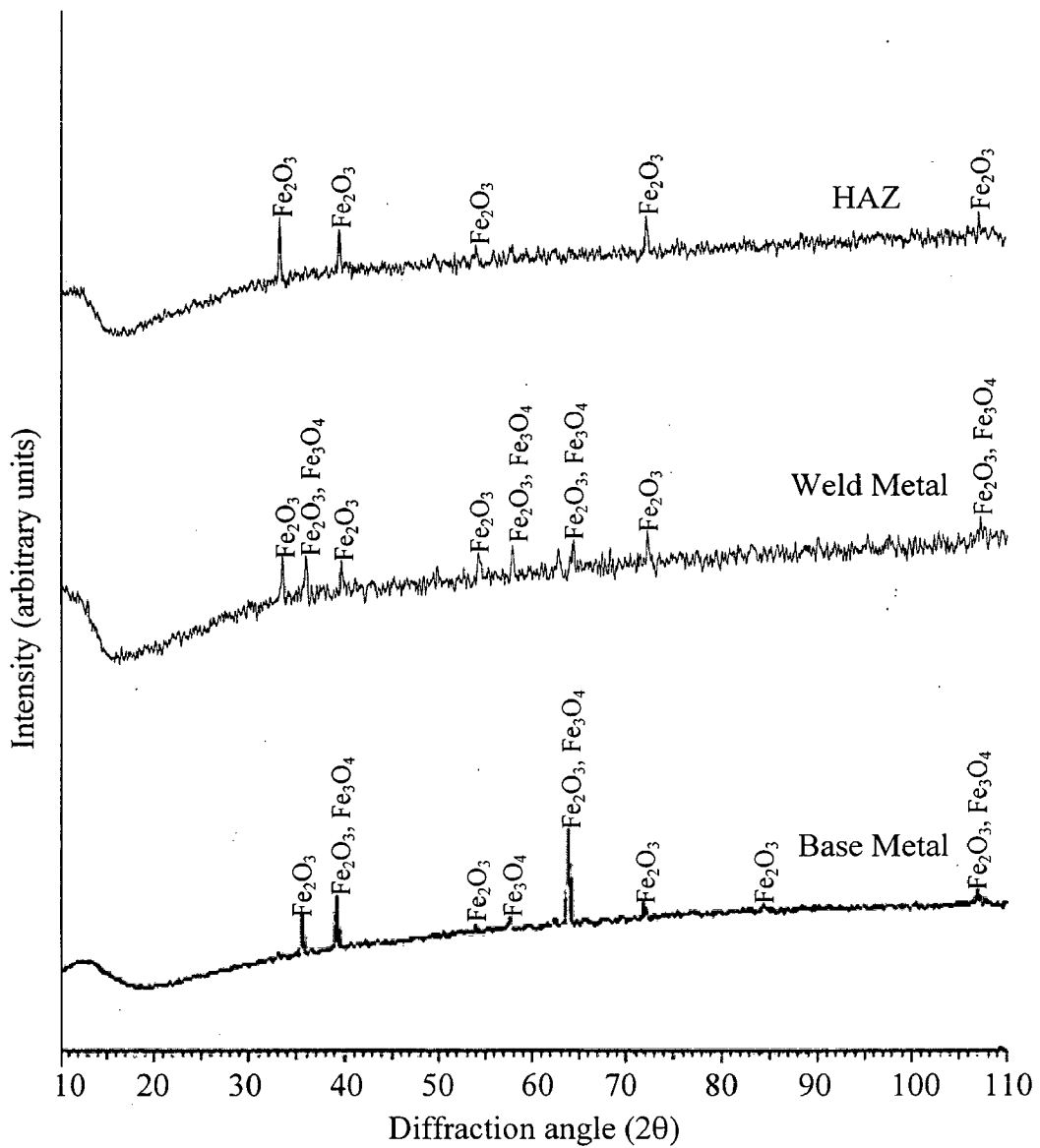
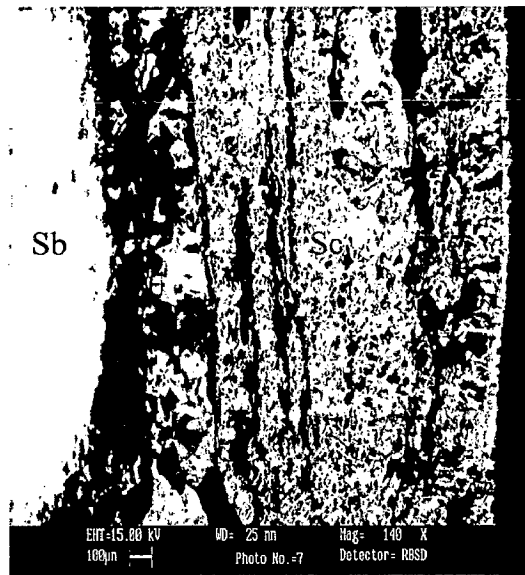
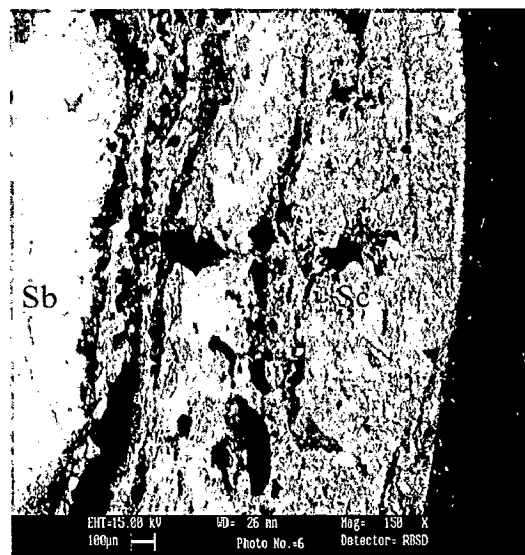


Fig. 6.59: X-ray diffraction profiles for different regions of TIG weldment in GrA1steel exposed to cyclic hot corrosion in Na₂SO₄-60%V₂O₅ at 900°C for 50 cycles.



(a)



(b)

Fig. 6.60: SEM back scattered image of the cross section of different regions of TIG weldment in GrA1 steel exposed to cyclic hot corrosion in Na_2SO_4 -60% V_2O_5 at 900°C for 50 cycles (a) Weld Metal, 140X (b) HAZ, 150X.

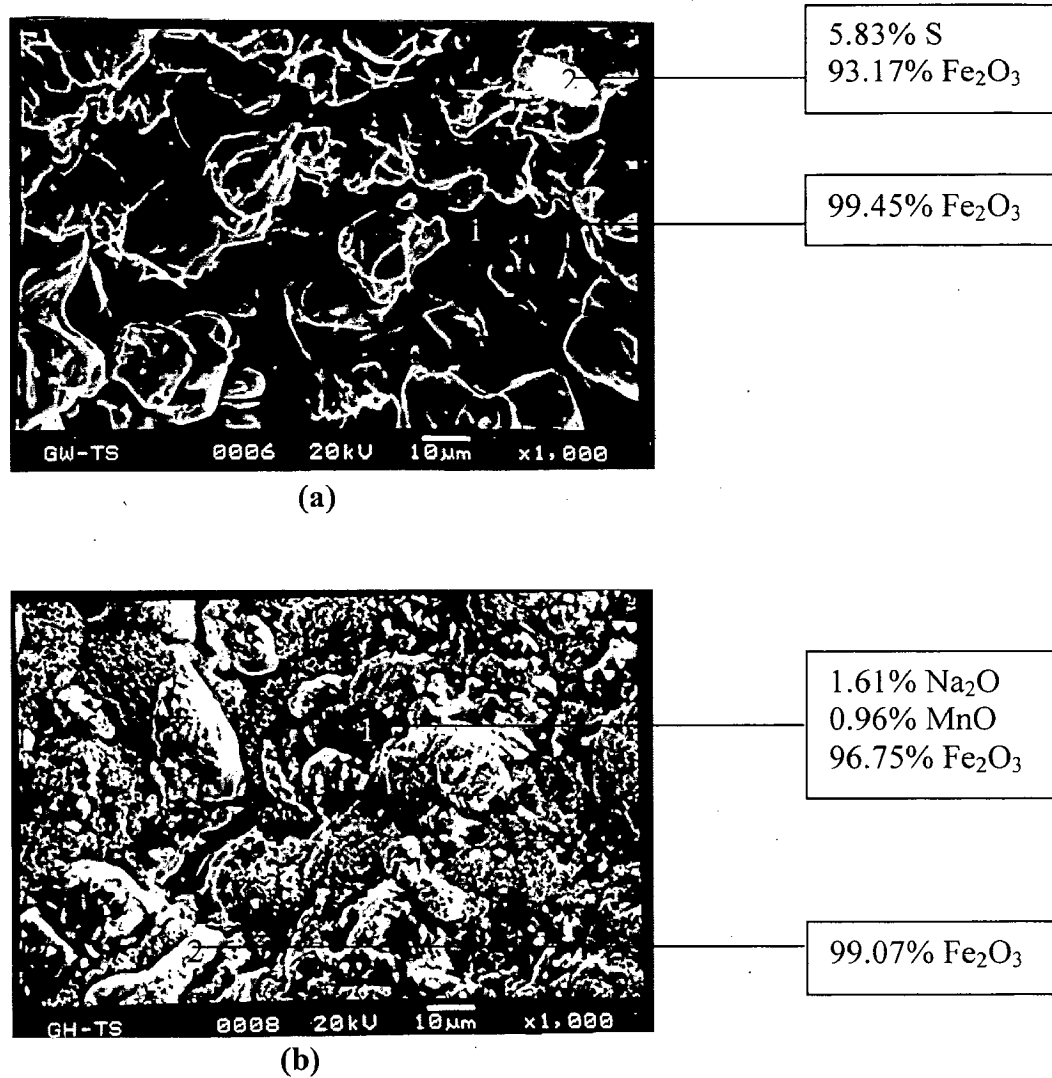


Fig. 6.61: SEM micrographs of surface morphology and EDAX analysis for different regions of TIG weldment in GrA1 steel exposed to Na_2SO_4 -60% V_2O_5 at 900°C for 50 cycles (a) Weld Metal, 1000X and (b) HAZ, 1000X.

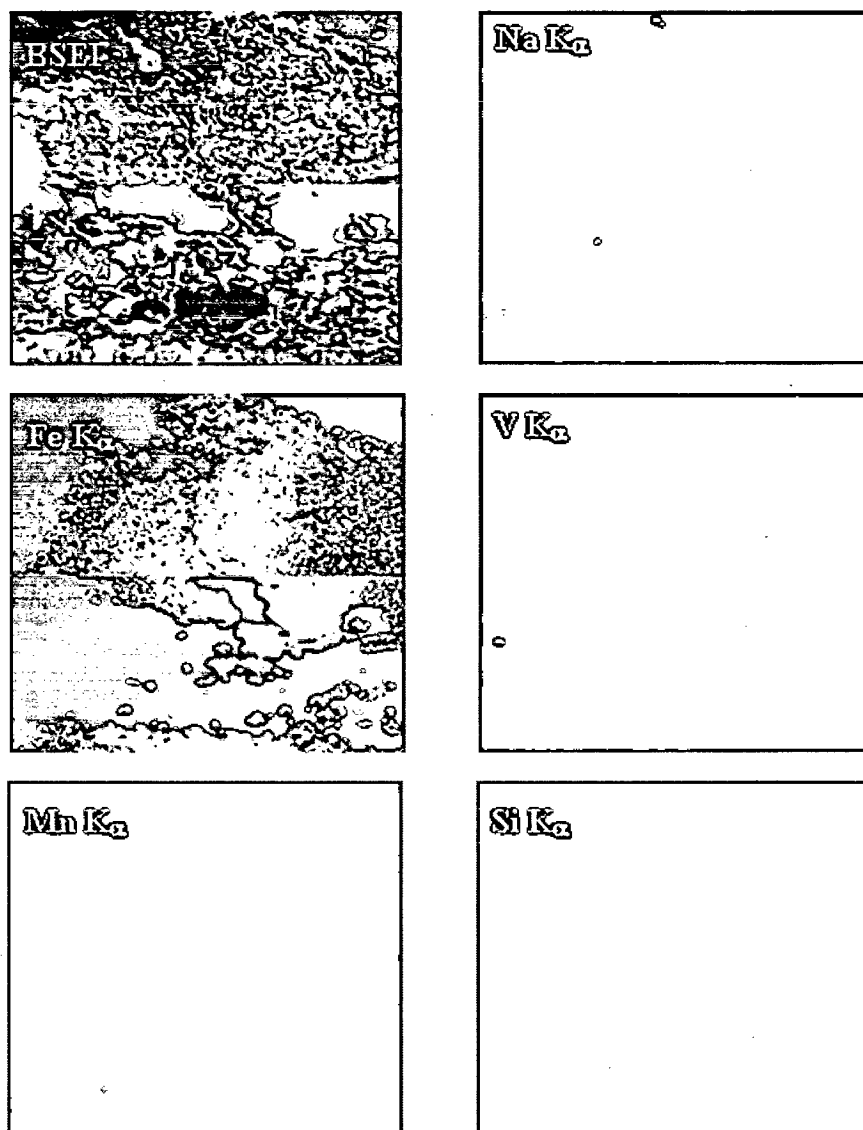


Fig. 6.62: BSEI and X-ray mapping of the cross-section of weld metal of TIG weldment in GrA1 steel subjected to cyclic oxidation in Na₂SO₄- 60% V₂O₅ at 900°C for 50 cycles, 200X.

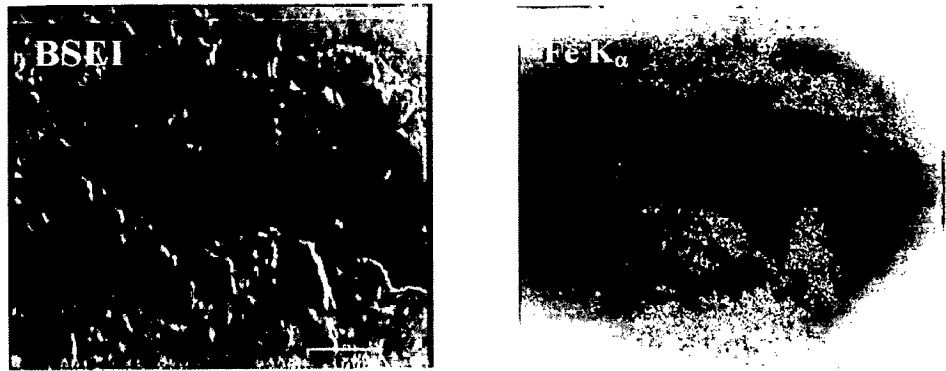


Fig. 6.63: BSEI and X-ray mapping of the cross-section of HAZ of TIG weldment in GrA1 steel subjected to cyclic oxidation in Na_2SO_4 - 60% V_2O_5 at 900°C for 50 cycles, 200X.

6.2.5 Different Regions of TIG Weldment i.e. Base Metal, Weld Metal and HAZ exposed to Molten Salt at 900°C in T11 Steel

6.2.5.1 Visual Examination

The macrographs for base metal, weld metal and HAZ regions of TIG weldment in T11 steel after hot corrosion at 900°C for 50 cycles are shown in Fig. 6.64. It can be seen from the macrograph given in Fig. 6.64(b) that intense spalling was there at the edges for weld metal. Little cracks seen in the middle of the surface of oxide scale during 30th cycle. The colour of oxide scale turned black from blackish gray during fifth cycle. Spalling just started after 18th cycle and gradually increased in the subsequent cycles. Intense spalling was observed during 32nd and 38th cycle.

For HAZ light black spot seen on the black oxide surface during 1st cycle. With increasing number of cycles this spot disappeared. Very small spalling of scale was observed during 10th cycle. No cracks were seen in the scale upto the 50 cycle. Little increase in spalling was noticed during 37th cycle.

6.2.5.2 Thermogravimetric Data

Weight gain per unit area expressed in mg/cm² is plotted as a function of time expressed in number of cycles for oxidized different regions of TIG weldment in T11 steel is shown in Fig. 6.65. Weld metal showed the maximum weight gain and is around 1.55 times than that of HAZ in given aggressive environment. Weight gain square (mg²/cm⁴) plotted as a function of time (number of cycles) in Fig. 6.66, from where it can be inferred that all the three regions followed almost parabolic behaviour. The parabolic rate constants, K_p for base metal, weld metal and HAZ are 10.416, 20.710 and 8.213×10^{-8} g² cm⁻⁴ s⁻¹ respectively. The parabolic rate constant of weld metal is larger than the other two regions and is around 2.5 times of that for HAZ.

6.2.5.3 X-ray Diffraction Analysis

The XRD analysis for different regions of TIG weldment in T11 steel after exposure to molten salt at 900°C for 50 cycles is shown in Fig. 6.67 and these diffractograms has almost similar phases for all the regions. As obvious from the composition all the regions of the weldment have indicated the formation of iron oxide (Fe₂O₃) as a main phase.

6.2.5.4 Scale Thickness Measurement

The samples were cut across the cross-section after exposure to molten salt at 900°C for 50 cycles and mounted. The scale thickness values were measured from SEM back scattered images shown in Fig. 6.68. The SEM micrograph shows the fragile and cracked scale for weld metal and HAZ. The scale was debonding at the scale/metal interface in the HAZ. Thick oxide scale was identified in case of weld metal. The scale thickness values are 1.157, 1.725 and 1.371 mm for base metal, weld metal and HAZ respectively.

6.2.5.5 SEM/EDAX Analysis

6.2.5.5.1 Surface Morphology

The SEM micrograph of the GrA1 base steel exposed to Na₂SO₄-60%V₂O₅ environment at 900°C given in Fig. 6.69 (a) indicates the formation of predominantly Fe₂O₃ scale on the weld metal. EDAX analysis revealed that the top scale consists of mainly Fe₂O₃ (97.155%) with little amount of Na₂O (1.19%). Whereas the inner scale mainly consist of Fe₂O₃ (96.69%) with SiO₂ (1%).

The SEM and EDAX analysis indicate the top oxide scale on the HAZ consist of S (1.57%), Cr₂O₃ (5.90%) with main phase Fe₂O₃ (91.35%) point 2. Spalled regions contains SiO₂ (10.30%), S (1.02%), Cr₂O₃ (7.11%) and Fe₂O₃ (80.42%) point 1 in Fig. 6.69 (b).

6.2.5.6 EPMA Analysis

BSEI and X-ray mapping for weld metal exposed to Na₂SO₄-60%V₂O₅ at 900 °C for 50 cycles are shown in Fig. 6.70. The scale mainly contains iron oxide. Large irregular streaks of chromium are also indicated. Na is also present in scattered manner in less quantity. V is present in the middle of scale. EPMA analysis shows thick scale for weld metal.

The EPMA analysis for the exposed cross-section of HAZ steel is shown in Fig. 6.71. EPMA indicates the formation of a multilayered scale, whole of the scale contains mainly iron. V is distributed in little more concentration in middle of scale. Na is also scattered in the scale. Cr is present near the metal/oxide interface as a thin layer. Silicon is seen as pockets in the scale. Mn is absent in the scale.

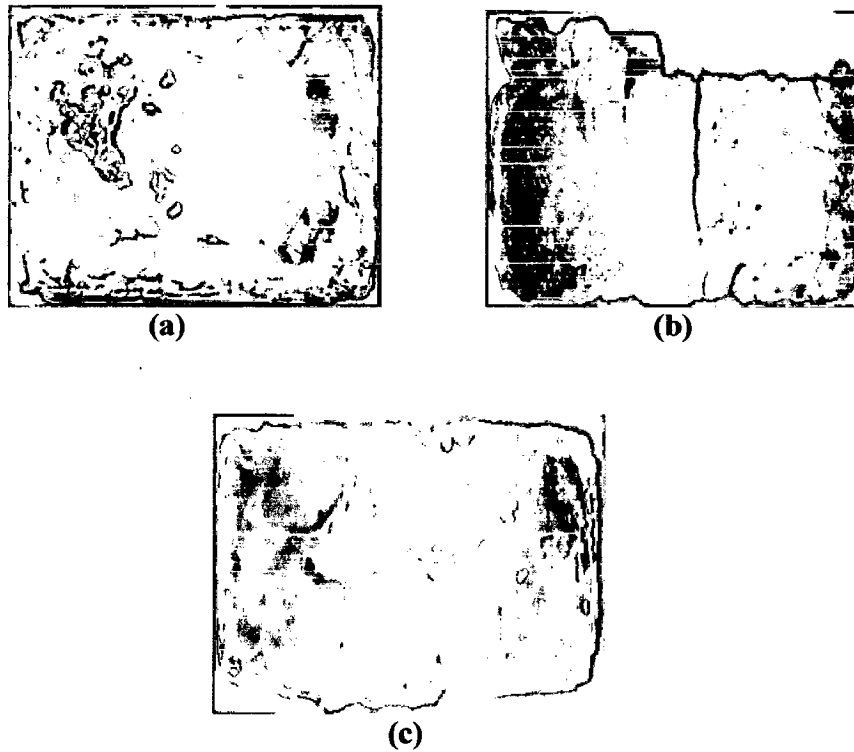


Fig. 6.64: Macrographs of different regions of TIG weldments in T11 steel subjected to cyclic hot corrosion in $\text{Na}_2\text{SO}_4\text{-60}\%\text{V}_2\text{O}_5$ at 900°C for 50 cycles (a) Base Metal, (b) Weld Metal and (c) HAZ.

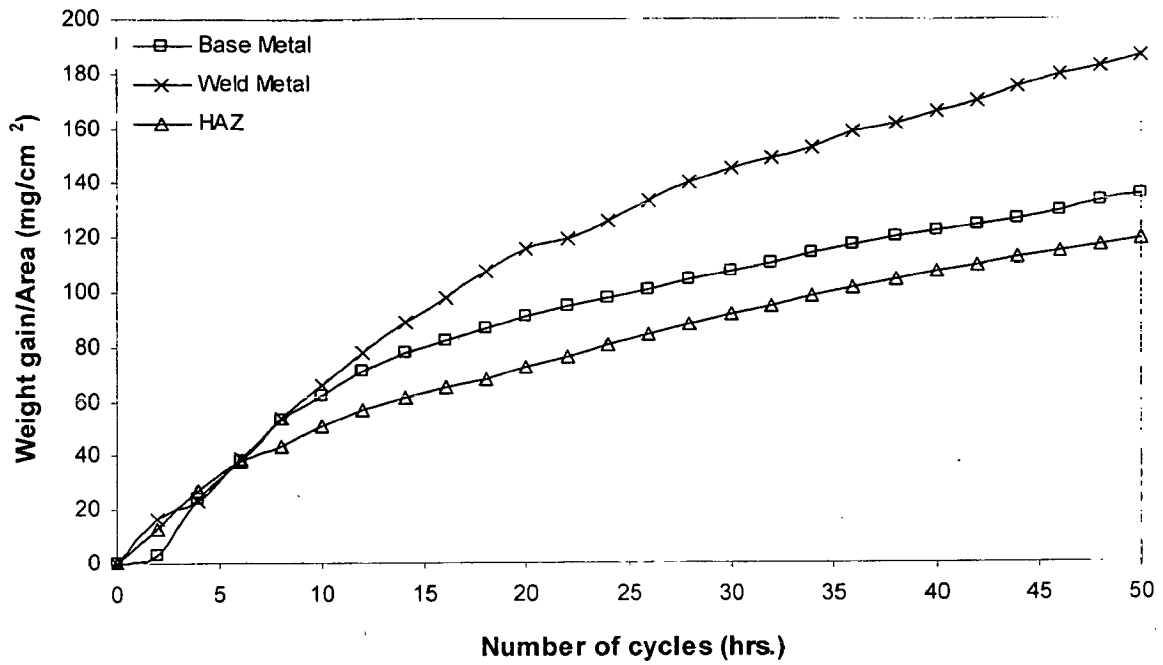


Fig. 6.65: Weight gain plot for different regions of TIG weldment in T11 steels exposed to Na_2SO_4 -60% V_2O_5 at 900°C for 50 cycles.

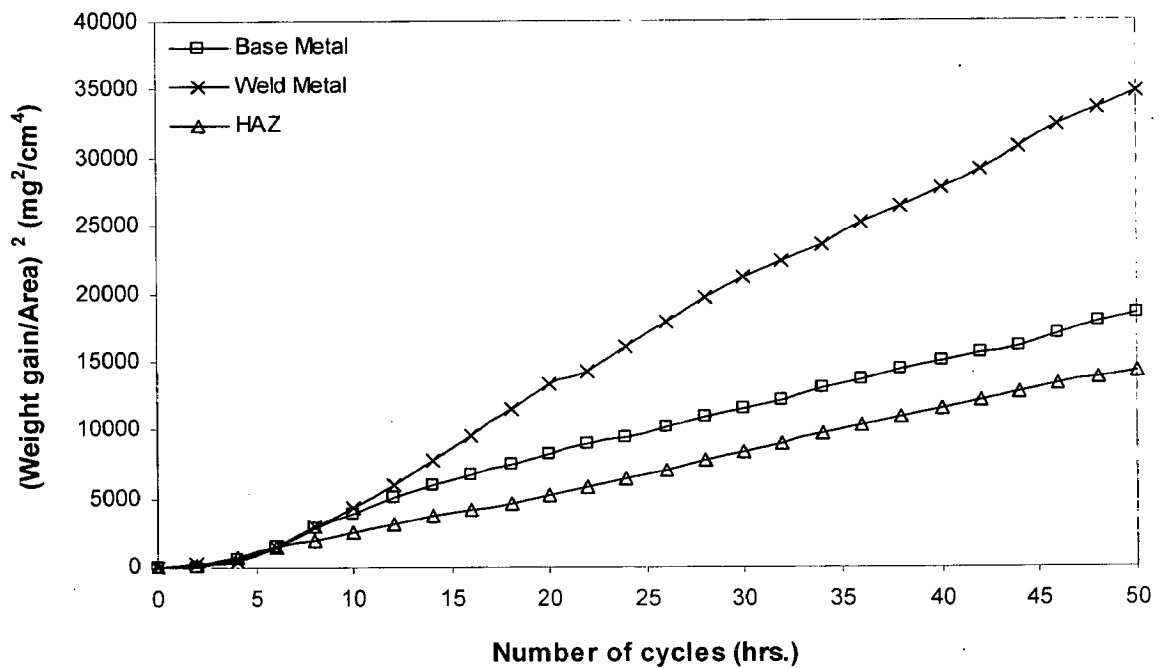


Fig. 6.66: Weight gain square (mg^2/cm^4) plot for different regions of TIG weldment in T11 steel exposed to cyclic hot corrosion in Na_2SO_4 -60% V_2O_5 at 900°C for 50 cycles.

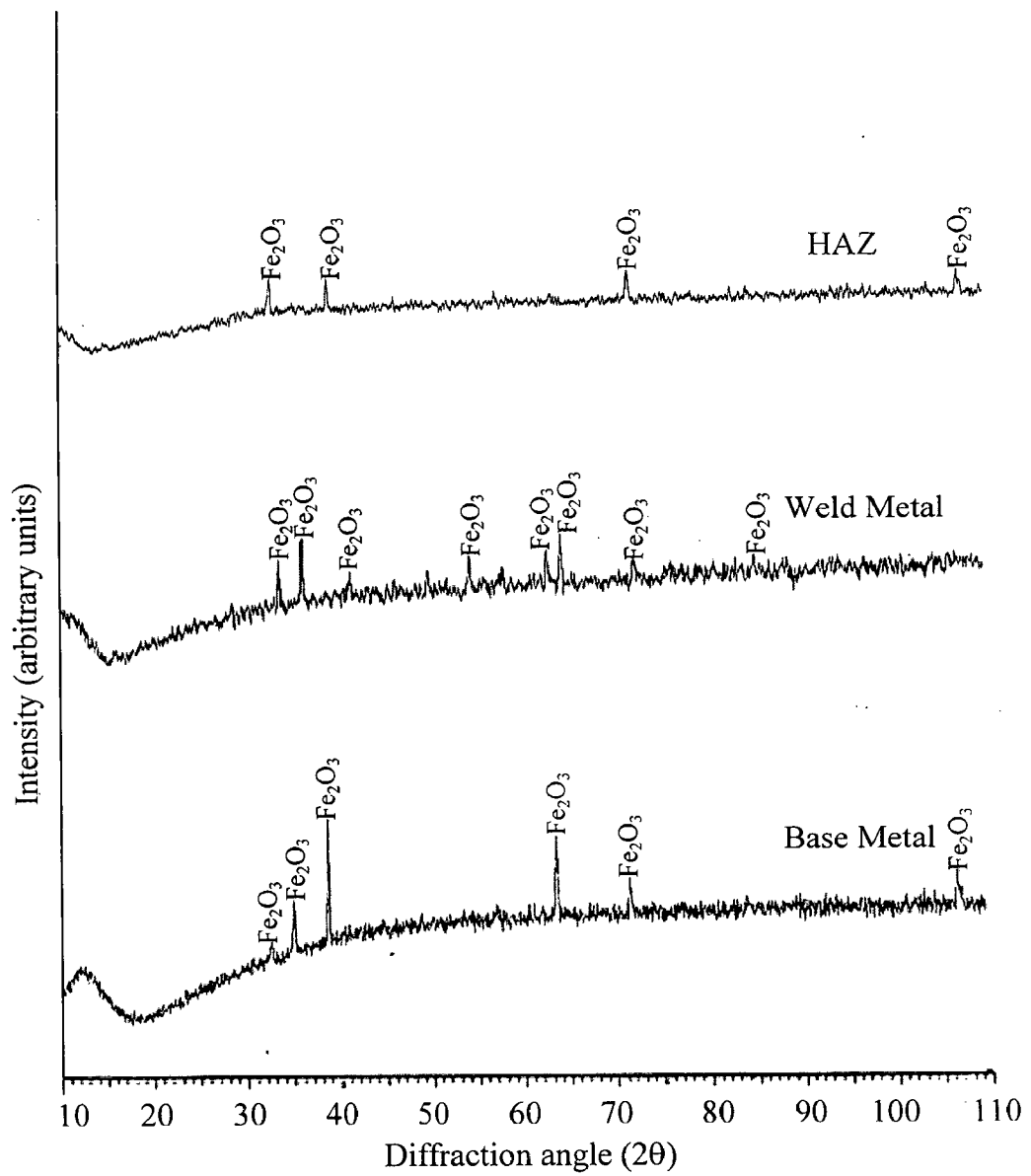
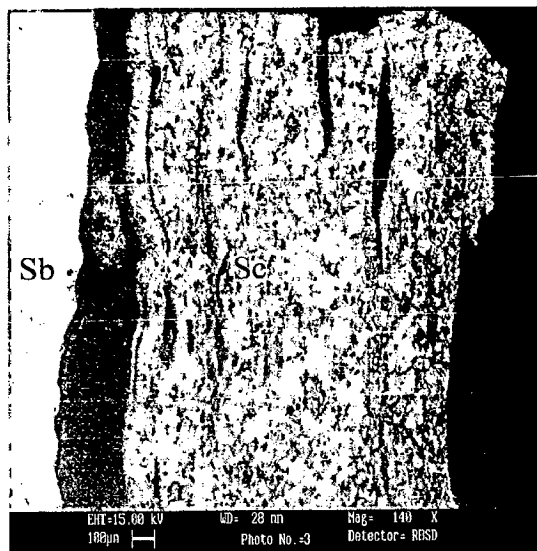
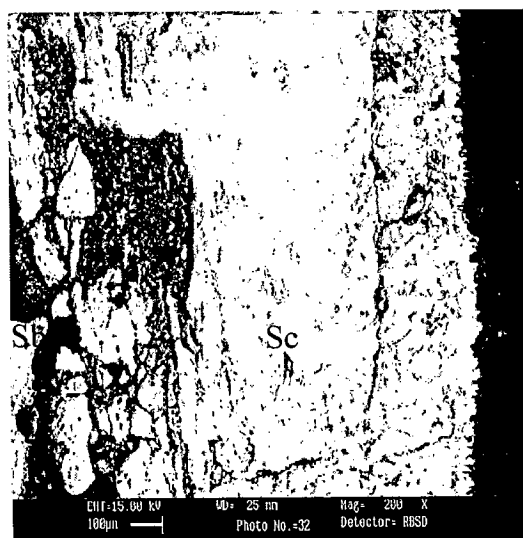


Fig. 6.67: X-ray diffraction profiles for different regions of TIG weldment in T11 steel exposed to cyclic hot corrosion in $\text{Na}_2\text{SO}_4\text{-60\%V}_2\text{O}_5$ at 900°C for 50 cycles.



(a)



(b)

Fig. 6.68: SEM back scattered image of the cross section of different regions of TIG weldment in T11steel exposed to cyclic hot corrosion in $\text{Na}_2\text{SO}_4\text{-60\%V}_2\text{O}_5$ at 900°C for 50 cycles. (a) Weld Metal, 140X (b) HAZ, 200X.

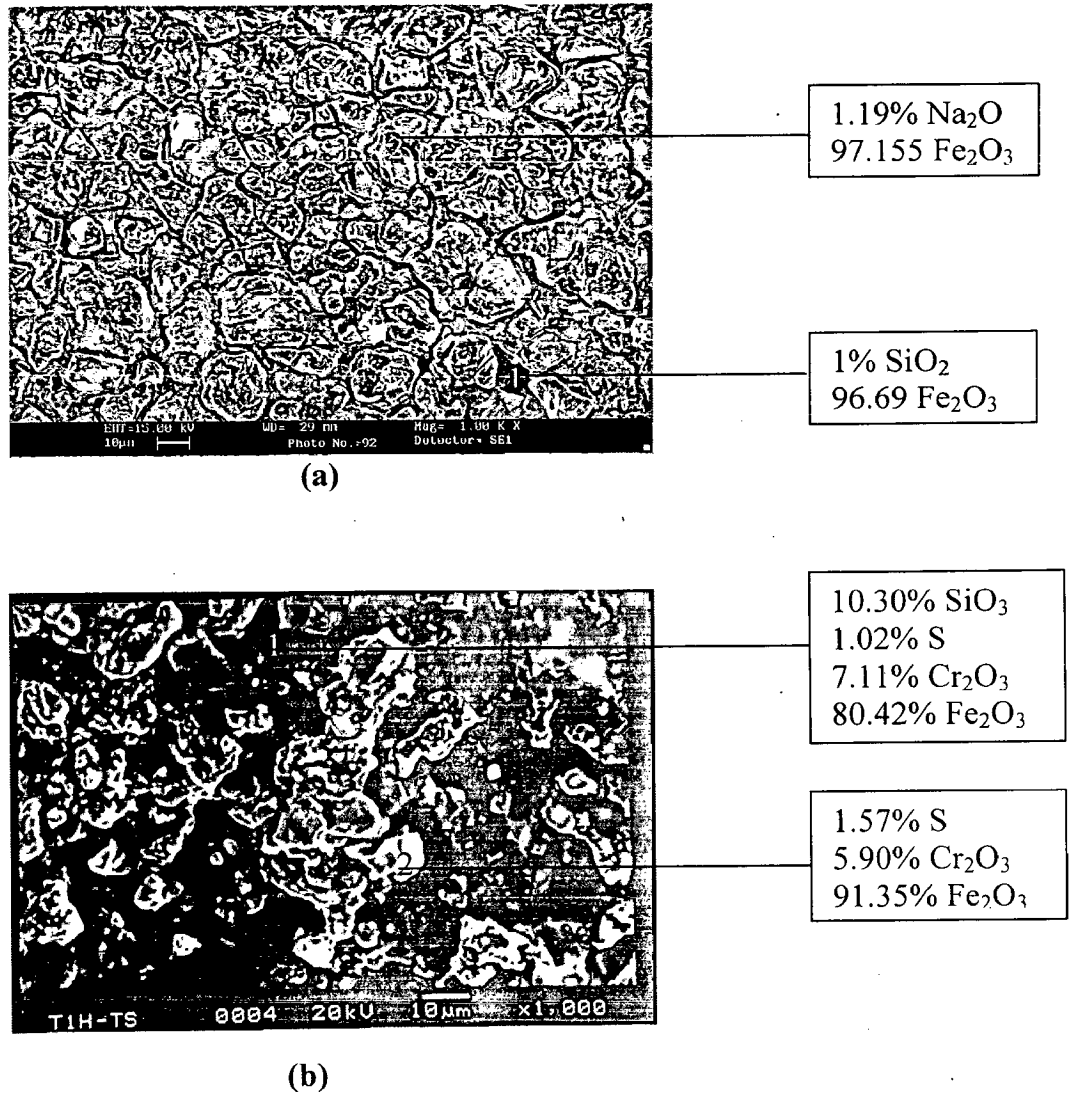


Fig. 6.69: Surface morphology and EDAX analysis for different regions of TIG weldment in T11 steel exposed to Na₂SO₄ -60% V₂O₅ at 900°C for 50 cycles (a) Weld Metal, 1000X and (b) HAZ, 1000X.

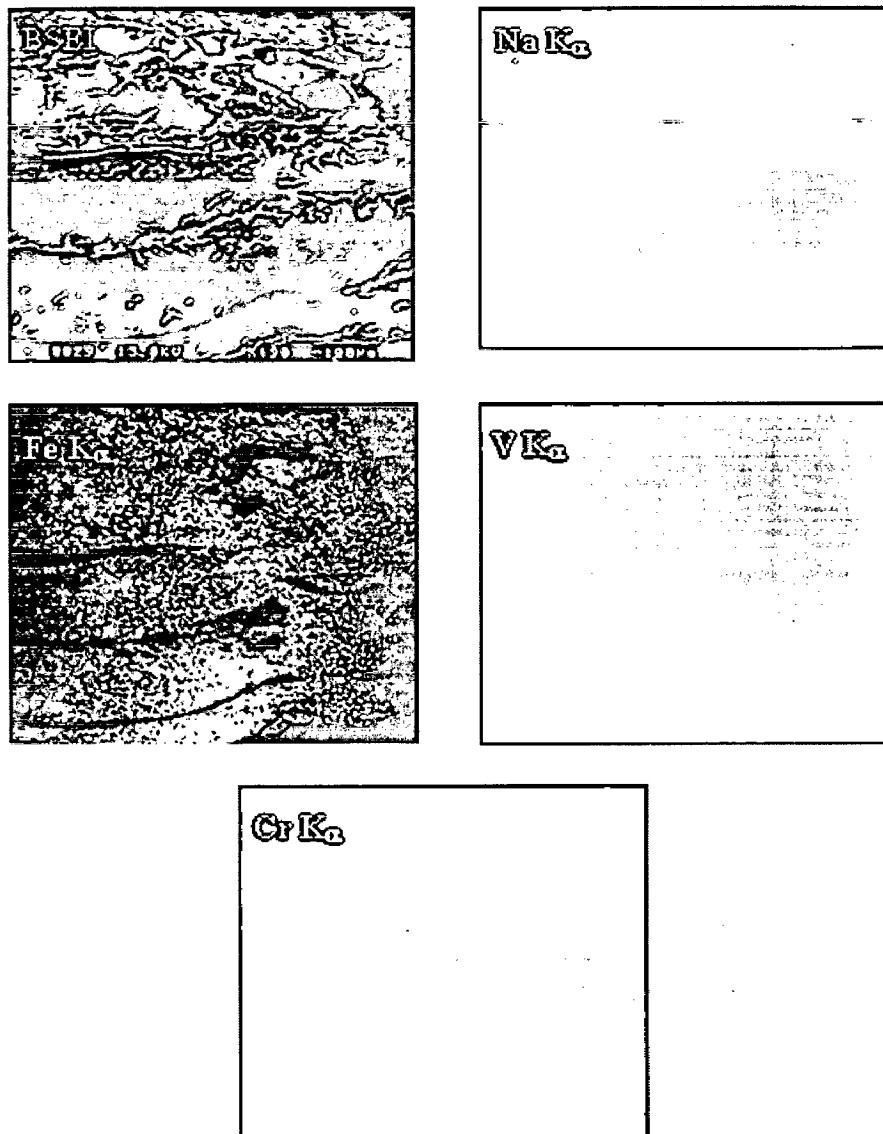


Fig. 6.70: BSEI and X-ray mapping of the cross-section of weld metal of TIG weldment in T11 steel subjected to cyclic oxidation in Na₂SO₄-60% V₂O₅ at 900°C for 50 cycles, 200X.

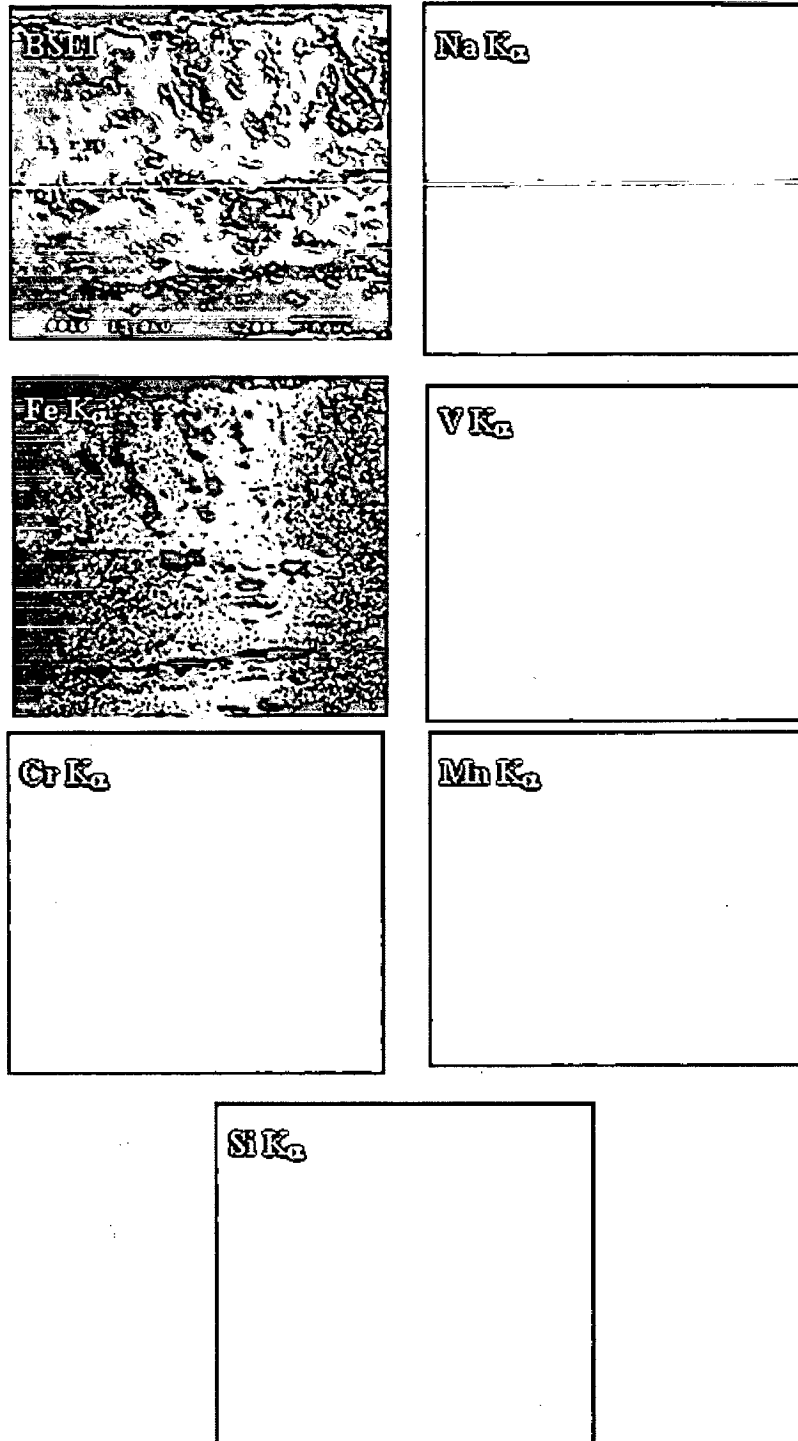


Fig. 6.71: BSEI and X-ray mapping of the cross-section of HAZ of TIG weldment in T11 steel subjected to cyclic oxidation in Na₂SO₄ -60% V₂O₅ at 900°C for 50 cycles, 200X.

6.2.6 Different Regions of TIG Weldment i.e. Base Metal, Weld Metal and HAZ exposed to Molten Salt at 900°C in T22 Steel

6.2.6.1 Visual Examination

The macrographs for the corroded surfaces of different regions of TIG weldment in T22 steel are shown in Fig. 6.72. It was observed that for weld metal, the colour of the scale surface turned black during first cycle. Spalling of oxide scale was indicated during the 3rd cycle. Even little cracks appeared on the scale at 13th cycles, after that there was increase in the number and width of these cracks and oozing out of oxides from these cracks was observed. Intense cracking was observed. Colour of the scale was dark blackish gray after 50th cycles.

In case of HAZ blackish gray colour was observed on this region during 1st cycle. A thin layer of oxide scale got spalled during 17th cycle. The scale of HAZ specimen started cracking during 32nd cycle. Scale was oozing out at the edges in the consequent cycles. Whereas in case of base metal intense spalling and cracking was observed upto 50th cycle.

6.2.6.2 Thermogravimetric Data

Weight gain (mg/cm^2) data plotted with time expressed in number of cycles for different regions of TIG weldments in T22 steel is given in Fig. 6.73. It can be inferred from the plots that the weight gain for base metal is very much larger as compared to weld metal. The total weight gain after 50 cycles for base metal is around 1.78 times more than that of weld metal. All the regions of TIG weldment followed the parabolic behaviour as can be inferred from the square of weight change (mg^2/cm^4) plotted with number of cycles in Fig. 6.74. The parabolic rate constants (K_p in $10^{-8} \text{ g}^2 \text{ cm}^{-4} \text{ s}^{-1}$) for these regions are 76.233 (base metal), 23.098 (weld metal) and 65.408 (HAZ).

6.2.6.3 X-ray Diffraction Analysis

The XRD analysis for different regions of TIG weldment in T22 steel after exposure to $\text{Na}_2\text{SO}_4\text{-60}\%\text{V}_2\text{O}_5$ at 900°C for 50 cycles is shown in Fig. 6.75 and these diffractograms has almost similar phases for all the regions. As obvious from the composition all the regions of the weldment have indicated the formation of iron oxide (Fe_2O_3). Where as weak peaks of Cr_2O_3 along with Fe_2O_3 are indicated in all the oxide scale of three regions.

6.2.6.4 Scale Thickness Measurement

Scanning electron back scattered micrographs for different regions of TIG weldment in T22 steel after hot corrosion in molten salt at 900°C for 50 cycles are shown in Fig. 6.76.

Oxide scale was debonding at the interface of oxide/metal in HAZ Fig.6.76 (b). Big cracks along the cross-section of oxide scale were identified in case of the scale on the weld metal Fig. 6.76 (a). The oxide scale thickness values for weld metal and HAZ are 1.3 mm, and 1.17 mm respectively.

6.2.6.5 SEM/EDAX Analysis

6.2.6.5.1 Surface Morphology

SEM micrograph and EDAX analysis for different regions of TIG weldment in T22 steel after cyclic hot corrosion are shown in Fig. 6.77. EDAX analysis indicates the top scale of weld metal consists of mainly Fe_2O_3 (96.57%) with MnO (2.85%), whereas inner scale contain SiO_2 (3.17%), Cr_2O_3 (1.24%), MnO (1.88%) along with main phase Fe_2O_3 (92.83%) in Fig. 6.77 (a)

SEM micrograph of the scale on HAZ region show more corrosion of grain boundary Fig.6.77 (b). The upper oxide scale mainly consists of MnO (4.59%) and Fe_2O_3 (94.64%). The inner scale along the boundary contains little amount of SiO_2 (9.87%), MnO (3.80%) with iron oxide Fe_2O_3 (85.63%) point 1 Fig. 6.77 (b).

6.2.6.6 EPMA Analysis

The EPMA of the cross-section of the exposed specimen (weld metal of TIG weldment in T22 steel) Fig. 6.78 indicates mainly presence of iron in the whole oxide scale. EPMA analysis of scale on the weld metal revealed that chromium is indicated as layer in the lower part of scale. Vanadium is also distributed in very small concentration in the bottom scale. At some places small concentration of Na is also indicated in the upper and lower part of the scale.

EPMA shows in Fig.6.79 for scale on the HAZ where iron is main element present throughout the scale. Sodium and Vanadium are also scattered in the whole scale. Small concentration of Cr is also indicated in the upper scale. Mn is present in the upper layer of oxide scale.

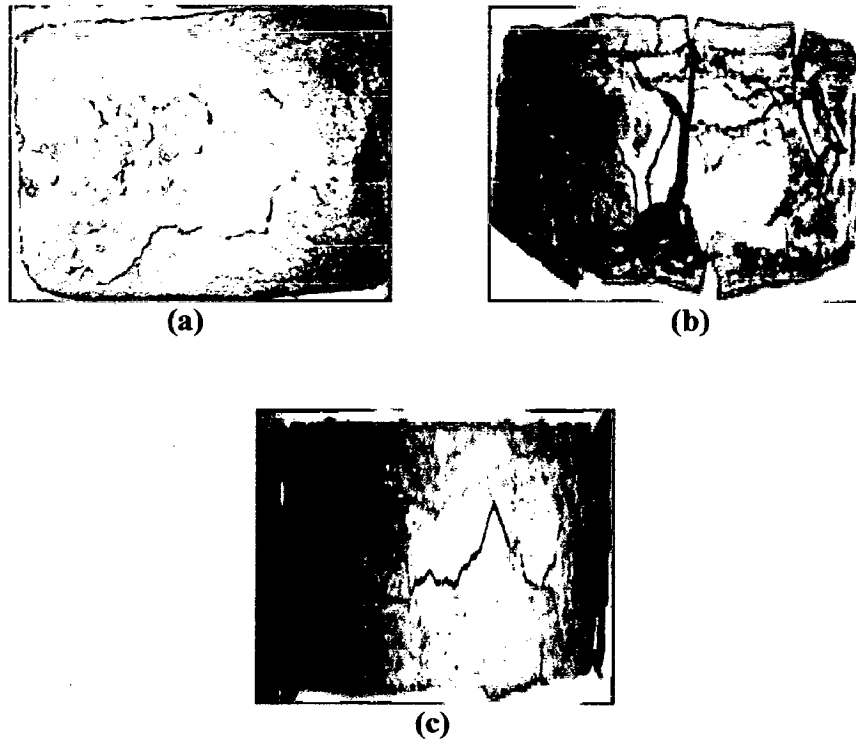


Fig. 6.72: Macrographs of different regions of TIG weldments in T22 steel subjected to cyclic hot corrosion in $\text{Na}_2\text{SO}_4\text{-60}\%\text{V}_2\text{O}_5$ at 900°C for 50 cycles (a) Base Metal, (b) Weld Metal and (c) HAZ.

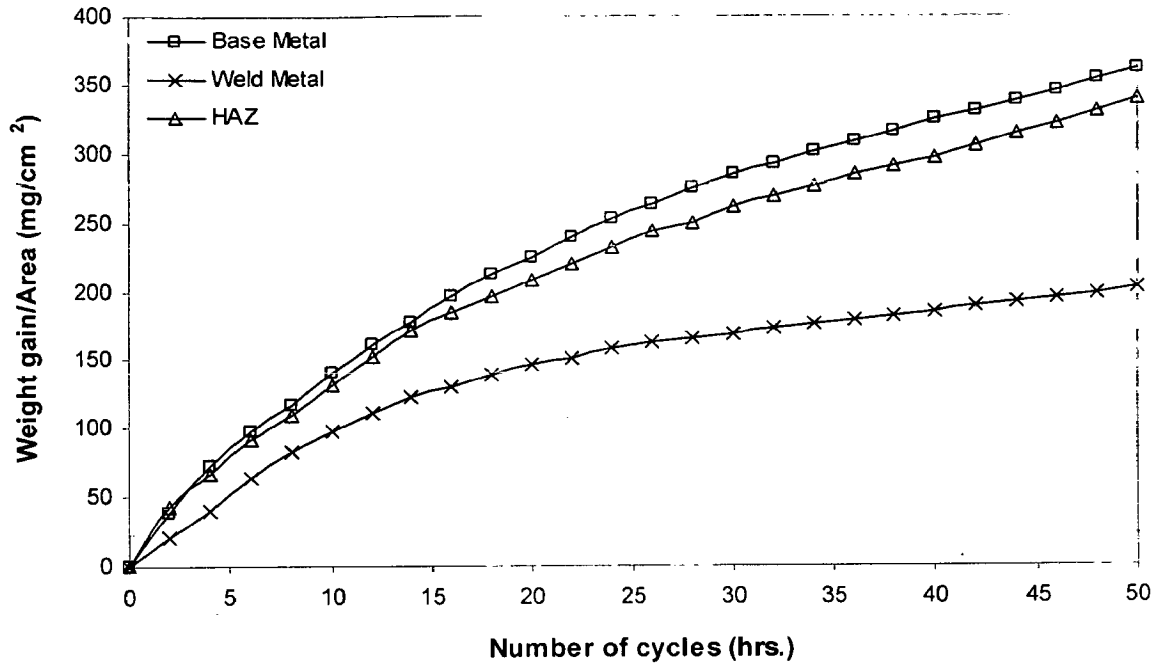


Fig. 6.73: Weight gain plot for different regions of TIG weldment in T22 steels exposed to $\text{Na}_2\text{SO}_4\text{-60\%V}_2\text{O}_5$ at 900°C for 50 cycles.

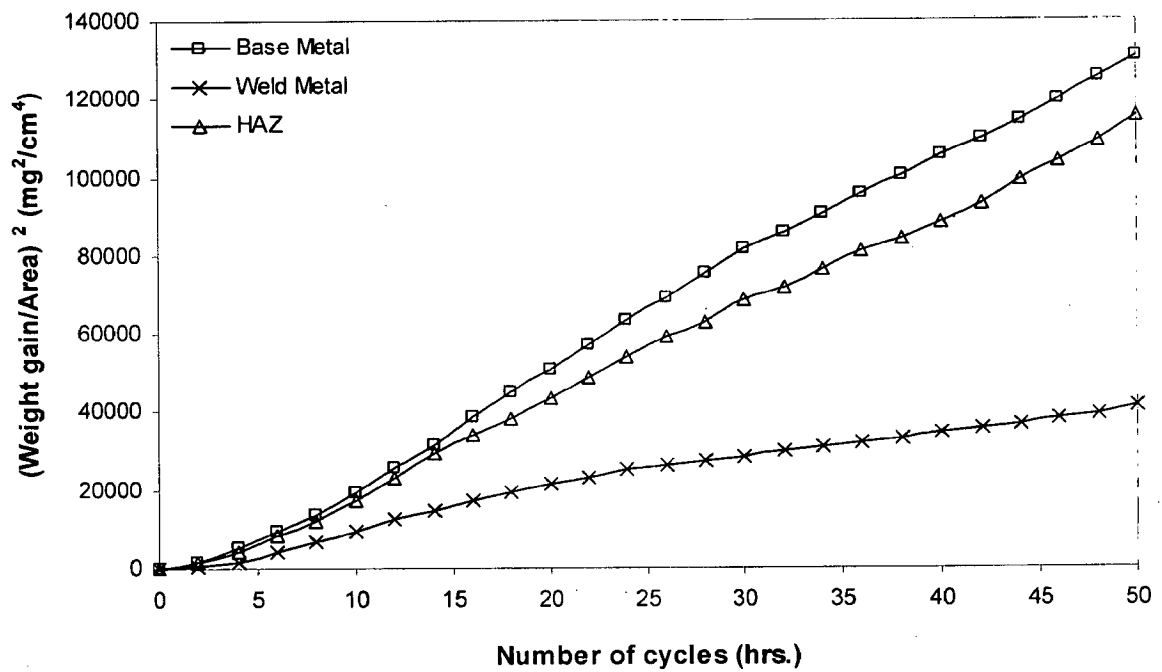


Fig. 6.74: Weight gain square (mg^2/cm^4) plot for different regions of TIG weldment in T22 steel exposed to cyclic hot corrosion in $\text{Na}_2\text{SO}_4\text{-60\%V}_2\text{O}_5$ at 900°C for 50 cycles.

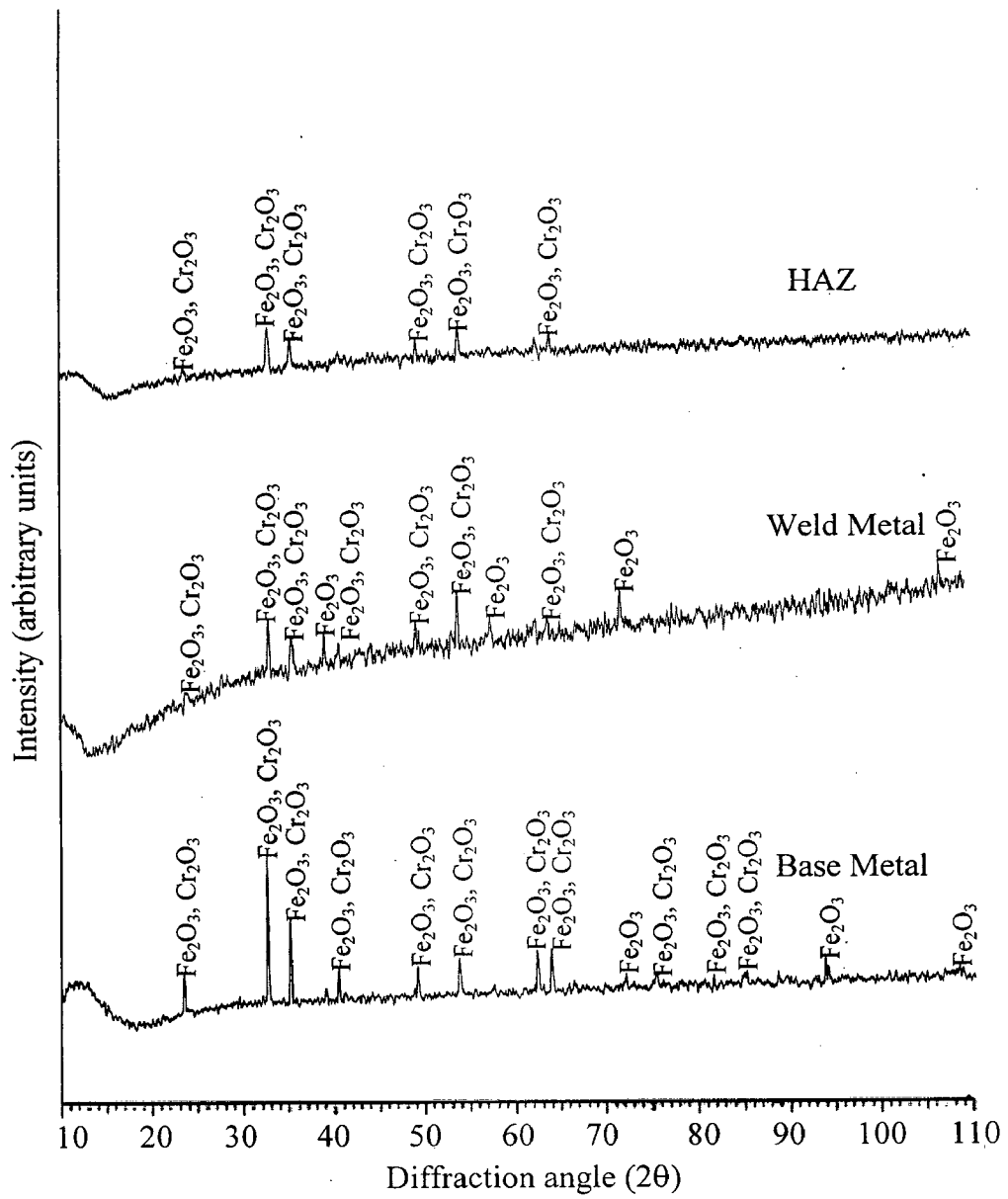
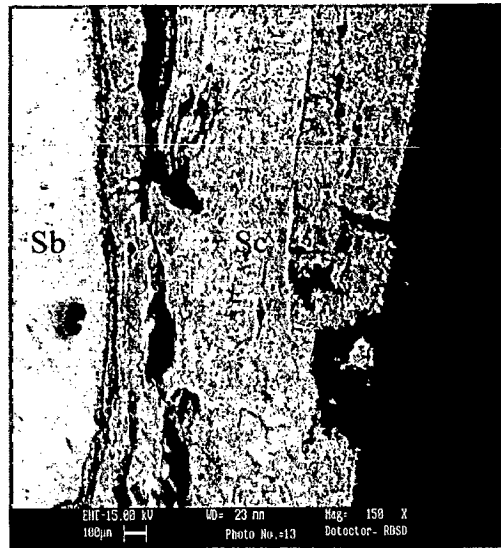
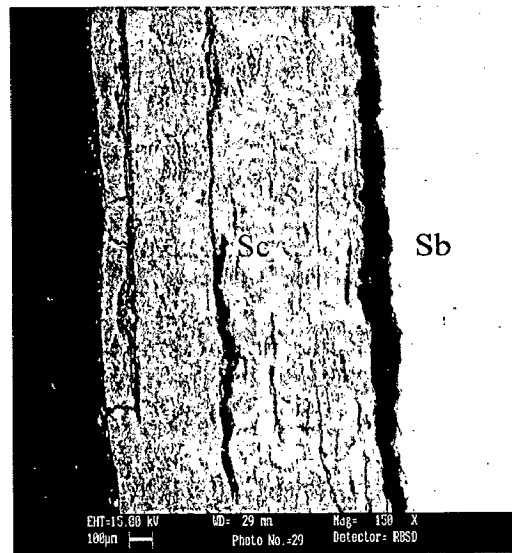


Fig. 6.75: X-ray diffraction profiles for different regions of TIG weldment in T22 steel exposed to cyclic hot corrosion in Na₂SO₄-60%V₂O₅ at 900°C for 50 cycles.



(a)



(b)

Fig. 6.76: SEM back scattered image of the cross section of different regions of TIG weldment in T22 steel exposed to cyclic hot corrosion in $\text{Na}_2\text{SO}_4\text{-60}\%\text{V}_2\text{O}_5$ at 900°C for 50 cycles (a) Weld Metal, 150X (b) HAZ, 150X.

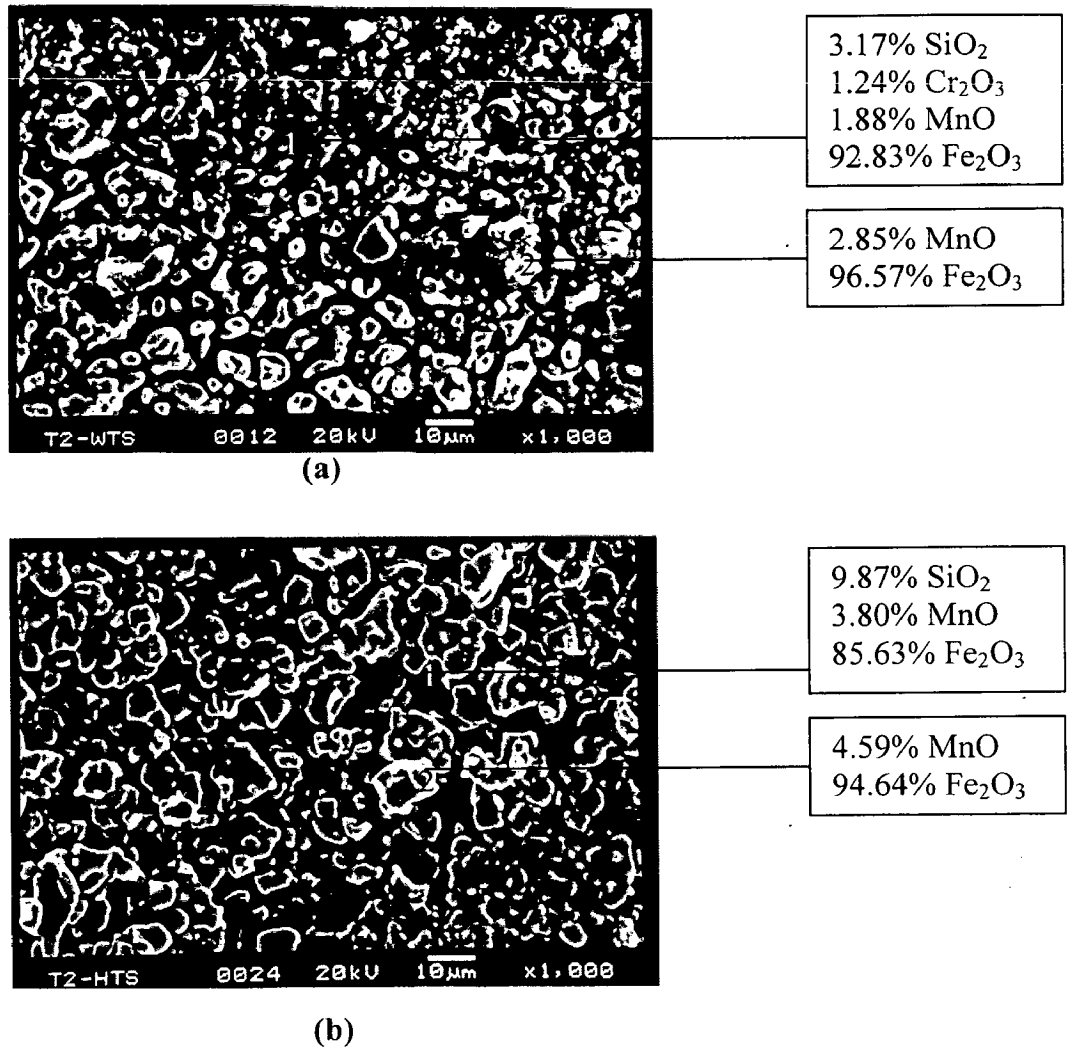


Fig.6.77: Surface morphology and EDAX analysis for different regions of TIG weldment in T22 steel exposed to cyclic hot corrosion in Na₂SO₄-60%V₂O₅ at 900°C for 50 cycles (a) Weld Metal, 1000X (b)HAZ, 1000X.

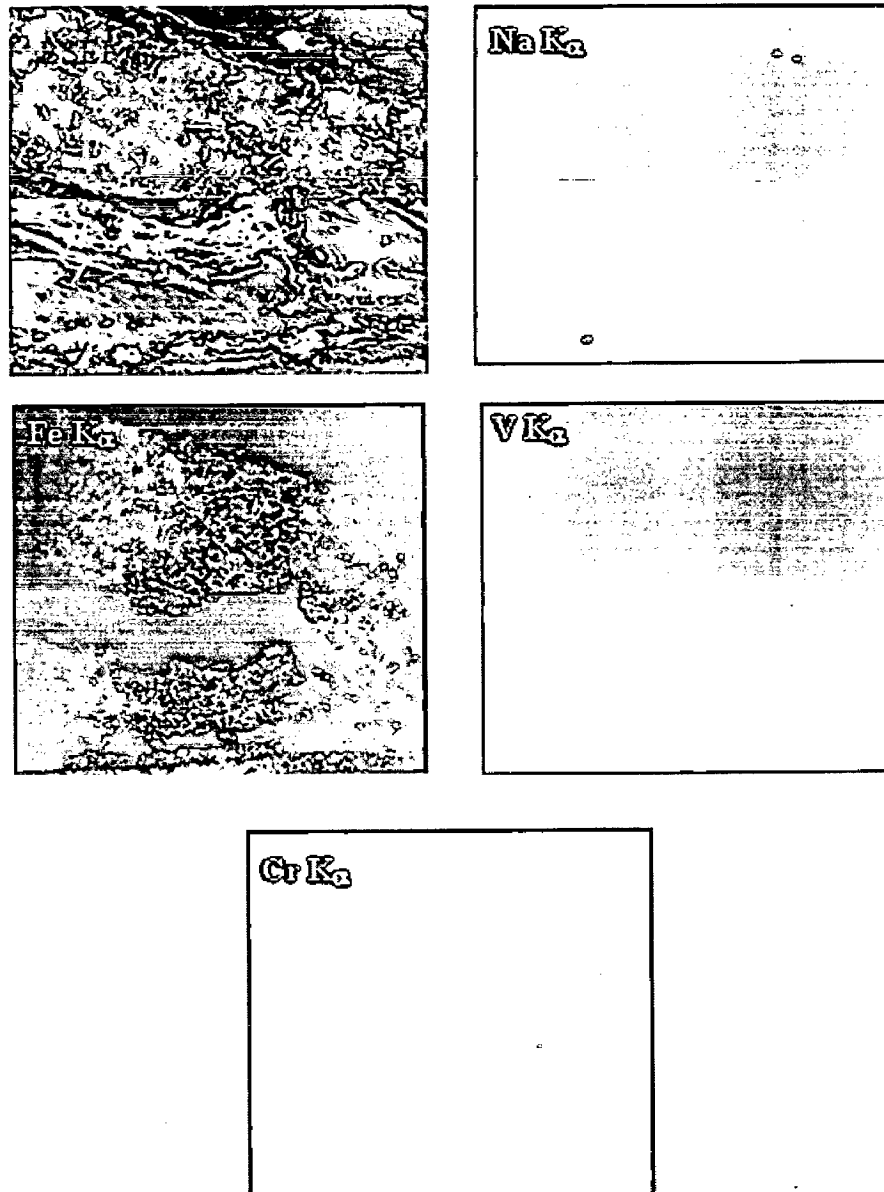


Fig. 6.78: BSEI and X-ray mapping of the cross-section of weld metal of TIG weldment in T22 steel subjected to cyclic oxidation in Na_2SO_4 - 60% V_2O_5 at 900°C for 50 cycles, 200X.

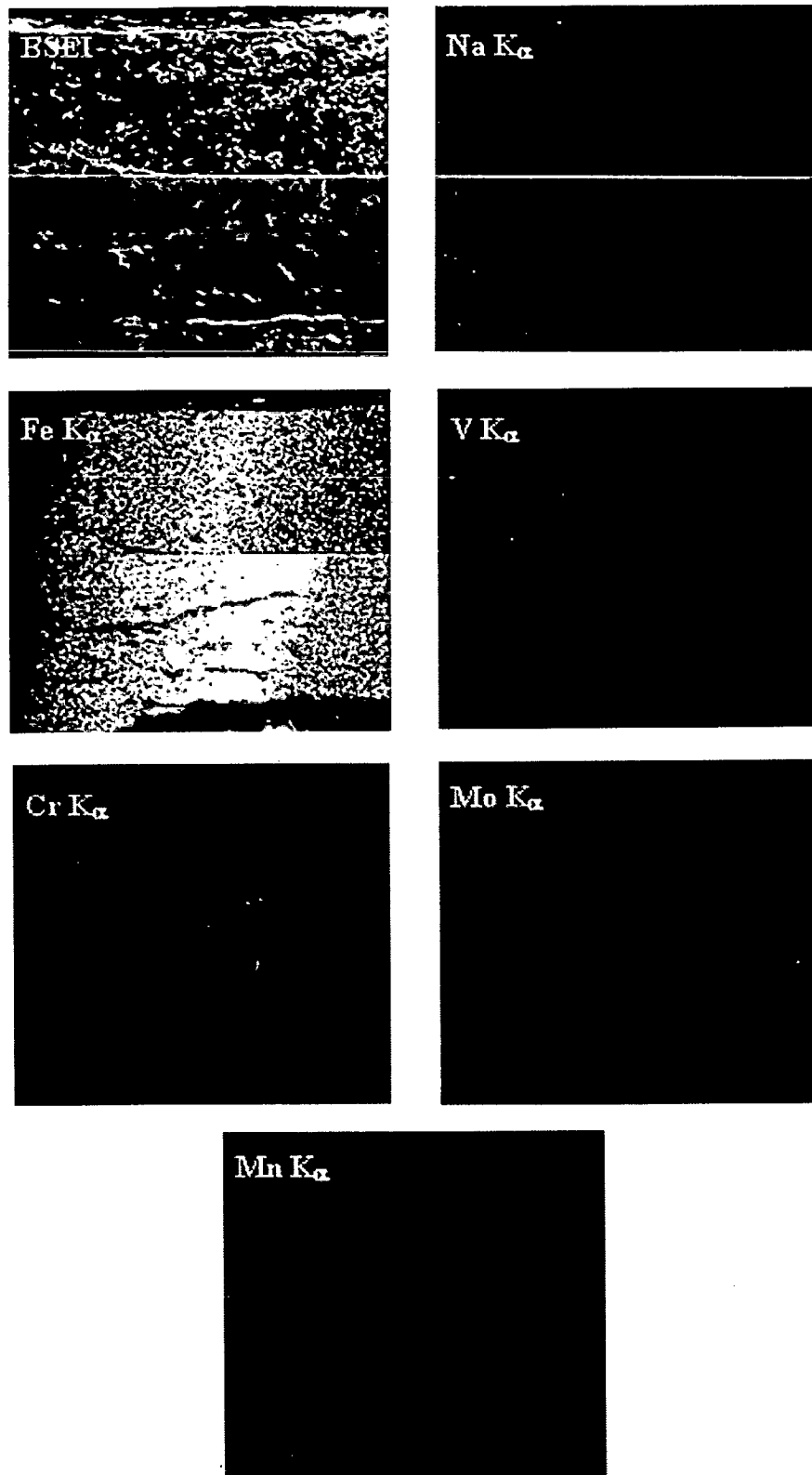


Fig. 6.79: BSEI and X-ray mapping of the cross-section of HAZ of TIG weldment in T22 steel subjected to cyclic oxidation in Na_2SO_4 -60% V_2O_5 at 900°C for 50 cycles, 200X.

6.3 SUMMARY OF RESULTS

Results as obtained after hot corrosion of weldments, different regions of weldment and unwelded steels in molten salt environment are summarised in Table 6.1. These tabulated results are ready reference to compare the hot corrosion behaviour of weldments, different regions of weldments and unwelded steels.

Table 6.1: Summary of the results for weldments, different regions of weldments and unwelded steels oxidised in molten salt ($\text{Na}_2\text{SO}_4\text{-60\%V}_2\text{O}_5$) at 900°C for 50 cycles.

Base steel	Base Metal Weldments	Scale thickness mm	Weight gain mg/cm^2	$K_p (10^{-8} \text{g}^2\text{cm}^{-1}\text{s}^{-1})$	XRD analysis	Remarks
GrA1	Base Metal	2.177	288.480	49.394	Fe_2O_3 and Fe_3O_4	Spalling indicated. Scale cracked during 36 th cycle.
	SMAW weldment	1.190 (weld) 1.297 (HAZ)	231.921	31.686	Fe_2O_3	Dark black shining spot on weld region, spalling during 7 th cycle. Scale cracked during 29 th cycle.
	TIG weldment	1.092 (weld) 1.228 (HAZ)	283.288	47.731	Fe_2O_3 and Fe_3O_4	Weld region indicated cracks during 5 th cycle. Dark blackish gray colour of scale.
	Weld metal (SMAW)	0.9	101.347	6.055	Fe_2O_3	Scale seen black from 1 st cycle. Little spalling indicated. No cracks upto 50 cycle.
	HAZ (SMAW)	0.821	84.307	4.148	Fe_2O_3	Spalling indicated in form of very fine particles. Scale cracked during 42 nd cycle.
	Weld metal (TIG)	1.9	185.407	20.335	Fe_2O_3 and Fe_3O_4	Black colour of oxide scale. Oxide scale cracking and oozing out at edges during 27 th cycle.
	HAZ (TIG)	1.555	197.368	22.531	Fe_2O_3	Spalling and cracking indicated. Scale oozing out at edges as stick.
T11	Base Metal	1.157	135.801	10.416	Fe_2O_3	Spalling indicated. Scale is lustrous and cracked during 32 nd cycle only.
	SMAW weldment	0.975 (weld) 0.994 (HAZ)	154.772	13.186	Fe_2O_3 and Fe_3O_4	Dark black shining spot on weld region. Scale cracked during 12 th cycle.
	TIG weldment	0.893 (weld) 1.793 (HAZ)	172.193	15.797	F_2O_3 and MnO	Minor cracks appeared during 8 th cycle.
	Weld metal (SMAW)	0.905	144.532	11.608	F_2O_3 and MnO	Dark blackish gray colour of oxide. Cracking and spalling noticed during 29 th cycle.
	HAZ (SMAW)	0.993	93.787	4.575	Fe_2O_3 and MnO	Colour of Oxide scale appeared black. Spalling noticed at the edges.

	Weld metal (TIG)	1.725	186.258	20.710	Fe ₂ O ₃	Intense spalling at edges during 38 th cycle. Little cracks appeared after 30 th cycle.
	HAZ (TIG)	1.371	119.606	8.213	Fe ₂ O ₃	Shining black spot appeared on oxide during 1 st cycle. Spalling noticed. No cracks.
T22	Base Metal	Intense spalling	361.105	76.233	Fe ₂ O ₃ , Cr ₂ O ₃	Intense spalling and sputtering indicated. Almost all the scale spalled off.
	SMAW weldment	1.955 (weld) 1.862 (HAZ)	377.307	84.372	Fe ₂ O ₃ , Cr ₂ O ₃ and Fe ₃ O ₄	Cracks appeared just after 1 st cycle and spalling was indicated. Drastic increase in cracks appeared during 27 th cycle.
	TIG weldment	1.242 (weld) 2.274 (HAZ)	309.250	57.738	Fe ₂ O ₃ , Cr ₂ O ₃ and FeS	Weld region seem shining black during 2 nd cycle. Cracks and spalling appeared just after 4 th cycle.
	Weld metal (SMAW)	1.104	122.836	9.388	Fe ₂ O ₃ and Cr ₂ O ₃	Blackish brown colour of oxide. Spalling noticed during 10 th cycle. Cracks appeared during 33 rd cycle.
	HAZ (SMAW)	0.931	155.821	14.818	Fe ₂ O ₃ , Cr ₂ O ₃ and MnO	Spalling noticed during 8 th cycle. Cracks appeared on surface and edges just after 28 th cycle.
	Weld metal (TIG)	1.3	202.704	23.098	Fe ₂ O ₃ and Cr ₂ O ₃	Colour of scale appeared black during 1 st cycle. Spalling noticed during 3 rd cycle. Cracks appeared during 13 th cycle. and intense cracks observed for subsequent cycle. Dull appearance of oxide surface.
	HAZ (TIG)	1.170	340.131	65.408	Fe ₂ O ₃ and Cr ₂ O ₃	Thin layer of oxide scale spalled during 17 th cycle. Little Cracks appeared during 32 nd cycle. Spalling observed at edges.

6.4 DISCUSSION

6.4.1 Unwelded Steels

The unwelded steels after cyclic oxidation in the molten salt mixture at 900⁰C have shown parabolic behaviour. Whereas intense spalling and higher corrosion rate was noticed for T22 type of steel. Parabolic rate constant of this type of steel is approximately 7.3 times more than the T11 type of steel. The higher corrosion rate for this steel inspite of more amounts of chromium than other two boiler steels might be attributed to the presence of molybdenum (1.06%) in this steel. This might have led to the acidic fluxing of the protective oxide scale. Identical results have been reported by Peters et al (1976), Fryburg et al (1982), Pettit and Meier (1984) and Misra (1986). This has been further confirmed by the absence of Mo in the final scale. The same condition was also discussed by Sidhu (2003A) in his Ph.D. thesis.

The severe corrosion observed in the present study in case of T22 steel upto the end of exposure may be in accordance with the findings of Misra (1986). During his hot corrosion studies for molybdenum containing nickel base alloy in Na₂SO₄ environment at 750-950⁰C, the author reported that higher the concentration of Mo, the sooner the melt would attain the MoO₃ activity necessary for the formation of solid NiMoO₄ and this would cause a decrease in the length of the period of accelerated corrosion. Lower percentage of Mo (1.06) in the concerned alloy for the present study might have increased the period of accelerating corrosion upto the end of 50 cycles. Probably this factor is responsible for the higher weight gain for this steel as compared to the other two steel inspite of more amount of chromium than other two boiler steels. Whereas lesser weight gain in case of T11 steel as compared to GrA1 steel might be due to some amount of chromium in the alloy. The protection might have been due to the formation of iron chromium spinel in the scale presence of which has further been confirmed by the EDAX analysis. The presence of some percentage of chromium in the subscale as revealed by the EDAX and EPMA analysis across the cross-section for T11 and T22 steel is in accordance with the findings of Sadique et al. (2000). The authors have reported that Fe-Cr alloys in oxygen at higher temperature (950-1050⁰C) form spinel (FeCr₂O₄) and Cr₂O₃ on the inner side and Fe₂O₃ on the outer side of the scale. This can also be attributed to depletion of iron due to oxidation to form the upper scale thereby leaving chromium rich pockets those further get oxidised to form iron chromium spinel

The surface XRD indicated the formation of Fe₂O₃ as the main constituent of the top scale. The formation of Fe₂O₃ has also been observed by Shi (1993) for the oxidation of iron by Na₂SO₄ at 750⁰C and by Sidhu (2003A) during hot corrosion of boiler steel in the Na₂SO₄-60%V₂O₅

environment at 900⁰C. Weak intensity peaks of Cr₂O₃ in the scale of T22 steel may due to the presence of some amount of chromium in the alloy steel. The presence of Fe₃O₄ in the scale of GrA1 steel is identical with the findings of Shi (1993).

6.4.2 SMAW Weldment

Exposure to the given salt environment resulted in internal oxidation, cracking and oozing out of material from beneath for the welded boiler steel identical to the results observed during oxidation of this weldment as reported in Chapter 5. The presence of blackish gray colour look in the surface scale of all the three type of steels might be attributed to the formation of Fe₂O₃. This has further been supported by the results of XRD analysis where Fe₂O₃ peaks are more intense in all the three type of steels. Internal oxidation in the scale of weldment might be attributed to the pits and cracks. Intense spalling and cracking has also been observed in unwelded specimen and its weldment of 2.25 Cr-1Mo (SA-213T-22) type of steel reported by Kumar et al. (2007).

Further, the presence of cracks in the scale for given molten salt environment can also be contributions to the penetration of species containing sodium through the pores as observed by EPMA for most of the welded steels. It is further observed that the decomposition of Na₂SO₄ gives rise to the penetration of SO₂ in the oxide of weldment and diffuse to the metal. This diffusion will be blocked by the metal which possesses high density. Therefore, SO₂ temporarily piles up in the oxide/metal interface region. The pile up of SO₂ in this region might be very harmful to the metal. It reacts with carbon and iron in the substrate at hot corrosion temperature and results in the formation of FeS, which leads to the internal sulphidation of the metal as also discussed by (Ahila, et al, 1994A) in case of welded 2.25 Cr-1Mo steel at 650⁰C.

However, presence of more cracks in case of welded T22 steels may be attributed to the existence of 1.06% molybdenum. The presence of a gap at the metal/oxide interface for welded T22 steels might be contributed by formation and evaporation of MoO₃. From the weight gain values indicated in Fig. 6.10 the resistance indicates better welded T11 steel to above environment. All the welded GrA1, T11 and T22 steels followed the parabolic rate law. Comparatively lesser hot corrosion is observed to welded T11 steel but still its weight gain is more than that for unwelded steel. The rate of corrosion for welded T22 steel is nearly equal to unwelded T22 steel during initial period of oxidation. This may be attributed to the development of cracks in the scale on the weld region of T22 steel as large numbers of cracks

were observed visually after 28th cycle. The better resistance to hot corrosion for welded T11 steels is further confirmed from BSEI (Fig. 6.13 (c, d)), where the oxides scale is intact with the metal. Whereas oxide scale of welded T22 steel seems to be fragile and got cracked as can be seen in Fig. 6.13 (e, f).

X-ray diffraction analysis indicate the formation of Fe₂O₃, Cr₂O₃, and Fe₃O₄ phases for welded T22 steel, those are in good agreement with the findings of Ahila et al (1994) in molten salt (K₂SO₄-NaCl) environment at 650°C. The resistance to hot corrosion might be due to the adherent oxides. Surface EDAX analysis of the corroded steels also supported the formation of such phases. Presence of Fe₃O₄ might be attributed to the diffusion of iron from the metal surface.

The EPMA results further confirm the formation of these oxides throughout the cross-section of scale. Some diffusion of vanadium through the cracks has been indicated. Diffusion of sodium into the oxide scale was there. Chromium rich layer in the bottom scale revealed that the accumulation of chromium during welding and form oxides in the scale.

The SMAW weldment followed the parabolic behaviour for the whole range of exposure. The weight gain for SMAW welded boiler steels followed the trend:

$$T22 > GrA1 > T11$$

6.4.3 TIG Weldment

TIG welded steel have shown better corrosion resistance than unwelded steels. Minimum corrosion rate has been indicated by TIG welded T11 steel and followed by welded GrA1 steel. Whereas slightly higher corrosion rate is indicated by welded T22 steel, but still it is less than the similar unwelded steel. The reason of relatively more attack in case of T22 steel weldment might be attributed to the presence of molybdenum. The cracks in the scale on weldment have been noticed for welded T22 steel just after 15th cycle which might have been responsible for comparatively higher corrosion rate than other welded steels. The corroding species might have passed through these cracks to reach the metal for further attack. The development of cracks in the scale of welded steel might have originated due to uneven expansion and contraction.

The TIG weldment followed the almost parabolic behaviour for the whole range of exposure. The weight gain for TIG welded boiler steels followed the trend:

$$T22 > GrA1 > T11$$

This sequence is further supported by the SEM backscattered image of the corroded cross-section of oxide scale in the welded steels as shown in Fig. 6.24. The scale is intact with

the GrA1 and T11 steels except for welded T22 steel where it is fragile and contributed to more weight gain value for this welded steel.

X-ray diffraction analysis indicate the formation of Fe_2O_3 , Cr_2O_3 , and FeS phases for welded T22 steel, These results are in accordance with the surface EDAX analysis. In case of welded T11 steel MnO phase has been identified by the X-ray diffractograms in addition to the Fe_2O_3 . The similar phases have also been reported by Sidhu and Prakash (2003) for hot corrosion of substrate boiler steel in molten salt environment at 900°C . The formation of the vanadates has been confirmed by the Electron Probe Micro Analyser (Fig. 6.29) where Fe, Na and V are coexisting in the outer scale.

The scale on welded T22 steel was composed of three layers, an inner continuous layer of Cr_2O_3 with Fe_2O_3 , thickness of which increases with increase in temperature, an outer Fe_2O_3 layer and an intermediate layer composed of oxides rich in iron. The presence of such layer in this study has also been confirmed by the surface EDAX analysis (Fig. 6.25 (e, f)). Intergranular attack is indicated by the EDAX analysis of welded T11 type of steel (Fig. 6.25 (c, d)).

6.4.4 Different Regions of SMAW and TIG Weldment in GrA1 Steel

The visual observation has indicated lower extent of cracking for the scale on HAZ in case of TIG weldment as compared to SMAW weldment. The XRD analysis of the scale revealed the oxides of iron in all the regions. More oxidation rate of base metal is observed due to the formation magnetite (Fe_3O_4). The cracks in the oxide scale were only noticed for weld metal of SMAW. The material oozing out from these cracks has been identified by the EDAX analysis to be mainly iron oxide (Fe_2O_3) along with MnO and SiO_2 as shown in Fig. 6.37 (a). It is further confirmed by EPMA the oxide scale mainly consists of iron oxide. The penetration of vanadium is indicated in the upper oxide scale in case of HAZ (SMAW) Fig. 6.39. The voids in the inner scale were confirmed by EPMA Fig. 6.63. From the weight gain values it can be inferred that the weld metal has been observed to have better resistance to the hot corrosion in TIG welding processes. The sequence of hot corrosion in terms of weight gain for different region of SMAW and TIG weldment in GrA1 steel is as follows:

Base metal > Weld Metal > HAZ for SMAW weldment

Base metal > HAZ > Weld Metal for TIG weldment.

6.4.5 Different Regions of SMAW and TIG Weldment in T11 Steel

It can be inferred from the weight gain data that corrosion rates of different regions of SMAW weldment in T11 type of steels are comparable to each other.

The XRD analysis indicates the formation of iron oxides along with the MnO in case of SMAW. The visual observation has indicated lower extent of cracking of scale in case of TIG welding as compared to SMAW welding. The cracks were noticed for scale on the weld metal of SMAW. The cracks in the scale on the weld metal have been identified by the EDAX analysis to be mainly iron oxide along with MnO as shown in Fig. 6.45 (a). Further EPMA has revealed the formation of noncontinuous chromium layer near the oxide scale/metal interface of weld metal Fig. 6.46. The voids and internal oxidation must have contributed to higher corrosion rate.

From the weight gain values it can be inferred that the weld metal has provided better to resistance to the hot corrosion. The sequence of hot corrosion in terms of weight gain for different region of SMAW and TIG weldment in T11 steel is as follows:

Weld metal > base metal > HAZ for SMAW and TIG weldment

6.4.6 Different Regions of SMAW and TIG Weldment in T22 Steel

The XRD analysis revealed the oxides of iron along with the chromium oxide (Cr_2O_3) as also suggested by (Ahila et al, 1993) in molten salt hot corrosion study. The visual observation has indicated lower extent of cracking of the scale in case of weld metal of TIG weldment as compared to SMAW weldment. The cracks were noticed in the scale on the weld metal of SMAW. The material oozing out from these cracks has been identified by the EDAX analysis to be mainly iron oxide (Fe_2O_3) along with MnO as shown in Fig. 6.53 (a). Whereas in case of HAZ the scale mainly consists of Fe_2O_3 along with MnO, SiO_2 and Cr_2O_3 Fig. 6.53 (b).

From the weight gain values it can be inferred that the weld metal has been indicated better to resistance to the hot corrosion. The sequence of hot corrosion in terms of weight gain for different region of SMAW and TIG weldment in T22 steel is as follows:

Base metal > HAZ > weld metal for SMAW and TIG weldment

It can be inferred from the weight gain data that corrosion rates of different regions of SMAW weldment in T22 type of steel are comparable to each other. The base metal showed the more weight gain than that of HAZ and weld metal and the reason may be the intense spalling and cracking of the oxide scale. From the scale thickness measurement (BSEI) it can be concluded that the multilayer scale on the HAZ specimen was thicker as compared to scale on the weld metal. Further it is confirmed by EPMA that the scale mainly contained oxide of iron with small concentration of chromium as shown in case of the scale on HAZ Fig. 6.79.

COMPREHENSIVE DISCUSSION

The important results of the present investigations covering all the two environments are discussed in this chapter. It includes comparative discussion for the results obtained in air and molten salt environment in view of the existing literature. Efforts have been made to find out the mechanisms and mode of corrosion wherever possible. Further the comparative corrosion resistance of different regions of weldments in boiler steel in similar environments has also been discussed.

The weldments were obtained in the different boiler steel by SMAW and TIG welding technique. The macrostructure shown that the all the weldments made by SMAW and TIG process were of 'V' shape with good penetration (Fig. 4.2 and 4.3). Heat affected zone in SMAW weldments is wider as compared HAZ in case of TIG weldments.

The weld zone of T22 weldment made by SMAW and TIG is 12 mm and 10 mm respectively, which is higher as compared to weld zone of T11 and GrA1 weldment (Table 4.3). The porosity measurement indicated that the SMAW weldment showed higher porosity as compared to TIG weldment (Table 4.4).

The average hardness value across the weld zone for T22 weldment made by SMAW and TIG is 350 (HV). Whereas the hardness value of T11 and GrA1 weldments were around 225 (HV). The fluctuation in hardness profile is more across the weldment made by TIG process as compared to the weldment made by SMAW (Fig. 4.4 and 4.5).

The ultimate tensile strength for all the boiler steel weldment made by SMAW is around 600 MPa. Whereas the same for one made by TIG process was found to be around 500 MPa. The percentage of elongation for the weldment made by SMAW is higher as compared to the weldments made by TIG. Also it was observed that the failure of the test samples occurred on HAZ during tensile test for all the weldments (Table 4.5).

The microstructure plots for all the weldments made by SMAW and TIG indicates the dendrite formation in the weld zone and the grain growth was observed in HAZ region. Some carbides precipitation in the interface was also revealed.

The histograms showing the weight gains in air and molten salt environments, for unwelded, weldments and its different regions in steels are presented in Figs. 7.1 and 7.2 respectively. From these histograms it can be inferred that TIG weldment provided maximum resistance to degradation.

The weldments of different boiler steels made by SMAW and TIG exposed in air at 900°C. The weight gain was noted after 50 cycles for different steels and arranged in the following order.

Table 7.1: The weight gain for different steel when exposed in air at 900 °C.

Welding technique	Weight gain for different steels		
	Weldment	Weld zone	HAZ
SMAW	T22>GrA1>T11	GrA1>T22>T11	T22>T11 > GrA1
TIG	T22>GrA1>T11	T22>GrA1>T11	T22>GrA1>T11

The weldment of different boiler steels made by SMAW and TIG exposed in Na₂SO₄-60% V₂O₅ at 900 °C. The weight gain was noted after cycles for different steels and arranged in the following order.

Table 7.2: The weight gain for different steels when exposed in Na₂SO₄-60% V₂O₅ at 900 °C.

Welding technique	Weight gain for different steels		
	Weldment	Weld zone	HAZ
SMAW	T22>GrA1>T11	T11>T22>GrA1	T22>T11>GrA1
TIG	T22>GrA1>T11	T22>T11 >GrA1	T22> GrA1>T11

The hot corrosion of parent boiler steel was also studied under air and molten salt (Na₂SO₄-60% V₂O₅) environment at 900 °C for comparison. The weight gain for different steels is arranged in the following order.

GrA1> T11>T22 in air

T22>GrA1>T11 in molten salt

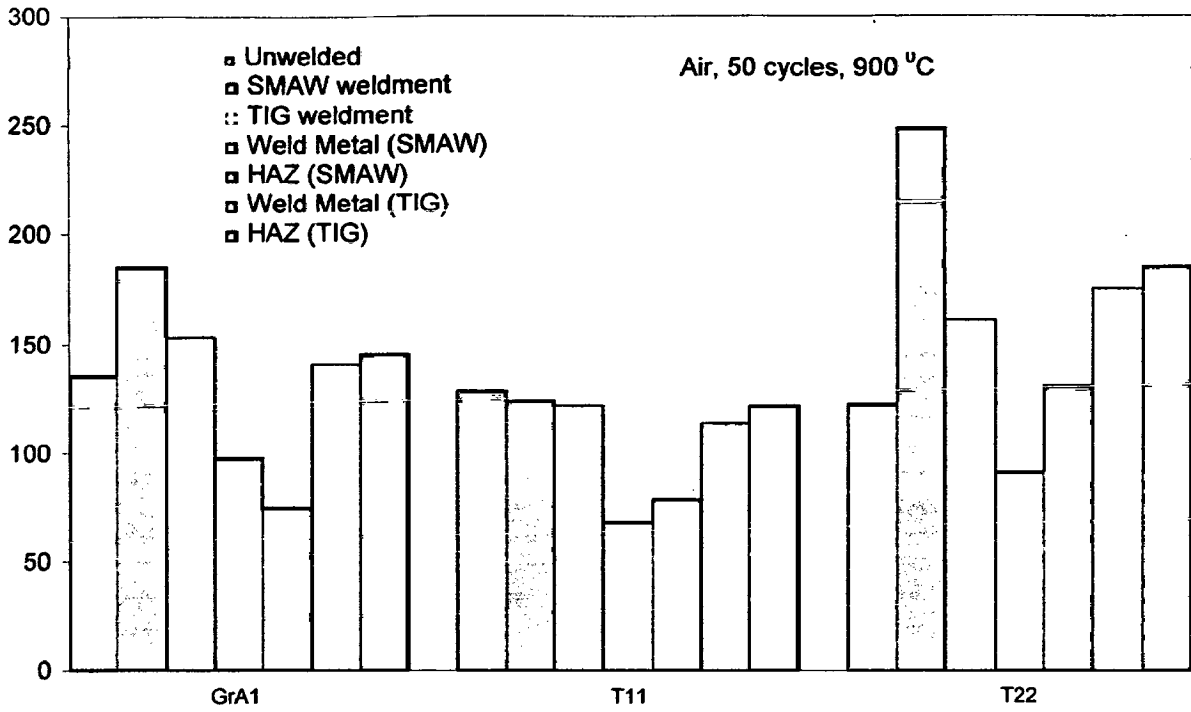


Fig. 7.1 Bar chart indicating weight gain (mg/cm^2) for weldments, different regions of weldment and unwelded steels exposed to cyclic oxidation in air at 900°C for 50 cycles.

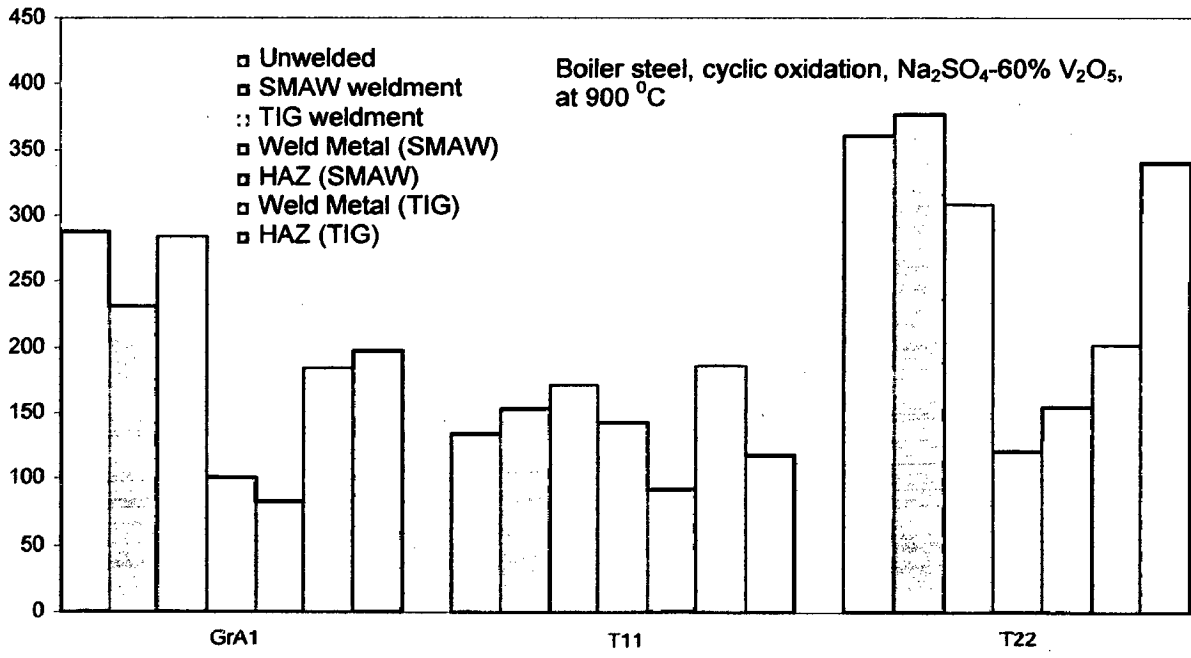


Fig. 7.2 Bar chart indicating weight gain (mg/cm^2) for weldments, different regions of weldment and unwelded steels exposed to cyclic hot corrosion in Na_2SO_4 -60% V_2O_5 at 900°C for 50 cycles.

Most of the weldments had behaved well during testing in air and molten salt environment. The damage occurring in the base metal provides paths by which corrosive gases can actively react with the grain boundary and will thus allow significant grain boundary corrosion attack. Raman and Gnanamoorthy (1993) subjected microstructurally different regions of weld metal, heat affected zone (HAZ) and base metal to oxidation for different durations from 2 to 500 h in air at 773 K. They reported that all three types of specimens followed parabolic kinetics until the weld metal suffered spallation. They further observed the oxidation rates of the base metal and the weld metal were similar, the HAZ had a much higher rate than those in the other regions. The composite weldment, consisting of the three regions, when oxidized at 773 K, was found to have developed a considerably thicker oxide scale over the HAZ as compared to those of the base metal and the weld metal.

Chatterjee et al (2001) have proposed that the cracking of the scale results from the enrichment by Mo at the substrate-scale interface where MoO_2 is formed. This oxide converts into MoO_3 on further oxidation which is in liquid form at the given temperature of exposure and penetrates along the alloy-scale interface. They further opined that molten MoO_3 exerts dissolving action on other oxides such as Fe_2O_3 and Cr_2O_3 and this fluxing may be further accelerated by the enthalpy of formation of Fe_2O_3 and Cr_2O_3 which tends to increase the temperature at the alloy-scale interface. In such a situation Fe_2O_3 and Cr_2O_3 transport through the molten MoO_3 layer and precipitation at the MoO_3 (liquid)-solid oxide interface which is comparatively cooler.

T22 steel which contains 2.64% chromium still has more resistance to oxidation in air at 900°C relative to T11 steel having only 0.91% chromium perhaps due to higher amount of Mo (1.06%). Further this steel showed inferior resistance to Na_2SO_4 -60% V_2O_5 which may be attributed to reaction of molten salt with MoO_3 to form lower melting point phase like Na_2MoO_4 which could have led to acidic fluxing of the protective oxide scale as suggested by Fryburg et al (1984) and Pettit and Meier (1984).

From the observation it was noted that the corrosion rate of the weldment (Base Metal +Weld Metal +HAZ) under molten salt environment is higher as compared to individual weld metal as well as HAZ. This is because of the variation of microstructure and composition

between base metals, weld metal and HAZ might have lead to a galvanic corrosion under molten salt at 900 °C which acts as an electrolyte.

The higher oxidation rate of the HAZ and the formation of a thicker scale over it in case of 2.25 Cr- 1Mo (T22) steel have been attributed to absence of a protective inner scale of Fe-Cr oxides, due to the non-availability of free Cr in this region as suggested by Raman and Gnanamoorthy (1993).

CONCLUSIONS

The conclusions from the present study on shielded metal arc weldment and tungsten inert gas weldment in three types of boiler tube steels namely SA210-Grade A1 (GrA1), SA213-T11 (T11) and SA213-T22 (T22) have been summarized here. The weldments, its different regions and unwelded steels were further subjected to oxidation in air and molten salt (Na_2SO_4 -60% V_2O_5) environment.

- (1) SMAW and TIG weldments were successfully made in the boiler tube steels with minimum heat input to obtain narrow HAZ and minimum carbide formation.
- (2) All these weldments showed very less porosity (0.05-0.1%) indicating formation of sound welds.
- (3) Total width of SMAW weldment was limited to approximately 11-12 mm whereas it was 9-10 mm in case of TIG weldment.
- (4) Microhardness measurement across the cross-section of weldments for both as SMAW and TIG welded samples showed that the weld region and HAZ have higher hardness as compared to the base metal. This difference in hardness has been attributed to the formation of carbides during weld thermal cycle.
- (5) All the above weldments showed appreciable higher corrosion rates in the air and molten salt environment. SMAW and TIG welded T11 steel showed the lowest weight gain as compared to same welded GrA1 and T22 steels in case of air and molten salt environment studies.
- (6) TIG weldment has shown lesser weight gain with oxidation in air and hot corrosion in Na_2SO_4 -60% V_2O_5 environment. XRD analysis has indicated the presence of Fe_2O_3 as a predominant phase in the oxidation in air and hot corrosion environment.
- (7) The cracks were observed nearly in all the scales on the welded steel specimens subjected to cyclic oxidation in air and cyclic hot corrosion in molten salt environment. This has been attributed to difference in the coefficients of thermal expansion of the

base metal and scale. The oozing out of iron oxide from the cracks indicates that through these cracks the oxidizing environment could reach the substrates.

- (8) The chemical compositions of protrusions have been confirmed to be iron oxide by EDAX analysis. This trend was seen for all the weldments.
- (9) The most common feature in case of TIG weldment where oxidation and hot corrosion resistance is found to be better in the given environments is perhaps due to the presence of chromium rich layer revealed in the scale just above the scale-metal interface.
- (10) In case of studies in air the general trend regarding the oxidation resistance provided by these SMAW and TIG weldments in boiler tube steels is as follows: T11 > GrA1 > T22
- (11) All the given weldments show the parabolic behaviour in both air and molten salt environment, so far as the corrosion kinetics is concerned.
- (12) Oxidation resistance in hot corrosion environment of base metal, weld metal and HAZ varied with the weldments obtained by SMAW and TIG welding process. The trend of oxidation resistance of various specimen from different regions of the welds in the steels are as follows:

Base metal < Weld Metal < HAZ for SMAW weldment in GrA1 steel

Base < HAZ < Weld metal for TIG weldment in GrA1 steel

Weld metal < Base metal < HAZ for SMAW and TIG weldment in T11 steel

Base metal < HAZ < Weld metal for SMAW and TIG weldment in T22 steel

- (13) In case of welded and unwelded T11, T22 steels samples subjected to molten salt environment, presence of chromium layer have been identified at scale/metal interface and at the bottom of the scale in some cases.
- (14) The over all trend of corrosion resistance in the given environment is as follows:
 - TIG > SMAW weldment in air oxidation for all the three steels
 - SMAW > TIG weldment in the molten salt environment in case of GrA1 and T11 steel
 - TIG > SMAW weldment in the molten salt environment in case of T22 steel.

SUGGESTIONS FOR FUTURE WORK

- (1) Studies on hot corrosion behaviour of these weldments should also be done in the actual industrial environment such as in the actual running boiler for longer durations with longer cycles.
- (2) Modeling and Simulation of the Corrosion criteria of the weldments may be performed to establish the corrosion phenomenon in weldments.
- (3) Other welding techniques like electron beam welding and friction welding may be used to form the welds and they may be compared with the present investigation.
- (4) Corrosion studies on weldments may be performed in different aggressive chloride containing environments at high temperature.
- (5) Corrosion studies on weldments and its different regions should be done in aqueous environment also.
- (6) Mechanical properties of the obtained weldment may be studied in order to study the correlation of Mechanical properties with the Corrosion and Corrosion mechanism like measurement of residual stresses.
- (7) Attempts can be made to estimate the useful life of the weldments by extrapolation of the laboratory data by mathematical modeling.

APPENDIX

Table A.1: Thermal expansion coefficients and Thermal diffusivity of substrate steels.

Alloy	Thermal expansion coefficient (10^{-6} per $^{\circ}\text{C}$)	Reference
1Cr-0.5 Mo steel (T11)	13.9	Metal Hand Book (1961)
2.25Cr-1Mo steel (T22)	14.2	
	Thermal Diffusivity (ft^2/hr)	
C-Mn-Si steel (GrA1)	0.454	ASME Boiler and Pressure vessels code (1978)
1Cr-0.5Mo steel (T11)	0.502	
2.25Cr-1Mo steel (T22)	0.408	

Table A.2: Values of parabolic rate constant K_p ($10^{-8} \text{ g}^2\text{cm}^{-4}\text{s}^{-1}$) for weldments, different regions of weldment and unwelded steels exposed to air and molten salt environment for 50 cycles at 900°C .

Weldments	Air, 900°C Parabolic rate constant (K_p)			Molten salt environment, 900°C Parabolic rate constant (K_p)		
	SA-210 Grade A1	SA-213 T11	SA-213 T22	SA-210 Grade A1	SA-213 T11	SA-213 T22
Base Metal	10.282	9.384	8.515	49.394	10.416	76.233
SMAW weldment	20.365	8.832	36.447	31.686	13.186	84.372
TIG weldment	13.074	8.348	20.371 (The behaviour was parabolic from 22 nd to 50 th cycle)	47.731	15.797	57.738
Weld metal (SMAW)	5.558	2.469	4.859	6.055	11.608	9.388
HAZ (SMAW)	3.102	3.344	9.826	4.148	4.575	14.818
Weld metal (TIG)	10.927	6.962	17.107 (The behaviour was not parabolic from 38 th to 50 th cycle)	20.335	20.710	23.098
HAZ (TIG)	11.656	8.323	19.752 upto 40 th cycle	22.531	8.213	65.408

Table A.3: Scale thickness values of weldments, different regions of weldment and unwelded steels exposed to air and molten salt environment for 50 cycles at 900°C.

Weldments	Air, 900°C Scale thickness (mm)			Molten salt environment, 900°C Scale thickness (mm)		
	SA-210 Grade A1	SA-213 T11	SA-213 T22	SA-210 Grade A1	SA-213 T11	SA-213 T22
Base Metal	1.1	1.289	0.763	2.177	1.157	Intense spalling
SMAW weldment	1.110(weld) 1.196(HAZ)	1.250 (weld) 1.373 (HAZ)	1.333 (weld) 1.386 (HAZ)	1.190 (weld) 1.297 (HAZ)	0.975 (weld) 0.994 (HAZ)	1.955(weld) 1.862(HAZ)
TIG weldment	0.704(weld) 0.843(HAZ)	1.080(weld) 0.795(HAZ)	1.095 (weld) 0.940 (HAZ)	1.092 (weld) 1.228 (HAZ)	0.893 (weld) 1.793 (HAZ)	1.242(weld) 2.274(HAZ)
Weld metal (SMAW)	0.866	0.618	0.689	0.9	0.905	1.104
HAZ (SMAW)	0.822	0.726	0.735	0.821	0.993	0.931
Weld metal (TIG)	0.812	1.334	0.8	1.9	1.725	1.3
HAZ (TIG)	1.370	1.050	0.831	1.555	1.371	1.170

Table A.4: Chemical composition (Wt%) for boiler tube steels and electrode/ filler metal, used for obtaining the weldments and the environment of study

Boiler Tube Steels													Weldments made by		Exposure Time	Exposure Temperature	
Type of Steel	ASTM code	Composition	Chemical Composition (Wt %)									Process	Arc Current	Exposure Time	Exposure Temperature		
			C	Mn	Si	S	P	Cr	Mo	Fe							
GrA1	SA210	Nominal	0.27	0.93	0.1	0.058	0.048	-	-	-	-	-	-	SMAW and TIG welding	95 Ampere	<ul style="list-style-type: none"> • 50 cycles each cycle of 1 hr heating followed by 20 min. cooling at ambient conditions • Air, 900 °C • Air, 900 °C after thin coat of Na₂SO₄-60% V₂O₅ 	
	Grade A1	Actual	0.2952	0.5977	0.2873	0.0056	0.0089	-	-	-	-	-	-				
T-11	SA213	Nominal	0.15	0.3-0.6	0.5-1	0.03	0.03	1-1.5	0.44-0.65	-	-	-	-	SMAW and TIG welding	95 Ampere	<ul style="list-style-type: none"> • 50 cycles each cycle of 1 hr heating followed by 20 min. cooling at ambient conditions • Air, 900 °C • Air, 900 °C after thin coat of Na₂SO₄-60% V₂O₅ 	
	-T-11	Actual	0.1359	0.4272	0.3056	0.0064	0.0123	0.9113	0.5135	-	-	-	-				
T-22	SA213	Nominal	0.15	0.3-0.6	0.5	0.03	0.03	1.9-2.6	0.87-1.13	-	-	-	-	SMAW and TIG welding	95 Ampere	<ul style="list-style-type: none"> • 50 cycles each cycle of 1 hr heating followed by 20 min. cooling at ambient conditions • Air, 900 °C • Air, 900 °C after thin coat of Na₂SO₄-60% V₂O₅ 	
	-T-22	Actual	0.1359	0.1703	0.4458	0.0092	0.0210	2.6460	1.0652	-	-	-	-				
Electrode/Filler Metal																	
Process/ Materials	Electrode specification	AWS	Chemical Composition (Wt %)														
			C	Mn	Si	S	P	Cr	Mo	Fe							
SMAW/ GrA1	AWS A5.1 E 7018		0.08	1.2	0.52	0.016	0.015	-	-	-	-	-	-				
SMAW/ T11	AWS A5.5 E8018-B2		0.08	0.65	0.48	0.023	0.018	1.3	0.48	-	-	-	-				
SMAW/ T22	AWS A5.5 E9018-B3		0.08	0.6	0.54	0.021	0.019	2.37	1.15	-	-	-	-				
TIG/ GrA1	AWS A5.18 ER 70S-2		0.05	1.15	0.45	0.018	0.02	-	-	-	-	-	-				
TIG/ T11	AWS A5.28 ER 80S-B2		0.09	0.55	0.48	0.006	0.012	1.35	0.55	-	-	-	-				
TIG/T22	AWS A5.28 ER 90S-B3		0.10	0.62	0.48	0.006	0.009	2.55	2.55	-	-	-	-				

REFERENCES

1. **Ahila, S., Iyer, S. R. and Radhakrishnan V.M., (1994), "Hot Corrosion of 2.25 Cr-1Mo Boiler Steel and Its Weldments," Part I Thermogravimetric and Metallurgical study, Trans. IIM, Vol. 47, No. 2-3, pp. 169-182.**
2. **Ahila, S., Iyer, S. R. and Radhakrishnan V.M., (1994A), "Hot Corrosion of 2.25 Cr-1Mo Boiler Steel and Its Weldments," Part II Corrosion Mechanism, Trans. IIM, Vol. 47, No. 2-3, pp. 183-191.**
3. **Ahila, S., Iyer, S. R. and Radhakrishnan V.M., and Prasad P.B. S. N. V., (1993), "A comparative study of Hot Corrosion of Welded and Unwelded 2.25 Cr- 1Mo Steel," Materilas Letters, Vol. 16, , pp. 130-133.**
4. **Ahila, S., Iyer, S. R. and Radhakrishnan V.M., and Prasad P.B. S. N. V., (1993A), "Accelerated of High Temperature oxidation of Manual Metal arc Welded 2.25 Cr -1 Mo Steel by Sulphate- Chloride mixture," Materilas Letters, Vol. 17, pp. 155-158.**
5. **American Society of Mechanical Engineers (ASME), (1978), Boiler and Pressure Vessel Code, Section VIII- Pressure Vessels, pp. 1-102.**
6. **Anderson, T. L., (1981), Edwards, G. R., "Corrosion susceptibility of 2/one quarter/ Cr- 1 Mo steel in a lithium-17.6 wt pct lead liquid," Journal of Materials for Energy Systems, Vol. 2, No. 4, pp. 16-25.**
7. **AWS D 1.1, (1998), Welding practice for Cr- Mo Boiler Steel, AWS Manual.**
8. **Baalu, T.R.T., (2005), NACE International Conference on Corrosion (CORCON 2005), NACE International India section, November 2005, Chennai, Tamil Nadu, India.**
9. **Balakrishnan, K. (1994), "Metallurgical aspects of Corrosion," Bull. Mater. Sci., Vol. 17, No. 6, pp. 671-684.**
10. **Bass, H., Pickles, C. A., Prince, J., (1994), "Effect of Operating Temperature Expo sure on Non- Post-Weld Heat Treated 2.25 Cr-1 Mo Steel* Weldments," Canadian Metallurgical Quarterly, Vol. 33, No. 4, pp. 345.**
11. **Baxter, D. J., (1986), "The performance of pack-diffusion aluminized and/or chromized low-alloy and carbon steels in sulphur-containing coal gasifier environments," High Temp. Tech., Vol. 4, pp. 207-18.**
12. **Bhadeshia, H. K. D. H. and Svensson, L.E., (1993), "Mathematical Modelling of Weld Phenomena," eds H. Cerjak, K. E. Easterling, Institute of Materials, London, pp. 109-182.**

13. **Birks**, N. and Meier, G. H., (1983), "Introduction to High Temperature Oxid. Met.," Edward Arnold (Publ.) Ltd., 41 Bedford Square, London WC1B 3DQ.
14. **Bornstein**, N. S. and Decrescente, M. A., (1970), "The Role of Sodium and Sulfur in the Accelerated Oxidation Phenomena-Sulfidation," *Corrosion*, Vol. 26, No. 7, pp. 209-214.
15. **Bruce** R. S. and Alan W. P., (1994), "Welding Failure Analysis," *Materials Characterization*, Vol. 33, pp. 295-309.
16. **Burman**, C. and Ericsson, T., (1983), "Study of Plasma sprayed FeCrAlY coatings after Various Post-Treatments," Proc. Sympos. High Temperature Protective Coatings, March 7-8, Atlanta, GA, USA, Ed-Singhal, S. C., Pub. Metall. Soc of AIME, Warrendale, PA, USA, pp. 51-59.
17. **Cary**, H. B., (1979), "Modern Welding Technology," Practice Hall Inc., Englewood cliffs, NJ.
18. **Castro**, R.J., De Cadenet, J.J., (1975), "Welding Metallurgy of Stainless Steel and heat resisting Steels," Cambridge university press, London, U. K.
19. **Chatterjee**, U. K., Bose, S. K. and Roy, S. K., (2001), "Environmental Degradation of Metals," Pub., Marcel Dekker, 270 Madison Avenue, New York.
20. **Colot**, D., Petelot, D., Hoch, P. and Beranger, G., (1997), "Mechanisms of Hot Corrosion in Coal Fired Boilers Gas T91 and EM12 Steels," *Mater. Sci. Forum*, Vol. 251-254, pp. 641-48.
21. **Danyluk**, S. and Park, J. Y., (1979), "Technical Note: Corrosion and Grain Boundary Penetration in Type 316 Stainless Steel Exposed to a Coal Gasification Environment," *Corrosion*, Vol. 35, No. 12, pp. 575-76.
22. **Deb**, D, Iyer, S. R. and Radhakrishnan, V. M., (1996), "A Comparative Study of Oxidation and Hot Corrosion of a Cast Nickel Base Superalloy in Different Corrosive Environments," *Mater. Letters*, Vol. 29, pp. 19-23.
23. **Dooley**, B., (1993), "Boiler Tube Failure Metallurgical Guide, Volume 1: Technical Report," EPRI Report TR-102433-V1.
24. **Dube**, C. A., Aaronson, H. I. and Mehl, R. F., (1958), "The Formation of Proeutectoid Ferrite in Plain Carbon Steels," *Rev. Met.*, Vol. 55, pp. 201.
25. **Exworthy**, L. F., Little, W. J. and Flewitt, (2002), "Diagnosis of cracking in the boiler shell seam weld at Sizewell A Power Station," *International Journal of Pressure Vessels and Piping*, Vol. 79, pp. 413-426.

26. **Fleming**, A., Maskell, R. V., Buchanan, L. W. and Wilson, T., (2000), "Material Developments for Supercritical Boilers and Pipe work in Materials for High Temperature Power Generation and Process Plant Applications," Edited by Strang, A. Institute of Materials Publication Book No. 728., pp. 32-77.
27. **Fryburg**, G. C., Kohl, F. J., Stearns, C. A. and Fielder, W. L., (1982), "Chemical Reactions involved in the Initiation of Hot Corrosion of B-1900 and NASA-TRW VIA," J. Electrochem. Soc., Vol. 129, No. 3, pp. 571-85.
28. **Fryburg**, G. C., Kohl, F. J. and Stearns, C.A., (1984), "Chemical Reactions Involved in the Initiation of Hot Corrosion of IN-738," J. Electrochem. Soc., Vol. 131, No. 12, pp. 2985-2996.
29. **Gardiner**, C. P. and Melchers, R. E., (2002), "Corrosion of Mild Steel by Coal and Iron Ore," Corros. Sci., Vol. 44, No. 12, pp. 2665-73.
30. **Goebel**, J. A. and Pettit, F. S., (1970), "Na₂SO₄ - Induced Accelerated Oxidation (Hot Corrosion) of Nickel," Met. Trans., Vol. 1, pp. 1943-54.
31. **Goebel**, J. A., Pettit, F. S. and Goward, G. W., (1973), "Mechanisms for Hot Corrosion of Nickel -Base alloys," Metall. Trans. Vol. 4, pp. 261-275.
32. **Hammond**, J. P.; Patriarca, P.; Slaughter, G. M.; Maxwell, W. A., (1973), Welding Journal(Miami, Fla), Vol. 52, No. 6, pp. 268 -280.
33. **Hancock**, P., (1987), "Vanadic and Chloride Attack of Superalloys," Mater. Sci. Technol., Vol. 3, pp. 536-44.
34. **He**, J. L., Chen, K. C., Chen, C. C., Leyland, A. and Matthews, A., (2001), "Cyclic Oxidation Resistance of Ni-Al Alloy Coatings Deposited on Steel by a Cathodic Arc Plasma Process," Surf. Coat. Technol., Vol. 135, pp. 158-65.
35. **Heckel**, R. W. and Paxton, H. W., (1961), "On the Morphology of Proeutectoid Cementite," Transactions ASM, 53, pp. 539.
36. **Heubner**, U., and Hoffman, F., (1989), "Special aspects of localized High-Temperature Corrosion," Werkstoffe und Korros, Vol. 40, pp. 363-369.
37. **Hocking**, M. G., (1993), "Coatings Resistant to Erosive/Corrosive and Severe Environments," Surf. Coat. Technol., Vol. 62, pp. 460-66.
38. **Hodgkiess**, T., Eid, N. and Hanbury, W. T., (1978), "Corrosion of Welds in Seawater," Desalination, Vol. 27, pp. 129-136.
39. **Hussain**, N., Shahid, K. A., Khan, I. H. and Rahman, S., (1994), "Oxidation of High Temperature Alloys at Elevated Temperatures in Air: I," Oxid. Met. Vol. 41, No. 3-4, pp. 251-269.

40. **Hwang**, Y. S. and **Rapp**, R. A., (1989), "Thermochemistry and Solubilities of Oxides in Sodium Sulfate-Vanadate Solutions," *Corrosion*, Vol. 45, No. 11, pp. 933-37.
41. **Indacochea** J. E., "Cr-Mo Steel Welding Metallurgy," (1992), *Key Engineering Materials*, Trans. Tech Publication, Vol. 69-70, pp.47-94.
42. **James**, P. J. and **Pinder**, L. W., (1997), "Effect of Coal Chlorine on the Fireside Corrosion of Boiler Furnace Wall and Superheater/Reheater Tubing," *Materials at High Temperatures*, Vol. 14, No. 3, pp. 187.
43. **Kane**, R. H., (1980), "Characterization of High Temperature Gaseous Environments," *Corrosion*, Vol. 36, No. 3, pp. 112-18.
44. **Kazuhio**, O., **Yoshiiatsu**, S., **Nobuo**, O., **Hiroyuki**, H., **Atsushi**, N. and **Shigeru**, M., (1995), "Mechanical and Corrosion Properties of High Strength 18% Cr Austenitic Stainless Steel Weldment for Boiler," *ISIJ International*, Vol. 35, No.10, pp.1258-1264.
45. **Kerby**, R. C. and **Wilson** J. R., (1973), "Corrosion of Metals by Liquid Vanadium Pentoxide and the Sodium Vanadates," *Trans. ASME*, January, pp. 36-44.
46. **Khanna**, A. S. and **Jha**, S. K., (1998), "Degradation of Materials Under Hot Corrosion Conditions," *Trans. Indian Inst. Met.*, Vol. 51, No. 5, pp. 279-90.
47. **Khare**, A.K., (1981) "Ferritic steels for High Temperature Applications," *ASM Metal Park, OH, Conf., Warren, PA.*
48. **Kingerley**, D. G., (1994), Chapter 17.4 "Boiler and Feedwater Treatment," in **Shreir**, L.L., **Jarman**, R.A. and **Burstein**, G.T. 'Corrosion, Third Edition' Butterworth Heinemann, London 1994.
49. **Kofstad**, P., (1990), "High Temperature Corrosion of Metals," *Proc. of Conf. on Microscopy of Oxidation*, London, pp. 1-9.
50. **Kolta**, G. A., **Hewaidy**, L. F. and **Felix**, N. S., (1972), "Reactions between Sodium Sulphate and Vanadium Pentoxide," *Thermochim. Acta*, Vol. 4, pp. 151-64.
51. **Koopman**, J. G., **Marselli**, E. M., **Jonakin**, J. and **Ulmer**, R. C., (1959); *Proc. Amer. Pwr. Conf*, 21, pp. 236.
52. **Krishna**, B. V. and **Sidhu**, R. K., (2002), "Pitting Corrosion of Steel Tubes in an Air Preheater, Practical Failure Analysis," *ASM Int.*, Vol. 2, No. 5, pp. 61-66.
53. **Kuiry**, C., **Seal**, S., **Bose**, S. K. and **Roy**, S. K., (1994), "Effect of Surface Preparation on the High-Temperature Oxidation Behaviour of AISI 316 Stainless Steel," *ISIJ Int.*, Vol. 34, No. 7, pp. 599-606.

54. **Kumar, R., Tewari, V. K. and Prakash, S., (2007),** "Studies on Hot Corrosion of the 2.25 Cr-1Mo Boiler Tube Steel and Its Weldments in the Molten Salt Na₂SO₄-60 pct V₂O₅ Environment," Metallurgical and Materials Transaction A, Vol. 38, pp. 54-57.
55. **Lai, G. Y., (1990),** "High Temperature Corrosion of Engineering Alloys," ASM International Book.
56. **Lambert, P., Chanpaigne, B. and Arseneault, B., (1991),** "Oxidation and Hot Corrosion in Na₂SO₄-10%V₂O₅ of Ni-17Cr-6Al-0.5Y and Ni-16 Cr-5.7Al-0.47Y-5Si, MCrAlY Alloys at 700^oC," Can. Metall. Quart., Vol. 30, No. 2, pp. 125-130.
57. **Liaw, P.K., Logsdon, W.A.; Begley, J.A., (1989),** "Fatigue crack growth behavior of pressure vessel steels and submerged arc weldments in a high-temperature pressurized water environment," Metallurgical Transactions A (Physical Metallurgy and Materials Science), Vol. 20A, No. 10, Oct. 1989, pp. 2069-2086.
58. **Lundin, C. D., Kelly, S. C., Menon, R. and Kruse, B. J., (1986),** "Stress Rupture Behavior of Postweld Heat Treated 2 1/4Cr-1Mo Steel Weld Metal," Welding Research Council Bulletin 315, New York, USA.
59. **Luthra, K. L. and Shores, D. A., (1980),** "Mechanism of Na₂SO₄ Induced Corrosion at 600-900 ^oC," J. Electrochem. Soc., Vol. 127, No. 10, pp. 2202-10.
60. **Luthra, K. L., (1985),** "Kinetics of the Low Temperature Hot Corrosion of Co-Cr-Al Alloys," J. Electrochem. Soc., Vol. 132, No. 6, pp. 1293-98.
61. **Lvan, H., (1995),** "Weldability of Modern Steel Materials," ISIJ International, Vol. 35, No. 10, pp. 1148-1156.
62. **Mayer, K. H., Bendick, W., Husemann, R.U., Kern, T. and Scarlin, R. B (1998),** "New Materials for Improving the Efficiency of Fossil-Fired Thermal Power Stations," VGBPowerTech (1998) No.1 pp 22-27.
63. **Metal Hand book, (1976),** Welding and Brazing, ASM International, Metals Park, Oh., 9th Ed, Vol. 6.
64. **Misra, A. K., (1986),** "Mechanism of Na₂SO₄-Induced Corrosion of Molybdenum Containing Nickel-Base Superalloys at High Temperatures," J. Electrochem. Soc., Vol. 133, No. 5, pp. 1029-1037.
65. **Moujahid, S. E., (1987),** "High Temperature Corrosion of Cast Iron Chains by Coal Ash," Proc. of 10th ICMC, Madras, India, Vol. I, pp. 857-60.
66. **Natarajan, S. and Sivan, V., (2003),** "Weldment corrosion and its inhibition in power-generating components," Jrl. of Corrosion prevention and control, Vol. 50, No.1, pp 7- 19.

67. **Natarajan, S.** and Babu, S. P. K., (2006) "Corrosion and its inhibition in SA213-T22 TIG Weldments used in power plants under neutral and alkaline environments," *Materials Science and Engineering: A*, Vol. 432, No.1-2, pp. 47-51.
68. **Natesan, K.**, (1985), "High-Temperature Corrosion in Coal Gasification Systems," *Corrosion*, Vol. 41, No. 11, pp. 646-55.
69. **Nelson, W.** and Cain, C., (1960), "Corrosion of Superheaters and Reheaters of Pulverised Coal Fired Boilers," *J. Eng for Power*, Vol. 82, Ser A, No. 3, pp. 194-201.
70. **Olson, D. L.**, North, T. H. (eds), (1992), "Ferrous alloy Weldments," Trans Tech publications.
71. **Oreper, G. M.** and Szekely, J., (1984), "Heat and fluid flow phenomena in Weld Pools," *Journal of fluid Mechanics*, Vol. 147, pp. 53- 79.
72. **Otero, E.**, Merino, M. C., Pardo, A., Biezma, M. V. and Buitrago, G., (1987), "Study on Corrosion Products of IN657 Alloy in Molten Salts," *Proc. of 10th ICMC, Madras, India*, Vol. IV, pp. 3583-91.
73. **Otero, E.**, Pardo, A., Hernaez, J. and Perez, F. J., (1992), "The Corrosion of Some Superalloys (At 1000 K) in Molten Eutectic Mixture 60% V₂O₅- 40% Na₂SO₄, the Influence of the Oxygen and Carbon residues," *Corros. Sci.*, Vol. 34, pp. 1747-57.
74. **Pantony, D. A.** and Vasu, K. L., (1968), "Studies in the Corrosion of Metals Under Melts-1. Theoretical Survey of Fire-Side Corrosion of Boilers and Gas-Turbines in the Presence of Vanadium Pentoxide," *J. Inorg. Nucl. Chem.*, Vol. 30, pp. 423-32.
75. **Parker, J. D.**, Sidey, D. (1986), *Materials Forum*, Vol. 9, n1-2, 1st- 2nd Quarter, pp. 78-89.
76. **Paulo, J. M.**, Eustaquio, R. A., Iaci, M. P., (2000), "TIG Welding with single- component fluxes," *Journal of Materials Processing Technology*, Vol. 99, pp. 260 -265.
77. **Peddle, B.E.** and Pickles, C. A., (2001) "Carbide development in the Heat affected zone of tempered and post weld heat treated 2.25 Cr-1 Mo Steel weldments," *Canadian Metallurgical Quarterly*, Vol. 40, No 1, pp. 105-126.
78. **Peddle, B. E.**, Pickles, C. A., (2000), "Carbide and Hardness Development in the Heat Affected Zone of Tempered and Postweld Heat Treated 2.25 Cr-1Mo Steel Weldments," *Journal of Materials Engineering and Performance*, Vol. 9, No. 5, pp. 477-488.
79. **Peters, K. R.**, Whittle, D. P. and Stringer, J., (1976), "Oxidation and Hot Corrosion of Nickel -Based Alloys Containing molybdenum," *Corros. Sci.*, Vol. 16, pp. 791-804.
80. **Pettit, F. S.** and Giggins, C. S., (1987), "Hot Corrosion, Ch. 12," *Superalloys II*, Sims, C. T., Stolof, N. S. and Hagel, W. C. (Eds.), Wiley Pub., N. Y.

81. **Pettit**, F. S. and **Meier**, G. H., (1984), "Oxidation and Hot corrosion of Superalloys," Superalloys (1984), M. Gell, C. S. Kartovich, R. H. Bricknel, W. B. Kent, J. F. Radovich.
82. **Prakash**, S., **Singh**, S., **Sidhu**, B. S. and **Madeshia**, A., (2001), "Tube Failures in Coal Fired Boilers," Proc. National Seminar on Advances in Material and Processing, 9-10th Nov., IIT, Roorkee, India, pp. 245-53.
83. **Prakash**, S. and **V.K. Tiwari**, (1992), QIP Short-Tent Course Proceedings, U.O.R., Roorkee, June23-July 07.
84. **Raman**, R. K. S., (1999), "Role of Gaseous Environment and Secondary Precipitation in Microstructural Degradation of Cr-Mo Steel Weldments at High Temperatures," Metallurgical and Materials Transactions A, Vol. 3, pp. 2103-2113.
85. **Raman**, R. K. S., (2000), "Relevance of High Temperature Oxidation in Life Assessment and Microstructural Degradation of Cr-Mo Steel Weldments," Metallurgical and Materials Transactions A, Vol. 31 A, pp. 3101-08.
86. **Raman**, R. K. S., (1998) "Role of Microstructural Degradation in the HAZ of 2.25Cr-1Mo Steel Weldments on Sub-scale Features during Steam Oxidation and their Role in Weld Failures," Met. & Mat. Trans A, Vol. 29A, pp. 577-585.
87. **Raman**, R. K. S., (1995), "Influence of Microstructural Variations on the Oxidation of Weldment of 2.25 Cr -1 Mo Steel," Met. & Mat. Trans A, Vol. 26A, pp. 1847-1858.
88. **Raman**, R. K. S., (2002), "Thermal Scaling Behaviour of Weldments of 9Cr-1Mo Steel and its Relevance to the Life Assessment of Fossil Fuel Power Plant Components," Metallurgical and Materials Transactions A (Physical Metallurgy and Materials Science), Vol. 33A, No. 10, pp. 3296.
89. **Raman**, R. K. S. and **Muddle B.C.**, (2000A), "Role of High Temperature Corrosion in Life Assessment and Microstructural Degradation of Cr-Mo Steel Weldments," International Journal of Pressure Vessels & Piping, Vol. 77, pp 117-123.
90. **Raman**, R. K. S. and **Muddle B.C.**, (2002A), "High Temperature Oxidation in the context of life assessment and Microstructural Degradation of weldments of 2.25Cr-1Mo Steel," International Journal of Pressure Vessels & Piping, Vol. 79, pp. 585-590.
91. **Raman**, R. K. S., **Tyagi**, A. K., **Gnanamoorthy**, J. B., **Baldev**, R., **Roy**, S.K., (1998A), "Secondary Ion Mass Spectroscopy and Surface Profilometric Characterisation of Oxide Scales Developed over Welds Metal, Heat Affected Zone and Base Metal Regions in the Weldments of 9Cr-1Mo steel," Materials Science and Technology, Vol. 14, No. 4, pp. 357-366.

92. **Raman**, R. K. S., Laha, K., Gnanamoorthy, J. B. and Roy, S.K., (1994), "Oxidation behaviour of Microstructurally-Different Regions in the weldments of 9 Cr- 1 Mo Steel," *Oxidation of Metals*, Vol. 42, No.1/2, pp. 31-48.
93. **Raman**, R. K. S., Gnanamoorthy, J.B., (1995A), "Oxidation Behaviour of the Weld Metal, the Heat Affected Zone and the Base Metal Regions in the Weldment of 'Cr-Mo Steels," *Welding Journal* (Miami, Fla), Vol. 74, No. 4, pp. 133-139.
94. **Raman**, R. K. S., Gnanamoorthy, J. B., (1993), "The Oxidation Behaviour of the Weld Metal, Heat Affected Zone and Base Metal in the Weldments of 2.25 Cr -1 Mo Steel," *Corrosion Science*, Vol. 34, No. 8, pp. 1275-88.
95. **Raman**, R. K. S., Khanna, A.S., Tiwari, R. K. and Gnanamoorthy, J.B. (1992), "Influence of Grain size on the Oxidation Resistance of 2.25Cr 1Mo steel," *Oxid. Met.*, Vol. 37, pp. 1-12.
96. **Rapp**, R. A. and Zhang, Y. S., (1994), "Hot Corrosion of Materials: Fundamental Studies," *JOM*, Vol. 46, No. 12, pp. 47-55.
97. **Rapp**, R. A., (1986), "Chemistry and Electrochemistry of the Hot Corrosion of Metals," *Corrosion*, Vol. 42, No. 10, pp. 568-77.
98. **Rapp**, R. A., (2002), "Hot Corrosion of Materials: A Fluxing Mechanism," *Corros. Sci.*, Vol. 44, No. 2, pp. 209-21.
99. **Rapp**, R. A. and K. S. Goto, (1981), "The Hot Corrosion of Metals by Molten Salts," Symposium on Fused Salts, J. Braunstein and J. R. Selman (Eds.), The Electrochemical Society, Pennington, N. J., pp.159.
100. **Ray**, A. K., Sahay, S. K. and Goswami, B., (2003), "Assessment of service exposed Boiler Tubes," *Engineering Failure Analysis*, Vol. 10, No. 6, pp. 645-654.
101. **Reid**, W. T., (1971), "External Corrosion and Deposits - Boilers and Gas Turbines," American Elsevier Publishing Company Inc. New York, 1971.
102. **Sachs**, K., (1958), "Accelerated High Temperature Oxidation due to Vanadium Pentoxide," *Metallurgia*, pp. 167-173.
103. **Sadique**, S. E., Mollah, A. H., Islam, M. S., Ali, M. M., Megat, M. H. H. And Basri, S., (2000), "High Temperature Oxidation behaviour of Iron Chromium-Aluminium Alloys," *Oxid. Met.*, Vol. 54, Nos. 5-6, pp. 385-400.
104. **Seiersten**, M. and Kofstad, P., (1987), "The Effect of SO₃ on Vanadate-Induced Hot Corrosion," *High Temp. Technol.*, Vol. 5, No. 3, pp. 115-22.

105. **Sharma, R. N.**, (1996), "Hot Corrosion behaviour of Iron and Nickel Base Superalloys in Salt Environments at Elevated Temperatures," Ph.D. Thesis, Met. And Mat. Engg. Deptt. UOR, Roorkee, India.
106. **Shi, L.**, (1993), "Accelerated Oxidation of Iron Induced by Na₂SO₄ Deposits in Oxygen at 750⁰C- A New Type Low-Temperature Hot Corrosion," *Oxid. Met.*, Vol. 40, Nos. 1-2, pp. 197-211.
107. **Shores, D. A.**, (1983), "New Perspectives on Hot Corrosion Mechanisms," High Temperature Corrosion, R.A. Rapp (Ed.), NACE, Houston, Texas.
108. **Sidhu, B.S., Prakash S.**, (2003), "Evaluation of the corrosion behaviour of plasma-sprayed Ni₃Al coatings on steel in oxidation and molten salt environments at 900 °C," *Surf. Coating Technol.*, Vol. 166, pp. 89–100.
109. **Sidhu, B. S.**, (2003A), "Studies on the role of Coatings in improving Resistance to Hot Corrosion and Degradation," Ph.D. Thesis, Met. And Mat. Engg. Deptt. IITR, Roorkee, India.
110. **Sidky and Hocking**, (1987), "The hot corrosion of Ni-based ternary alloys and superalloys for application in gas turbines employing residual fuels," *Corros. Sci.*, 27(5), pp. 499.
111. **Srinivasan, P. B., Sharkawy, S.W., Dietzel, W.**, (2004) "Hydrogen assisted stress-cracking behaviour of electron beam welded supermartensitic stainless steel weldments," *Materials Science and Engineering A*, Vol. 385, No. 1-2, pp. 6-12.
112. **Staubli, M., Bendick, W., Orr, J., Deshayes, F. and Henry, Ch.**, (1998), "European Collaborative Evaluation of Advanced Boiler Materials" in *Materials for Advanced Power Engineering*, Proceedings of a Conference held in Liege, Belgium, 5-7, October 1998, Edited by Lecomte-Beckers, J. et al. Forschungszentrum Julich GmbH, pp. 87-104.
113. **Stott, F. H.**, (1998), "The Role of Oxidation in the Wear of Alloys," *Trib. Int.*, Vol. 31, No. 1-3, pp. 61-71.
114. **Suito, H. and Gaskell, D. R.**, (1971), "The Thermodynamics of Melts in the System VO₂-V₂O₅," *Metall. Trans.*, Vol. 2, pp. 3299-303.
115. **Tiwari, S. N. and Prakash, S.**, (1996), "Hot Corrosion Behaviour of an Iron-Base Superalloy in Salt Environment at Elevated Temperatures," *Proc. of Symp. on Metals and Materials Research*, IIT, Madras, 4-5th July, pp. 107-17.
116. **Tiwari, S. N.**, (1997), "Investigations on Hot Corrosion of Some Fe-, Ni- and Co-Base Superalloy in Na₂SO₄-V₂O₅ Environment Under Cyclic Conditions," Ph. D. Thesis, Met. and Mat. Engg. Deptt., UOR, Roorkee, India.

117. **Tsay, L.W., Lin, W.L., Che .W. and Lei 3.,** (1997) "hydro it corrosion cracking of 2.25Cr-Mo Steel Weldments," *Corrosion Science*, Vol. 39, No. pp. 1165-1176.
118. **Tsuge, H., Tarutani, Y. and Kudo, T.,** (1988), "The effect of nitrogen on the localize corrosion resistance of duplex stainless steel simulated Weldments," *Corrosion (NACE)* Vol. 44, No. 5, pp. 305-14.
119. **Viswanathan, R. and Bakker, W.** (2001), "Materials for Ultrasupercritical Coal Power Plants - Boiler Materials: Part 1," *Journal of Materials Engineering and Performanc* Vol.10, No 1, pp. 81 - 95.
120. **Viswanathan, R., Gandy, D. W.,** (1999), "Performance of Repair Welds on Aged Cr-Mo Piping Girth Welds," *Journal of Materials Engineering and Performance*, Vol. 8, pp. 579-90.
121. **William, E., W.,** (1992) "Observations of the influence of Microstructure on Corrosion of Welded conventional and Stainless Steels", *Materials Characterization*, Vol. 28, pp. 349-358.
122. **Wood, G. C. and Stott, F. H.,** (1995), "Directions for future research in high-temperature," *Oxidation of Metals*, Vol. 44, No. 1-2, pp. 375-397.